UNIVERSITEIT VAN PRETORIA
UNIVERSITY OF PRETORIA
YUNIBESITHI YA PRETORIA

Analysis of hyperbolic-type partial differential equations for non-Fourier type heat conduction models

by

Rheinhardt Hendrik Sieberhagen

Student number: 90462752

Supervisor: Prof NFJ van Rensburg

Submitted in fulfilment of the requirements for the degree

Philosophiae Doctor

in the Faculty of Natural and Agricultural Sciences

University of Pretoria
Pretoria

October 2023

DECLARATION

I declare that the thesis, which I hereby submit for the degree Philosophiae Doctor at the University of Pretoria, is my own work and has not previously been submitted by me for a degree at this or any other tertiary institution.

Signature:

Name: Rheinhardt Hendrik Sieberhagen

Date: October 2023

Summary

by Rheinhardt Hendrik Sieberhagen

Supervisor: Prof NFJ van Rensburg

Heat transfer modelling is routinely used to model the interaction between a heat source and a material specimen in applications such as additive manufacturing and medical surgery.

The Fourier heat conduction model is well-known in the field of heat transfer, but in cases involving ultra-short heat pulses, or extremely small specimens, alternative models such as the Cattaneo-Vernotte (C-V) and dual-phase-lag (DPL) models are proposed. These two models are based on the concept of lagging responses (or lag times) in the heat flux and the temperature gradient.

In 1982 an article appeared that reported on the existence of unwanted oscillations related to a so-called "benchmark" problem that is based on the C-V model. This problem was studied and it was shown that the unwanted oscillations is the result of an ill-posed problem and not due to the choice of the numerical technique used to solve the problem. The problem was re-formulated to have a smooth initial condition and divided into auxiliary problems. It was solved using D'Alembert's and the finite element method, resulting in an oscillation-free solution.

The theory and terminology of vibration analysis, *e.g. overdamped and underdamped modes*, were incorporated into the Fourier, C-V and DPL heat conduction models. Weak variational formulations of these models, in terms of bilinear forms, were presented and the well-posedness of the model problems was established, based on a general existence result published in 2002.

The modal analysis method was applied to the model problems and formal series solutions were derived. Convergence of the series solutions was proved in terms of the energy and inertia norms. This was used as a guideline to ensure accurate approximations for the series solutions of the model problems.

Realistic lag time values were derived using modal analysis. This relied on the assumption that the solutions for the C-V and Fourier models will be the same after a sufficiently long time.

The concept of a *wane time* was introduced as the time instant at which the Fourier and C-V model predictions will correspond. This was proved with numerical experiments based on a continuous-heating model problem.

Two model problems, based on single- and multi-pulse heating, were used to study aspects such as the contribution of overdamped and underdamped modes to the predicted temperature, the influence of the lag time values on the C-V and DPL model predictions, and the effect of heating parameters, *e.g.* the duty ratio and the number of heating pulses on the model predictions.

In conclusion, modal analysis proved to be successful in determining reliable lag times values and was effective for the numerical investigations into the properties of the solutions of the model problems. Future research should focus on investigating model problems that resemble reliable experimental techniques, thereby facilitating comparison of theory with practice.

Contents

Chapter 1

Introduction

1.1 Mathematical models for heat conduction

Thermal energy is transported through a specimen by a process of heat transfer. Heat transfer is generally described by the well-known Fourier model (also known as the parabolic model or diffusion equation) and given by

$$\partial_t T = \frac{k}{\rho c_p} \nabla^2 T, \tag{1.1.1}$$

where T denotes the temperature, k the thermal conductivity, ρ the density and c_p the specific heat.

The derivation of the Fourier model is based on the assumption that the heat flux vector and temperature gradient occur simultaneously. An important consequence of this assumption is that a thermal disturbance propagates at an infinite speed through the specimen [CT82]. For modelling heat transfer induced by short-pulse lasers, or in cases where the material specimen has small dimensions this assumption may not hold ([TZ98], [ZCG14]). Several alternative models have been derived based on the concept of lagging responses in the heat flux and the temperature gradient. These include models such as the Cattaneo-Vernotte (C-V) model (also known as the hyperbolic model or the thermal wave model) and the *linearized* dual-phase lag (DPL) model.

The C-V model ([CT82], [NBB15], [OT94]) is given by

$$\tau \partial_t^2 T + \partial_t T = \frac{k}{\rho c_p} \nabla^2 T, \tag{1.1.2}$$

where τ is the relaxation (or lag) time associated with the setting up of the heat flux vector. The model is based on the assumption that the temperature gradient causes heat to flow, while the heat flux becomes the effect of the temperature gradient. The C-V model introduces the concept of a finite wave speed c at which the thermal disturbance travels. The wave speed is related to the lag time through the relation $c^2 = k/(\rho c_p \tau)$ [Tzo97].

Similarly, the *linearized* DPL model ([Tzo97], [Tzo95a]) is given by

$$\tau_q \partial_t^2 T + \partial_t T = \frac{k}{\rho c_p} \left(\nabla^2 T + \tau_T \partial_t (\nabla^2 T) \right) \tag{1.1.3}$$

where τ_q and τ_T are the phase lags of the heat flux vector and the temperature gradient, respectively. The *linearized* DPL model allows either the temperature gradient or the heat flux vector to be the cause, with the remaining quantity becoming the effect. (In the remainder of this thesis we will refer to the "DPL" model.) We take $\tau = \tau_q$, in order to compare the C-V and DPL models.

These models are routinely used to model the interaction between heat sources and a material specimen. Additive and subtractive manufacturing processes, as well as bio-heating procedures rely on the generation of heat within a material specimen by a laser or other suitable source ([KG07], [ULY21], [YKN04]). Modelling the heat transfer allows one to observe the effect of the relevant process parameters, *e.g.* the laser pulse width, on the predicted temporal and spatial behaviour of the heat energy induced in a given specimen. Heat transfer modelling also plays a crucial role in determining the thermal diffusivity α, defined by $\alpha = k/(\rho c_p)$, from experimentally obtained data. The laser flash ([BTY11], [PJBA61]) and thermoreflectance ([BYTW10], [TBO01]) methods rely, respectively, on single-pulse or multi-pulse heating of a given specimen.

Our main concern is the different models proposed as alternatives to the Fourier model. The following articles, published from 2014 to 2022, prove that the C-V and DPL models continue to be of interest to the international research community: Zhang *et al* [ZCG14] developed a technique to better analyse the damping behaviour of thermal waves, as predicted by models such as the C-V and DPL models. They believe that this will benefit the analysis of experimental and engineering problems. In [NBB15] the C-V model is recommended above the Fourier model, the argument being that the Fourier model is not suitable when the dimensions of the specimen is comparable with, or smaller than the phonon mean free path. Tan *et al* ([TWZWO18]) derived a hyperbolic heat conduction equation to model the process of laser ablation by combining the C-V model's constitutive equation with the energy

conservation equation, including a source term. The authors found that the model predictions based on the C-V model, is in better agreement with experimental results than the predictions based on the Fourier model. Jha and Oyelade ([JO22]) studied a transient free convection flow problem, typically encountered in applications such nuclear reactors and solar energy collectors. They compared the Fourier, C-V and DPL models, emphasizing the effect that the lag times have on the model predictions in the case of the DPL model.

Also of interest are the publications reporting on the application of the C-V and DPL models in bio-heat transfer problems. G R Ströher and G L Ströher [SS14] calculated numerical solutions to the Fourier and C-V models and compared this to analytical solutions of the same models reported on in the literature. Kumar *et al* [KSR16] modelled bio-heat transfer in various biological tissues using the Fourier, the single-phase-lag (SPL) and the DPL models and came to the conclusion that the results obtained with the DPL model best agrees with experimental results. Majchrzak and Stryczyński ([MS21]) studied a problem concerning the use of thermal therapy to treat a tumour embedded in biological tissue. They used the DPL model to predict the temperature distribution in the blood vessels surrounding the tissue, as well as in the heated tumour present in the tissue. They compared the DPL model with the Pennes model, which is based on the Fourier model. Noticeable differences were found between the respective model predictions.

1.2 Research aim

Our initial research aim was to identify suitable mathematical techniques to solve heat transfer problems modelled after the Fourier, C-V and DPL models, and then to compare the respective model predictions, given well-defined model problems. During subsequent literature studies it came to our attention that some researchers obtained unwanted or spurious oscillations when solving the C-V heat equation numerically. This led us to investigate the so-called "benchmark" problem which was originally formulated by Carey and Tsai [CT82] and later on referred to as the "benchmark" problem by Huang and Wu [HW06]:

$$\begin{aligned} \partial_t^2 T(x,t) + 2\partial_t T(x,t) &= \partial_x^2 T(x,t), \\ T(0,t) = 1 \qquad \partial_x T(1,t) &= 0, \\ T(x,0) = \partial_t T(x,0) &= 0. \end{aligned}$$

We will refer to it as the *CT-benchmark* problem.

Carey and Tsai, and Huang and Wu, as well as other researchers ([JLZ02] [LC04] [LCP05]), reported on the presence of spurious numerical oscillations in their results when solving problems based on the C-V model. A common conclusion was that these oscillations are due to the presence of sharp wave fronts [LC04]. In many cases the researchers attempted to remove or reduce the oscillatory behaviour by applying various numerical techniques.

We aim to show that the oscillations are due to the fact that the problems are not well-posed, and not a consequence of the choice of numerical technique. Furthermore, we want to re-formulate the benchmark problem into a form that is well-posed, resulting in an oscillation-free solution, not only to the benchmark problem, but also to problems with similar initial conditions. Clearly it is necessary to explain what is meant by a *well-posed* problem. This is done in Section 4.4.

We then turn our attention to the models proposed as alternatives to the Fourier model, *i.e.* the C-V and DPL models. From the literature we have seen arguments against and in favour of using either the Fourier, the C-V or the DPL model to predict heat transfer in solids. It appears that factors such as the magnitude of the parameters as well as the dimensions of the specimen determines the suitability of a specific model to a given problem. Matters are further complicated by the lack of reliable parameters, especially the lag times τ, τ_q and τ_T that are associated with the C-V and DPL models. Some researchers are in favour of calculating these parameters theoretically, whilst others prefer to determine these parameters experimentally, even though their experimental methodologies, and analysis of results, are criticised ([Mai19] [OA12]).

Our main aim is to determine the validity of these models and determine the lag times by deriving conclusions from the mathematical analysis of these models and not from experimental results. By mathematical analysis we include all mathematical approaches, *i.e.* theoretical derivations, theoretical computations and numerical comparisons.

1.3 Discussion of research objectives

As stated earlier, our initial aim was to validate the C-V and DPL models against the Fourier model, using suitable mathematical techniques to solve the models. Subsequent literature studies revealed two crucial aspects that have to be addressed before attempting to solve these models: firstly, ensure that the model problem is well-posed, *i.e.* a solution must exist and it has

to be unique; secondly, determine reliable lag times τ, τ_q and τ_T ([CT82] [HW06] [OA12]). As mentioned in Section 1.2, we will defer the discussion of well-posed problems to Section 4.4.

We start in Chapter 2 with a summary of the mathematical models for heat transfer. With the focus of our study being the Fourier, C-V and DPL models, we restrict our discussion mainly to these models, briefly referring to other models where applicable. We elaborate on the DPL model since it is described as a *unified* model, *i.e.* it accommodates all the fundamental mechanisms associated with phono-electron interaction, phonon scattering, thermal waves and diffusion ([Tzo95a]). Dimensionless versions of these mathematical models are derived. We introduce our heat absorption model and use it as input when deriving the boundary and initial conditions for our model problems. Our heat absorption model stems from the model problem that Tzou and others ([BH69] [Tzo97]) regarded as ideal to study the influence of the lag times τ_q and τ_T. This model problem concerns a case where a specimen is suddenly exposed to a continuous heat source at one end. The heat source is modelled by specifying the boundary condition at the boundary that is being heated. We extend this model to a case where a specimen is heated by a single step pulse, or a multiple of step pulses. Three model problems are therefore formulated: continuous, single-pulse and multi-pulse heating. The validation of the heat transfer models is done by comparing the respective model predictions retrieved from using these model problems.

In Chapter 3 we suggest two options for formulating well-posed alternatives to the CT-benchmark problem ([SV11]): either include a jump condition; or smooth the initial value by adjusting the initial condition $T(x,0) = 0$ so that it has an initial smooth temperature distribution near $x = 0$ ([Wei95]). In this way we show that the cause of the unwanted oscillations in the case of the benchmark problem is the fact that the problem is not well-posed, and not a result of the choice of numerical technique.

Chapters 4 and 5 discusses the well-posedness of our model problems, as well as the convergence of the solutions ([CVV18] [VV02]). An abstract hyperbolic-type heat transfer model is formulated in a Hilbert space setting. The weak variational formulations of the respective model equations are derived so that existence theory can be applied. Formal series solution approximations of the problems are derived using a generalised separation of variables method, and the validity thereof is proved. The convergence of the partial sums is addressed.

We mentioned at the beginning of this chapter that reliable lag times for the C-V and DPL models are not available. Yet, it is critical to have reliable

values for the lag times when modelling heat transport. Researchers rely on either calculating these lag times theoretically or measuring it experimentally. There is however no consensus on this matter, as highlighted by Ordóñez-Miranda and Alvarado-Gil [OA12].

Our approach in finding reliable lag time parameters involve a comparison of the Fourier, the C-V and the DPL models using separation of variables. We formulate our model problems such that the model-specific partial differential equation together with its boundary and initial conditions, constitute a well-posed problem. The formal series solution approximations of the problems, developed in Chapter 5, are applied to the model problems. We define three model problems to compare the Fourier, C-V and DPL models. The first two problems are studied in Chapter 6. The first problem concerns a specimen that is heated continuously at one endpoint (*i.e.* the problem suggested by Tzou to illustrate the lagging behaviour of the DPL model ([Tzo97])). The second problem deals with a single heat pulse applied to the endpoint. The third problem is aimed at two physical applications, thermoreflectance and bio-heating, where the endpoint is heated by multiple pulses (Chapter 7).

We rely on the series solution approximation to find reliable lag time parameters ([VVS21]). For τ ($= \tau_q$) our strategy is to determine if the results from the C-V and Fourier models will be the same (within a user-specified error) after some time t, at least for the first mode. This strategy is based on the assumption that the Fourier model will yield physically realistic results after a sufficiently long time. A ballpark value for τ is determined based on a user-defined accuracy and considerations based on practical measurement capability. The DPL model is then compared with the Fourier and C-V models. As $\tau = \tau_q$ is aready determined for the C-V model, the value of τ_T has to be such that the DPL solution will also be overdamped for the same number of modes than the C-V model.

Since the models are dimensonless, it follows that the lag time values are also dimensionless. The lag time values are used for the model problems involving constant heating as well as single-pulse heating. For the the third model problem we introduce scaling factors suitable to the physical scenarios being investigated to convert to dimensionless problems. This simplifies interpretation of the results.

Chapter 8 provides a comprehensive summary of the work done, key results, and lastly, suggestions for future research.

For convenience, an appendix is included that lists the mathematics and physics notation frequently used in this thesis. In addition, the notation associated specifically with heat transfer, is summarized in Section 2.2.

Chapter 2

Mathematical models for heat transfer

The main part of this chapter provides a physics-based discussion and derivation of the heat conduction models of interest to us. The last two sections, Sections 2.7 and 2.8, introduces the boundary and initial conditions, as well as the dimensionless mathematical models on which our theoretical derivations and model problem formulations are based.

It is necessary to do a review of the current state of knowledge on the topic of heat transfer in solids before attempting new research. As mentioned in Chapter 1, there is an ongoing debate to decide on the most suitable model for heat transfer in solids. This review is an attempt to provide a concise report on the heat transfer models most commonly studied by researchers.

Engineering applications require that the thermal conductivity k, the thermal diffusivity α, and the lag times τ, τ_q and τ_T be well known under various conditions (such as high temperatures) and for the same medium, but for different microstructures of this medium (*e.g* solid versus thin film) [Tzo97]. Maillet criticises a number of published papers reporting on the use of the Fourier, C-V and DPL models [Mai19]. He concludes that proper experimental design and analysis of results are essential when comparing different models and attempting to derive heat transfer parameters. Ordòñez-Miranda *et al* gave a good summary of the situation regarding the determination of the lag time τ associated with the C-V model [OA12]. They reported that some researchers determine the lag time experimentally and others rely on theoretical calculation.

A good example of the controversy surrounding the experimental measurement of τ is the work done on heat transport in non-homogeneous materials

(such as biological tissue and sand). Some researchers claim that hyperbolic effects are easily observed during experiments, reporting lag times in the order of seconds in processed meat, copper-coated lead spheres and synthetic sand ([Kam90] [MKVM95]). There experimental methods, and therefore also their results, were met with criticism from other researchers who performed similar measurements and claimed that they could find no evidence of the hyperbolic effect, concluding that the Fourier model is sufficient in this case [OA12]. Roetzel *et al* [RPD03] studied this case, in the end disagreeing with both teams' experimental philosophies. There main critisism was that both research teams determined τ and α independently, whilst according to them, it should be measured simultaneously.

Tzou provides us with an example of a theoretical calculation [Tzo95a]. He describes how he calculated the lag times for various metals using formulas that he derived from the parabolic two-step model for heat transfer. He did however point out that his method of calculation only yields reliable results if constant thermal properties are assumed, ballistic electron component effects are excluded and if thin specimens are studied (although he did not specify any actual thickness).

From the above discussion, it is clear that reliable values for the lag times present in the C-V and DPL models are not available. Our point of departure is to get more clarity on how to determine reliable values for these lag times. We will attempt do determine these values through mathematical analysis and not through experimentation – this will be dealt with in Chapter 6.

2.1 Heat transfer in solids

Heat transfer in solids is a physical phenomenon that is brought about by a number of physical mechanisms (characteristic of the type of material that is involved, *e.g.* metals, semiconductors, insulators etc.) and further influenced by factors such as the physical dimensions of the material and the temporal nature of the applied heat source. In a microscopic sense, heat transfer can be described as a process whereby energy carriers collide with each other, transferring energy from one carrier to another. The average distance travelled by a carrier between two successive collisions are defined as the mean free path and the time required to travel this average distance, the mean free time.

If we consider a solid, crystalline substance, we can describe it as a periodic structure made up of atoms or molecules. This is known as the lattice, with

the atoms/molecules situated at the lattice nodes. It is customary in the field of solid state physics to model the atoms as a system of coupled harmonic oscillators which vibrate collectively according to their vibrational normal modes. The energy associated with such a vibrational mode is known as a phonon [CDL77]. When phonons interact with each other it is commonly referred to as phonon-scattering or phonon collisions. When electrons interact with phonons (for example in the case of a metal), it is referred to as phonon-electron interaction. Although a phonon is not a real physical particle, its modes of interaction is described as if it is a particle that possesses energy and can transfer its momentum. The phonons and electrons therefore act as the heat (or energy) carriers.

Various mathematical models have been developed over the years, based on the underlying physical mechanisms that are believed to be responsible for heat transfer. These models may be classified under three types [Tzo97] [TZ98]:

- Macroscopic models
- Microscopic models
- Phase-lag models

The best known macroscopic model is the parabolic model, based on Fourier's law. We will refer to this model as the *Fourier model*. This model describes heat transport as a diffusive process that takes place on a macroscopic level both in space and time. A macroscopic process will require that a large number of heat carriers ($e.g \sim 10^{23}$) interact with each other within a large physical domain ($i.e$ much larger than the mean free path), and over a long time (*i.e.* much longer than the mean free time) before an observation is made. Fourier's law relies on the basic assumption that the onset of heat flow follows immediately after the establishment of a temperature gradient across a material specimen. This assumption was however criticised and the idea started to develop that a time delay (or time lag) exists between the instant when heat flow starts and the establishment of a temperature gradient. This resulted in the development of a thermal wave model (popularly known as the C-V model). Although the thermal wave model is classified as a macroscopic model, it does, according to Tzou [Tzo97], describe microscale effects in time.

Further research into heat transport led to the belief that the microscopic characteristics of materials should be considered when attempting to model heat transport. The microscopic situation exists when the physical dimensions of the specimen is of the same order as the mean free path of the energy

carriers and the interaction time is of the same order as the mean free time. With these models it becomes important to make a distinction between different material types, since different energy carriers are involved in the heat transfer process. In metallic films it is believed that heat transport is brought about by the interaction between phonons and electrons, whilst in the case of dielectric materials, semiconductors and insulators, phonon scattering is responsible for heat transfer. This resulted in the microscopic models that include models such as the two-step and phonon-scattering models.

The phase-lag (or time lag) models (single-phase lag and dual-phase lag) is intended to link the macroscopic and microscopic approaches in modelling heat transfer. From the phase-lag models it is possible to derive the parabolic model, the C-V model, the two-step models and the phonon-scattering model.

2.2 Conservation of energy and constitutitve equations

Key to any model for heat transfer is the conservation of energy. To describe this mathematically, we define a fixed domain Ω for the specimen and consider an arbitrary region $\mathcal{D}$ (where $\mathcal{D}$ is in Ω) with a boundary defined as $\mathcal{E}$. Table 2.1 summarizes the notation typically associated with heat transfer, used throughout this and subsequent chapters.

Table 2.1: Heat transfer notation

Symbol	Description	Units
$[\rho]$	(Volume density)	$kg\,m^{-3}$
$[c_p]$	(Specific heat capacity)	$J\,kg^{-1}\,K^{-1}$
$[k]$	(Thermal conductivity)	$W\,m^{-1}\,K^{-1}$
$[\alpha]$	(Thermal diffusivity)	$m^2 s^{-1}$
$[q]$	(Heat flux)	$W\,m^{-2}$
$[T]$	(Temperature)	K or $^\circ C$
$[\tau]$	(Relaxation time)	s
$[\tau_q]$	(Lag time associated with q)	s
$[\tau_T]$	(Lag time associated with ∇T)	s

The quantity of heat that is required to raise the temperature of the material

in $\mathcal{D}$ from 0 K to T K is

$$\iiint_{\mathcal{D}} \rho c_p T \, dV.$$

We define n as the outward unit vector that is normal to $\mathcal{D}$. Then the heat flux q across $\mathcal{E}$ into $\mathcal{D}$ is given by

$$-\iint_{\mathcal{E}} q \cdot n \, dS.$$

The basic assumption of the theory is that the quantity of heat entering $\mathcal{D}$ per unit time must equal the amount of flux entering into it:

$$\frac{d}{dt} \iiint_{\mathcal{D}} \rho c_p T \, dV = -\iint_{\mathcal{E}} q \cdot n \, dS.$$

A consequence of the conservation of heat energy is that

$$\rho c_p \partial_t T = -\nabla \cdot q. \tag{2.2.1}$$

The response of the heat flux q to a temperature gradient ∇ is determined when the relation for the conservation of energy is combined with a constitutive equation. Three different constitutive equations are of interest in this study: Fourier's law, the Cattaneo-Vernotte equation and the linearized dual-phase-lag equation. These are respectively given by

$$q = -k\nabla T, \tag{2.2.2}$$

$$q + \tau \partial_t q = -k\nabla T \tag{2.2.3}$$

and

$$q + \tau_q \partial_t q = -k \left[\nabla T + \tau_{_T} \partial_t \left(\nabla T\right)\right]. \tag{2.2.4}$$

Combining these constitutive equations with the energy conservation equation, and combining the thermal constants k, ρ and c_p into $\alpha = k/\rho c_p$, which is known as the thermal diffusivity, leads to the following governing equations for heat transfer:

The well-known Fourier model (or diffusion equation)

$$\partial_t T = \alpha \nabla^2 T, \tag{2.2.5}$$

the Cattaneo-Vernotte (C-V) model

$$\tau \partial_t^2 T + \partial_t T = \alpha \nabla^2 T \tag{2.2.6}$$

and the dual-phase-lag (DPL) model

$$\tau_q \partial_t^2 T + \partial_t T = \alpha \nabla^2 T + \alpha \tau_T \partial_t (\nabla^2 T). \tag{2.2.7}$$

As mentionded before, one of the goals set out for this study is to compare the C-V and the dual-phase lag (DPL) models with the parabolic model. These models have been the topic of interest for many years and are still considered to be valid [Lam13]. Whether or not a model is considered valid, depends on its range of applicability [EGJA06].

To determine the range, factors such as the time scale, the length scale and the specimen temperature should be considered. The parabolic model is considered valid when the specimen length is much larger than the mean free path of the electrons or phonons and when the time scale of the process being investigated is much larger than the mean free time of the electrons or phonons. Zhang *et al* [ZCG14] explained that the parabolic model is not valid for situations where pulsed high-power heat sources are used, ultra-low temperature conditions are present and microscale specimens or biological tissue are investigated.

Another argument (supported by experimental evidence [JLZ02]), is that the pulse duration of the thermal disturbance should be short enough and the heat flux high enough, to observe thermal behaviour that deviates from that predicted by the parabolic model – this provides a case for models such as the C-V and DPL models. They also concluded that the C-V and DPL models predicted their experimental results at least qualitatively.

Tang *et al* [TA99] used the C-V model to predict the results obtained by other researchers under experimental conditions of ultra-low temperatures and high-speed heating. They found good agreement with the experimental results.

Further evidence of the validity of the C-V and DPL models can be found in recently published articles. Nasri *et al* [NBB15] studied heat transport in semiconductor microstructures using the C-V model. They argued that the dimensions of the specimen was comparable to the phonon mean free path and therefore the parabolic model would not be suitable. Kumar *et al* [KSR16] studied heat transfer in biological tissue, comparing the parabolic, SPL and DPL models – their conclusion was that the DPL model yields the best results. As a final example, Askarizadeh and Ahmadikia [AA15] studied heat transfer in skin tissue, comparing the DPL, C-V and Pennes (a parabolic model based on Fourier's law) models.

2.3 Macroscopic heat transfer

2.3.1 Fourier model

The Fourier model is widely accepted for many engineering applications ([Sin94] [TZ98] [YS97a]). Typical engineering applications consider the media to be a macroscopic continuum, dealing only with macroscopic information. The Fourier model therefore ignores heat transfer mechanisms that take place on a microscopic level, *e.g.* heat transfer via electron-phonon interaction. The conditions under which the Fourier model is valid, is summarized by Tamma [TZ98] as follows:

1. $L/\Delta \gg 1$: The physical dimension L of a specimen is much larger than the mean free path Δ of the heat carriers. This condition is referred to as the *macroscopic space scale*.

2. $t/\tau_r \gg 1$: The physical process time t is considerably larger than the relaxation time τ_r. This condition is referred to as the *macroscopic time scale*.

3. $T \gg 0$ Kelvin: The Fourier model predicts experimental results accurately for operating conditions close to room temperature T.

Probably the most important aspect to keep in mind is that the derivation of the Fourier model is based on the assumption that the heat flux vector and temperature gradient occur simultaneously. An important consequence of this assumption is that a thermal disturbance propagates at an infinite speed through the specimen [CT82].

2.3.2 Cattaneo-Vernotte Model

The Cattaneo-Vernotte (C-V) model is also known as the thermal wave model ([CT82] [OT94]). It is based on the concept of a delay between the heat flux vector and the temperature gradient during heat conduction [Tzo95a]. This implies that the heat propagates at a finite speed, as opposed to an infinite speed, as is the case with the Fourier model. They argued that Fourier's law should in fact make provision for a relaxation time τ. The concept of a relaxation time is well-described by Joseph and Preziosi [JP89]: in an ideal solid thermal energy is transported by free electrons and by phonons. The phonons and electrons undergo collisions, dissipating energy in the process

and this can be viewed as a "thermal resistance" in the solid. The time period associated with the onset of these collisions and the moment when resistive heat flow commences, is then defined as the relaxation time τ. They added that different relaxation times or processes may exist during heat propagation and that it is difficult to determine the average relaxation time.

Although the C-V model is attributed to Cattaneo [Cat48][Cat58] and Vernotte [Ver58a][Ver58b], they were not the only researchers to point out the problem with an infinite speed of heat propagation. Morse and Feshbach suggested that provision should be made for a finite speed, proposing Eq. (2.2.3), and commenting that the Fourier model is indeed valid after a long time [MF53]. Maxwell also derived Eq. (2.2.3), but then ignored the time-derivative term since it "..may be neglected, as the rate of conduction will rapidly establish itself"[Max67].

From the available literature, it seems that no one is entirely clear on how Cattaneo and Vernotte arrived at Eq. (2.2.3) [JP90][Mul87]. Müller's interpretation of Cattaneo's work is that the heat flux depends on the temperature gradient as follows:

$$q = -k_1 \partial_x T + k_2 \partial_t (\partial_x T). \tag{2.3.1}$$

What Eq. (2.3.1) suggests is that, for a one-dimensional case, the heat flux at (x,t) is proportional to the temperature gradient at (x,t), and on the temperature gradient at an earlier time at the same position x. Combining this with the one-dimensional version of the energy conservation law Eq. (2.2.1), results in

$$\partial_t T = \frac{k_1}{\rho c_\rho} \partial_x^2 T - \frac{k_2}{\rho c_\rho} \partial_t (\partial_x^2 T). \tag{2.3.2}$$

According to Müller, Cattaneo noticed that this predicts propagation of heat at infinite speed. Cattaneo then proceeded to re-write Eq. (2.3.1) to

$$q = -k_1 \left[1 - \tau \partial_t\right] \partial_x T, \tag{2.3.3}$$

where $\tau = k_2/k_1$. Re-arranging terms, and with the requirement that $k_2 \ll k_1$, results in

$$q + \tau \partial_t q \approx -k_1 \partial_x T, \tag{2.3.4}$$

which resembles the familiar form of the C-V equation as proposed by Cattaneo (with $k = k_1$):

$$q + \tau \partial_t q = -k \nabla T. \tag{2.3.5}$$

As shown in the previous section, the combination of this constitutive equation with the energy conservation law results in a hyperbolic heat conduction equation:

$$\tau\partial_t^2 T + \partial_t T = \alpha\nabla^2 T. \tag{2.3.6}$$

This equation models heat transfer as a damped wave [Tzo97].

2.4 Microscopic heat transfer

In Chapter 7 we conduct numerical experiments related to thermoreflectance measurements of a gold thin film. The focus of our discussion here is therefore on heat transfer in metal thin films subject to ultrafast laser pulse heating. The intention is to provide a concise description of the basic concepts involved in heat transfer in metals, and is therefore not a comprehensive text on the topic of heat transfer in metals. The interested reader may consult textbooks in the field of solid state and statistical physics ([Bla74] [Kit05] [Pat72] [Ros90]).

Fortunately the theory of heat transfer in metals is also the basis of the development of the *two-step* (or *two-temperature*) models. As we will see in the case of a metal, distinction is made between the electron and lattice temperature – therefore the term: "*two-temperature*". It is interesting to note that in the case of biological materials, distinction is also made between two temperatures: the temperature of the vascular region (blood vessels) and the extravascular region (tissue), suggesting that the two-temperature models may be adapted to model heat transfer in biological materials ([KKR16] [MT14] [ZCL17]).

The microscopic models are based on the belief that heat transfer in solids relies either on phonon-electron interaction (in metals) or on phonon scattering (in dielectrics, insulators and semiconductors). The microscopic models mentioned most frequently are: the two-step models (where distinction is made between the parabolic and the hyperbolic two-step models), the phonon-scattering model and the phonon radiative transfer model ([TC94] [Tzo97]).

2.4.1 Heat transfer in metal thin films

We consider here the situation where metal thin films are heated by short laser pulses. A general description of the heating process distinguishes between different steps or stages. The electrons first have to absorp the photon

energy, then the energy is transferred from the electrons to the crystal lattice and finally heat is transferred throughout the specimen [QT93a]. The topic of heat transfer in metals is however still much-debated and experimental evidence suggests that more stages should be considered, especially when the applied heat pulse is in the femtosecond range [SVAIF94] [TM94] [BDFW00] [NTYB11] [WHGM99] [HN09]. These stages are associated with the different heat transfer mechanisms in metal thin films, owing to the interaction between the different energy carriers. With each mechanism is associated a characteristic time duration, which should be considered together with the experimental time scales of interest when comparing experimental results with theoretical predictions.

We start with the energy absorption stage. Electrons close to the metal surface are excited into higher energy levels, resulting in a hot, non-thermalised (*i.e.* non-equilibrium) electron gas. Initially it was believed that during this stage, the hot electrons thermalise rapidly (within approximately 20 fs) via electron-electron scattering, attaining a Fermi-Dirac distribution and establishing an electron temperature ([BDFW00] [Bro90]). This idea of a rapid thermalisation time followed from the assumption that the large electron population affords optimal electron-electron interaction, allowing thermalisation to take place within a very short time-span [SVAIF94]. With this assumption, the thermalisation time scale is therefore much shorter than the typical laser pulse duration of about 100 fs to 150 fs, used in femtosecond spectroscopic studies.

It is however suggested that after laser excitation, the electrons being in a highly non-equilibrium state, first undergo nondiffusive ballistic transport. An electron temperature T_e is therefore not yet established ([BDFW00] [WHGM99]). Experimental results show that the thermalisation time can be extended to a few hundred femtoseconds – measurements on gold thin films for example yielded a thermalisation time of approximately 700 fs which is comparable to electron-phonon relxation times of approximately 1 ps ([HMWM97] [Sin10] [SVAIF94]). Again using the example of gold, the non-equilibrium electrons penetrate into the material with ballistic velocities in the order of 10^6 m.s^{-1} and can reach a ballistic range of 100 nm in the case of a 100 fs pulse. The assumption is then that within the time frame spanning the (femtosecond) laser pulse, no temperature gradient exists within the electron gas ($i.e\ \nabla T_e = 0$).

Distinction should be made between transition metals and noble metals, as this determines the extent of the ballistic range. For transition metals the ballistic range is of the same order as the optical absorption depth, but for

noble metals, the ballistic transport range is significant longer and has to be considered when modeling the heat transport [WHGM99].

The ballistic stage is followed by the relaxation stage where excited electrons relax via electron-electron scattering to restore equilibrium (therefore having a Fermi-Dirac distribution). It now makes sense to assign an "electron temperature". During this time the lattice temperature is considered to be unchanged since the electron heat capacity is much smaller than that of the lattice – the lattice is assumed to have a Planck distribution. (Values reported for gold has the lattice heat capacity $C_l = 2,5 \times 10^6$J m^{-3} K^{-1} and the electron heat capacity $C_e = 2,1 \times 10^4$J m^{-3} K^{-1}). The electron temperature T_e is considerably higher than the lattice temperature T_ℓ and therefore the electron gas and the lattice is in non-equilibrium. This temperature gradient is responsible for the diffusion of hot electrons into the specimen.

Equilibrium between the electron gas and the lattice is restored via electron-phonon scattering, so that $T_e = T_\ell > T_0$, where the equilibrium temperature is higher than the initial thin film temperature T_0 [SVAIF94]. The time required to restore thermal equilibrium between the electron gas and the lattice is known as the relaxation time and is considered to be in the order of picoseconds [QT92].

During the last stage thermal diffusion into the specimen takes place, with the electron gas returning to the original temperature T_0 – this requires about 100 ps [SVAIF94]. The diffusion length or distance is determined by the electron-phonon coupling strength.

Remark Although it may appear that heat transfer in metals is described as a series of sequential steps, the transfer of heat from the electron gas to the lattice commences once the ballistic and diffusive electron transport processes start [BDFW00]. This is supported by Tas and Maris that reported that the electron-phonon interaction substantially changes the electron distribution, even before the electron gas has time to fully thermalise [TM94].

2.4.2 Two-Step Models

Initial developments in the theory of heat transfer in metals suggested a two-step process. This is atrributed to Kaganov *et al* [KLT57] and Anisimov *et al* [AKP74] who decided to model heat transfer in a metal as a two-step process. This model became known as the parabolic two-step model (PTS), otherwise known as the two-temperature model (TTM). Qiu and

Tien [QT93a] developed the hyperbolic two-step (HTS) model, which can be viewed as a three-step process. This model was derived from the Boltzmann transport equation, accounting for ballistic heat transport in the electron gas, and is prescribed when the laser pulse length is considerably shorter than the electron-phonon relaxation time [QT93a] [Tzo97].

Mathematically the hyperbolic two-step model is described by three coupled equations, which include two energy equations ([QT93a] [Tzo95b]):

$$C_e \partial_t T_e = -\nabla \cdot q_e - G(T_e - T_\ell) \tag{2.4.1}$$

and

$$C_\ell \partial_t T_\ell = G(T_e - T_\ell), \tag{2.4.2}$$

and the constitutive equation

$$q_e = -k\nabla T_e - \tau_{_F} \partial_t q_e. \tag{2.4.3}$$

In the above equations G is the electron-lattice coupling constant, k is the thermal conductivity of the phonon-electron system, C_e and C_ℓ are the electron- and lattice heat capacities respectively and $\tau_{_F}$ is the thermalisation time evaluated at the Fermi surface, or simply the thermalisation [1] time of the electron gas [Dug16][Tzo95b]. Equation (2.4.1) models the heating of the electron gas and Eq. (2.4.2) the heating of the lattice via electron-phonon interaction. Equation (2.4.3) models the heat propagation through the electron gas, with the last term in this equation, representing the thermalisation stage in the electron gas.

G is given by

$$G = \frac{\pi^4}{18} \frac{(n_e u k_B)^2}{k_{eq}}, \tag{2.4.4}$$

where k_B is the Boltzmann constant, n_e is the electron number density, u is the speed of sound, and k_{eq} is the equilibrium thermal conductivity, where the electrons and phonons are in thermal equilibrium (considered to be the case during slow-rate heating). The equilibrium thermal conductivity may also be interpreted as the *inherent* or macroscopic thermal conductivity (which is the typical value used in thermal engineering applications), *i.e.* its value is not influenced by the measurement conditions. The effective thermal conductivity k of the phonon-electron system, not being in equilibrium, is related

[1] Qiu and Tien [QT93a] and Tzou [Tzo97] uses the term *relaxation time* to refer to the mean time for electrons to change their states (it is characteristic of whether the electron-dynamics are diffusive or ballistic), whereas we use the term *thermalisation time* in this thesis.

to the equilibrium thermal conductivity k_{eq} through

$$k = k_{eq}\frac{T_e}{T_\ell}. \tag{2.4.5}$$

Equation (2.4.5) points to the reasoning that the thermal conductivity is modified by the local electron and phonon temperatures during short-rate heating, *i.e.* whilst the electron and phonon temperatures are different, the ratio k/k_{eq} is proportional to T_e/T_ℓ [QT93a].

Using Eq. (2.4.2) we express T_e in terms of T_ℓ (or T_ℓ in terms of T_e), substitute the expressions for T_e (or T_ℓ) into Eq. (2.4.1), and combine the result with the constitutive equation, Eq. (2.4.3), to arrive at the hyperbolic two-step (HTS) model [Tzo95b]:

$$\begin{aligned}\nabla^2 T + \left(\frac{C_\ell}{G}\right)\partial_t(\nabla^2 T) &= \frac{\tau_{_F} C_e C_\ell}{kG}\partial_t^3 T + \frac{\tau_{_F}(C_e + C_\ell)}{k}\partial_t^2 T \\ &\quad + \frac{C_e C_\ell}{kG}\partial_t^2 T + \frac{(C_e + C_\ell)}{k}\partial_t T,\end{aligned} \tag{2.4.6}$$

where $T = T_\ell$ (or $= T_e$). This is a single equation, governing either the lattice or the electron temperature. The electron-lattice coupling constant G is strongly affected by size effects according to Qiu and Tien [QT93b]. They developed a model that predicts that, decreasing the size of a specimen, will increase the magnitude of G. Increasing G implies that the relaxation time is reduced, which in turn implies that lattice peak-temperature will increase.

If the duration of the applied heat pulse is of the same order as the relaxation time, and therefore an order of magnitude longer than the thermalisation time, it implies that the electron-gas itself is in equilibrium. What remains is that equilibrium between the electron gas and lattice has to be restored. A two-step process is then sufficient [QT92]: relaxation via electron-phonon interaction, and thermal diffusion into the lattice [QT92]. Mathematically the two-step model is described by the same energy equations belonging to the HTS model, Eq. (2.4.1) and Eq. (2.4.2), but with the exeption that the constitutive equation does not include the electron thermalisation process:

$$q_e = -k\nabla T_e. \tag{2.4.7}$$

The derivation of the parabolic two-step model (PTS) is similar to the hyperbolic two-step model, except that the constitutive equation used, is Eq. (2.4.7). The parabolic two-step model (PTS) is given by the single equation

$$\nabla^2 T + \left(\frac{C_\ell}{G}\right)\partial_t(\nabla^2 T) = \frac{C_e C_\ell}{kG}\partial_t^2 T + \frac{(C_e + C_\ell)}{k}\partial_t T, \tag{2.4.8}$$

governing either the lattice or the electron temperature. A wave term is present in Eq. (2.4.8) even though heat transport throught the electron gas is governed by diffusion.

If the laser pulse duration is considerably longer than the relaxation time, there is ample time to establish thermal equlibrium between the electrons and the metal lattice. The conclusion is then that the heating is a one step process, *i.e.* the Fourier model may be used, and it is not necessary to consider microscopic effects.

Returning to Eq. (2.4.6) we observe that if τ_F approaches zero, the HTS model approaches the PTS model (Eq. (2.4.8)). If τ_F approaches zero and G infinity, the HTS model resembles the Fourier model. To confirm that this is the case, we refer to the expression for energy conservation, Eq. (2.2.1), where the specific heat capacity c_p, with units $J\,kg^{-1}\,K^{-1}$ is used and the thermal diffusivity is defined as $\alpha = k/\rho c_p$. C_e and C_ℓ in the two-step models are defined as *volumetric* heat capacities, with units $J\,m^{-3}\,K^{-1}$. With the reasoning that the electrons and lattice are in thermal equilibrium at this point, it can be argued that c_V is the equilibrium heat capacity of the electron-phonon system, and k is the equilibrium thermal conductivity of the same system. We realise that the equilibrium thermal conductivity that we refere to here, is exactly the effective thermal conductivity defined in Eq. (2.4.5), with $T_e = T_\ell$. The thermal diffusivity in the two-step model framework, is then defined as $\alpha = k/c_V$. The units of α , in both definitions are $m^2\,s^{-1}$ confirming then that the HTS model equation, Eq. (2.4.6) resembles the Fourier model equation, Eq. (2.2.5), when τ_F approaches zero and G infinity.

2.5 Phase lag models

We will see in this section how the linearized dual-phase lag (DPL) model follows from the parabolic two-step model. In general, the DPL model is intended to be a unified model that combines the theories of the macroscopic and microscopic models, at the same time accommodating the transition between the different models [Tzo95a][Tzo97]. The DPL model therefore describes heat transfer processes in other materials as well, including as we have already mentioned, dielectrics, insulators and semiconductors, porous materials and also biological materials ([KKR16] [MT14] [ZCL17]).

2.5.1 The unified field approach

The phase-lag models, developed by Tzou [CXW08], are based on the notion that finite times are required for the substructural interactions to take place within a given material type. Our earlier discussion in Section 2.4 already introduced this notion with the thermalisation and relaxation times associated with heat transfer in metals. We should also consider other material types. Porous materials, such as fine blasting sand, mainly consist of randomly distributed gaseous pores surrounded by solid structures (sand particles) and can be viewed as a microstructural material. When heat flow reaches a pore, most of heat energy circulates around the pore, relying mainly on the solid particle to conduct the heat. This is due to the thermal conductivity of the solid particle being higher than that of the gaseous pore. The remainder of the heat exchanges energy with the gas (air) trapped inside the pore. The heat transfer via the solid particles versus the pores are distinguished by finite and distinct delay times. Amorphous materials such as silica aerogels and random metal-sphere assemblies are noncrystalline in nature, implying the absence of a periodic lattice structure. The material structure can best be desribed as a "non-continuous" or "disordered" arrangement of atoms/molecules or particles, resulting in clusters inside the material with localised thermal behaviour. As is the case with porous materials, heat transfer through these materials is characterised by finite and distinct delay times ([LT20] [DA08] [Sos18] [Win16]). Dielectric crystals, insulators and semiconductors all have a crystalline structure and heat transfer relies on phonon scattering. Two types of phonon scattering mainly occurs: momentum-conserving and momentum-nonconserving. A distinct and finite relaxation time is associated with both types [JP89][Tzo97].

In all the examples mentioned here, the materials are seen as consisting of distinct substructures (ranging from meso- to nanoscale) characterised by finite and distinct delay or lag-times, that influence the transfer of heat through the material. Tzou introduced the phase-lag approach by suggesting that there is a time-lag between the heat flux vector and the temperature gradient [Tzo93b][Tzo97].

The phase-lag models most frequently studied, include the single-phase-lag (SPL) ([CXW08] [PRDSS00]) and dual-phase-lag (DPL) models ([Tzo95a] [Tzo95b] [WXZ01]). A three-phase-lag model has also been developed in recent years, finding application in bioheat transfer problems ([HAA20] [ZSY20]).

We start with the SPL model, in which case a phase-lag is introduced in the heat flux vector q, with the Fourier constitutive equation changing to ([MR16] [Tzo93b] [Tzo97]):

$$q(r, t + \tau_q) = -k\nabla T(r, t). \tag{2.5.1}$$

According to Tzou, this implies that the temperature gradient $\nabla T(r, t)$ is the cause and the heat flux q the effect. Once the temperature gradient is established, heat flow is assumed to be instantaneous. Using a first-order Taylor expansion of τ_q around t, and assuming that τ_q is small so that the higher order terms may be ignored, Tzou arrived at

$$q + \tau_q \partial_t q \approx -k\nabla T. \tag{2.5.2}$$

Equation (2.5.2) has the same form as the C-V model constitutive equation, Eq. (2.2.3), but one should keep in mind that these models were developed along different physical arguments [JP90]. Combining Eq.(2.5.2) then with the energy conservation law, Eq. (2.2.1), leads to the linearized SPL model

$$\frac{\tau_q}{\alpha}\partial_t^2 T + \frac{1}{\alpha}\partial_t T = \nabla^2 T. \tag{2.5.3}$$

Tzou, by considering the macroscopic models (describing diffusion, thermal waves and his single-phase-lag concept) together with the microscopic models (describing phonon-electron interaction and phonon scattering), saw the opportunity to develop a unified model or "generalized lagging response", referred to as the dual-phase-lag (DPL) model. The intention with the DPL model is to capture all the different microstructural and temporal effects on a microscopic level, into a single macroscopic model that relies on finite lag times to accommodate the various microstructural interactions that take place within a specimen ([Tzo95a][Tzo95b]). Tzou therefore wanted a model that describes the microscopic phonon-electron interaction during heat transfer in a metal film in a microscopic fashion. At the same time this model should accommodate diffusion, thermal waves, phonon-electron interactions and even phonon scattering, thereby including heat transfer in other material types.

The generalized lagging response is illustrated by the two-step model applied to the case where a metal is subject to pulsed laser heating [Tzo95a]. We recall from Section 2.4 that a nonequilibrium thermodynamic situation exists; therefore whilst energy is exhanged between the lattice and free electrons, the lattice temperature remains unchanged. From a microscopic perspective,

the increase in lattice temperature is delayed due to the phonon-electron interactions and this delay is known to be the relaxation time. Tzou describes this continued build up of phonon-electron interaction as a macroscopic delayed response or lagging between the temperature gradient and the heat flux vector. To address the lagging response between the temperature gradient and heat flux vector, he introduces two phase lags in the Fourier constitutive equation, Eq. (2.2.2): τ_q, the phase lag of the heat flux vector, and τ_T, the phase lag of the temperature gradient. As mentioned earlier, the C-V model assumes that the temperature gradient precedes the heat flux. The DPL model however allows for two situations: the temperature gradient preceding the heat flux, *i.e.* $\tau_T < \tau_q$, or the heat flux preceding the temperature gradient, *i.e.* $\tau_T > \tau_q$.

The Dual-Phase-Lagging (DPL) constitutive equation is then

$$q(r, t + \tau_q) = -k\nabla T(r, t + \tau_T), \tag{2.5.4}$$

where τ_q is described as the delay in heat-flow, departing from a position r in the material, and τ_T as the delay in establishing a temperature gradient after the heat flow has arrived at a point r. Tzou aimed to derive a governing equation that is equivalent to the PTS model equation. He observed that a first-order Taylor expansion of the delayed constitutive equation (Eq. 2.5.4), in both τ_q and τ_T, results in equivalence. Taking the first-order Taylor expansion of Eq. (2.5.4) with respect to t, yields [Tzo95a]:

$$q + \tau_q \partial_t q \approx -k \left[\nabla T + \tau_T \partial_t \left(\nabla T\right)\right]. \tag{2.5.5}$$

Combining this with the energy conservation law, Eq. (2.2.1), results in the linearized DPL model.

$$\frac{\tau_q}{\alpha}\partial_t^2 T + \frac{1}{\alpha}\partial_t T = \nabla^2 T + \tau_T \partial_t(\nabla^2 T). \tag{2.5.6}$$

Remark: The phase lags are assumed to be temperature-independent and may be regarded as effective values averaged over a nominal temperature range [TC01].

2.5.2 Interpretation of the DPL model and its time lags

Tzou gives a synopsis of the characteristics of the DPL model with its associated lag times, serving as a guideline on how to interpret the DPL model

from a physical perspective and also how the values of the lag times, influences the mathematical solutions obtained when applying the DPL model to a heat transfer problem [Tzo97]. Together with Tang and Araki[TA99], interesting observations are made about the characteristics of Eq. (2.5.6) with respect to the values of τ_T and τ_q, and how, with specific lag time values, the DPL model can reduce to either the C-V or even the Fourier model.

Tzou lists a number of characteristics of the DPL model, which according to him, best describe the model's potential to act as a unified model that allows all the fundamental mechanisms associated with phonon-electron interaction, phonon scattering, thermal waves and diffusion, to be captured by one single model.

1. If $\tau_q = \tau_T = 0$, Eq. (2.5.6) reduces to the Fourier model equation.
2. If $\tau_T = 0$, thereby removing the mixed-derivative term, Eq. (2.5.6) reduces to the C-V model equation, with $\tau_q \equiv \tau$. τ_q is therefore responsible for the wave nature.
3. τ_q induces thermal waves with sharp wave-fronts, separating the heated and unheated zones in the solid.
4. If $\tau_q = \tau_T \neq 0$, the temperature prediction resembles that of the Fourier model. This is motivated by re-writing Eq. (2.5.6) as follows:
$$(\nabla^2 T - \frac{1}{\alpha}\partial_t T) + \tau_q \partial_t (\nabla^2 T - \frac{1}{\alpha}\partial_t T) = 0.$$
In the case of a homogeneous initial temperature, the above equation has the general solution
$$\nabla^2 T - \frac{1}{\alpha}\partial_t T = 0,$$
which is the Fourier model equation.
5. τ_T can be seen as adding a diffusion-like nature into the equation through the inclusion of the mixed-derivative term; it smooths the wave fronts by promoting conduction in the specimen material.
6. If $\tau_T > \tau_q$, the temperature prediction is described as "over-diffusion behaviour". In this case the temperature gradient follows after the heat flux vector.
7. If $\tau_q > \tau_T > 0$, the temperature prediction is described as "wavy behaviour". In this case, the temperature gradient precedes the heat flux vector.

2.5.3 The PTS model versus DPL model

Tzou performed a detailed comparison between his DPL model and the parabolic two-step model. We observe the similarity between Eqs. (2.4.8) and (2.5.6) in terms of time and space derivatives. Comparing the coefficients in Eqs. (2.4.8) and (2.5.6) results in

$$\alpha = \frac{k}{C_e + C_\ell}; \quad \tau_q = \frac{1}{G}\left[\frac{1}{C_e} + \frac{1}{C_\ell}\right]^{-1}; \quad \tau_T = \frac{C_\ell}{G}. \tag{2.5.7}$$

From the theory of the parabolic two-step (PTS) model we know that G, C_e and C_ℓ are microscopic properties that cause the time lags (microscale effects in time) on a macroscopic level. In both the PTS and the DPL models, temperature-independent thermal properties are assumed, and therefore the similarity between Eqs. (2.4.8) and (2.5.6) are only valid for temperature-independent thermal properties [Tzo95c].

It is insightful to mention the similarity between the phonon-scattering model and the DPL model as well. The phonon-scattering model was developed along a similar fashion than the PTS model, by Guyer and Krumhansel [GK66][Tzo95a]. As we mentioned in Section 2.5, there are two processes that occur during phonon-scattering: a momemtum-nonconserving process and a momentum-conserving process. A relaxation time is associated with both processes: $\tau_{_R}$ when momentum is lost, and $\tau_{_N}$ when momentum is conserved. The resulting energy equation is

$$\frac{3}{c^2}\partial_t^2 T + \frac{3}{\tau_{_R} c^2}\partial_t T = \nabla^2 T + \frac{9\tau_{_N}}{5}\partial_t(\nabla^2 T), \tag{2.5.8}$$

where c is the average phonon speed. Comparing the coefficients in Eqs. (2.5.8) and (2.5.6) we find that [Tzo95c]

$$\alpha = \frac{\tau_{_R} c^2}{3}; \quad \tau_q = \tau_R; \quad \tau_T = \frac{9\tau_{_N}}{5}. \tag{2.5.9}$$

These similarities between the DPL model and the PTS and phonon-scattering models, allows for the calculation of the macroscopic phase-lags from the microscopic thermal properties, *e.g.* $\tau_{_T}$ and τ_q can be calculated from the experimentally determined values of G, C_e and C_ℓ. This is indeed what Tzou does in [Tzo95a], as we mention at the beginning of this chapter.

2.6 Heat absorption model

We need to discuss the heat absorption models for the model problems investigated in Chapter 6 and 7. We follow the approach suggested by Tzou [Tzo97] and restrict ourselves to a straightforward model that, according to Tzou, depicts the effect of the phase lags. Tzou studies a problem where the temperature at the boundary $x = 0$ is raised instantaneously (and continuously) to a temperature T_b, modeled by the boundary condition $T(0, t) = T_b$. We adopt this model for the case of continuous heating applied to the boundary of a specimen (Sections 6.6 and 6.8).

The heat absorption model used for the single- and multi-pulse cases are based on Tzou's approach for continuous heating. Our decision to adopt Tzou's model is based on the following assumptions of the heat delivery to, and absorption by the specimen: Considering that laser sources are common to both the applications that we investigate in Section 7.5 (thermoreflectance) and Section 7.6 (bio-heating), we base our discussion on pulsed laser sources. In a physical setup the pulsed laser source, focused at $x = 0$, and with the assumption that the laser pulse has a *top-hat* temporal profile [BFAPB12], provides energy to the boundary surface of the specimen. We assume that all the optical energy contained in the laser pulse is absorbed by the heat carriers of the specimen, at the boundary $x = 0$. In the thermoreflectance application we consider a metal (gold) thin film, where the electrons and the phonons are the heat carriers [QT93a]. In the bio-heating application, the blood vessels (vascular region) and the surrounding tissue (extravascular region) act as the heat carriers [MT14]. Absorption of the laser energy causes a thermal pulse (or disturbance) within the *skin layer* (*i.e.* close to $x = 0$) of the specimen by increasing the thermal energy of the heat carriers in this region [Ros90]. The thermal disturbance is quantified by the change in temperature of the specimen at $x = 0$ [TC01]. We assume then that a change in temperature at *e.g* $x = 0$ resembles the conversion of the absorbed optical energy at $x = 0$ to heat energy. It follows that the temperature pulse therefore inherits the pulse characteristics of the laser source.

We proceed to model the step heat pulse (for the single-pulse case) as a step function of the temperature at $x = 0$, *i.e.* at $t = 0$ the temperature T rises instantaneously to say T_b, and returns instantaneously to $T = 0$ at the time instant when the laser pulse stops. The multi-pulse case is modeled using this same step function, repeated for multiple cycles, with a set time period between the onset of consecutive pulses. We model the heat absorption process in the three different cases mathematically by describing the boundary conditions at $x = 0$.

2.7 Boundary and initial conditions

Consider the wave equation in a multi-dimensional bounded domain denoted by Ω. We limit ourselves to surface-based conduction boundary conditions – convection and radiation boundary conditions are not considered here. Then, the heat flux and the temperature has to be prescribed at the boundary surfaces as required. We will not consider cases where the flux q varies at a boundary, but will allow for the temperature T to vary. We use the notation $\bar{g}$ to indicate a vector quantity, and g to indicate a scalar quantity. Let $\bar{n}$ be a unit outer normal vector to the boundary $\partial\Omega$ and let Σ be part of the boundary $\partial\Omega$. We have different boundary conditions on Σ and $\partial\Omega - \Sigma$:

On Σ : $\bar{q} \cdot \bar{n}$ must be prescribed and on $\partial\Omega - \Sigma : T$ must be prescribed.

Consider an insulated boundary Σ, *i.e.* $\bar{q} \cdot \bar{n} = 0$ on Σ. It follows that $\partial_t \bar{q} \cdot \bar{n} = \partial_t(\bar{q} \cdot \bar{n}) = 0$.

DPL model

We consider the constitutive equation for the DPL model:

$$\bar{q} \cdot \bar{n} + \tau_q \partial_t \bar{q} \cdot \bar{n} = -k\nabla T \cdot \bar{n} - \tau_T k \nabla(\partial_t T \cdot \bar{n})$$

With an insulated boundary then, we have

$$0 = -k\nabla T \cdot \bar{n} - \tau_T k \nabla(\partial_t T \cdot \bar{n}), \tag{2.7.1}$$

so that

$$\nabla T \cdot \bar{n} = 0 \quad \text{on} \quad \Sigma.$$

The directional temperature derivative, $\nabla T \cdot \bar{n} = dT/dn$, is zero at the boundary Σ, *i.e* the boundary is insulated.

Remark It follows from conservation of energy that

$$\rho c_p \partial_t T \cdot \bar{n} = -\nabla \cdot (\bar{q} \cdot \bar{n}) = 0.$$

C-V model

Setting $\tau_T = 0$, the C-V model is a special case of the linear DPL model. It follows then that

$$\nabla T \cdot \bar{n} = 0 \quad \text{on} \quad \Sigma.$$

Fourier model

For the Fourier model, it follows from Eq. (2.2.2) that

$$0 = -k\nabla T \cdot \bar{n}.$$

Then

$$\nabla T \cdot \bar{n} = 0 \quad \text{on} \quad \Sigma.$$

The boundary input at $\partial\Omega - \Sigma$, for all three models, is given by

$$T = T_b \quad \text{on} \quad \partial\Omega - \Sigma, \tag{2.7.2}$$

where T_b is a prescribed non-zero function on $\partial\Omega - \Sigma$.

Initial conditions

It remains to specify the initial conditions. At $t = 0$ the specimen is at a uniform temperature T_0. Therefore for all three the models being investigated,

$$T(r, 0) = T_0, \tag{2.7.3}$$

where r denotes the three-dimensional position coordinate. For the C-V and DPL modes the inital time-rate change of the temperature $\partial_t T(r, 0)$ has to be specified as well. Let

$$\partial_t T(r, 0) = T_1. \tag{2.7.4}$$

2.8 Dimensionless forms

With the objective of having a model containing only two parameters, dimensionless variables are introduced in both the energy conservation law and the respective constitutive equations belonging to the above models, through

the following transformation of parameters:

$$\begin{aligned} T^* &= \frac{T}{T_0} \\ r^* &= \frac{r}{D} \\ t^* &= \frac{t}{t_0} \\ q^* &= \frac{qt_0}{D\rho c_\rho T_0} \\ \mathcal{S}^* &= \frac{\mathcal{S}t_0}{\rho c_p T_0} \\ \tau_q^* &= \tau_q/t_0 \\ \tau_{_T}^* &= \tau_{_T}/t_0 \\ \alpha^* &= \alpha t_0/D^2. \end{aligned} \tag{2.8.1}$$

Here T_0 is a suitable temperature scaling factor (*e.g* the initial temperature), D is the specimen spatial dimension, defined by $D = \sqrt{x^2 + y^2 + z^2}$ and t_0 is a suitable time scaling factor (we suggest an approach that may be used to calculate t_0 in Section 2.8.1). $\mathcal{S}$ represents an internal, volumetric heat source.

The dimensionless forms of the respective models are derived making use of the dimensionless parameters defined by Eq. (2.8.1). Although the model problems we study do not include an internal heat source, we formulate the problems here as general as possible for the sake of the theoretical derivations performed in Chapter 4. The energy conservation law (Eq. (2.2.1)), with the addition of a source term $\mathcal{S}^*$ then becomes

$$\partial_{t^*} T^* = -\nabla^* \cdot q^* + \mathcal{S}^*. \tag{2.8.2}$$

Substituting the dimensionless parameters into Eq. (2.2.2), the dimensionless constitutive equation for the Fourier model becomes

$$q^* = -\alpha^* \nabla^* T^*. \tag{2.8.3}$$

Substituting the dimensionless parameters into Eq. (2.2.4), the dimensionless constitutive equation for the DPL model becomes

$$q^* + \tau_q^* \partial_{t^*} q^* = -\alpha^* \nabla^* T^* - \alpha^* \tau_{_T}^* \partial_{t^*} (\nabla^* T^*). \tag{2.8.4}$$

With $\tau_{_T} = 0$ it follows that the dimensionless constitutive equation for the C-V model is expressed as

$$q^* + \tau_q^* \partial_{t^*} q^* = -\alpha^* \nabla^* T^*. \tag{2.8.5}$$

Returning to the original notation, we present the energy conservation law

$$\partial_t T = -\nabla \cdot q + \mathcal{S} \tag{2.8.6}$$

and the respective constitutive equations for the DPL, C-V and Fourier models

$$q + \tau_q \partial_t q = -\alpha \nabla T - \alpha \tau_T \partial_t (\nabla T), \tag{2.8.7}$$

$$q + \tau_q \partial_t q = -\alpha \nabla T, \tag{2.8.8}$$

and

$$q = -\alpha \nabla T. \tag{2.8.9}$$

Combining the energy conservation law with the respective constitutive equations leads to

$$\partial_t T = \alpha \nabla^2 T + \mathcal{S}, \tag{2.8.10}$$

$$\tau_q \partial_t^2 T + \partial_t T = \alpha \left(\nabla^2 T + \tau_T \partial_t (\nabla^2 T) \right) + \mathcal{S} + \tau_q \, \partial_t \mathcal{S} \tag{2.8.11}$$

and

$$\tau_q \partial_t^2 T + \partial_t T = \alpha \nabla^2 T + \mathcal{S} + \tau_q \, \partial_t \mathcal{S}. \tag{2.8.12}$$

The boundary and initial conditions have the same form as given in Section 2.7.

2.8.1 Determining t_0 and α^*

It is proposed to determine t_0, making use of the 1-dimensional form of the parabolic model. We use separation of variables and consider the first mode $k = 1$:

$$u_1(t) = e^{-\alpha \pi^2 t / 4d^2}, \tag{2.8.13}$$

where α and d are the specimen parameters. t_0 is then defined as the time at which $u_1(t_0) = 0.99 u_1(0)$. We then have

$$\exp(-\alpha \pi^2 t_0 / 4d^2) = 0.99.$$

$$\therefore \; t_0 = -\frac{4 \ln(0.99) d^2}{\alpha \pi^2} = k_1 \times \frac{d^2}{\alpha},$$

where $k_1 = \frac{-4 \ln(0.99)}{\pi^2}$.

Next, α^* is calculated using

$$\alpha^* = \frac{\alpha t_0}{d^2} = k_1.$$

We observe that α^* is independent of the length d and diffusivity α, the same being true for τ^*.

Chapter 3

Tracking a sharp crested wave front

This chapter is the article "Tracking a sharp crested wave front in hyperbolic heat transfer" by R H Sieberhagen and N F J van Rensburg, published in Applied Mathematical Modelling 36 (2012), 3399-3410, virtually unchanged. To avoid unnecessary errors, few changes were made.

3.1 Introduction

Heat transfer problems relying on the hyperbolic model, are routinely approximated using numerical techniques. Over the years researchers have reported on the presence of oscillations and how they proceeded to suppress or eliminate these oscillations from their results. It is commonly believed that the main cause of these oscillations, is the presence of sharp wave fronts – see e.g. Liu and Chen [LC04]. A few examples from the literature serves to highlight the issue of numerical oscillations. Carey and Tsai [CT82] studied a one-dimensional problem using finite elements and various time integration techniques that resulted in "fictitious numerical oscillations" near the wave front. Li et al [LCP05] stated that fictitious numerical oscillations are a major problem when solving the hyperbolic equation numerically, particularly when sharp propagation fronts and reflective boundaries are present. Jiang et al [JLZ02] eliminated numerical oscillations and the sharp discontinuity, believed to be brought about by the numerical differencing of the hyperbolic equation. Huang and Wu [HW06] studied the same problem (referring to it as the "benchmark" problem) as did Carey and Tsai [CT82] and claimed

that they derived a formula to reduce the oscillatory behaviour of the numerical solution. As already indicated in the Introduction, we will refer to this problem as the *CT-benchmark* problem.

These numerical oscillations are not surprising and in this chapter we will indicate why it is to be expected. We focus on the one-dimensional CT-benchmark problem studied by Carey and Tsai [CT82] as well as Huang and Wu [HW06]. The problem concerns a propagating heat wave reflected off a boundary. We show that the origin of the reported oscillations does not lie with the numerical techniques, but rather with the fact that the problem, as formulated, is not well-posed. We re-formulate the problem to one where the solution is smooth, that is, a classical solution can be obtained (see *e.g* [Wei95]). However, a sharp-crested wave front is still present which will be problematic to track. Our remedy is to construct a solution by dividing the problem into three auxiliary problems and solve them by different techniques. The result is an oscillation-free solution.

The outline of this chapter is as follows. The model problem is derived in Section 3.2, starting with the dimensionless form and then proceeding to an alternative formulation of the problem. We discuss in Section 3.3 a set of auxiliary problems that is used to construct a solution to the model problem. D'Alembert's method and the finite element approximation, used to solve the auxilliary problems, are discussed in Sections 3.4 and 3.5 respectively. The solutions obtained to the auxiliary problems are combined in Section 3.6 to arrive at the final solution of the model problem. A jump condition, necessary to render the model problem well-posed in the event of a discontinuity at the wave front, is derived in Section 3.8. Finally, the conclusion is given in Section 3.9.

3.2 The model problem

3.2.1 Transformation of the model problem

Recall the dimensionless hyperbolic model derived in Section 2.8. In order to address the issues raised by Carey and Tsai [CT82] as well as Huang and Wu [HW06], the one-dimensional form of this model will be used here:

$$\tau \partial_t^2 T(x,t) + \partial_t T(x,t) = \alpha\, \partial_x^2 T(x,t). \tag{3.2.1}$$

It is re-written as

$$\partial_t^2 T(x,t) + 2\gamma \partial_t T(x,t) = c^2\, \partial_x^2 T(x,t), \tag{3.2.2}$$

where $2\gamma = 1/\tau$ and $c^2 = \alpha/\tau$. With $c^2 = 1$ and $\gamma = 1$, it is the same as the CT-benchmark problem studied by Huang and Wu[HW06]. The CT-benchmark problem was derived from Eq. (3.2.2) through the following transformation of variables

$$\begin{aligned} T^* &= \frac{T}{T_0} \\ x^* &= \frac{cx}{2\alpha} \\ t^* &= \frac{c^2 t}{2\alpha} \\ q^* &= \frac{\alpha q}{ckT}. \end{aligned} \tag{3.2.3}$$

The CT-benchmark problem will now be referred to as Problem 1.

Problem 1

$$\begin{aligned} \partial_t^2 T(x,t) + 2\gamma \partial_t T(x,t) &= c^2\, \partial_x^2 T(x,t), \\ T(0,t) = 1 \qquad \partial_x T(1,t) &= 0, \\ T(x,0) = \partial_t T(x,0) &= 0. \end{aligned}$$

The "solution" is supposed to have a jump along the line $x = t$.

As mentioned earlier, the problem is not well-posed; a classical or smooth solution does not exist for the problem as formulated. On the other hand, if discontinuities are allowed with no jump condition, there are more than one solution. Consider for example the following "solution": For $t \geq 0$, $T = 0$ for $t < x$ and $T = 1$ for $t \geq x$. It satisfies the partial differential equation except on the line $x = t$, the boundary conditions and initial conditions.

To address the well-posedness of the problem, it is convenient to consider an equivalent problem (Problem 2). Let $\theta = T - 1$, then θ is a solution of a different problem: one boundary condition changes to $\theta(0,t) = 0$ and one initial condition changes to $\theta(x,0) = -1$.

Problem 2

$$\begin{aligned} \partial_t^2 \theta + 2\gamma \partial_t \theta - c^2 \partial_x^2 \theta &= 0, \\ \theta(0,t) = \partial_x \theta(1,t) &= 0, \\ \theta(x,0) = \theta_{in}(x), \qquad \partial_t \theta(x,0) &= 0. \end{aligned}$$

Let $\theta_{in}(x) = -1$, then $T = \theta + 1$ is a solution of Problem 1 (the CT-benchmark problem) if and only if θ is a solution of Problem 2.

Problem 2 has a unique classical solution if the function θ_{in} is twice continuously differentiable on the closed interval [0,1] and if

$$\theta_{in}(0) = (\theta_{in})'(1) = (\theta_{in})''(0) = 0, \tag{3.2.4}$$

see e.g. Section 26 in Weinberger [Wei95]. Note that, if $\theta_{in}(x) = -1$, then the function does not satisfy the condition $\theta_{in}(0) = 0$ above. However it is possible to formulate an initial smooth temperature distribution that is an excellent approximation of the inadmissable initial value.

Initial value for Problem 2

Let $0 < \delta < 1$ and $\theta_{in}(x) = \theta_\delta(x)$, where θ_δ is twice continuously differentiable on the closed interval $[0, 1]$,

$$\theta_\delta(0) = (\theta_\delta)'(1) = (\theta_\delta)''(0) = 0, \tag{3.2.5}$$

and

$$\begin{aligned} -1 \le \theta_\delta(x) &\le 0 \qquad \text{for } 0 \le x < \delta \\ \theta_\delta(x) &= -1 \qquad \text{for } \delta \le x \le 1. \end{aligned}$$

This means that θ_δ does satisfy the conditions for the existence of a classical solution while it is equal to -1 on an interval $[\delta, 1]$ for an arbitrary small δ. We present an example:

$$\begin{aligned} \theta_\delta(x) &= -6(\frac{x}{\delta})^5 + 15(\frac{x}{\delta})^4 - 10(\frac{x}{\delta})^3 \quad \text{for} \quad 0 \le x < \delta, \\ \theta_\delta(x) &= -1 \quad \text{for} \quad \delta \le x \le 1. \end{aligned} \tag{3.2.6}$$

Straightforward calculation yields $\theta_\delta(0) = \theta'_\delta(0) = \theta''_\delta(0) = 0$. Note also, that $\theta_\delta(\delta) = -1$ and θ''_δ is continuous at $x = \delta$. With the choice $\theta_{in}(x) = \theta_\delta(x)$, we now have a sufficiently smooth initial value which is a good approximation of the inadmissable constant initial value when δ is small.

How to track the sharp crested wave front remains a problem. The strategy to deal with it, is outlined in the next section.

Remark From a physical perspective, the choice of δ should take into account the absorption depth of a laser source. This implies that δ should be extremely small. When the problem is approximated using a numerical method (such as finite differences or finite elements), obvious complications will arise.

3.3 Auxiliary problems

The strategy is to use a set of auxiliary problems to construct a solution for Problem 2. These problems are formulated here, followed by an explanation of the method.

Problem A1

$$\begin{aligned} \partial_t^2 u &= c^2 \partial_x^2 u \\ u(0,t) &= \partial_x u(1,t) = 0, \\ u(x,0) &= \theta_{in}(x), \\ \partial_t u(x,0) &= \gamma \theta_{in}(x). \end{aligned}$$

Problem A2

$$\begin{aligned} \partial_t^2 w + 2\gamma \partial_t w - c^2 \partial_x^2 w + \gamma^2 w &= 0, \\ w(0,t) = \partial_x w(1,t) &= 0, \\ w(x,0) = \theta_{in}(x), \qquad \partial_t w(x,0) &= 0. \end{aligned}$$

Problem A3

$$\begin{aligned} \partial_t^2 v + 2\gamma \partial_t v - c^2 \partial_x^2 v &= \gamma^2 f \\ v(0,t) = \partial_x v(1,t) &= 0, \\ v(x,0) = \partial_t v(x,0) &= 0. \end{aligned}$$

An exact solution for Problem A1 is constructed in the next section. An exact solution of Problem A2 is obtained from the solution of Problem A1 as follows. Suppose u is the solution of Problem A1. Let $w(x,t) = e^{-\gamma t} u(x,t)$, then $u(x,t) = e^{\gamma t} w(x,t)$. Consequently

$$\begin{aligned} \partial_t u &= \gamma e^{\gamma t} w + e^{\gamma t}\, \partial_t w, \\ \partial_t^2 u &= \gamma^2 e^{\gamma t} w + 2\gamma e^{\gamma t}\, \partial_t w + e^{\gamma t}\, \partial_t^2 w. \end{aligned}$$

It is easy to see that w satisfies the partial differential equation and boundary conditions. Also,

$$\begin{aligned} w(x,0) &= u(x,0) = \theta_{in}(x), \\ \partial_t w(x,0) &= \partial_t u(x,0) - \gamma u(x,0) = 0. \end{aligned}$$

We conclude that w is a solution of Problem A2.

Finally, if $f(x,t) = w(x,t)$ in Problem A3, then $\theta(x,t) = v(x,t) + w(x,t)$ is a solution of Problem 2.

An approximation for the solution of Problem A3 can be obtained using any standard numerical method. Note that the initial values for Problem A3 are zero and there is no prominent wave front.

The solution $u(x,t)$ of Problem 1 has a prominent wave front when $\theta_{in} = \theta_\delta$ and δ is small. Consequently the same will be true for the solution of $w(x,t) = e^{-\gamma t}\, u(x,t)$ of Problem A2.

3.4 D'Alembert's method for Problem A1

In this section we construct an exact solution for Problem A1 using D'Alembert's method. This method is well known, see Chapter 1 Weinberger [Wei95] for an explanation and justification. The method is valid for any sufficiently smooth θ_{in} that satisfies (3.2.4), hence we may use $\theta_{in} = \theta_\delta$ as specified in Subsection 3.2.1.

Solution of Problem A1

We solve the problem for the two cases: u_1 a solution of Problem A1, but with $\frac{\partial u_1}{\partial t}(x,0) = 0$ and u_2 a solution of Problem A1, but with $u_2(x,0) = 0$. The solutions u_1 and u_2 are then added.

Case 1: Construct an extension g_1 of θ_{in} which is twice continuously differentiable on $(-\infty,\infty)$ with period 4, is symmetric with respect to $x = 1$ and skew symmetric with respect to $x = 0$. To be precise

$$g_1(x) = -g_1(-x) \qquad \text{and} \qquad g_1(x) = g_1(2-x).$$

A sketch of $g_1(x)$ is provided in Figure 3.1 for the case where $\theta_{in} = \theta_\delta$ and with $c^2 = 1$. (The function $g_1(x)$ appears to have discontinuities because δ is extremely small.)

The function u_1 given by

$$u_1(x,t) = \frac{1}{2}g_1(x+ct) + \frac{1}{2}g_1(x-ct)$$

is a solution of the wave equation that satisfies the initial conditions and boundary conditions. This is easily verified by direct calculations.

Case 2: Let $g_2' = g_1$ with $g_2(0) = 0$. Consequently

$$g_2(x) = g_2(-x) \qquad \text{and} \qquad g_2'(x) = g_2'(2-x).$$

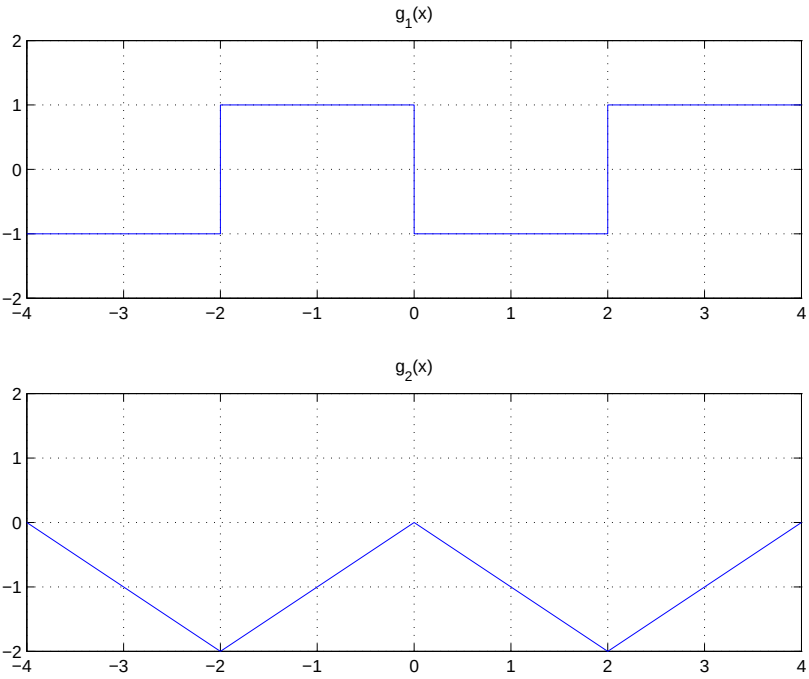

Figure 3.1: The functions $g_1(x)$ and $g_2(x)$

A sketch of $g_2(x)$ is provided in Figure 3.1 for the case where $\theta_{in} = \theta_\delta$.

The function u_2 given by

$$u_2(x,t) = \frac{\gamma}{2c} g_2(x+ct) - \frac{\gamma}{2c} g_2(x-ct)$$

is a solution of the wave equation that satisfies the initial conditions and boundary conditions.

Finally, the solution of Problem A1 is $u = u_1 + u_2$.

The Wave Front

We now consider the two cases $\theta_{in}(x) = \theta_\delta(x)$ and $\theta_{in}(x) = \theta_0(x) = -1$. If the initial condition for Problem A1 is $\theta_\delta(x)$, then a classical solution of Problem A1 exists for any positive value of δ (but not for $\delta = 0$). We denote this solution by u_δ.

If $\delta = 0$, then Problem A1 does not have a solution. However, the D'Alembert construction can still be implemented. Now g_1 is periodic with period 4 and

$$g_1(x) = \begin{cases} 1 & \text{for} \quad -2 \le x < 0 \\ 0 & \text{for} \quad x = 0 \\ -1 & \text{for} \quad 0 < x < 2. \end{cases}$$

Similarly, g_2 is periodic with period 4 and

$$g_2(x) = \begin{cases} x & \text{for} \quad -2 \leq x < 0 \\ -x & \text{for} \quad 0 \leq x < 2. \end{cases}$$

The function $g_1(x)$ is discontinuous as well as the derivative of $g_2(x)$. The D'Alembert construction yields the function

$$u_0(x,t) = \frac{1}{2}g_1(x+ct) + \frac{1}{2}g_1(x-ct) + \frac{\gamma}{2c}g_2(x+ct) - \frac{\gamma}{2c}g_2(x-ct). \quad (3.4.1)$$

It is obvious that

$$u_\delta(x,t) \to u_0(x,t) \quad \text{as} \quad \delta \to 0. \quad (3.4.2)$$

For the mathematical model it is desirable that δ be extremely small, so we may consider the function u_0 (although not a solution) as an approximation to the solution u_δ. In Section 3.6 we show how u_0 can be used to track the wave front.

3.5 Finite element approximation

In this section we consider the finite element approximation for a solution of Problem A3. The first step is to write the problem in variational form. Multiply the partial differential equation by a function ϕ that is differentiable on $[0,1]$ and integrate. Integration by parts yields

$$\begin{aligned} & \int_0^1 \frac{\partial^2 v}{\partial t^2}(x,t)\phi(x)dx + 2\int_0^1 \frac{\partial v}{\partial t}(x,t)\phi(x)dx + \int_0^1 \frac{\partial v}{\partial x}(x,t)\phi'(x)dx \\ = \; & -\frac{\partial v}{\partial x}(0,t)\phi(0) + \int_0^1 f(x,t)\phi(x)dx. \end{aligned}$$

For the procedure to be valid, it is necessary for $\partial v/\partial x$ to be continuous. This is the case for the solution of Problem A3. However, the situation is different for the CT-benchmark problem, since $\partial T/\partial x$ is not continuous.

A function ϕ is called a test function if its derivative is continuous on the closed interval $[0,1]$ and $\phi(0) = 0$.

Variational form of Problem A3

Find v such that for each $t > 0$, $v(x,t)$ is a test function and

$$\begin{aligned} & \int_0^1 \frac{\partial^2 v}{\partial t^2}(x,t)\phi(x)dx + 2\int_0^1 \frac{\partial v}{\partial t}(x,t)\phi(x)dx + \int_0^1 \frac{\partial v}{\partial x}(x,t)\phi'(x)dx \\ = \; & \int_0^1 f(x,t)\phi(x)dx \end{aligned} \quad (3.5.1)$$

for all test functions ϕ, with initial conditions $v(x,0) = 0$ and $\partial v/\partial t(x,0) = 0$.

Next we consider test functions $\phi_1,\ \phi_2,\ \ldots,\ \phi_n$ and denote the span of this set by S^h. The following problem is the finite element approximation.

Galerkin approximation

Find v^h such that for each $t > 0$,

$$v^h(x,t) = \sum_{j=1}^{n} v_j(t)\phi_j(x) \tag{3.5.2}$$

and

$$\begin{aligned} &\int_0^1 \frac{\partial^2 v^h}{\partial t^2}(x,t)\phi_i(x)dx + 2\int_0^1 \frac{\partial v^h}{\partial t}(x,t)\phi_i(x)dx + \int_0^1 \frac{\partial v^h}{\partial x}(x,t)\phi_i'(x)dx \\ = &\int_0^1 f(x,t)\phi_i(x)dx \quad \text{for} \quad i = 1,\ 2,\ \ldots,\ n, \end{aligned} \tag{3.5.3}$$

while $v^h(x,0) = 0$ and $\partial v^h/\partial t(x,0) = 0$.

We find that v^h satisfies Eq. (3.5.3) if and only if

$$\begin{aligned} &\sum_{j=1}^{n} v_j''(t)\int_0^1 \phi_j\phi_i + 2\sum_{j=1}^{n} v_j'(t)\int_0^1 \phi_j\phi_i + \sum_{j=1}^{n} v_j(t)\int_0^1 \phi_j'\phi_i' \\ = &\int_0^1 f(x,t)\phi_i(x)dx \quad \text{for} \quad i = 1,\ 2,\ \ldots,\ n. \end{aligned}$$

Next we introduce notation to rewrite the system of ordinary differential equations for the functions v_j. Let

$$K_{ij} = \int_0^1 \phi_j'\phi_i', \quad M_{ij} = \int_0^1 \phi_j\phi_i \quad \text{and} \quad f_i(t) = \int_0^1 f(x,t)\phi_i(x)dx,$$

then the vector function $\bar{v} = [v_1\ v_2 \ldots v_n]^T$ satisfies an initial value problem for a system of ordinary differential equations.

$$M\bar{v}'' + 2M\bar{v}' + K\bar{v} = \bar{f}(t) \quad \text{with} \quad \bar{v}(0) = \bar{v}'(0) = \bar{0}. \tag{3.5.4}$$

This is known as a semi-discrete problem. The well known *piecewise linear basis functions*, see *e.g.* Strang and Fix[SF73] and Becker, Carey and Oden [BCO81], are sufficiently accurate to approximate the solution of Problem A3, as can be seen from Table 3.1. The matrices M and K for piecewise linear basis functions are given in these references. There are of course other possibilities.

A stable finite element method for the wave equation

We use a special case of a Newmark scheme (see *e.g.* Zienkiewicz [Zie77]). The following scheme is (theoretically) unconditionally stable for the finite element method.

$$\frac{1}{(\delta t)^2}\, M\, [\bar{v}_{k+1} - 2\bar{v}_k + \bar{v}_{k-1}] + \frac{1}{\delta t}\, M\, [\bar{v}_{k+1} - \bar{v}_{k-1}]$$
$$+ \quad \frac{1}{4}\, K\, [\bar{v}_{k+1} + 2\bar{v}_k + \bar{v}_{k-1}\,] = \frac{1}{4}[\bar{f}(t_{k+1}) + 2\bar{f}(t_k) + \bar{f}(t_{k-1})]. \quad (3.5.5)$$

3.6 Tracking the wave front

Recall that u_δ is the solution of Problem A1 with the initial condition $\theta_{in}(x) = \theta_\delta(x)$ and the solution of Problem A2 is $w_\delta(x,t) = e^{-t}u_\delta(x,t)$. The function $w_0 = e^{-t}u_0$ is not a solution of Problem A2 but the limit of $w_\delta = e^{-t}u_\delta$ as $\delta \to 0$. Using this fact and the fact that δ is extremely small, we may use w_0 as an approximation for the solution w_δ of Problem A2. It is necessary to change Eq. 14 accordingly and use the approximation $f(x,t) = w_0(x,t) = e^{-t}u_0(x,t)$.

Consider the semi-discrete problem, Eq. (3.5.4). Since we use $f(x,t) = e^{-t}u_0(x,t)$ we have $f_i(t) = e^{-t}\int_0^1 u_0(x,t)\phi_i(x)dx$. It is convenient to approximate $u_0(x,t)$ by its interpolant

$$\sum_{j=1}^{n} u_0(x_j,t)\phi_j(x). \quad (3.6.1)$$

As a result we have $e^{-t}M\bar{u}(t)$ instead of $\bar{f}(t)$, where $u_j(t) = u_0(x_j,t)$ and (3.5.4) becomes

$$M\bar{v}'' + 2M\bar{v}' + K\bar{v} = e^{-t}M\bar{u}(t) \quad \text{with} \quad \bar{v}(0) = \bar{v}'(0) = \bar{0}.$$

Remark The function $u_0(x,t)$ is equal to its interpolant except on the element containing the wave front, hence the approximation is accurate.

The Newmark scheme (3.5.5) for the FEM approximation now changes to

$$\frac{1}{(\delta t)^2}\, M\, [\bar{v}_{k+1} - 2\bar{v}_k + \bar{v}_{k-1}] + \frac{1}{\delta t}\, M\, [\bar{v}_{k+1} - \bar{v}_{k-1}]$$
$$+ \quad \frac{1}{4}\, K\, [\bar{v}_{k+1} + 2\bar{v}_k + \bar{v}_{k-1}\,] = \frac{1}{4}\, e^{-t_k}\, M\, [e^{-\delta t}\bar{u}(t_{k+1}) + 2\bar{u}(t_k) + e^{\delta t}\bar{u}(t_{k-1})\,].$$

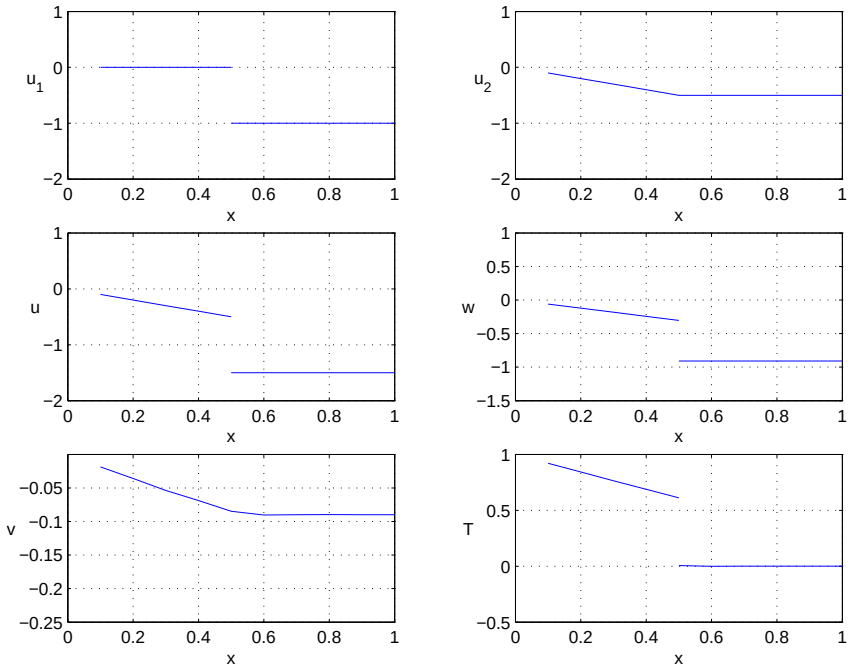

Figure 3.2: Illustration of the Solution Strategy

The solution strategy is illustrated by Figure 3.2 for $t = 0.5$. The functions u_1, u_2, u, w, v and T are shown. The approximate solution to Problem 1 is given by $T = \theta + 1 = v + w + 1$. The wave front is contained in w, whilst v does not contain any prominent wave front.

3.7 Numerical Experiments and Results

Numerical experiments were performed to study the convergence of the solution to Problem 3. Note that $\gamma = 1$ and $c^2 = 1$ to resemble the CT-benchmark problem. The numerical calculations were performed with a maximum of 2560 elements. Experiments showed that the results are reliable for at least 3 significant digits. The following ratio between the element lengths and time increments was used during calculations: $r = (\delta t/\delta x)^2 = 1$. The number of time steps was consequently determined by r and the number of elements.

The solution of Problem 1 evaluated at times $t = 0.5$, $t = 0.9$ and $t = 1.1$ are given by Figures 3.3, 3.4 and 3.5. No oscillations can be seen in these graphs, before or after reflection from the boundary. To ensure that the scaling used

Table 3.1: The function $v(x,t)$ for $t = 0.5$

x	v	x	v
0.4968	-0.0897	0.5008	-0.0901
0.4976	-0.0898	0.5016	-0.0902
0.4984	-0.0899	0.5024	-0.0902
0.4992	-0.0900	0.5032	-0.0902
0.5000	-0.0901	0.5040	-0.0902

in these graphs do not hide possible oscillations, the actual values of v as a function of x were examined. No evidence of oscillations was found. This is illustrated by data for the case $t = 0.5$, given in Table 3.1. It shows v as a function of x for $t = 0.5$. The values of v decreases monotonically with x. These results prove that this solution strategy does provide oscillation-free results.

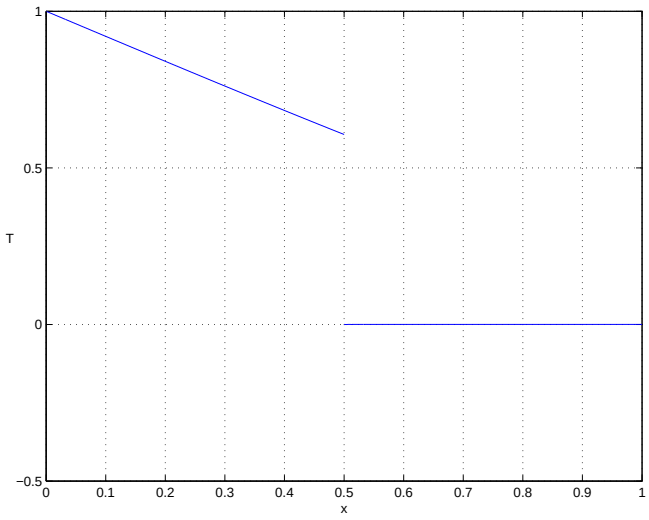

Figure 3.3: Result for Problem 1: $t = 0.5$

3.8 Jump condition

In this section we derive a jump condition that will render the CT-benchmark problem well posed. Recall that $T = \theta + 1$ and $\theta = v + w$. The function v and its partial derivatives are continuous, hence the discontinuities in T and its partial derivatives must be attributed to the function w. To determine

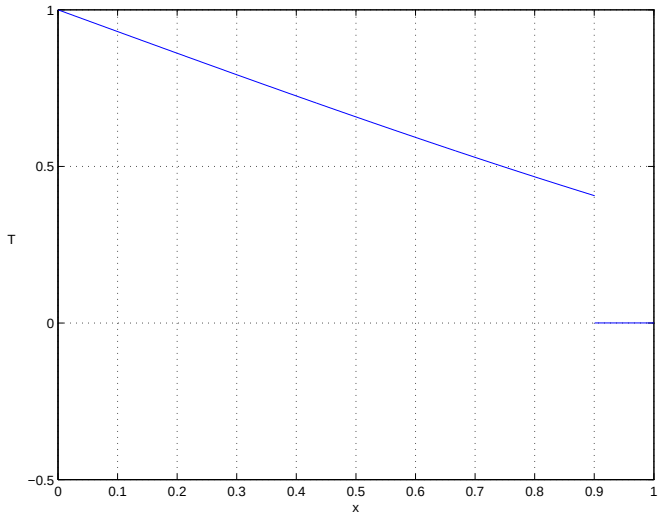

Figure 3.4: Result for Problem 1: $t = 0.9$

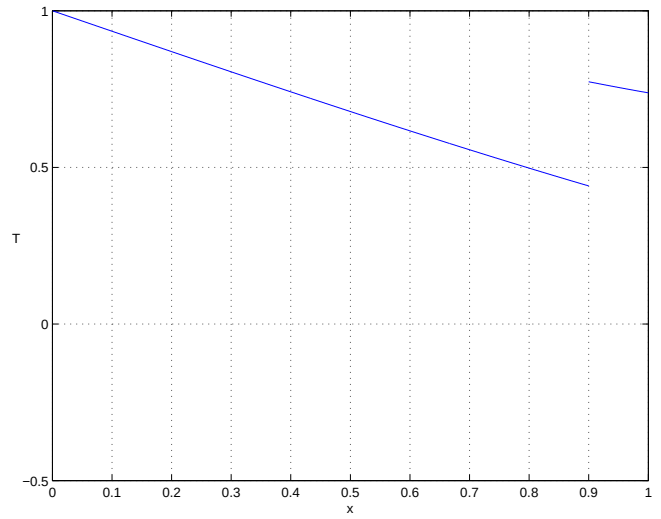

Figure 3.5: Result for Problem 1: $t = 1.1$

the discontinuities of w_0 we consider w_δ before and after the sharp crested wave and take the limit as $\delta \to 0$. The jump in w_0 is

$$[w_0] = \lim_{\delta \to 0} \{w_\delta(x, x+\delta) - w_\delta(x, x-\delta)\}.$$

The wave front is contained in a strip around the line $x = t$. To be precise, the front is between the lines $t = x+\delta$ and $t = x-\delta$. Since $w_\delta(x,t) = e^{-t}u_\delta(x,t)$, we calculate $u_\delta = u_1 + u_2$ at $(x, x+\delta)$ and $(x, x-\delta)$:

$$\begin{aligned} u_1(x, x+\delta) &= \frac{1}{2}g_1(2x+\delta) + \frac{1}{2}g_1(-\delta) \\ &= -\frac{1}{2} + \frac{1}{2} = 0, \\ u_1(x, x-\delta) &= \frac{1}{2}g_1(2x-\delta) + \frac{1}{2}g_1(\delta) \\ &= -\frac{1}{2} - \frac{1}{2} = -1. \end{aligned}$$

Consequently

$$u_1(x, x+\delta) - u_1(x, x-\delta) = 1.$$

Next

$$\begin{aligned} u_2(x, x+\delta) &= \frac{1}{2}g_2(2x+\delta) - \frac{1}{2}g_2(-\delta), \\ u_2(x, x-\delta) &= \frac{1}{2}g_2(2x-\delta) - \frac{1}{2}g_2(\delta). \end{aligned}$$

Therefore

$$\begin{aligned} & u_2(x, x-\delta) - u_2(x, x-\delta) \\ = \; & \frac{1}{2}g_2(2x+\delta) - \frac{1}{2}g_2(2x-\delta) - \left[\frac{1}{2}g_2(-\delta) - \frac{1}{2}g_2(+\delta)\right]. \end{aligned}$$

Since g_2 is continuous,

$$\lim_{\delta \to 0} \{u_2(x, x+\delta) - u_2(x, x-\delta)\} = 0.$$

It follows that

$$[u_0] = \lim_{\delta \to 0} \{u_\delta(x, x+\delta) - u_\delta(x, x-\delta)\} = 1$$

and therefore $[w_0] = e^{-t}$ (as can be seen in Figure 3.2).

Now consider the partial derivatives of w_δ. Note that $\partial w_\delta/\partial x = e^{-t}\partial u_\delta/\partial x$ and $\partial w_\delta/\partial t = -e^{-t}u_\delta + e^{-t}\partial u_\delta/\partial t$. Reasoning as above, we find that

$$\left[\frac{\partial u_0}{\partial x}\right] = -1 \quad \text{and} \quad \left[\frac{\partial u_0}{\partial t}\right] = 1.$$

Consequently

$$\left[\frac{\partial w_0}{\partial x}\right] = e^{-t}\left[\frac{\partial u_0}{\partial x}\right] = -e^{-t}$$

and

$$\left[\frac{\partial w_0}{\partial t}\right] = -e^{-t}[u_0] + e^{-t}\left[\frac{\partial u_0}{\partial t}\right] = -e^{-t} + e^{-t} = 0.$$

It follows that $[w_0] + [\partial w_0/\partial x] = 0$.

We conclude that the jump condition to be imposed on the CT-benchmark problem (Problem 1) across the characteristic $x = t$ is

$$[T] + \left[\frac{\partial T}{\partial x}\right] = 0$$

and the solution is

$$T = w_0 + v + 1.$$

3.9 Conclusion

We have shown how to find an accurate solution to a so-called "benchmark" problem, that is not well-posed. It is reportedly plagued by oscillations when solved numerically. A discontinuity arises where $T = 0$ at $t = 0$ while $T(0, t) = 1$ for $t > 0$. This in turn, leads to a discontinuous wave front. To have a well-posed problem, a jump condition needs to be specified. We provide an initial smooth temperature distribution as an alternative to the inadmissable initial value, thereby "smoothing" the jump and leading to a solution with a sharp crested wave front but no discontinuity.

A numerical method was developed that allows for the jump, *i.e.* the jump condition must be incorporated in the algorithm. This was done by splitting the problem into auxilliary problems which we solved by different methods. This resulted in a solution free of oscillations.

To conclude this chapter, we note that the existence of a weak solution for the CT-benchmark problem was not considered. This is postponed to be treated in Chapter 4.

Chapter 4

Second order hyperbolic-type problems

4.1 Vibration models

In this section we introduce model problems for mechanical vibrations. We then proceed to show that these problems are similar to the hyperbolic-type heat problems. It is useful to interpret these hyperbolic-type heat conduction models in terms of mechanical vibrations. We also borrow the terminology weak damping and strong damping; underdamped and overdamped modes.

Multi-dimensional wave equation

In the two-dimensional case the wave equation models the vibration of a membrane [Inm, Section 6.6]. We have the partial differential equation

$$\rho\partial_t^2 w \quad = \quad \tau\,\nabla^2 w - k\partial_t w,$$

where ρ is the mass per unit area, τ the constant tension per unit length, and k a damping constant.

In the three-dimensional case the wave equation models the propagation of sound waves. The following derivation follows [PR05, Section 1.4.2] with some modification.

Consider a gas at rest, i.e. the velocity $\mathbf{v} = 0$. Suppose the pressure is p_0 and the density is ρ_0. A small disturbance leads to motion in the gas, and the pressure p and density ρ are no longer constant. The linear approximation for the continuity equation is

$$\partial_t\,\rho^* + \rho_0 \nabla\cdot\mathbf{v} = 0, \tag{4.1.1}$$

where $\rho^* = \rho - \rho_0$. The linear approximation for the equation of motion for an ideal gas is

$$\rho_0 \partial_t \mathbf{v} + \nabla p^* = 0, \tag{4.1.2}$$

where $p^* = p - p_0$ and where modified pressure is considered.

We use the approximation

$$\rho^* = f(p) - f(p_0) \doteqdot c p^* \tag{4.1.3}$$

where $c = f'(p_0)$. Combining Equations (4.1.1), (4.1.2) and (4.1.3) yields the acoustic wave equation

$$c\partial_t^2 p^* - \nabla^2 p^* = 0.$$

General case

Consider the wave equation in an n-dimensional bounded domain ($n = 2$ or 3) denoted by Ω. The boundary of Ω is denoted by $\partial\Omega$ and the unit outer normal vector to Ω at $\partial\Omega$ by $\mathbf{n}$.

Let Σ be part of the boundary $\partial\Omega$. We have different boundary conditions on Σ and $\partial\Omega - \Sigma$. Given functions f, u_0 and u_1, find w defined on $\bar{\Omega} \times [0, T]$ such that

$$\begin{aligned} \rho\partial_t^2 w &= \nabla \cdot (A\nabla w) - k\partial_t w + f \quad \text{in} \quad \Omega \times (0, T), \\ w &= 0 \quad \text{on} \quad \partial\Omega - \Sigma, \\ (A\ \nabla w) \cdot \mathbf{n} &= 0 \quad \text{on} \quad \Sigma, \end{aligned}$$

while $w(\cdot, 0) = u_0$ and $\partial_t w(\cdot, 0) = u_1$.

For the sake of generality, the given parameters in the problem are presented as the matrix of functions $A = (a_{ij})$ and the functions k and ρ. However in this thesis the parameters are constant in all the cases that we investigate.

Vibration of a beam

The Rayleigh beam model can be found in many books, *e.g.* [Inm, Section 6.5]. This beam model is convenient to illustrate the three types of damping that we discuss here. (See *e.g* [VV02].) The equations of motion for the deflection u of the beam is given by

$$\rho A\partial_t^2 u = \partial_x V + Q, \tag{4.1.4}$$

$$\rho I\partial_t^2 \partial_x u = V + \partial_x M. \tag{4.1.5}$$

In these equations M denotes the moment, V the shear force and Q a transverse force density.

The constitutive equation is given by

$$M = EI\partial_x^2 u. \tag{4.1.6}$$

Combining (4.1.4), (4.1.5) and (4.1.6) yields the partial differential equation:

$$\rho A\partial_t^2 u = \partial_x(\rho I\partial_t^2\partial_x u) - \partial_x^2(EI\partial_x^2 u) + Q.$$

Less well known are examples of the different types of damping. Three examples are given in [VV02] as motivation for the theory in the article.

Example 1 *Viscous damping*

Here $Q = q - k\partial_t u$ for a given $k > 0$ and q is the load. Equation (4.1.4) takes the form

$$\rho A\partial_t^2 u + k\partial_t u = \partial_x V + q \text{ in } (0,\ell) \text{ for } t \geq 0.$$

Example 2 *Kelvin-Voigt damping*

The constitutive equation (4.1.6) is replaced by

$$M = EI\partial_x^2 u + \mu\partial_t\partial_x^2 u.$$

(This constitutive equation is also used in [Inm, Section 6.7]). The transverse force Q in (4.1.4) is now the load q.

For Examples 1 and 2 we consider a cantilever beam, so the boundary conditions are given by

$$\begin{aligned} u(0,t) &= \partial_x u(0,t) = 0, \\ V(\ell,t) &= M(\ell,t) = 0. \end{aligned} \tag{4.1.7}$$

For the last example the boundary conditions, Eq. (4.1.7), are retained but damping terms are introduced at the other end point.

Example 3 *Boundary damping*

Suppose $k_1 > 0$ and $k_0 > 0$ are given. Consider the undamped problem where $Q = q$ and the constitutive equation is given by (4.1.6). We now have damping at the boundary $x = \ell$:

$$\begin{aligned} V(\ell,t) &= -k_0\partial_t u(\ell,t), \\ M(\ell,t) &= -k_1\partial_t\partial_x u(\ell,t). \end{aligned}$$

Variational forms

To obtain the variational form, multiply the equations of motion (4.1.4) and (4.1.5) by arbitrary functions v and w and integrate. Using integration by parts we have

$$\begin{aligned}\int_0^\ell \rho A \partial_t^2 u\, v &= \int_0^\ell (\partial_x V + Q)\, v \\ &= -\int_0^\ell V\, v' + V(\ell)v(\ell) - V(0)v(0) + \int_0^\ell Q\, v \quad (4.1.8)\end{aligned}$$

and

$$\begin{aligned}\int_0^\ell \rho I \partial_t^2 \partial_x u\, w &= \int_0^\ell (V + \partial_x M)\, w \\ &= \int_0^\ell V\, w - \int_0^\ell M\, w' + M(\ell)w(\ell) - M(0)w(0) (4.1.9)\end{aligned}$$

Now replace w by v' in equation (4.1.9) and add the resulting equation to equation (4.1.8). The result is

$$\begin{aligned}&\int_0^\ell \rho A \partial_t^2 u\, v + \int_0^\ell \rho I \partial_t^2 \partial_x u\, v' \\ &\quad = -\int_0^\ell M\, v'' + V(\ell)v(\ell) - V(0)v(0) + M(\ell)v'(\ell) - M(0)v'(0) + \int_0^\ell Q\, v.\end{aligned}$$

Test functions

Define the space of test functions by

$$T[0,\ell] = \{v \in C^2[0,\ell] : v(0) = v'(0) = 0\}.$$

Using suitable notation, all three the examples may be written in the same variational form. The bilinear forms b and c for all three examples are given by

$$b(u,v) = EI \int_0^\ell u''\, v'' \quad \text{and} \quad c(u,v) = \rho A \int_0^\ell uv + \rho I \int_0^\ell u'v' \quad \text{for} \quad u, v \in \mathcal{C}^2[0,\ell].$$

The bilinear form a is different for each example.

Example 1: $a(u,v) = k \int_0^\ell u\, v$,

Example 2: $a(u,v) = \mu \int_0^\ell u''\, v''$,

Example 3: $a(u,v) = k_1 u'(\ell)v'(\ell) + k_0 u(\ell)v(\ell)$.

The variational equation for each case is then

$$c(\partial_t^2 u(\cdot,t), v) + a(\partial_t u(\cdot,t), v) + b(u(\cdot,t), v) = (q(\cdot,t), v) \tag{4.1.10}$$

for all $v \in T[0,\ell]$.

In [VV02] the damping in Examples 1 and 2 are classified as weak and strong damping respectively. The damping in Example 3 is neither weak nor strong. We will see in Section 4.4 how this classification is applied to the C-V and DPL models.

In Section 5.2 we introduce the concept of "conservation" of the dimensionless energy $\mathcal{E}$ of a solution u to prove convergence of the partial sums. It follows that $\mathcal{E}(t) \leq \mathcal{E}(0)$. This is a mathematical definition, based on the principle of energy conservation which states that the sum of the kinetic and potential energy (*i.e.* the mechanical energy) of a body cannot increase and remains constant with time in the absence of damping. See [CVV18].

Kinetic energy

The kinetic energy of a particle or system is defined by

$$T(t) = \frac{1}{2} c(\partial_t u(\cdot,t), \partial_t u(\cdot,t)).$$

Potential energy

The potential energy of a particle or system is defined by

$$V(t) = \frac{1}{2} b(u(\cdot,t), u(\cdot,t)).$$

Mechanical energy

The sum $T(t) + V(t)$ yields the total or mechanical energy $\mathcal{E}(t)$:

$$\mathcal{E}(t) = T(t) + V(t)$$

which is constant or decreasing.

4.2 Heat conduction models

In this section we formulate the heat conduction models to be studied. Consider an n-dimensional bounded domain ($n = 2$ or 3) denoted by Ω. Let n be a unit outer normal vector to the boundary $\partial\Omega$ and let Σ be part of the boundary $\partial\Omega$. We have different boundary conditions on Σ and $\partial\Omega - \Sigma$:

Remark If we consider an insulated boundary Σ, then $q \cdot n = 0$ on Σ. It follows that $\partial_t q \cdot n = \partial_t (q \cdot n) = 0$.

Recall the dimensionless versions of the energy conservation law and the three different constitutive equations associated with the DPL, C-V and Fourier model respectively (discussed in Section 2.8).

The problems are as general as possible for theoretical purposes.

Problem DPL

The energy conservation law is

$$\partial_t T = -div\ q + \mathcal{S}, \tag{4.2.1}$$

and the constitutive equation is

$$q + \tau_q \partial_t q = -\alpha \nabla T - \alpha \tau_T \partial_t (\nabla T). \tag{4.2.2}$$

The boundary conditions are $q \cdot n = Q$ on Σ and the temperature T_b on the boundary $\partial\Omega - \Sigma$.

Initial conditions: $T(x,0) = T_0(x)$ for $x \in \Omega$; $\partial_t T(x,0) = T_d(x)$ for $x \in \Omega$.

Remark If we consider an insulated boundary Σ, then $q \cdot n = 0$ on Σ. It follows that $\partial_t q \cdot n = \partial_t (q \cdot n) = 0$.

Problem C-V

The problem is the same as Problem DPL except that Eq. (4.2.2) is replaced by

$$q + \tau_q \partial_t q = -\alpha \nabla T. \tag{4.2.3}$$

Initial conditions: $T(x,0) = T_0(x)$ for $x \in \Omega$; $\partial_t T(x,0) = T_d(x)$ for $x \in \Omega$.

Assumptions on the parameters for DPL and C-V models

1. $\tau_q, \tau_T, \alpha \in C^1(\bar{\Omega})$.

2. There exist positive constants c_1 and c_2 such that
   $c_1 \leq \tau_q \leq c_2, \quad c_1 \leq \tau_T \leq c_2$ and $c_1 \leq \alpha \leq c_2$.

Remark Recall that only constant values are used in numerical experiments.

Problem F

The Fourier model is given by the energy conservation law Eq. (4.2.1) and the constitutive equation

$$q = -\alpha \nabla T. \tag{4.2.4}$$

The requirements on the boundary conditions are the same as for the previous models.

Initial condition: $T(x, 0) = T_0(x) \quad \text{for} \quad x \in \Omega$.

Assumptions on the parameters for the F model

1. $\alpha \in C^1(\bar{\Omega})$.

2. There exist positive constants c_1 and c_2 such that
   $c_1 \leq \alpha \leq c_2$.

4.3 Variational forms

The variational form of a problem is used to determine well-posedness and for application of the finite element method.

Divergence theorem (or Gauss's theorem)

If $G_i \in C^1(\bar{\Omega})$ for $i = 1, 2, 3$, then

$$\iiint_{\Omega} div\ G\ dV = \iint_{\partial\Omega} G \cdot n\ dS.$$

where $div\ G$ is the divergence of the vector G, n is the unit outward normal vector and dS indicates the surface integral.

Proposition 4.3.1. *Green's formula*

If $G \in C^2(\bar{\Omega})$ *and* $v \in C^1(\bar{\Omega})$, *then*

$$\iiint_\Omega (div\ G)v\ dV = -\iiint_\Omega G \cdot (grad\ v)\ dV + \iint_{\partial\Omega} vG \cdot n\ dS.$$

Proof Since $div\ (Gv) = (div\ G)v + G \cdot (grad\ v)$ we have that

$$\iiint_\Omega (div\ G)v\ dV = \iiint_\Omega div\ (Gv)\ dV - \iiint_\Omega G \cdot (grad\ v)\ dV.$$

The result follows from the divergence theorem (Gauss's theorem). □

To derive the variational form, we first introduce the test functions.

Test functions

$$T(\Omega) = \{v \in C^1(\bar{\Omega}) \mid v = 0 \ \text{ on } \ \partial\Omega - \Sigma\}.$$

Next, we multiply Eq. (4.2.1) by an arbitrary function v and integrate. Using Green's formula we have

$$\begin{aligned}\iiint_\Omega \partial_t T v\ dV &= \iiint_\Omega q \cdot \nabla v\ dV + \iiint_\Omega \mathcal{S} v\ dV \\ &\quad - \iint_{\partial\Omega} v\ q \cdot n\ dS. \end{aligned} \tag{4.3.1}$$

Using the fact that $v = 0$ on $\partial\Omega - \Sigma$ and $q \cdot n = 0$ on Σ, we have

$$\iiint_\Omega \partial_t T v\ dV = \iiint_\Omega q \cdot \nabla v\ dV + \iiint_\Omega \mathcal{S} v\ dV.$$

Substitute Eq. (4.2.2) into Eq. (4.3.2):

$$\begin{aligned}&\iiint_\Omega \partial_t T v\ dV + \iiint_\Omega \alpha \nabla T \cdot \nabla v\ dV + \iiint_\Omega \alpha \tau_{_T}\, \partial_t(\nabla T) \cdot \nabla v\ dV \\ = &-\iiint_\Omega \tau_q\, \partial_t q \cdot \nabla v\ dV + \iiint_\Omega \mathcal{S} v\ dV. \end{aligned} \tag{4.3.2}$$

We next differentiate Eq. (4.2.1) with respect to time t, and then multiply throughout with τ_q. Finally, interchanging the partial derivative ∂_t and the divergence operator div, yields

$$\tau_q\, \partial_t^2 T = -\tau_q\, div(\partial_t q) + \tau_q\, \partial_t \mathcal{S}.$$

Multiply by v and integrate (again using Green's formula).

$$\iiint_\Omega \tau_q \, \partial_t^2 T v \; dV = \iiint_\Omega \tau_q \, \partial_t q \cdot \nabla v \; dV + \iiint_\Omega \tau_q \, \partial_t \mathcal{S} v \; dV. \tag{4.3.3}$$

From Eq. (4.3.2) and Eq. (4.3.3) we have, if T is a solution of Problem DPL, then for each $v \in T(\Omega)$, the variational form of Problem DPL is

$$\begin{aligned} &\iiint_\Omega \tau_q(\partial_t^2 T)v \; dV + \iiint_\Omega (\partial_t T)v \; dV + \iiint_\Omega \alpha \; (\nabla \; T) \cdot (\nabla \; v) \; dV \\ &+ \iiint_\Omega \alpha \tau_{_T} [\partial_t (\nabla \; T) \cdot (\nabla \; v)] \; dV \\ &= \iiint_\Omega \mathcal{S} v \; dV + \iiint_\Omega \tau_q \, \partial_t \mathcal{S} v \; dV. \end{aligned} \tag{4.3.4}$$

The variational form of the C-V model follows as a special case from the DPL model:

$$\begin{aligned} &\iiint_\Omega \tau_q(\partial_t^2 T)v \; dV + \iiint_\Omega (\partial_t T)v \; dV \\ = \; &- \iiint_\Omega \alpha \; (\nabla \; T) \cdot (\nabla \; v) \; dV + \iiint_\Omega \mathcal{S} v \; dV \iiint_\Omega \tau_q \, \partial_t \mathcal{S} v \; dV. \end{aligned}$$

The Fourier model follows trivially from the equation above

$$\iiint_\Omega (\partial_t T)v \; dV = - \iiint_\Omega \alpha \; (\nabla \; T) \cdot (\nabla \; v) \; dV + \iiint_\Omega \mathcal{S} v \; dV.$$

$T(\Omega)$ is the subset of $C^1(\bar{\Omega})$ that vanish on $\partial\Omega - \Sigma$. We substitute the defined bilinear forms into Eq. (4.3.4).

Notation for the inner product and norm of $\mathcal{L}^2(\Omega)$: For functions f and g in $\mathcal{L}^2(\Omega)$ let

$$(f, g)_\Omega = \iiint_\Omega fg \; dV$$

and

$$\|f\| = \sqrt{(f, f)_\Omega}.$$

Bilinear forms for Problem DPL

$$a_\nabla(u, v) = \iiint_\Omega \alpha \tau_{_T} \nabla u \cdot \nabla v \; dV \tag{4.3.5}$$

$$b(u, v) = \iiint_\Omega \alpha \, \nabla u \cdot \nabla v \; dV, \tag{4.3.6}$$

$$c(u, v) = \iiint_\Omega \tau_q uv \; dV, \tag{4.3.7}$$

For convenience we introduce the function F:

$$F(x,t) = \mathcal{S}(x,t) + \tau_q \, \partial_t \mathcal{S}(x,t).$$

Problem DPLV

Find T such that for each $t > 0$ and $T(\cdot,t) \in T(\Omega)$, we have

$$c(\partial_t^2 T(\cdot,t), v) + (\partial_t T(\cdot,t), v)_\Omega + a_\nabla(\partial_t T(\cdot,t), v) + b(T(\cdot,t), v) = (F(\cdot,t), v)_\Omega \tag{4.3.8}$$

for each $v \in T(\Omega)$, with $T(\cdot,0) = T_0$ and $\partial_t T(\cdot,0) = T_d$.

From a mathematical point of view the C-V model is a special case of the DPL model where $\tau_{_T} = 0$.

Problem C-VV

Find T such that for each $t > 0$ and $T(\cdot,t) \in T(\Omega)$, we have

$$c(\partial_t^2 T(\cdot,t), v) + (\partial_t T(\cdot,t), v)_\Omega + b(T(\cdot,t), v) = (F(\cdot,t), v)_\Omega \tag{4.3.9}$$

for each $v \in T(\Omega)$, with $T(\cdot,0) = T_0$ and $\partial_t T(\cdot,0) = T_d$.

Formally, the Fourier model can be derived from Eq. (4.3.9) by letting $\tau_q = 0$.

Problem FV

Find T such that for each $t > 0$ and $T(\cdot,t) \in T(\Omega)$, we have

$$(\partial_t T(\cdot,t), v)_\Omega + b(T(\cdot,t), v) = (\mathcal{S}(\cdot,t), v)_\Omega \tag{4.3.10}$$

for each $v \in T(\Omega)$, with $T(\cdot,0) = T_0$.

Up to this point it is possible to consider the C-V model as a special case of the DPL model when $\tau_{_T} = 0$. However, when it comes to existence theory and modal analysis, this is not the case.

Kinetic energy and potential energy may be defined for any hyperbolic-type model. The physical relevance is not clear but the concepts are useful for the mathematical analysis, see *e.g* Chapter 5.

Referring to our discussion in Secton 4.1, we introduced three types of damping associated with vibrating beam problems and defined bilinear forms for each, classifying it as weak or strong damping, or the case where it is neither weak nor strong. The precise definitions of these damping types are given in Sections 4.5.1 and 4.5.2. We will adopt the terminology *damping*, *weak*

damping etc. also for heat conduction models, and classify the C-V model as the weak damping case, and the DPL model as the strong damping case.

One-dimensional models

The models are given by (4.3.8), (4.3.9) and (4.3.10) with some changes to the notation.

Notation for the inner product and norm of $\mathcal{L}^2(0,1)$:

$$(f,g) = \int_0^1 fg$$

and

$$\|f\| = \sqrt{f,f}.$$

The bilinear forms now become

$$\begin{aligned} a_{\nabla}(u,v) &= \int_0^1 \alpha\tau_{T} u'v'\ dx \\ b(u,v) &= \int_0^1 \alpha\, u'v'\ dx, \\ c(u,v) &= \int_0^1 \tau_q\ uv\ dx, \end{aligned}$$

4.4 Weak variational forms

In order to apply existence theory to our model problems, we first need to derive the weak variational forms of the respective problems. Introducing

$$a_{D}(u,v) = (u,v)_{\Omega} + a_{\nabla}(u,v),$$

we rewrite Eq. (4.3.8) as

$$c(\partial_t^2 T(\cdot,t),v) + a_{D}(\partial_t T(\cdot,t),v) + b(T(\cdot,t),v) = (F(\cdot,t),v)_{\Omega} \qquad (4.4.1)$$

for each $v \in T(\Omega)$.

Let $V(\Omega)$ be the closure of $T(\Omega)$ with respect to the norm of $H^1(\Omega)$. The bilinear forms c and a are defined for functions in $\mathcal{L}^2(\Omega)$ whilst b is defined for functions in $H^1(\Omega)$ using weak derivatives. However, the partial derivatives $\partial_t T$ and $\partial_t^2 T$ do not make sense when a function may be changed arbitrarily on a set of measure zero.

We define a function $w(t) = T(\cdot, t)$. Then $w'(t)$ may be defined with respect to the norm of $\mathcal{L}^2(\Omega)$, or other norms depending on the situation.

For the time interval we consider a bounded or unbounded interval of real numbers J that contains zero. We then have that J is either an unbounded interval containing zero, or $J = [0, T)$, or $J = [0, \infty)$. It is left to define the derivative of a function $u'(t)$ in terms of the norm of a given (Banach) space Y. The function u should have its values in Y.

Definition 4.4.1. *Derivative*
Let t be any interior point of J. Suppose there exists a $v \in Y$ such that

$$\lim_{\|h\| \to 0} \left\| h^{-1}\big(u(t+h) - u(t)\big) - v \right\|_Y = 0,$$

then v is the derivative of u at t. The derivative is denoted by $u'(t)$ and $u'(t) \in Y$ to avoid confusion. The derivative (function) u' is defined in the usual way as $u'(t)$ for every $t \in J$, with u'' defined by $(u')'$.

Notation

$u \in C\,(J, Y)$ if u is continuous on J with respect to the norm of Y.

$u \in C^k\,(J, Y)$ if $u^{(k)} \in C^k\,(J, Y)$.

Instead of Eq. (4.4.1) consider

$$c(u''(t), v) + a_{_D}(u'(t), v) + b(u(t), v) = (F(\cdot, t), v)_\Omega \tag{4.4.2}$$

for each $v \in V(\Omega)$. Equation (4.4.2) is the weak form of Eq. (4.4.1).

Problem DPLW

Find a function T with $T'(t) \in V(\Omega)$ and $T''(t) \in \mathcal{L}^2(\Omega)$ such that

$$c(T''(t), v) + a_{_D}(T'(t), v) + b(T(t), v) = (F(t), v)_\Omega \tag{4.4.3}$$

for each $v \in V(\Omega)$, while $T(0) = T_0$ and $T'(0) = T_d$.

Problem C-VW

If $\tau_{_T} = 0$, then $a_{_C}(u, v) = (u, v)_\Omega$. Find T, with $T'(t) \in V(\Omega)$ and $T''(t) \in \mathcal{L}^2(\Omega)$ such that

$$c(T''(t), v) + a_{_C}(T'(t), v) + b(T(t), v) = (F(t), v)_\Omega \tag{4.4.4}$$

for each $v \in V(\Omega)$, while $T(0) = T_0$ and $T'(0) = T_d$. Formally, Problem C-VW is a special case of Problem DPLW. If $\tau_{_T} = 0$, then $a_{_C}(u, v) = a(u, v) = (u, v)_\Omega$.

Problem FW

If $\tau_q = 0$, then $a_C(u, v) = (u, v)_\Omega$. Find T, with $T'(t) \in V(\Omega)$ such that

$$a_C(T'(t), v) + b(T(t), v) = (\mathcal{S}, v)_\Omega \tag{4.4.5}$$

for each $v \in V(\Omega)$, while $T(0) = T_0$. Formally, Problem FW is a special case of Problem C-VW.

4.5 Existence of solutions

As we have already pointed out in Section 1.3, it is essential that a mathematical problem is well-posed, *i.e*, a solution must exist and be unique. This is further emphasized in Chapter 3 where we discuss a so-called benchmark problem that is not well-posed and therefore does not have a classical or smooth solution. Non-smooth solutions were not considered. We point out that the discontinuous initial condition is the problem, and then propose a strategy to better formulate and solve such a problem. Many researchers attempted to solve this and similar problems (obtaining unacceptable results and blaming the numerical techniques for this), not realizing that it is not well-posed.

Regarding existence, it is convenient to use the general second order hyperbolic equation or general linear vibration problem in variational form as set out in [VV02]. (It may be helpful to consider also [VS19].) We also considered the theory in the book by Evans [Eva98] but concluded that it would require lengthy explanations. The same can be said about Chapter 5 in the book of Showalter [Sho77].

Now, following [VV02], we generalize Problems DPLW and C-VW. Let X, W and V denote real Hilbert spaces such that $V \subset W \subset X$.

Notation

X has inner product $\langle \cdot, \cdot \rangle_X$ and norm $\| \cdot \|_X$.

W has inner product c and norm $\| \cdot \|_W$.

V has inner product b and norm $\| \cdot \|_V$.

a denotes a bilinear form defined on V

Recall J, a bounded or unbounded interval of real numbers (refer to Section 4.4). Consider a bilinear form a defined on V and the following general problem.

Problem G

Given a function $f : J \to X$, find a function $u \in C^1(J; V)$ such that u' is continuous at 0 and for each $t \in J$, with

$$u'(t) \in V, \quad u''(t) \in W$$

and

$$c\big(u''(t), v\big) + a\big(u'(t), v\big) + b\big(u(t), v\big) = \big(f(t), v\big)_X \quad \text{for each } v \in V, \quad (4.5.1)$$

$$\text{with} \quad u(0) = u_0\,, \quad u'(0) = u_1\,.$$

Note that $u'(t) \in V$ implies that the derivative is defined in the normed space V (see the previous section).

Assumptions on spaces

The following assumptions are required for existence theory (as well as finite element convergence theory).

E1 V is dense in W and W is dense in X.

E2 There exists a positive constant C_b such that $\|v\|_W \leq C_b\|v\|_V$ for each $v \in V$.

E3 There exists a positive constant C_c such that $\|w\|_X \leq C_c\|w\|_W$ for each $w \in W$.

The general case for damping is first considered in [VV02].

E4 The bilinear form a is non-negative, symmetric and bounded on V, i.e. there exists a positive constant C_a such that for $v, w \in V$, $|a(u, v)| \leq C_a\|u\|_V\|v\|_V$.

The following general result is from [VV02].

Theorem 4.5.1. *Suppose Assumptions **E1**, **E2**, **E3** and **E4** hold. If $u_0 \in V$ and $u_1 \in V$, and there exists some $y \in W$ such that*

$$b(u_0, v) + a(u_1, v) = c(y, v) \quad \text{for each } v \in V, \tag{4.5.2}$$

then, for each $f \in C^1([0,T), X)$ there exists a unique solution

$$u \in C([0,T), V) \cap C^1([0,T), W) \cap C^1((0,T), V) \cap C^2((0,T), W)$$

for Problem G. If $f = 0$ then $u \in C^1([0,\infty), V) \cap C^2([0,\infty), W)$.

Remark In [VV02] there is a typo. It is stated that $u_1 \in W$ is required which is not sufficient. The condition in the theory above is correct according to the proof in [VV02].

Remark Problems DPLW and C-VW in the previous section are special cases of Problem G.

Application to heat conduction problems

Consider Problems DPLW and C-VW. For both problems the space X is $\mathcal{L}^2(\Omega)$ and the space W is the set $\mathcal{L}^2$ with inner product $c(\cdot,\cdot)$. Recall that $V(\Omega)$ is the closure of $T(\Omega)$ with respect to the norm of $H^1(\Omega)$.

Remark Deka and Dutta [DD19] refer to [VV02] but provide little detail regarding the applicability of the results in [VV02].

4.5.1 Problem G with weak damping

Assumption E4W *Weak damping*

The bilinear form a is non-negative, symmetric and bounded on W, i.e. there exists a positive constant C_W such that for $u, v \in W$, $|a(u,v)| \leq C_W \|u\|_W \|v\|_W$.

Definition

$$E_b = \{\, x \in V \;\big|\; \text{there exists a } y \in W \text{ such that } c(y,v) = b(x,v) \text{ for all } v \in V \,\}.$$

The following result is from [VV02].

Theorem 4.5.2. *Suppose Assumptions **E1**, **E2**, **E3** and **E4W** hold. Let J be an interval containing zero, then there exists a unique solution*

$$u \in C^1(J, V) \cap C^2(J, W)$$

for Problem G for each $u_0 \in E_b$, $u_1 \in V$ and each $f \in C^1(J, X)$. If $f = 0$ then $u \in C^1((-\infty, \infty), V) \cap C^2((-\infty, \infty), W)$.

Remark Theorem 4.5.2 may be applied to the undamped case ($a = 0$).

Application to Problem C-VW

For the C-V model, $\tau_T = 0$, and $a_C(u, v) = (u, v)_\Omega$, which implies that

$$|a_c(u, v)| \leq \|u\|\|v\| \leq \tau_q^2 \|u\|_W \|v\|_W$$

(by the Cauchy-Schwarz inequality). Therefore Theorem 4.5.2 can be applied to Problem C-VW.

In order to use Theorem 4.5.2. it must be verified that T_0, T_d and F meet the requirements in the theorem. Firstly T_0 and T_d must both belong to $V(\Omega)$. Using the definition of E_b above existence of a $y \in W$ such that $b(T_0, v) = c(y, v)$ is required.

Next consider whether $T_0 \in E_b$. We now use Eqs. (4.3.6) and (4.3.7). If $T_0 \in C^2(\bar{\Omega})$ and satisfy the boundary conditions then using integration by parts, we find that

$$\begin{aligned} b(T_0, v) = \iiint_\Omega \alpha \nabla T_0 \cdot \nabla v \, dV &= \iiint_\Omega \alpha \nabla^2 T_0 \cdot v \, dV \\ &= \frac{\alpha}{\tau_q} c(\nabla^2 T_0, v). \end{aligned} \tag{4.5.3}$$

It follows from the theory in [VV02] that $T(t) \in E_b$ if $T(0) = T_0 \in E_b$. This means that $T(\cdot, t)$ is at least in $H^2(\Omega)$ for each t.

For convenience we repeat the definition of the function F:

$$F(x, t) = \mathcal{S}(x, t) + \tau_q \, \partial_t \mathcal{S}(x, t).$$

Consequently, the range of F is in $\mathcal{L}^2(\Omega) \times V(\Omega)$ and it is required that

$$F \in C^1(J; \mathcal{L}^2(\Omega) \times V(\Omega)).$$

This means that the derivative $\partial_t^2 \mathcal{S}$ must exist.

Application to the CT-benchmark problem

The equivalent problem formulation of the CT-benchmark problem is a special case of Problem C-V, with $\alpha = 1$, $\tau_q = 1$ and the damping coefficient is 2. Following from the discussion in Chapter 3, based on the work by Weinberger [Wei95], a classical solution of the equivalent, and therefore CT-benchmark problem is possible, provided that $\theta_{in}(0) = (\theta_{in})'(1) = (\theta_{in})''(0) = 0$, and $\theta_{in} \in \mathcal{C}^2[0,1]$.

If the CT-benchmark problem is to have a weak solution, it is required that $\theta_{in} \in E_b$ and $\theta'_{in} \in V$. It is clear that the CT-benchmark problem does not even have a weak solution. (The conditions $\theta_{in} \in E_b$ and $\theta'_{in} \in V$ are necessary conditions.)

4.5.2 Problem G with strong Damping

Assumption E5S *Strong damping*
The bilinear form a is positive definite on V, *i.e.* there exists a $K > 0$ such that $a(u,u) \geq K\|u\|_V^2$ for any $u \in V$.

Theorem 4.5.3. *Suppose Assumptions **E1**, **E2**, **E3**, **E4** and **E5S** hold. Let $f : [0,T] \to W$ be locally Lipschitz. Then there exists a unique solution*

$$u \in C\left([0,T),V\right) \cap C^1\left([0,T),W\right) \cap C^2\left((0,T),W\right)$$

for Problem G, for any $u_0 \in V$, $u_1 \in W$. If $f = 0$ then

$$u \in C\left([0,\infty),V\right) \cap C^1\left([0,\infty),W\right) \cap C^\infty\left((0,\infty),V\right).$$

Remark It follows from the definitions of weak and strong damping and Assumption E2 that damping cannot be weak and strong.

Application to Problem DPLW

We defined $a_{_D}(u,v) = (u,v)_\Omega + a_\nabla(u,v)$ in Section 4.4. It follows that

$$a_D(u,u) \geq a_{_\nabla}(u,u) = \iiint_\Omega \alpha\tau_{_T} \nabla u \cdot \nabla u \, dV = \tau_{_T} b(u,u).$$

Thus the damping is strong in the case of the DPL model.

Using the one-dimensional bilinear forms defined in Section 4.3 we have the same situation:

$$a_{_D}(u,u) \geq \tau_{_T} \int_0^1 \alpha u'u'\,dx = \tau_{_T}\, b(u,u). \tag{4.5.4}$$

As mentioned above, the damping in the DPL model cannot be considered as weak.

To apply Theorem 4.5.3 consider the conditions. The condition on the function F is the same as in Subsection 4.5.1. For the initial condition we only need $T_0 \in V(\Omega)$ and $T_d \in \mathcal{L}^2(\Omega)$.

4.6 FEM approximation

In this section we discuss convergence of the FEM approximation for second order hyperbolic-type problems briefly.

The assumptions made for existence theory (for example assumptions on spaces) are also required for convergence of the FEM approximation. However, more assumptions must be made to obtain optimal error estimates.

In only a minor part of this thesis is FEM relevant. Nevertheless it is worth noting that several publications on FEM can be used to determine convergence and error estimates for Problems C-VW, DPLW and FW. We mention two articles which are convenient since the formulation of the weak variational problems are the same as in Section 4.4.

The results derived in [BV13] are applicable to the case of weak damping for Problem G, *i.e.* Problem C-VW. For Problem DPLW, the strong damping case, one may use the results from [BSV17] which are valid for general damping. It is therefore also valid for strong damping.

In Chapter 3 the FEM is used to solve Problem A3. Since the forcing function f and initial conditions are sufficiently smooth, the problem has a classical solution. As a result optimal error estimates can be derived.

Chapter 5

Modal analysis

5.1 Introduction

It is well known that Problem 1 Section 3.2 can be "solved" using separation of variables. If f_n is an eigenfunction of the eigenvalue problem

$$c^2 f_n'' + \lambda_n f_n = 0$$

with corresponding eigenvalue λ_n, then

$$T'' + 2\gamma T' + \lambda_n T = 0$$

can be solved. The function $u_n(x,t) = T_n(t)f_n(x)$ is referred to as a modal solution for the PDE. It also satisfies the boundary conditions. The idea is that the solution of Problem 1 can be approximated by partial sums of modal solutions. Convergence of the approximation can be proved, see *e.g.* [Wei95, Section 26]. (A rigorous proof as in the book is not trivial.)

Modal analysis can also be done on the problem in variational form, even when classical solutions do not exist. It turns out that convergence of partial sums depends on completeness of eigenfunction expansions. The theory can be found in the *Functional Analysis* textbook by Zeidler [Zei95]. One may also consider Evans' book [Eva98].

For this thesis the article [CVV18] is convenient. The theory is presented in [CVV18] using a variational approach.

For the heat conduction models the general abstract formulation, Problem DLPW, is developed in Section 4.4. The associated eigenvalue problem can be one, two or three dimensional, depending on the spatial dimension of the

model. But it is possible to derive conditions in terms of the physical parameters of the models whether the modes are underdamped or overdamped.

This chapter must be seen as a preparation for the important Chapter 6. It does not contain new mathematics; it is rather a new approach that connect the second order variational problem to Functional Analysis. The chapter was written before 2018 when [CVV18] was published but I was informed of this approach and thank the authors. Writing up the Chapter is my own work.

Of course, one may consider other methods to solve problems of this type, but we found modal analysis convenient. Modal analysis provides a means to estimate the unknown lag times. Also, it provides a link to the work in [CVV18] and finite element analysis.

5.2 Modal solutions

5.2.1 Eigenvalue problem

Consider **Problem G** (in Section 4.5) with modal damping and $f = 0$:

$$\begin{aligned} &c\big(u''(t), v\big) + a\big(u'(t), v\big) + b\big(u(t), v\big) = 0 \text{ for each } v \in V, \quad (5.2.1)\\ &u(0) = u_0 \quad \text{and} \quad u'(0) = u_1. \end{aligned}$$

Consider a possible solution of the form $u(t) = y(t)w$, $w \in V$. Substituting this trial solution into Eq. (5.2.1), we obtain:

$$c\big(y''(t)w, v\big) + a\big(y'(t)w, v\big) + b\big(y(t)w, v\big) = 0. \quad (5.2.2)$$

For the undamped case where $a = 0$, u is a solution of Eq. (5.2.1) if and only if

$$y''(t) + \lambda y(t) = 0$$

and

$$b(w, v) - \lambda\, c(w, v) = 0 \quad \text{for each} \quad v \in V.$$

It is therefore necessary to consider the following eigenvalue problem.

Problem EG

Find $w \in V$ and $\lambda \in C$ such that $w \neq 0$ and

$$b\big(w, v\big) = \lambda\, c\big(w, v\big) \text{ for each } v \in V. \quad (5.2.3)$$

If the pair (λ, w) is a solution of Problem EG, then λ is called an eigenvalue and w an associated eigenvector. It follows that $u(t) = y(t)w$ is a solution of Eq. 5.2.1, called a modal solution.

If $a \neq 0$, the method still works if *modal damping* is assumed; i.e.

$$a(\cdot,\cdot) = k_1\, c(\cdot,\cdot) + k_2\, b(\cdot,\cdot)$$

where k_1, k_2 are non-negative real numbers.

Then a trial solution of the form $u(t) = y(t)w$ has to satisfy

$$(y''(t) + k_1 y'(t))\; c\big(w, v\big) + (k_2 y'(t) + y(t))\; b\big(w, v\big) = 0 \quad \text{for each} \quad v \in V.$$

Therefore u is a solution of Eq. (5.2.1) if and only if (λ, w) is a solution of Problem EG and the function y is a solution of

$$y''(t) + (k_1 + \lambda k_2)\; y'(t) + \lambda y(t) = 0. \tag{5.2.4}$$

Note that the undamped case ($a = 0$) is included as a special case of modal damping ($k_1 = k_2 = 0$) and it need not be considered separately.

The idea is to use the series

$$\sum_{k=1}^{\infty} y_k(t) w_k$$

as a solution for Eq. (5.2.1). In order to establish the validity of this formal series solution, the following general notation is introduced.

Notation

Consider an arbitrary Hilbert space H with inner product $\langle \cdot, \cdot \rangle$ and norm $\| \cdot \|$. Suppose $x \in H$ and $(\phi_n) \subset H$ is an orthonormal sequence. The partial sums s_n are defined as follows:

$$s_n = \sum_{k=1}^{n} \langle x, \phi_k \rangle\; \phi_k \quad \text{for each } n.$$

Definition Complete orthonormal sequence

An orthonormal sequence (ϕ_n) is called *complete* (or total), when

$$\|s_n - x\| \to 0 \text{ as } n \to \infty \text{ for each } x \in H.$$

If $\|s_n - x\| \to 0$ as $n \to \infty$, we write

$$x = \sum_{k=1}^{\infty} \langle x, \phi_k \rangle \phi_k.$$

Consider Problem EG for the Hilbert spaces V and W from Section 4.5, and recall Assumptions E1 to E4 for these spaces. For modal damping, it is clear that the bilinear form a satisfies Assumption E4.

As b is symmetric and nonnegative, it is important to note that $\lambda \neq 0$. Assuming that $\lambda = 0$, implies that $u = 0$, which is not an eigenvector. It is also not difficult to prove the following:

(a) The eigenvalues are real and non-negative.

(b) The eigenvectors are orthogonal in W with respect to the inner product c.

These facts and more follow from Theorem 5.2.1 below. Note that for the space V an additional assumption is required.

Assumption C1 Any bounded set in V is relatively compact in W.

Theorem 5.2.1. *Consider the eigenvalue problem EG. Suppose assumptions E1, E2, E3 and C1 hold, then:*

(a) All the eigenvalues λ are real and two eigenvectors that correspond to different eigenvalues are orthogonal.

(b) Each eigenspace is finite dimensional.

(c) There exists a sequence of orthonormal eigenvectors (w_k) with a corresponding increasing sequence of eigenvalues (λ_k).

(d) For this increasing sequence (λ_k), we have $\lambda_k \to \infty$ as $k \to \infty$.

(e) The orthonormal sequence (w_k) of eigenvectors is complete in W.

Proof: See Section 5.5.

5.2.2 Series solution

From Theorem 5.2.1, Problem EG has an increasing sequence λ_k of eigenvalues with corresponding eigenvectors w_k, *i.e.* $b(w_k, v) = \lambda_k\, c(w_k, v)$. Consequently, if y_k is a solution of Eq. (5.2.4), then $u_k(t) = y_k(t)w_k$ is a solution of Eq. (5.2.1) and

$$c\big(y_k''(t)w_k, v\big) + a\big(y_k'(t)w_k, v\big) + b\big(y_k(t)w_k, v\big) = 0 \quad \text{for } k = 1, 2, \ldots . \tag{5.2.5}$$

As Eq. (5.2.1) is a linear problem, superposition of solutions is allowed, and the partial sum u_N defined by

$$u_N(t) = \sum_{k=1}^{N} y_k(t)w_k, \tag{5.2.6}$$

is also a solution of Eq. (5.2.1).

In general u_N will not satisfy the specified initial conditions $u_N(0) = u_0$ and $u_N'(0) = u_1$.

Formal series solution

To solve Eq. (5.2.1) for specified initial conditions, a series solution is used:

$$u(t) = \sum_{k=1}^{\infty} y_k(t)w_k. \tag{5.2.7}$$

The question then arises whether it is possible to write given initial values u_0 and u_1 as eigenfunction expansions.

Approximation of initial values

From Theorem 5.2.1, it follows that for $u_0 \in W$ and $u_1 \in W$,

$$u_0 = \sum_{k=1}^{\infty} c(u_0, w_k)w_k \quad \text{and} \quad u_1 = \sum_{k=1}^{\infty} c(u_1, w_k)w_k.$$

The coefficients $c(u_0, w_k)$ and $c(u_1, w_k)$ are called generalised Fourier coefficients for u_0 and u_1. See Section 5.4. Hence, the following initial values should be used for y_k when solving Eq. (5.2.4):

$$y_k(0) = c(u_0, w_k) \quad \text{and} \quad y_k'(0) = c(u_1, w_k).$$

Fourier coefficients and orthogonal eigenvectors

If (w_k) is an orthogonal sequence of eigenvectors, the formal series solution can be written as

$$u(t) = \sum_{k=1}^{\infty} y_k(t) w_k.$$

As v_k is not necessarily normalized in W, the eigenvector expansions for u_0 and u_1 changes to

$$u_0 = \sum_{k=1}^{\infty} \|v_k\|_W^{-2}\ c(u_0, v_k) v_k \quad \text{and} \quad u_1 = \sum_{k=1}^{\infty} \|v_k\|_W^{-2}\ c(u_1, v_k) v_k \tag{5.2.8}$$

since $w_k = \|v_k\|_W^{-1} v_k$. Therefore the Fourier coefficients are given by

$$\|v_k\|_W^{-2}\ c(u_0, v_k) \quad \text{and} \quad \|v_k\|_W^{-2}\ c(u_1, v_k)$$

and the following initial values should be used for y_k when solving Eq. (5.2.4):

$$y_k(0) = \|v_k\|_W^{-2}\ c(u_0, v_k) \quad \text{and} \quad y_k'(0) = \|v_k\|_W^{-2}\ c(u_1, v_k). \tag{5.2.9}$$

These expressions for the series solution and the Fourier coeffients are used in applications.

5.2.3 Convergence in energy

In this subsection the word "energy" refers to a purely mathematical concept, and not to the thermal energy used in the heat conduction models ([CVV18]).

Consider Problem G with initial conditions $u(0) = u_0 \in V$ and $u'(0) = u_1 \in W$. The existence of a solution is proved in Section 4.5. For the approximation u_N in Eq. (5.2.6) of the solution u of Problem G, it is shown in [CVV18] that

$$\|u(t) - u_N(t)\|_V \to 0 \text{ as } N \to \infty.$$

In the proof the dimensionless energy expression, defined below, is used.

Definition Dimensionless energy

The *dimensionless energy* $\mathcal{E}$ associated with a function u is given by

$$\begin{aligned} \mathcal{E}(t) &= \frac{1}{2} c(u'(t), u'(t)) + \frac{1}{2} b(u(t), u(t)) \\ &= \frac{1}{2} \|u'(t)\|_W^2 + \frac{1}{2} \|u(t)\|_V^2. \end{aligned}$$

It is easy to see that for any solution u of Eq. (5.2.1), (as expected from physics)

$$\mathcal{E}(t) \leq \mathcal{E}(0). \tag{5.2.10}$$

If u is a solution of Eq. (5.2.1) on the interval J, $u \in C^1(J,V) \cap C^2(J,W)$, and

$$\begin{aligned} \mathcal{E}'(t) &= c(u''(t),u'(t)) + b(u(t),u'(t)) \\ &= -a(u'(t),u'(t)) \leq 0. \end{aligned}$$

Recall that u_N is a solution of Eq. (5.2.1) with initial conditions $u_N(0) = u_0^N$ and $u_N'(0) = u_1^N$. Hence the error function $u_N^E = u - u_N$ also satisfies Eq. (5.2.1) with $u_N^E(0) = u_0 - u_0^N$ and $(u_N^E)'(0) = u_1 - u_1^N$.

Let $\mathcal{E}^E(t)$ denote the energy associated with the error function u_N^E. The energy inequality Eq. (5.2.10) is valid for u_N^E:

$$\mathcal{E}^E(t) \leq \mathcal{E}^E(0) \text{ for all } t > 0.$$

Rewritten in terms of norms, this energy inequality yields:

$$\|u(t) - u_N(t)\|_V^2 + \|u'(t) - u_N'(t)\|_W^2 \leq \|u_0 - u_0^N\|_V^2 + \|u_1 - u_1^N\|_W^2. \tag{5.2.11}$$

For any $u_1 \in W$, it follows from Theorem 5.2.1 that there exist Fourier coefficients $c(u_1, w_k)$ such that

$$\|u_1 - u_1^N\|_W \to 0 \text{ as } N \to \infty.$$

But it is also necessary to approximate u_0 in the energy norm $\|\cdot\|_V$. This does not follow from Theorem 5.2.1.

Note that in addition to being orthogonal in W with respect to c, the eigenvectors $w_k \in V$ are also orthogonal with respect to b:

$$b(w_i, w_j) = \lambda_i c(w_i, w_j) = 0 \text{ for all } i \neq j.$$

Consequently, for any $x \in V$, Fourier coefficients can be calculated with respect to the inner product b. The following theorem is proved in [CVV18].

Theorem 5.2.2. *Consider any $x \in V$. If*

$$\eta_k = \frac{b(x,w_k)}{b(w_k,w_k)} \quad \textit{and} \quad x_N = \sum_{k=1}^{N} \eta_k w_k,$$

then $\|x - x_N\|_V \to 0$ as $N \to \infty$.

Note, that

$$\|w_k\|_V^2 = b(w_k, w_k) = \lambda_k c(w_k, w_k) = \lambda_k \|w_k\|_W^2 = \lambda_k \text{ for all } k. \tag{5.2.12}$$

For any $x \in V$, the following result follows from Eq. (5.2.3) combined with Eq. (5.2.12):

$$\eta_k = \frac{b(x, w_k)}{b(w_k, w_k)} = \frac{\lambda_k c(x, w_k)}{b(w_k, w_k)} = c(x, w_k).$$

(Recall that the eigenfunctions w_n are normalised with respect to the norm in W.) This means that the same Fourier coefficients for x are obtained, irrespective of whether they are calculated with respect to the inertia inner product c or the energy inner product b. The main significance of Theorem 5.2.2 is that convergence of the partial sums is obtained with respect to the energy norm $\|.\|_V$.

It follows from Theorem 5.2.2 that for any $u_0 \in V$ there exist Fourier coefficients η_k for u_0, such that

$$\|u_0 - u_0^N\|_V \to 0 \text{ as } N \to \infty, \tag{5.2.13}$$

and therefore that $\mathcal{E}^E(t) \to 0$ as $N \to \infty$.

Consequently, for all $t > 0$, we have convergence of the partial sum $u_N(t)$ to the solution $u(t)$ in the energy norm $\|.\|_V$ and convergence of $u'_N(t)$ to the derivative $u'(t)$ in the inertia norm $\|.\|_W$. In addition, the accuracy of these approximations in terms of the partial sums *can be guaranteed* as it depends only on the accuracy of the partial sum approximations of u_0 and u_1 at time $t = 0$.

Remark

In [CVV18] the following Parseval-type expressions are derived for $x \in V$:

$$\|x\|_W^2 = \sum_{k=1}^{\infty} \eta_k^2 = \sum_{k=1}^{\infty} c(x, w_k)^2, \tag{5.2.14}$$

$$\|x\|_V^2 = \sum_{k=1}^{\infty} \lambda_k \eta_k^2 = \sum_{k=1}^{\infty} \lambda_k c(x, w_k)^2. \tag{5.2.15}$$

If the eigenfunctions v_k are not normalised in W, as in Eq. (5.2.8), the partial sum x_N is written as

$$x_N = \sum_{k=1}^{N} c\left(x, \frac{v_k}{\|v_k\|_W}\right) \frac{v_k}{\|v_k\|_W} = \sum_{k=1}^{N} \frac{c(x, v_k)}{\|v_k\|_W} \frac{v_k}{\|v_k\|_W}$$

and the expressions in Eq. (5.2.14) and Eq. (5.2.15) change to

$$\|x\|_W^2 = \sum_{k=1}^{\infty} \frac{c(x,v_k)^2}{\|v_k\|_W^2}, \tag{5.2.16}$$

$$\|x\|_V^2 = \sum_{k=1}^{\infty} \lambda_k \frac{c(x,v_k)^2}{\|v_k\|_W^2}. \tag{5.2.17}$$

5.3 Heat conduction models

5.3.1 Weak formulation

Recall Problem DPLW in Section 4.4, and consider the homogeneous problem (with $F = 0$):

$$\begin{aligned} &c\big(T''(t),v\big) + a_{_D}\big(T'(t),v\big) + b\big(T(t),v\big) = 0, \text{for each } v \in V(\Omega), \\ &T(0) = T_0 \quad \text{and} \quad T'(0) = T_d. \end{aligned} \tag{5.3.1}$$

From this point onward we assume that α, τ_q and $\tau_{_T}$ are constant.

The bilinear form $b(\cdot,\cdot)$ is defined in Eq. (4.3.6). It is not desirable that the parameter α is "hidden" in b.

Notation Let $b^*(\cdot,\cdot) = \frac{1}{\alpha}\, b(\cdot,\cdot)$ and $\gamma = \frac{1}{2\tau_q}$.

Note that

$$b^*(u,v) = \iiint_{\Omega} \mathit{grad}\, u \cdot \mathit{grad}\, v \; dV.$$

Equation (4.3.8) in (Problem DPLV) now reads

$$\big(T''(t),v\big)_{\Omega} + 2\gamma\,\big(T'(t),v\big)_{\Omega} + \frac{\alpha}{\tau_q}\, b^*\big(T(t),v\big) + \frac{\alpha\tau_{_T}}{\tau_q}\, b^*\big(T'(t),v\big) = 0 \tag{5.3.2}$$

for each $v \in V(\Omega)$.

The C-V model follows directly when $\tau_{_T} = 0$:

$$\big(T''(t),v\big)_{\Omega} + 2\gamma\big(T'(t),v\big)_{\Omega} + \frac{\alpha}{\tau_q}\, b^*\big(T(t),v\big) = 0 \text{ for each } v \in V(\Omega). \tag{5.3.3}$$

Mutliplying throughout with τ_q and then letting $\tau_q = 0$, results in the Fourier model

$$\big(T'(t),v\big)_{\Omega} + \alpha\; b^*\big(T(t),v\big) = 0 \text{ for each } v \in V(\Omega). \tag{5.3.4}$$

5.3.2 Modal solutions

In the rest of this section we apply the theory from Section 5.2. Consider Problem DPLW and a possible solution of the form

$$T(t) = y(t)w, \quad w \in V(\Omega).$$

Substituting this trial solution into Eq. (5.3.2), we obtain

$$\left(y''(t)w, v\right)_\Omega + 2\gamma \left(y'(t)w, v\right)_\Omega + \frac{\alpha}{\tau_q} b^*\left(y(t)w, v\right) + \frac{\alpha\tau_T}{\tau_q} b^*\left(y'(t)w, v\right) = 0. \tag{5.3.5}$$

We therefore consider the following eigenvalue problem (a special case of Problem EG):

Problem EGH

Find $w \in V$ and $\lambda \in C$ such that $w \neq 0$ and

$$b^*\left(w, v\right) = \lambda \left(w, v\right)_\Omega \quad \text{for each} \quad v \in V(\Omega).$$

Now T is a solution of Eq. (5.3.1) if and only if (λ, w) is a solution of Problem EGH and

$$y'' + \left(2\gamma + \frac{\alpha\tau_T}{\tau_q}\lambda\right) y' + \frac{\alpha\lambda}{\tau_q} y = 0. \tag{5.3.6}$$

For the C-V model $\tau_T = 0$, and y is a solution of

$$y'' + 2\gamma y' + \frac{\alpha\lambda}{\tau_q} y = 0. \tag{5.3.7}$$

For the Fourier model multiply Eq. (5.3.7) by τ_q, set $\tau_q = 0$, and then y is a solution of

$$y' + \alpha\lambda y = 0. \tag{5.3.8}$$

From Section 5.2 follows that Problem EGH has a sequence λ_k of eigenvalues with corresponding eigenvectors w_k, *i.e.* $b^*(w_k, v) = \lambda_k \left(w_k, v\right)_\Omega$.

Remarks

1. Note that the same eigenvalue problem, Problem EGH applies to all three models.

2. The eigenvectors w_k are not necessarily normalized in $W(\Omega) = \mathcal{L}^2(\Omega)$ (as already mentioned in Section 5.2.2).

3. The ordinary differential equations for the time dependent function y for depend only on the eigenvalues λ determined in Problem EGH. The spatial dimensions of the eigenfunctions do not affect these solutions.

In the next chapter, we consider the solution y_k of the ordinary differential equation corresponding to the model under consideration, for each k. Initial values for the differential equations are the Fourier coefficients for T_0 and T_d, as explained in Section 5.2.2.

The series solution is given by

$$T(t) = \sum_{k=1}^{\infty} y_k(t) w_k. \tag{5.3.9}$$

5.4 Generalized Fourier series and symmetric compact operators

This section contains some important results from the literature on generalized Fourier series. It will be used in the next section to prove Theorem 5.2.1 in Section 5.2.

An inner product space X is a vector space X with an inner product $\langle \cdot, \cdot \rangle$ defined on it. The associated norm $\| \cdot \|$ is defined by $\|x\| = \langle x, x \rangle^{1/2}$.

The following notation is used by Kreyszig, [Kre89].

Assume that $(\phi_n) \subset X$ is an orthonormal sequence in X, and that $V_m = \text{span}\{\phi_1, \phi_2, \ldots, \phi_m\}$ for each m.

For any $u \in X$, let $c_k = \langle u, \phi_k \rangle$ for each k. These constants are called the Fourier coefficients of u.

The partial sums s_n are defined as:

$$s_n = \sum_{k=1}^{n} \langle u, \phi_k \rangle \, \phi_k = \sum_{k=1}^{n} c_k \phi_k \quad \text{for each } n.$$

A number of useful results regarding partial sums are listed here.

Theorem 5.4.1 ([Kre89]). *Using the notation above:*

(a) $\langle u - s_n, w \rangle = 0$ *for each* $w \in V_n$. *Consequently,* $\|u - s_n\| \leq \|u - w\|$ *for each* $w \in V_n$.

(b) $\|u - s_n\|^2 = \|u\|^2 - \|s_n\|^2$.

(c) $\lim_{n\to\infty} s_n = u$ *if and only if* $\lim_{n\to\infty} \|s_n\| = \|u\|$.

(d) $\|s_n\|^2 = \sum_{k=1}^{n} c_k^2$.

(e) $\lim_{n\to\infty} s_n = u$ *if and only if* $\sum_{k=1}^{\infty} \langle u, \phi_k\rangle^2 = \|u\|^2$.

(f) Let (ϕ_k) *be an orthonormal sequence in a Hilbert space* H*. If*

$$u = \sum_{k=1}^{\infty} c_k \phi_k$$

converges and the limit is u*, then the coefficients* c_k *are the Fourier coefficients* $\langle u, \phi_k\rangle$*, hence*

$$u = \sum_{k=1}^{\infty} \langle u, \phi_k\rangle \phi_k.$$

(g) If the Fourier series for u *converges to* w*, then the Fourier coefficients for* w *and* u *are the same and*

$$\langle u - w, \phi_k\rangle = 0 \quad \text{for each} \quad k.$$

(h) Let (ϕ_k) *be an orthonormal sequence in a Hilbert space* H*. Then for any* $u \in H$*, the series*

$$\sum_{k=1}^{\infty} c_k \phi_k$$

with Fourier coefficients $c_k = \langle u, \phi_k\rangle$*, converges in the norm of* H *(not necessarily to* u*).*

Definition Symmetric operator

A densely defined linear operator A is *symmetric* if, for all u and v in the domain of A,

$$\langle Au, v\rangle = \langle u, Av\rangle.$$

The following results for symmetric operators are valid for complex Hilbert spaces. In order to apply these results to a real Hilbert space H, the space H is embedded into a complex Hilbert space. See [Sch71, Section VI.5] for details.

Theorem 5.4.2 (Proposition 7.1.1 [Zei95])**.** *Let A be a linear bounded symmetric operator on H. Then*

(i) $\langle Au, u\rangle$ *is real for all* $u \in H$.

(ii) All the eigenvalues of A are real.

(iii) Two eigenvectors of A with different eigenvalues are orthogonal.

(iv) If (u_n) is a complete orthonormal sequence of eigenvectors of A, then the corresponding sequence (λ_n) of eigenvalues contains all the eigenvalues of A.

Definition Compact operator

For two normed spaces X and Y, a linear operator $A : X \to Y$ is called a compact operator if for every bounded subset $M \subset X$, the image $A(M)$ is relatively compact in Y; that is, the closure of $A(M)$ is compact in Y.

Theorem 5.4.3 (Theorem 4A [Zei95])**.** *Let $A : H \to H$ be a linear compact symmetric operator on the separable Hilbert space H with $H \neq \{0\}$, $A \neq 0$ and hence $\|A\| \neq 0$ (if $Au = 0$, then $u = 0$). Then, the following hold true:*

(i) Two eigenvectors of A that correspond to different eigenvalues are orthogonal.

(ii) The operator A has an orthonormal sequence of eigenvectors with corresponding eigenvalues.

(iii) Each eigenspace is finite dimensional.

(iv) For the sequence (λ_n) of eigenvalues, we have

$$\lambda_n \to 0 \quad as \quad n \to \infty.$$

(v) The orthonormal sequence (u_n) of eigenvectors is complete in H.

5.5 Bilinear forms

This section contains a discussion of the proof of Theorem 5.2.1 of Section 5.2 as presented in [CVV18].

It is necessary to show that a symmetric compact linear operator K can be constructed from the bilinear form b. The relationship between the eigenvalues and eigenvectors of b and K is the main result that is required in order to apply the general theory Fourier series for symmetric compact operators in Section 5.4.

Let X, W and V denote real Hilbert spaces such that $V \subset W \subset X$, as introduced in Section 4.5. Recall assumptions E1 to E4 from Section 4.5, as well as the additional assumption C1 from Section 5.2.

Proposition 5.5.1. *For each $f \in W$, there exists a unique $u \in V$ such that*

$$b(u, v) \;=\; c(f, v) \quad \textit{for each} \quad v \in V.$$

Proof Let $\phi(v) = c(f, v)$, then ϕ is a functional and it is clearly linear. For any $v \in V$,

$$\begin{aligned} |\phi(v)| &= |c(f, v)| \\ &\leq \|f\|_W \|v\|_W \\ &\leq C_b \|f\|_W \|v\|_V. \end{aligned}$$

Therefore we have that ϕ is a bounded linear functional on V.

Following from Riesz's Theorem [Kre89, Section 3.8], ϕ can be represented in terms of the inner product b on V:

$$b(u, v) \;=\; \phi(v) \;=\; c(f, v) \quad \text{for each} \quad v \in V.$$

Next an operator K is constructed from the bilinear form b:

$K\colon W \longmapsto V$, with $Kf = u$ if $b(u, v) = c(f, v)$ for all $v \in V$.

Lemma 5.5.1. *The operator K is linear, bounded and symmetric.*

Proof It is trivial to show that K is linear. To show that K is bounded, note that, from the Cauchy-Schwarz inequality,

$$\|Kf\|_V^2 \;=\; |b(Kf, Kf)| = |c(f, Kf)| \leq \|f\|_W \|Kf\|_W.$$

Since $Kf \in V$, Assumption E2 states that there exists a constant C_b such that $\|Kf\|_W \leq C_b \|Kf\|_V$. Therefore

$$\|Kf\|_V^2 \;\leq\; C_b \|f\|_W \|Kf\|_V$$

and hence

$$\|Kf\|_V \leq C_b\|f\|_W.$$

Therefore the linear operator K from $(W, \|\cdot\|_W)$ to $(V, \|\cdot\|_V)$ is bounded. Finally, it follows from the symmetry of b and c that

$$b(Kf, v) = c(f, v) = c(v, f) = b(Kv, f)$$

for each f and v in V. Therefore the operator K is symmetric.

Corollary *K is a compact linear operator from $(W, \|\cdot\|_W)$ to $(W, \|\cdot\|_W)$.*

Proposition 5.5.2. *K is invertible, i.e. for each $u \in \mathcal{R}(K)$, the range of K, there exists a unique $f \in W$ such that $u = Kf$.*

Proof To prove the uniqueness, we need to prove that $Kf = 0$ implies that $f = 0$. Let $Kf = 0$ then $b(Kf, v) = 0$ for all $v \in V$. That is $c(f, v) = b(Kf, v) = 0$ for all $v \in V$. Since V is dense in W it follows that $c(f, v) = 0$ for each $v \in W$, hence $f = 0$.

The relationship between the eigenvalues and eigenvectors of b and those of the operator K is stated in the following lemma.

Lemma 5.5.2. *$u \in V$ and $b(u, v) = \lambda c(u, v)$ for each $v \in V$ if and only if $Ku = \lambda^{-1}u$.*

Proof Recall that the eigenvalues of b can not be zero. From the definition of K we have $b(u, v) = c(K^{-1}u, v)$ for all $v \in V$. Hence $b(u, v) = \lambda c(u, v)$ for all $v \in V$ if and only if $\lambda c(u, v) = c(K^{-1}u, v)$ for all $v \in V$. Since V is dense in W, this is equivalent to $K^{-1}u = \lambda u$ or $Ku = \lambda^{-1}u$.

Proof of Theorem 5.2.1

This theorem is a reformulation of Theorem 5.4.3 of Section 5.4. Using the corollary to Lemma 5.5.1, and Lemma 5.5.2, the proof of this theorem is immediate.

Remark

An alternative approach, where the eigenfunction expansions are obtained directly from the bilinear forms, is developed in [Hil62].

Chapter 6

Comparison of heat conduction models

6.1 Introduction

In this study, three heat conduction models are used to describe the effects of intense heating in a short time interval, and in this chapter the main objective is to compare the predictions from the C-V and DPL models with that of the Fourier model.

The single-pulse problem as formulated in Section 6.9 is used for these comparisons. A single heat pulse is applied to one endpoint of a one-dimensional specimen for a short time interval. Of specific interest is the temporal and spatial behaviour of the heat pulse as it propagates through the specimen. The comparison between the models is presented in Section 6.10, but there are several issues to consider in preparation for this comparison. We start with a simpler case where heating is applied continuously to one of the endpoints of a one-dimensional specimen in Sections 6.6 and 6.8.

Three-dimensional models are derived in Section 2.8, but the simplified one-dimensional versions are presented in Section 6.2 and they are used for comparing the models. Investigating one-dimensional models is not only a simpler option, but it is standard practise to determine the diffusivity of materials relying on one-dimensional heat transfer modelling. In this case, the heat transfer is modelled as a one-dimensional process, whereby heat diffuses from the front face to the rear face of a given specimen; e.g. [Bab10] and [BTY11]. The diffusivity of the material is then calculated from the thickness of the specimen and the so-called heat diffusion time.

Separation of variables (discussed in Section 5.3) is used to find solutions for the three heat conduction models. Eigenfunction series expansions of the solutions are obtained. There are several advantages to using this approach rather than using numerical methods. The eigenvalue problem (Problem EGH in Section 5.3) is the same for all three models. The functions that model the time behaviour do not depend on the spatial dimension of the problem, *i.e.* do not depend on the dimension of the eigenvalue problem. But it is possible to derive conditions in terms of the physical parameters of the models for whether the modes are underdamped or overdamped. (The terms underdamped and overdamped are not commonly used in the context of heat conduction, but are borrowed from the theory of mechanical vibrations.) The conditions are derived in Section 6.2 for the three heat conduction models.

Another advantage of the separation of variables approach is that partial sums of the series can be used to find approximate solutions for the different models. As shown in Section 5.2.3, the accuracy of these approximations depends only on the accuracy of the partial sum approximations of the initial conditions. Consequently, an exact upper bound for the error at any time $t > 0$ is available.

Next we have to consider which initial temperature distribution to use for the models. As discussed in Chapter 3, a discontinuous initial temperature distribution is often used, but is inadmissible. For the models to be well-posed, a smooth initial condition has to be used, and the procedure for constructing a smooth initial condition arbitrarily close to the discontinuous one, is described in Section 3.2.1. However, calculating the Fourier coefficients for the smooth initial condition is not practical. For the convergence in energy approach discussed in Section 5.2.3, at least a continuous initial condition is required. A continuous piecewise linear function can be constructed that is arbitrarily close to the discontinuous initial value. This initial value can be used to determine the number of terms to use in the partial sums. The Fourier coefficients for the discontinuous initial condition are easy to obtain, and are used in the numerical simulations.

Physically realistic values for the two lag times τ_q, the phase lag of the heat flux, and τ_T, the phase lag of the temperature gradient, are required. One of the challenges in heat conduction modelling is that these lag times (or relaxation times) are not reliably known. The modal analysis allows for calculating feasible values for the lag times τ_q and τ_T. We find feasible values for the lag times based on the assumption that the Fourier model yields physically realistic results after a sufficiently long time [MF53]. This assumption follows from the reasoning that after a thermal disturbance is

brought about in a specimen, and the lag times have elapsed, the Fourier model is sufficient to predict the temperature. Therefore, to be feasible as heat conduction models in the context of intense heating in a short time interval, the solutions of the C-V and DPL models should equal the solution of the Fourier model after a sufficiently long time.

We first calculate a ballpark value for τ_q in Section 6.3, and use this value in the comparison of the Fourier and the C-V models. The C-V model predicts a prominent wave front, as shown in Chapter 3.

The same value for τ_q is then used to estimate values for τ_T. The DPL, C-V and Fourier models are compared. Two cases are considered for the DPL model: one where the value of τ_T is chosen such that both over- and underdamped modes are present, and the other, where τ_T is chosen such that only overdamped modes are present.

Once all these issues have been addressed, a comparison of the three models for the single-pulse problem is presented in Section 6.10.

In this chapter a numerical value for α is required for simulations and for other calculations. The calculation of α is described in Section 2.8.1, and $\alpha = 0.0040732$ is obtained. This value for α is used throughout this chapter.

6.2 One-dimensional heat conduction models

We start with the case where heating is applied continuously to one of the endpoints of a one-dimensional specimen, keeping the temperature constant at that endpoint. This is a simpler case than the single-pulse problem, but the results for this case are used for part of the single-pulse problem. In the next sections, the DPL and C-V models are compared to the Fourier model for this simpler case.

6.2.1 Model problem

The dimensionless DPL problem is described in Section 2.8 and the weak formulation is given in Problem DPLW. See Eq. (4.4.3). Consider the case where $F = 0$.

The one-dimensional DPL model problem for $T(x,t)$ is given by

$$\begin{aligned} \partial_t^2 T + 2\gamma\,\partial_t T - \frac{\alpha\tau_{_T}}{\tau_q}\,\partial_t\partial_x^2 T &= c^2\,\partial_x^2 T,\ 0<x<1,\ t>0 \qquad (6.2.1)\\ T(0,t) &= 1\\ \partial_x T(1,t) &= 0\\ T(x,0) &= T_0(x)\\ \partial_t T(x,0) &= T_d(x) \end{aligned}$$

where $2\gamma = \dfrac{1}{\tau_q}$ and $c^2 = \dfrac{\alpha}{\tau_q}$.

Setting $u(x,t) = 1 - T(x,t)$, yields the model that will be used in computations, as the boundary conditions are homogenised.

$$\begin{aligned} \partial_t^2 u + 2\gamma\,\partial_t u - \frac{\alpha\tau_{_T}}{\tau_q}\,\partial_t\partial_x^2 u &= c^2\,\partial_x^2 u,\ 0<x<1,\ t>0 \qquad (6.2.2)\\ u(0,t) &= 0\\ \partial_x u(1,t) &= 0\\ u(x,0) &= u_0(x)\\ \partial_t u(x,0) &= u_d(x) \end{aligned}$$

The expressions for the series solutions developed in Section 5.3 apply to this problem. The series solution Eq. (5.3.9) yields the solution for $u(x,t)$ as:

$$u(x,t) = \sum_{k=1}^{\infty} y_k(t) w_k(x).$$

The expression for the temperature $T(x,t)$ is then obtained as:

$$T(x,t) = 1 - u(x,t) = 1 - \sum_{k=1}^{\infty} y_k(t) w_k(x).$$

As before, the corresponding C-V model is obtained by setting $\tau_{_T} = 0$ in Eq. (6.2.2). Multiplying the C-V model by τ_q, and then setting $\tau_q = 0$ yield the Fourier model.

6.2.2 Eigenvalue problem

The eigenvalue problem associated with Eq. (6.2.2) is the same for all three models, and has homogeneous boundary values.

$$\begin{aligned} w_k''(x) + \lambda_k w_k(x) &= 0, \ 0 < x < 1, \\ w_k(0) &= 0, \\ w_k'(1) &= 0. \end{aligned}$$

The eigenfunctions are

$$w_k(x) = \sin \nu_k x, \ \text{for } k = 1, 2, \ldots \tag{6.2.3}$$

where $\nu_k = (2k-1)\pi/2$ and the eigenvalue is given by

$$\lambda_k = \nu_k^2. \tag{6.2.4}$$

Note that the eigenfunctions $w_k(x)$ are not normalized in $W = \mathcal{L}^2(0,1)$ as

$$\|w_k\|_W^2 = \int_0^1 \sin^2 \nu_k x \, dx = \frac{1}{2}.$$

6.2.3 The DPL model

For each k we require the solution $y_k(t)$ for the ordinary differential equation

$$y_k'' + \left(2\gamma + \frac{\alpha\tau_T\lambda_k}{\tau_q}\right) y_k' + \frac{\alpha\lambda_k}{\tau_q} y_k = 0. \tag{6.2.5}$$

Setting $2\gamma_k = 2\gamma + \dfrac{\alpha\tau_T\lambda_k}{\tau_q}$, the solutions of the characteristic equation of Equation (6.2.5) is given by

$$-\gamma_k \pm \sqrt{{\gamma_k}^2 - c^2\nu_k^2},$$

where $\gamma_k = \gamma + \dfrac{\alpha\tau_T\lambda_k}{2\tau_q}$, $c^2 = \dfrac{\alpha}{\tau_q}$ and $\nu_k = \sqrt{\lambda_k} = \dfrac{(2k-1)\pi}{2}$.

In the overdamped case (${\gamma_k}^2 > c^2\nu_k^2$), we have

$$y_k(t) = a_k e^{r_1^k t} + b_k e^{r_2^k t}, \tag{6.2.6}$$

with r_1^k and r_2^k given by

$$\begin{aligned} r_1^k &= -\gamma_k + \mu_k, \\ r_2^k &= -\gamma_k - \mu_k, \end{aligned}$$

where $\mu_k = \sqrt{{\gamma_k}^2 - c^2\nu_k^2}$.

Note that

$$\begin{aligned} y_k(0) &= a_k + b_k, \\ y_k'(0) &= r_1^k a_k + r_2^k b_k. \end{aligned}$$

Using the initial values $u_0(x)$ and $u_d(x)$, as explained in Eq. (5.2.9), it follows that

$$a_k + b_k = 2\int_0^1 u_0(x)w_k(x)\,dx, \tag{6.2.7}$$

$$r_1^k a_k + r_2^k b_k = 2\int_0^1 u_d(x)w_k(x)\,dx. \tag{6.2.8}$$

In the underdamped case (${\gamma_k}^2 < c^2\nu_k^2$), we have

$$y_k(t) = e^{-\gamma_k t}\left(c_k \cos\omega_k^d t + d_k \sin\omega_k^d t\right), \tag{6.2.9}$$

where $\omega_k^d = \sqrt{c^2\nu_k^2 - {\gamma_k}^2}$.

Note that

$$\begin{aligned} y_k(0) &= c_k, \\ y_k'(0) &= -\gamma_k c_k + \omega_k^d d_k. \end{aligned}$$

Again using the initial values $u_0(x)$ and $u_d(x)$ yields

$$c_k = 2\int_0^1 u_0(x)w_k(x)\,dx \tag{6.2.10}$$

$$-\gamma_k c_k + \omega_k^d d_k = 2\int_0^1 u_d(x)w_k(x)\,dx. \tag{6.2.11}$$

The case of critical damping ($\lambda_k^2 = c^2\nu_k^2$), is ignored, as it has little significance for practical applications.

The series solution is given by

$$u(x,t) = \sum_{k=1}^{\infty} y_k(t)w_k(x). \tag{6.2.12}$$

6.2.4 The C-V model

For each k we require the solution $y_k(t)$ for the ordinary differential equation

$$y_k''(t) + 2\gamma\, y_k'(t) + \frac{\alpha\lambda_k}{\tau_q}\, y_k(t) = 0. \tag{6.2.13}$$

The solutions of the characteristic equation of Eq. (6.2.13) are given by

$$-\gamma \pm \sqrt{\gamma^2 - c^2\nu_k^2}.$$

In the overdamped case ($\gamma^2 > c^2\nu_k^2$), we have

$$y_k(t) = a_k e^{r_1^k t} + b_k e^{r_2^k t}, \tag{6.2.14}$$

with r_1^k and r_2^k given by

$$\begin{aligned} r_1^k &= -\gamma + \mu_k, \\ r_2^k &= -\gamma - \mu_k, \end{aligned}$$

and where $\mu_k = \sqrt{\gamma^2 - c^2\nu_k^2}$.

In the underdamped case ($\gamma^2 < c^2\nu_k^2$), we have

$$y_k(t) = e^{-\gamma t}\left(c_k \cos\omega_k^d t + d_k \sin\omega_k^d t\right), \tag{6.2.15}$$

where $\omega_k^d = \sqrt{c^2\nu_k^2 - \gamma^2}$.

The procedure for calculating the coefficients a_k, b_k, c_k and d_k is exactly the same as for the DPL model. The only difference is that γ_k is replaced by γ. The series solution has the same form as for the DPL model.

6.2.5 The Fourier model

For each k we require the solution $y_k(t)$ for the ordinary differential equation

$$y_k'(t) + \alpha\lambda_k\, y_k(t) = 0. \tag{6.2.16}$$

The solution for Eq. (6.2.16) is given by

$$y_k(t) = a_k e^{-r_k t}; \quad r_k = \alpha\nu_k^2. \tag{6.2.17}$$

The series solution is given by

$$u(x,t) = \sum_{k=1}^{\infty} a_k e^{-r_k t} w_k(x). \tag{6.2.18}$$

Using the initial value $u_0(x)$ yields

$$a_k = \|w_k\|_\Omega^{-2}(u_0, w_k)_\Omega = 2\int_0^1 u_0(x) w_k(x)\, dx. \tag{6.2.19}$$

6.2.6 Initial values for numerical experiments

The initial value $u_d(x) = 0$ is used for simplifying the calculations. This condition is also required to compare the results of the C-V and DPL models with the Fourier model.

Choosing a suitable initial value $u_0(x)$ is more complicated.

Recall that

$$\theta_\delta(x) = \begin{cases} -6(\frac{x}{\delta})^5 + 15(\frac{x}{\delta})^4 - 10(\frac{x}{\delta})^3, & \text{for} \quad 0 \leq x < \delta, \\ -1, & \text{for} \quad \delta \leq x \leq 1. \end{cases}$$

For the model problem, the initial value $u_0(x) = -\theta_\delta(x)$ is specified when investigating whether the problem is well-posed. It is shown that this initial value is an admissible smooth function. Note that for this initial value $u(x,0) = 1$ for $\delta \leq x \leq 1$ and that $\delta \ll 1$.

For numerical experiments it is not practical to calculate the Fourier coefficients for this initial condition. But the inadmissible initial condition $u_0(x) = 1$ can be approximated arbitrarily closely by $-\theta_\delta$ by choosing δ sufficiently small.

However, note that for the one-dimensional DPL and C-V models, the inertia space is $W = \mathcal{L}^2(0,1)$, and the energy space $V \subset \mathcal{H}^1(0,1)$. The initial value $u_0(x) = 1$ is not an appropriate initial value, as the boundary condition $u(0,t) = 0$ implies that $u_0(x)$ does not belong to the energy space $V \subset \mathcal{H}^1(0,1)$. Therefore the convergence in energy results cannot be used.

However, this discontinuous function can be approximated arbitrarily closely by a continuous piecewise linear function $u_\delta(x)$ that does belong to V.

$$u_\delta(x) = \begin{cases} x/\delta, & 0 \leq x < \delta \\ 1, & \delta \leq x \leq 1 \end{cases} \tag{6.2.20}$$

A function $u_\delta(x)$ close to $u_0(x) = 1$ can be used to determine an indication of the number of terms to use in the partial sums of the series solutions. See Section 6.5 for details.

The Fourier coefficients for these three options will not differ much, and the initial value $u_0(x) = 1$ is used in the simulations.

6.2.7 Fourier coefficients for numerical experiments

With $u_0(x) = 1$ and $u_d(x) = 0$, the Fourier coefficients are given by

$$(u_0, w_k)_\Omega = 2\int_0^1 \sin \nu_k x \, dx = \frac{2}{\nu_k} = \frac{4}{(2k-1)\pi} \tag{6.2.21}$$

and

$$(u_d, w_k)_\Omega = 0. \tag{6.2.22}$$

DPL model

Overdamped case

To determine the coefficients a_k and b_k, we use Eq. (6.2.7) and Eq. (6.2.8).

$$\begin{aligned} a_k + b_k &= \frac{2}{\nu_k}, \\ r_1^k a_k + r_2^k b_k &= 0. \end{aligned}$$

It follows that

$$a_k = \frac{-2r_k}{\nu_k(1-r_k)} \text{ and } b_k = \frac{2}{\nu_k(1-r_k)} \text{ with } r_k = \frac{r_2^k}{r_1^k}.$$

The overdamped case in terms of a_k is then

$$y_k(t) = a_k \left(e^{r_1^k t} - \frac{1}{r_k} e^{r_2^k t} \right). \tag{6.2.23}$$

Underdamped case

The coefficients c_k and d_k are determined using Eq. (6.2.10) and Eq. (6.2.11).

$$\begin{aligned} c_k &= \frac{2}{\nu_k}, \\ -\gamma_k c_k + \omega_k^d d_k &= 0. \end{aligned}$$

It follows that $d_k = \dfrac{c_k \gamma_k}{\omega_k^d}$.

The underdamped case in terms of c_k is then

$$y_k(t) = c_k e^{-\gamma_k t} \left(\cos \omega_k^d t + \frac{\gamma_k}{\omega_k^d} \sin \omega_k^d t \right). \tag{6.2.24}$$

C-V model

The procedure for calculating the coefficients a_k, b_k, c_k and d_k is exactly the same as for the DPL model. The only difference is that γ_k is replaced by γ.

For the underdamped case the expression simplifies to

$$y_k(t) = c_k e^{-\gamma t}\left(\cos\omega_k^d t + \frac{1}{2\tau_q\omega_k^d}\sin\omega_k^d t\right). \tag{6.2.25}$$

Fourier model

From Eq. (6.2.19) the Fourier coefficient a_k is used directly in the series solution:

$$a_k = 2\int_0^1 \sin\nu_k x\,dx = \frac{2}{\nu_k} = \frac{4}{(2k-1)\pi}. \tag{6.2.26}$$

6.3 Lag time τ_q for the C-V model

As mentioned in the beginning of this chapter, the lag time τ_q is not reliably known. Our aim is to determine a realistic value for τ_q.

It is known that, especially in the case of metals, the Fourier model yields physically realistic results after a sufficiently long time. The main assumption we use for estimating realistic values for τ_q is that the solutions of the C-V and Fourier models will be the same (within a user-specified error) after a sufficiently long time. The eigenfunctions and eigenvalues are the same for both models, regardless of the spatial dimension, and therefore it is sufficient to compare the time-dependent functions.

The differential equation Eq. (5.3.7) for the time dependent function $y(t)$ in the C-V model can be written in the form

$$\tau_q y'' + y' + \alpha\lambda y = 0. \tag{6.3.1}$$

This form simplifies comparison with the Fourier model in Eq. (5.3.8). Note that if the dimensionless constant $\tau_q \ll 1$, then Eq (6.3.1) will approach Eq. (5.3.8).

Requiring that the two models give the same result after a sufficiently long time t, means that the solutions of the models should be approximately equal when only the first modes are used.

For the Fourier model, from Eq. (6.2.17) for $k = 1$,

$$y_1^p(t) = e^{-r_p^1 t};\quad r_p^1 = \alpha\nu_1^2. \tag{6.3.2}$$

For the C-V model, from Eq. (6.2.14) for $k = 1$,

$$y_1(t) = a_1 e^{r_1^1 t} + b_1 e^{r_2^1 t}, \tag{6.3.3}$$

with

$$\begin{aligned} r_1^1 &= -\gamma + \gamma\sqrt{1 - c^2\nu_1^2/\gamma^2} \\ r_2^1 &= -\gamma - \gamma\sqrt{1 - c^2\nu_1^2/\gamma^2}. \end{aligned}$$

From the assumption that $\tau_q \ll 1$, it follows that $\frac{c^2\nu_1^2}{\gamma^2} = 2\alpha\nu_1^2\tau_q \ll 1$. Using the fact that $(1-x)^{\frac{1}{2}}$ can be approximated by $(1 - \frac{1}{2}x)$ if x is sufficiently small, we obtain

$$\left(1 - \frac{c^2\nu_1^2}{\gamma^2}\right)^{\frac{1}{2}} \approx \left(1 - \frac{c^2\nu_1^2}{2\gamma^2}\right). \tag{6.3.4}$$

This approximation yields that

$$\begin{aligned} r_1^1 &\approx -\frac{c^2\nu_1^2}{2\gamma} = -\alpha\nu_1^2 \\ r_2^1 &\approx -2\gamma + \frac{c^2\nu_1^2}{2\gamma} = -2\gamma + \alpha\nu_1^2. \end{aligned}$$

Consequently, $y_1(t)$ may now be approximated by

$$y_1(t) \approx a_1 e^{-\alpha\nu_1^2 t} + b_1 e^{-2\gamma t} e^{\alpha\nu_1^2 t}.$$

Since we chose $2\gamma \gg 1$, it follows that $e^{-2\gamma t} \approx 0$, and therefore

$$y_1(t) \approx a_1 e^{-\alpha\nu_1^2 t}. \tag{6.3.5}$$

To find the value for a_1, the initial values $y_1(0) = 1$ and $y_1'(0) = 0$ are prescribed, as $y_1^p(0) = 1$.

Recall that the objective is to determine a realistic ballpark value of τ_q. Assuming that $\tau_q \ll 1$, it follows that $\dfrac{c^2\nu_1^2}{\gamma^2} \ll 1$. We now have to decide exactly how small $\dfrac{c^2\nu_1^2}{\gamma^2}$ should be. We start with assuming an accuracy $\varepsilon \geq \dfrac{c^2\nu_1^2}{\gamma^2} = \dfrac{1}{1000}$. Then τ_q is calculated from

$$\tau_q \leq \frac{\varepsilon}{\pi^2\alpha} = \frac{1}{1000\pi^2\alpha}. \tag{6.3.6}$$

Using $\alpha = 0.0040732$ yields $\tau_q = 0.024875$, and the coefficients for $y_1^p(t)$ and $y_1(t)$ can then be calculated:

$r_1^1 = -0.010;\ r_2^1 = -40.191; a_1 = 1.000;\ b_1 = -2.502 \times 10^{-4};\ r_p^1 = 0.010;$

Note that $r_1 = r_2^1/r_1^1 \approx 4000$.

Substituting these results into Eq. (6.3.2) and Eq. (6.3.5) shows that

$$y_1(t) \approx y_1^p(t). \tag{6.3.7}$$

It is also instructive to determine a maximum value of τ_q for which Eq. (6.3.7) will hold. This implies that we want to determine the largest value of τ_q for which r_1^1 does not differ noticeably from r_p^1. We increase τ_q by adjusting the user-specified accuracy ε and recalculating τ_q each time using Eq. (6.3.6).

Table 6.1 presents the values for r_1^1, r_2^1, r_p^1 and a_1 calculated for a range of values for ε.

Table 6.1: Parameters for $y_p^1(t)$ and $y_1(t)$ for a range of ε values

ε	τ_q	r_1^1	r_2^1	r_1	$-r_p^1$	a_1
0.0008	0.020	-0.010	-50.242	4998	-0.010	1.000
0.001	0.025	-0.010	-40.191	3998	-0.010	1.000
0.004	0.100	-0.010	-10.040	998	-0.010	1.001
0.02	0.498	-0.010	-2.000	198	-0.010	1.005
0.04	0.995	-0.010	-0.995	97.990	-0.010	1.010
0.2	4.975	-0.011	-0.190	17.944	-0.010	1.059
0.5	12.437	-0.012	-0.069	5.828	-0.010	1.207

With the assumption that practical measurements can be done with an accuracy of, for example, 5%, we decide that a noticeable difference would then also be approximately 5%.

For $\tau_q \leq 1$, we find that $r_1^1 \approx -r_p^1$. However for $\tau_q \approx 5$ and $\tau_q \approx 12.5$ the differences are 10% and 20% respectively.

For numerical simulations the value $\tau_q = 0.024875$ will be used.

6.4 Wane time for C-V model

From the discussion in Section 3.2.1 we know that for the initial condition $u_0(x) = 1$, a sharp wave front propagates into the specimen. The wave

front is associated with the "jump" that exists along the line $x = t$ (refer to Section 3.2.1). This prominent wave front disappears after some time. We refer to this time as the wane time. We assume that the Fourier and C-V models will predict the same results at the time that this wave front disappears.

Our objective is to determine the time instant t_w at which the wave front disappears. As a means to determine this time instant, we consider the solution of Problem A2, derived in Section 3.3:

$$w(x,t) = e^{-\gamma t}u(x,t).$$

The function $w(x,t)$ describes the height of the almost vertical wave front (see Figure 3.2) whilst $e^{-\gamma t}$ describes the rate at which this wave front diminishes. It is then proposed that t_w is the time t at which $e^{-\gamma t}$ has reduced to, *e.g* 1/1000 (a user-specified difference) of its value at $t = 0$:

$$t_w = -2\tau_q \ln(0.001).$$

Using $\tau_q = 0.024875$, we find $t_w = 0.344$.

It is also interesting to predict how far into the specimen the wave front will travel. The dimensionless distance x is calculated from the dimensionless wave front speed c.

The calculated dimensionless wave front speed is $c = \sqrt{\alpha/\tau_q} = 0.405$ ([TZ98]), from which the dimensionless penetration distance into the specimen may be calculated as $x = ct_w = 0.139$. Since α and τ_q are specimen independent, the dimensionless penetration depth x is also specimen independent.

6.5 Initial values and convergence in energy

As explained earlier, in the numerical experiments we choose $u_0(x) = 1$ and $u_d(x) = 0$.

In Chapter 5, it is shown that for appropriately chosen initial values $u_0(x)$ and $u_d(x)$, convergence in energy for the series solution can be guaranteed for any $t > 0$. The error estimates for the initial values can be used to determine the number of terms to use in the series approximation of the solutions for the C-V and Fourier models for any time $t > 0$.

For the one-dimensional DPL and C-V models, the inertia space is $W = \mathcal{L}^2(0,1)$, and the energy space $V \subset \mathcal{H}^1(0,1)$. The initial value $u_0(x) = 1$ is

not an appropriate initial value, as the boundary condition $u(0,t) = 0$ implies that $u_0(x)$ is discontinuous at $x = 0$ and does not belong to the energy space $V \subset \mathcal{H}^1(0,1)$. Therefore the convergence in energy results cannot be used. However, this initial value can be approximated arbitrarily closely by the following continuous piecewise linear function $u_\delta(x)$ that does belong to V.

$$u_\delta(x) = \begin{cases} x/\delta, & 0 \le x < \delta \\ 1, & \delta \le x \le 1 \end{cases} \tag{6.5.1}$$

In the following numerical investigation accurate approximations for $u_\delta(x)$ using the eigenfunctions are determined both in the inertia norm and the energy norm. The objective of these calculations is to determine an estimate for the number of terms to use in the series solutions in order to obtain accurate approximations for the solutions of the Fourier, C-V and DPL models.

6.5.1 Inertia norm calculations

The inertia norm for $u_\delta(x)$ is given by

$$\|u_\delta\|_W^2 = \frac{1}{\delta^2}\int_0^\delta x^2\,dx + \int_\delta^1 dx = 1 - \frac{2\delta}{3} \tag{6.5.2}$$

The Fourier coefficients $c_k^{u_\delta}$ for $u_\delta(x)$:

$$\begin{aligned} c_k^{u_\delta} &= \|w_k\|_W^{-1}\,(u_\delta, w_k)_\Omega \\ &= \sqrt{2}\left(\frac{1}{\delta}\int_0^\delta x\sin\nu_k x\,dx + \int_\delta^1 \sin\nu_k x\,dx\right) \\ &= \sqrt{2}\left(\frac{-1}{\nu_k}\cos\nu_k\delta + \frac{1}{\delta\nu_k^2}\sin\nu_k\delta - \frac{1}{\nu_k}\cos\nu_k + \frac{1}{\nu_k}\cos\nu_k\delta\right) \\ &= \frac{\sqrt{2}}{\delta\nu_k^2}\sin\nu_k\delta \end{aligned} \tag{6.5.3}$$

Inertia norm error for n terms:

$$\mathcal{E}^{u_\delta} = \left|\|u_\delta\|_W^2 - \sum_{k=1}^n (c_k^{u_\delta})^2\right| = \left|\left(1 - \frac{2\delta}{3}\right) - \sum_{k=1}^n (c_k^{u_\delta})^2\right| \tag{6.5.4}$$

Relative inertia norm error for n terms:

$$\mathcal{E}_{rel}^{u_\delta} = \left|\frac{\|u_\delta\|_W^2 - \sum_{k=1}^n (c_k^{u_\delta})^2}{\|u_\delta\|_W^2}\right| = \left|\frac{\left(1 - \frac{2\delta}{3}\right) - \sum_{k=1}^n (c_k^{u_\delta})^2}{1 - \frac{2\delta}{3}}\right| \tag{6.5.5}$$

6.5.2 Energy norm calculations

$$u'_\delta(x) = \begin{cases} 1/\delta, & 0 < x < \delta \\ 0, & \delta < x < 1 \end{cases} \tag{6.5.6}$$

The energy norm for $u_\delta(x)$:

$$\|u_\delta\|_V^2 = \int_0^\delta (u'_\delta)^2\,dx + \int_\delta^1 (u'_\delta)^2\,dx = \frac{1}{\delta} \tag{6.5.7}$$

The energy norm for the eigenfunction $w_k(x)$:

$$\|w_k\|_V^2 = \int_0^1 \nu_k^2 \cos^2 \nu_k x\,dx = \frac{\nu_k^2}{2} \tag{6.5.8}$$

The Fourier coefficients $c_k^{u_\delta,V}$ for $u_\delta(x)$ using the energy norm:

$$\begin{aligned} c_k^{u_\delta,V} &= \|w_k\|_V^{-1} b^*(u_\delta, w_k) \\ &= \frac{\sqrt{2}}{\nu_k}\left(\int_0^\delta u'_\delta(x)w'_k(x)\,dx + \int_\delta^1 u'_\delta(x)w'_k(x)\,dx\right) \\ &= \frac{\sqrt{2}}{\nu_k}\left(\frac{1}{\delta}\int_0^\delta \nu_k \cos\nu_k x\,dx\right) \\ &= \frac{\sqrt{2}}{\delta\nu_k}\sin\nu_k\delta \end{aligned} \tag{6.5.9}$$

Energy norm error for n terms:

$$\mathcal{E}^{u_\delta,V} = \left|\frac{1}{\delta} - \sum_{k=1}^n (c_k^{u_\delta,V})^2\right| \tag{6.5.10}$$

Relative energy norm error for n terms:

$$\mathcal{E}_{rel}^{u_\delta,V} = \left|\frac{\|u_\delta\|_V^2 - \sum_{k=1}^n (c_k^{u_\delta,V})^2}{\|u_\delta\|_V^2}\right| = \left|1 - \delta\sum_{k=1}^n (c_k^{u_\delta,V})^2\right| \tag{6.5.11}$$

Remark

Note that these calculations agree with the Parseval expressions Eq. (5.2.16) and Eq. (5.2.17):

$$\left(c_k^{u_\delta,V}\right)^2 = \frac{2(\sin\nu_k\delta)^2}{\delta^2\nu_k^2} = \lambda_k\,(c_k^{u_\delta})^2\,.$$

6.5.3 Approximation errors for u_δ

In Table 6.2 the inertia and energy errors and relative errors are presented for two functions $u_\delta(x)$ with $\delta = 0.01$ and $\delta = 0.001$.

Clearly, a large number of terms are required to obtain an accurate approximation for $u_\delta(x)$, and this means that an equally large number of terms are required when using the partial sums of the series solutions to obtain accurate approximations for the solutions of the heat conduction models.

Table 6.2: Approximation errors for u_δ

δ	n	$\mathcal{E}^{u_\delta}$	$\mathcal{E}^{u_\delta}_{rel}$	$\mathcal{E}^{u_\delta,V}$	$\mathcal{E}^{u_\delta,V}_{rel}$
0.01	16	0.007	0.0071	68.88	0.6888
0.01	100	2.763×10^{-5}	2.782×10^{-5}	9.718	0.09718
0.01	500	2.705×10^{-7}	2.723×10^{-7}	2.022	0.02022
0.001	16	0.0120	0.0120	968.0	0.9680
0.001	100	0.0014	0.0014	802.2	0.8022
0.001	500	3.898×10^{-5}	3.900×10^{-5}	226.3	0.2263
0.001	5000	2.705×10^{-8}	2.707×10^{-8}	20.22	0.02022

6.5.4 Approximating the initial condition $u_0(x) = 1$

We start by approximating the initial condition $u_0(x) = 1$ to verify the computational code and to determine how many terms to use in the series solution approximations.

For the approximation of the initial condition $u_0(x) = 1$, the Fourier coefficients in Eq. (6.2.21) and the eigenfunctions in Eq. (6.2.3) are used:

$$u_0(x) \approx f_n = \sum_{k=1}^{n} \frac{2}{\nu_k} \sin \nu_k x \tag{6.5.12}$$

In Figure 6.1 the series approximations f_{16} for $n = 16$ and f_{1000} for $n = 1000$ are shown.

For the chosen values of α and τ_q, the first 16 modes of the C-V model are overdamped and the other modes are underdamped. We notice that if only overdamped modes (f_{16}) are used, the approximation oscillates excessively about $u_0(x) = 1$. If both overdamped and underdamped modes are included

(f_{1000}), a good approximation is obtained. The difference f_{diff} indicates the contribution from the underdamped modes. Clearly including underdamped modes is essential for obtaining a reasonable approximation for the chosen initial value u_0.

For the DPL model the range of overdamped and underdamped modes differs from the C-V model case, but the same observation remains true.

The oscillations near $x = 0$ are expected as we are using a discontinuous initial condition $u_0(x) = 1$. These oscillations are known as the Gibbs phenomenon, and are typical of a Fourier series near a point of discontinuity (in this case at $x = 0$).

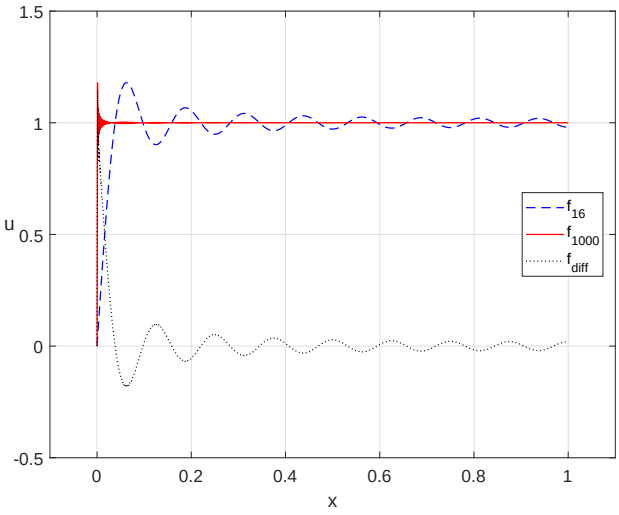

Figure 6.1: Series approximation for $u_0(x) = 1$.

6.6 Comparison of C-V and Fourier models

In this section the results of numerical simulation of the C-V model are presented. The numerical experiments are performed using $\tau_q = 0.024875$ and $\alpha = 0.004073$. Note that in these simulations the homogenised temperature distribution $u(x,t)$ is shown, and not the real temperature distribution $T(x,t) = 1 - u(x,t)$.

As mentioned before, in this case, the first 16 modes of the C-V model are overdamped, and the other modes are underdamped. This is an important

fact, as intuitively, the underdamped modes may lead to contradictions with the second law of thermodynamics.

We approximate the temperature distribution $u(x,t)$ for times $t > 0$ for the C-V model. The approximate solution u_{1000}^{CV} using $n = 1000$ terms is shown in each case, as well as the contribution from the overdamped modes u_{16}^{CV}. The decision to use $n = 1000$ terms is based on numerical experimentation and the calculations of approximation errors presented in Table 6.2.

Firstly, we present the results for $t = 0.075$ since the wave front had enough time to develop and to be clearly visible. The results predicted by the C-V model are compared with the Fourier model in Figure 6.2. Where the Fourier model predicts a smooth rise from 0 to 1, the C-V model predicts a distinct jump (wave front) in the temperature at $x \approx 0.03$. In Figure 6.3, the

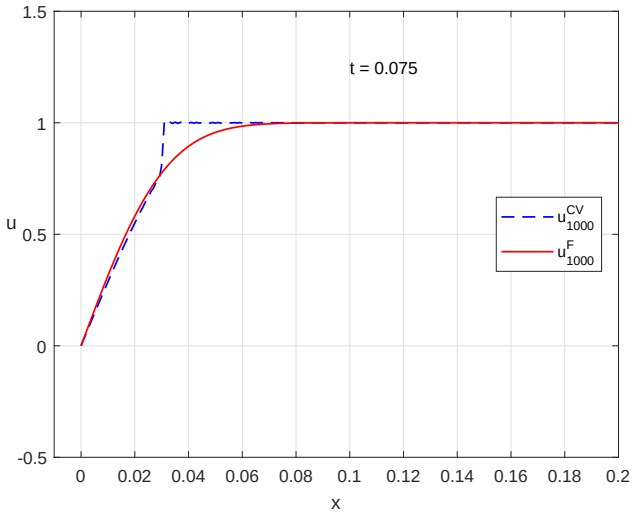

Figure 6.2: Spatial temperature distribution at $t = 0.075$; C-V and Fourier models.

contribution to u_{1000}^{CV} by the overdamped modes and underdamped modes are presented separately. The contribution from the underdamped modes u_{diff}^{CV} is calculated as the difference between u_{1000}^{CV} and u_{16}^{CV}. An important observation is that it is essential to include the underdamped modes of the C-V model in the calculation since these modes capture the wave front. The contribution u_{16}^{CV} from the overdamped modes shows no sign of the wave front. Increasing t has the effect that the wave front diminishes until it disappears at approximately $t = 0.35$ (see Figure 6.4). This corresponds well with the wane time $t_w = 0.344$ calculated in Section6.4, proving our

assumption that the Fourier and C-V models will predict the same results at $t = t_w$. Note that at $t = 0.35$ the contribution from the underdamped modes, u_{diff}^{CV}, is negligible. For smaller values of the time t, the number

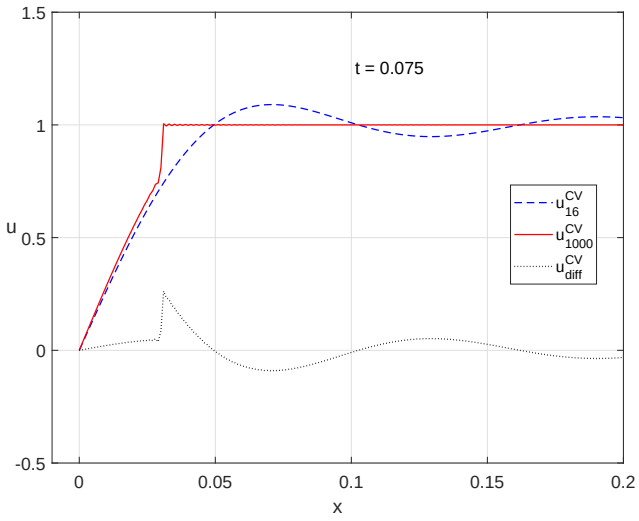

Figure 6.3: Spatial temperature distribution at $t = 0.075$; C-V model.

of terms n has to be increased to sufficiently reduce the effect of the Gibbs phenomenon. The oscillations are reduced in amplitude when more modes are used. For instance, for $t = 0.01$, we have to use $n = 2000$ in stead of $n = 1000$. The spatial progression of the wave front is studied by calculating $u(x,t)$ at various fixed x points, each time varying the time from $t = 0$ to $t = 0.35$. Figure 6.5 gives the result for $x = 0.02$. Note the jump in the u_{1000}^{CV} curve at $t \approx 0.05$. The arrow indicates the point on the curve that is considered to be the edge of the wave front. Table 6.3 gives the arrival time t_J of the wave front at point x, for x ranging between 0.005 and 0.050. A straight line fit through these data points produces a gradient of 0.404, which agrees well with the dimensionless wave front speed calculated in Section 6.4 as $c = \sqrt{\alpha/\tau_q} = 0.405$.

6.7 Lag times τ_q and τ_T for the DPL model

The lag times τ_q and τ_T for the DPL model are also not reliably known. In Section 6.3 realistic values for the lag time τ_q for the C-V model are calculated using the assumption that the solutions for the C-V and Fourier models will

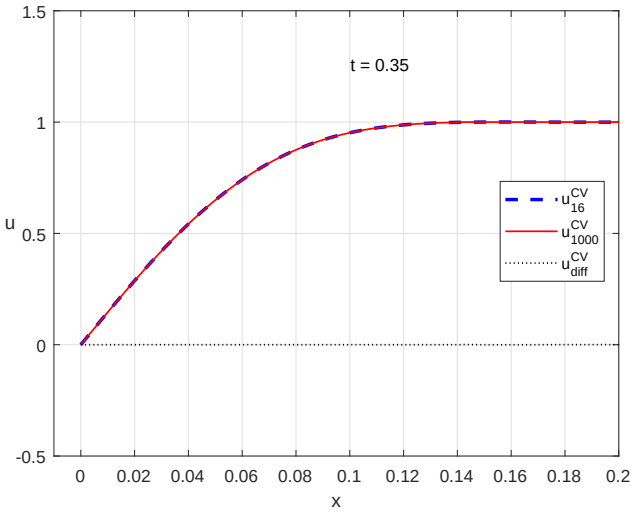

Figure 6.4: Spatial temperature distribution at $t = 0.35$; C-V model.

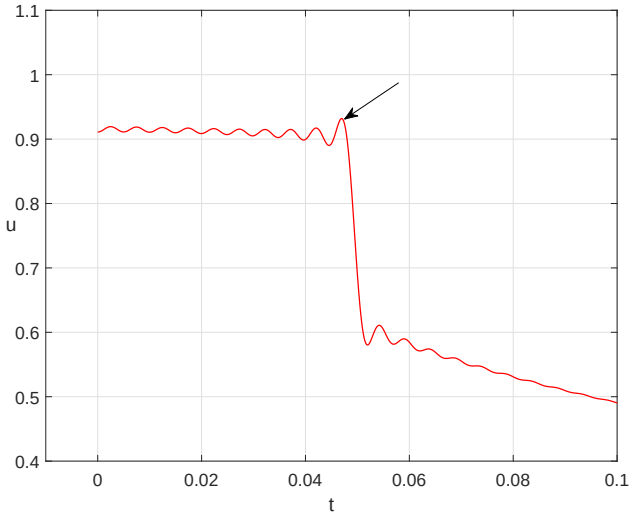

Figure 6.5: Temperature profile at $x = 0.02$; C-V model.

be the same (within a user-specified accuracy) after a sufficiently long time. The same assumption is used for the solutions of the DPL model.

The differential equation Eq. (5.3.6) for the time dependent function $y(t)$ in the DPL model can be written in the form

$$\tau_q y'' + (1 + \alpha\lambda\tau_T)y' + \alpha\lambda y = 0. \tag{6.7.1}$$

Table 6.3: Arrival time t_J of wave front at position x

x	t_J
0.005	0.0099
0.010	0.0223
0.020	0.0470
0.030	0.0718
0.050	0.1214

This form simplifies comparison with the Fourier model in Eq. (5.3.8) and the C-V model in Eq. (5.3.7). Note that if the dimensionless constant $\tau_T \ll 1$, then Eq (6.7.1) is close to Eq. (5.3.7). If both the constants $\tau_q \ll 1$ and $\tau_T \ll 1$, then Eq (6.7.1) is close to Eq. (5.3.8).

As for the C-V model, the assumption that the Fourier and DPL models give the same result after a sufficiently long time, means that the solutions of the two models should be approximately the equal when only the first modes are used.

For the Fourier model, from Eq. (6.2.17) for $k = 1$,

$$y_1^p(t) = e^{-r_p^1 t}; \quad r_p^1 = \alpha\nu_1^2. \tag{6.7.2}$$

For the DPL model, from Eq. (6.2.6) for $k = 1$,

$$y_1(t) = a_1 e^{r_1^1 t} + b_1 e^{r_2^1 t}, \tag{6.7.3}$$

with

$$\begin{aligned} r_1^1 &= -\gamma_1 + \gamma_1\sqrt{1 - c^2\nu_1^2/\gamma_1^2} \\ r_2^1 &= -\gamma_1 - \gamma_1\sqrt{1 - c^2\nu_1^2/\gamma_1^2}. \end{aligned}$$

At this point, we assume that $\frac{c^2\nu_1^2}{\gamma_1^2} \ll 1$. Using the fact that $(1-x)^{\frac{1}{2}}$ can be approximated by $(1 - \frac{1}{2}x)$ if x is sufficiently small, we obtain

$$\left(1 - \frac{c^2\nu_1^2}{\gamma_1^2}\right)^{\frac{1}{2}} \approx \left(1 - \frac{c^2\nu_1^2}{2\gamma_1^2}\right). \tag{6.7.4}$$

Using this approximation yields that

$$\begin{aligned} r_1^1 &\approx -\frac{c^2\nu_1^2}{2\gamma_1} \\ &= -\frac{\alpha\nu_1^2}{1+\alpha\nu_1^2\tau_T} \\ &= -\alpha\nu_1^2(1+\alpha\nu_1^2\tau_T)^{-1}. \end{aligned}$$

At this stage an additional condition is required: $\alpha\nu_1^2\tau_T \ll 1$. Using the fact that $(1+x)^{-1}$ can be approximated by $(1-x)$ if x is sufficiently small, we obtain

$$r_1^1 \approx -\alpha\nu_1^2.$$

Similarly,

$$r_2^1 \approx -2\gamma_1 + \frac{c^2\nu_1^2}{2\gamma_1} \approx -2\gamma_1 + \alpha\nu_1^2.$$

Consequently, $y_1(t)$ may now be approximated by

$$y_1(t) \approx a_1 e^{-\alpha\nu_1^2 t} + b_1 e^{-2\gamma_1 t} e^{\alpha\nu_1^2 t}.$$

Since we chose $2\gamma_1 \gg 1$, it follows that $e^{-2\gamma_1 t} \approx 0$, and therefore

$$y_1(t) \approx a_1 e^{-\alpha\nu_1^2 t}. \tag{6.7.5}$$

To find the value for a_1, the initial values $y_1(0) = 1$ and $y_1'(0) = 0$ are prescribed, as $y_1^p(0) = 1$.

Recall that the objective is to determine realistic values for τ_q and τ_T for the DPL model. The two conditions that ensure that the solutions of the DPL and Fourier models are the same after a sufficiently long time, are $c^2\nu_1^2/\gamma_1^2 \ll 1$ and $\alpha\nu_1^2\tau_T \ll 1$. We now have to decide exactly how small these quantities should be. We start with assuming an accuracy ε for both the quantities. Then an upper bound for τ_T is calculated from $\alpha\nu_1^2\tau_T \leq \varepsilon$, as

$$\tau_T \leq \frac{\varepsilon}{\alpha\nu_1^2} = \frac{4\varepsilon}{\alpha\pi^2}. \tag{6.7.6}$$

From $c^2\nu_1^2/\gamma_1^2 \leq \varepsilon$, follows

$$\frac{\alpha\nu_1^2}{\tau_q\gamma_1^2} = \frac{4\alpha\nu_1^2\tau_q}{(1+\alpha\nu_1^2\tau_T)} \leq \varepsilon,$$

and therefore

$$\tau_q \leq \frac{\varepsilon}{\alpha\pi^2}\left(1+\frac{\alpha\pi^2\tau_T}{4}\right)^2. \tag{6.7.7}$$

This means that the upper bound $\tau_q \leq \varepsilon/(\alpha\pi^2)$, used for the C-V model may be used for the DPL model as well, in order to compare the solutions of the models. This means that the same value for τ_q may be used for both the C-V and DPL models. The value for τ_T has to be chosen to satisfy Eq. (6.7.6).

6.8 Comparison of DPL, C-V and Fourier models

The aim is now to compare the results from the DPL model with both the C-V and Fourier models. We use the values for α and τ_q as calculated in Section 6.3: $\alpha = 0.004073$ and $\tau_q = 0.024875$ (with $\varepsilon = 0.001$).

In the C-V model, a constant damping constant 2γ is present in the differential equation for $y(t)$, but in the case of the DPL model (refer to Section 5.3.2), the damping constant increases with the mode number k according to:

$$2\gamma_k = 2\gamma + \frac{\tau_T\alpha}{\tau_q}\nu_k^2$$

where $2\gamma = 1/\tau_q$. We can simplify the above equation, using $c^2 = \alpha/\tau_q$, to obtain an expression for γ_k:

$$\gamma_k = \gamma + \frac{\tau_T c^2 \nu_k^2}{2}$$

The values of γ and c^2 are already fixed by τ_q and the choice of α. We now proceed to calculate a suitable value for τ_T. We consider two cases for the DPL model: firstly where both over- and underdamped modes are allowed and secondly, where only overdamped modes are allowed. Appropriate assumptions are required to find suitable values for τ_T for these two cases.

6.8.1 DPL-I model

Both overdamped and underdamped modes are allowed in this case. We refer to this case as "DPL-I".

For the problem investigated in Section 6.6, we have that the modes of the C-V model are overdamped up to $k = 16$ ($\gamma > c\nu_k$ for $k = 1, 2, \ldots, 16$).

Therefore, for the modes of the DPL model

$$\gamma_k = \gamma + \frac{\tau_T c^2 \nu_k^2}{2} > c\nu_k, \text{ for } k = 1, 2, \ldots, 16 \tag{6.8.1}$$

This means that the value of γ ensures that the modes of the DPL model are overdamped, at least up to $k = 16$.

We use the assumption that mode 17 of the DPL model is also overdamped to find a suitable value for τ_T. Assuming

$$\gamma_{17} > c\nu_{17}$$

provides the condition

$$\tau_T > \frac{2(c\nu_{17} - \gamma)}{c^2 \nu_{17}^2}, \tag{6.8.2}$$

With $\tau_q = 0.024875$ and $\alpha = 0.004073$, we determine that $\tau_T = 0.0041782$ is the smallest value that will ensure that the first 17 modes of the DPL model are overdamped.

Whether the higher modes of the DPL model are over- or underdamped is determined by the damping criterion $c^2\nu_k^2/\gamma_k^2$. From Figure 6.6 it can be seen that the modes from $k = 18$ to $k = 360$ are underdamped (*i.e.* where $c^2\nu_k^2/\gamma_k^2 > 1$), whilst the remaining modes, $k < 18$ and $k > 360$, are overdamped. Figure 6.7 shows the temperature distribution for the DPL-I model, calculated for $t = 0.075$. It is interesting to compare these results with those obtained for the Fourier model and the C-V model. Combining results from Figure 6.2 and 6.7 into one graph, Figure 6.8, we observe that the DPL-I model predicts a temperature distribution that has a shape very similar to that of the Fourier model. The DPL-I model does however predict that the maximum temperature is reached closer to the $x = 0$ boundary than is the case for the Fourier model. This means that, compared to the Fourier model, the DPL-I model predicts a slower spatial progression of the heat wave into the medium. Recall that the true temperature is given by $T(x,t) = 1 - u(x,t)$. If we compare Eq. (2.2.6) and (2.2.7), representing the C-V and DPL models respectively, note that if $\tau_T \approx 0$, the DPL-I model prediction will approach that of the C-V model. This observation is supported by the discussion in Section 5.3.2). In Figure 6.9 the solutions for the DPL-I model with $\tau_T = 0.0001$ and the C-V model are compared at $t = 0.075$. With this choice of τ_T, the underdamped modes range from $k = 17$ to $k = 15\,716$.

For the DPL-I model the damping constant γ_k for the underdamped modes increases with mode number, in contrast to the C-V model where the damping constant is γ. Even a small lag time τ_T generates a significant reduction

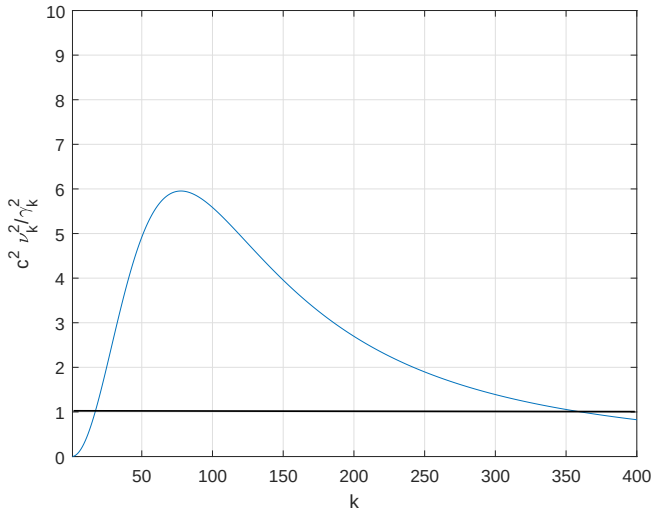

Figure 6.6: Quantity $\frac{c^2\nu_k^2}{\gamma_k^2}$ versus mode number k; DPL-I

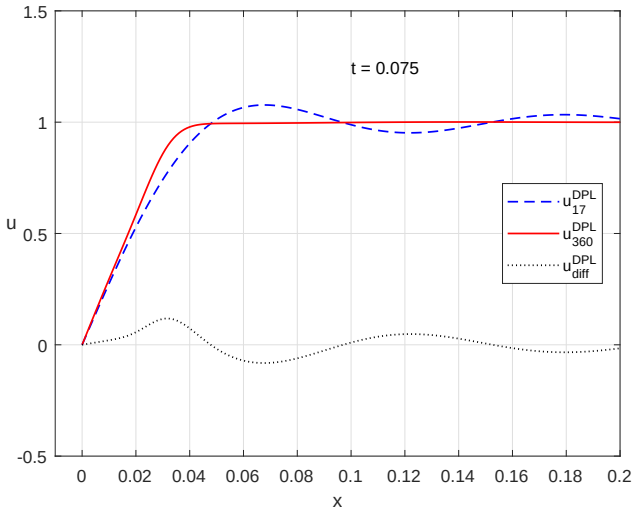

Figure 6.7: Spatial temperature distribution at $t = 0.075$; DPL-I model.

in the Gibbs oscillations (as seen in Figure 6.9) due to the increased damping of the higher modes. In Section 6.4 we make the assumption that the Fourier and C-V models will predict the same results at $t = t_w$ (where t_w is the wane time). We test this assumption by calculating the results at $t = t_w = 0.35$, including the DPL-I model in the comparison (Figure 6.10). We see that the difference between the respective model predictions is negligible, indicating

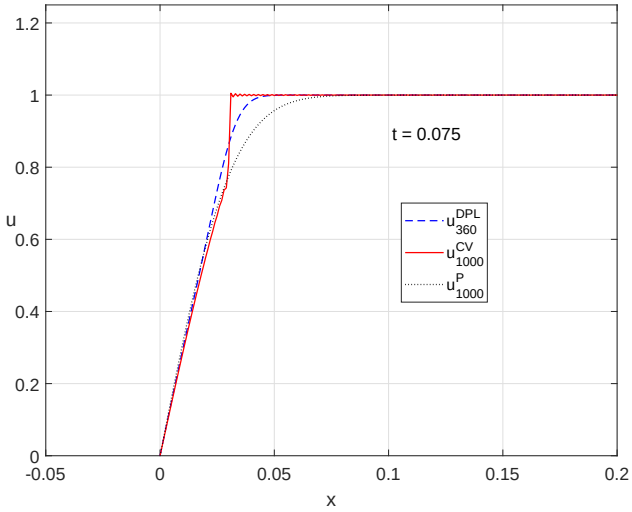

Figure 6.8: Spatial temperature distribution at $t = 0.075$; Fourier, C-V and DPL-I models.

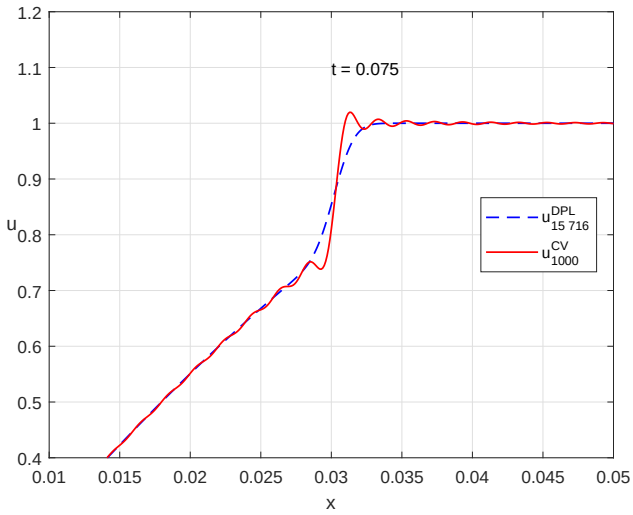

Figure 6.9: Spatial temperature distribution at $t = 0.075$; C-V and DPL-I models, with $\tau_T = 0.0001$.

that the wane time t_w can be used to estimate the time instant at which the DPL-I model will correspond to the Fourier model prediction.

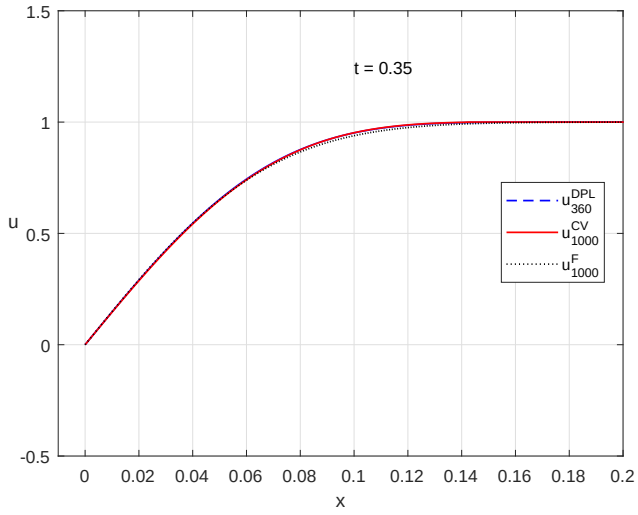

Figure 6.10: Temperature profiles at $t = t_w = 0.35$.

6.8.2 DPL-II model

Only overdamped modes are allowed in this case. We rewrite Eq. (6.8.1) in quadratic form:

$$\frac{\tau_T c^2}{2}\nu_k^2 - c\nu_k + \gamma > 0. \tag{6.8.3}$$

As before, since the values of c^2 and γ are fixed by the choice of τ_q and α, it is left to determine τ_T such that the inequality (6.8.3) is satisfied. From the discriminant of this inequality it follows that

$$\tau_T > \frac{1}{2\gamma}. \tag{6.8.4}$$

In order for all the modes of the DPL model to be overdamped, it is required that

$$\tau_T \geq \tau_q.$$

Figure 6.11 shows that with $\tau_T \geq \tau_q$, only overdamped modes are present for all k. Choosing $\tau_T = \tau_q$, only overdamped modes are used to calculate the partial sum for the DPL model. We chose $n = 1000$. Once again there are oscillations present in the vicinity of the $x = 0$ boundary. The amplitude of the oscillations are smaller than those found in the DPL-I results. We present the results for the Fourier, the C-V and the DPL-II models at $t = 0.075$ in Figure 6.12. Comparing Figure 6.12 with Figure 6.8, we see that the

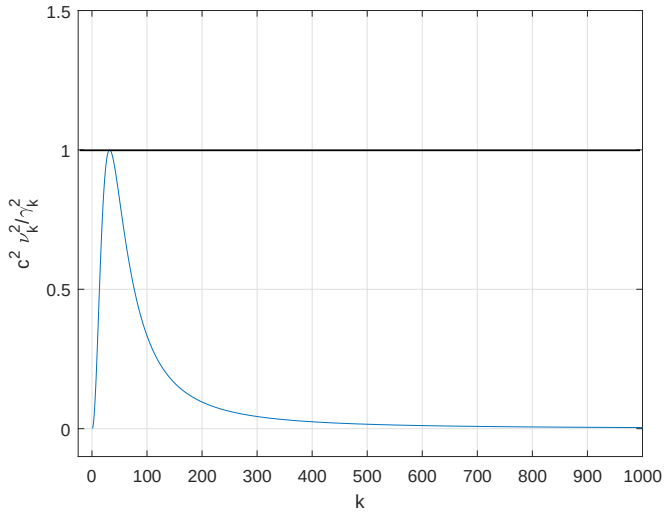

Figure 6.11: Quantity $\dfrac{c^2\nu_k^2}{\gamma_k^2}$ versus mode number k; DPL-II model.

DPL-II model predicts the maximum temperature at the same position in the specimen as does the Fourier model.

We are interested in comparing the DPL-II model with the Fourier and C-V models at $t = t_w$. The result is given by Figure 6.13. As is the case with the DPL-I model (Figure 6.10), there is no observable difference between the respective model predictions, and the wane time t_w can be used to estimate the time instant at which the DPL-II model will correspond to the Fourier model prediction.

In summary, if $0 < \tau_{_T} < \tau_q$, we have the DPL-I case, and if $0 < \tau_q < \tau_{_T}$, we have the DPL-II case. It is convenient to define $\delta \equiv \tau_{_T}/\tau_q$ – then $0 < \delta < 1$ indicates the DPL-I model and $\delta \geq 1$ indicates the DPL-II model. Recalling our discussion in Section 2.5.2, $0 < \delta < 1$ implies that the temperature gradient precedes the heat flux vector, and $\delta \geq 1$ that the temperature gradient follows after the heat flux vector.

6.9 Single-pulse problem

We use a numerical case study, involving a single heat pulse applied to a boundary of a one-dimensional specimen, to compare the DPL and C-V models with the Fourier model. The assumption is that the results, as predicted

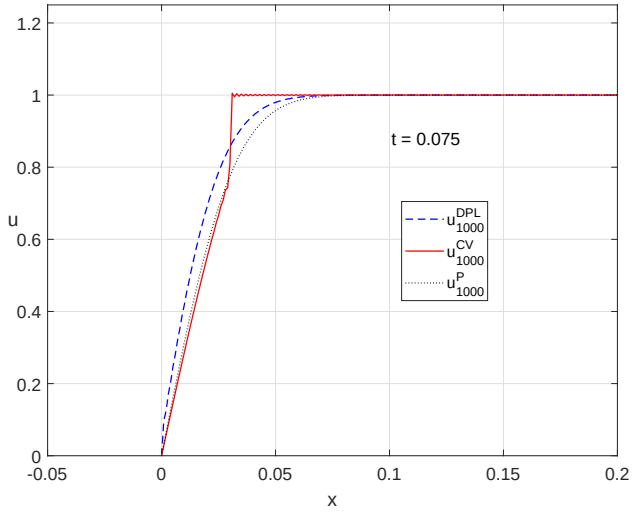

Figure 6.12: Spatial temperature distribution at $t = 0.075$; Fourier, C-V and DPL-II models.

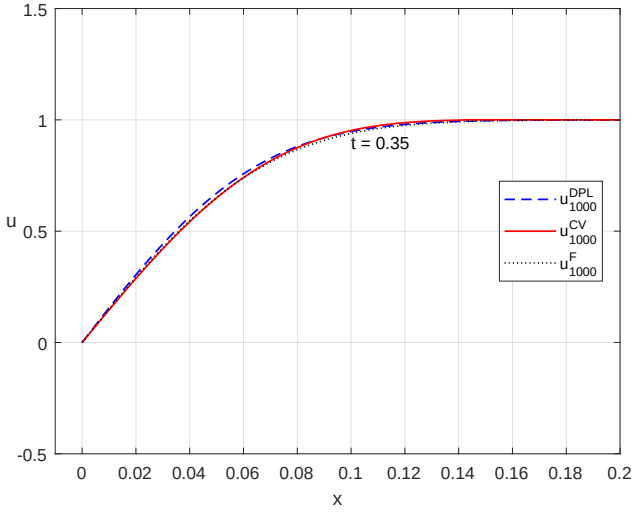

Figure 6.13: Temperature profiles at $t = t_w = 0.35$.

by the C-V and DPL models, will approach that of the Fourier model after some time t has elapsed. The main aim is therefore to test this assumption and not to develop a full, realistic mathematical model of an actual physical process, *e.g.* the heating of a thin metal film with a laser pulse.

We now formulate a mathematical model for the physical problem where a

single heat pulse is applied to the boundary of a specimen. Another assumption is made here: all the heat is absorbed at the boundary at $x = 0$.

6.9.1 Single-pulse problem for C-V model

The mathematical model is given by

$$\begin{aligned} \partial_t^2 T + 2\gamma\,\partial_t T &= c^2\,\partial_x^2 T \\ T(0,t) &= \begin{cases} 1, & 0 \le t < t_p \\ 0, & t \ge t_p \end{cases} \\ \partial_x T(1,t) &= 0 \\ T(x,0) &= 0 \\ \partial_t T(x,0) &= 0. \end{aligned} \tag{6.9.1}$$

where $2\gamma = 1/\tau_q$, $c^2 = \alpha/\tau_q$ and t_p is the time instant at which the pulse is stopped. The boundary condition $T(0,t) = 1$ for $t < t_p$ corresponds to when the heat pulse is applied to the boundary, and $T(0,t) = 0$ for $t \ge t_p$ corresponds to when the heat pulse is stopped. The boundary condition $T(0,t) = 0$ may be regarded as not being realistic since it implies that the temperature of the specimen immediately returns to its original temperature when the heat source is removed, but it can be justified based on the original assumption that the heat is only absorbed at $x = 0$. Refer to the discussion in Section 2.6.

The strategy used here is to divide this problem into two problems corresponding to the different boundary conditions at $x = 0$.

Problem 1: $T(0,t) = 1 \quad (0 \le t < t_p)$

As before, an equivalent problem with homogeneous boundary conditions is required. Let $u(x,t) = 1 - T(x,t)$. Then

$$\begin{aligned} \partial_t^2 u + 2\gamma\,\partial_t u &= c^2\,\partial_x^2 u \\ u(0,t) &= 0 \\ \partial_x u(1,t) &= 0 \\ u(x,0) &= 1 \\ \partial_t u(x,0) &= 0 \end{aligned} \tag{6.9.2}$$

The results derived in Section 6.2.7 may then be applied to solve for u and consequently for T. Setting $u_k(x,t) = y_k(t)w_k(x)$ and applying separation

of variables result in

$$u(x,t) = \sum_{k=1}^{\infty} b_k y_k(t) w_k(x), \tag{6.9.3}$$

with

$$u(x,0) = \sum_{k=1}^{\infty} b_k w_k(x).$$

$T(x,t) = 1 - u(x,t)$ is the general solution for Eq. (6.9.1) when $0 \leq t < t_p$.

Problem 2: $T(0,t) = 0 \quad (t \geq t_p)$

We denote the general solution to Problem 2 by $\tilde{T}(x,t)$. The values for $T(x,t_p)$ and $\partial_t T(x,t_p)$ now become the initial conditions for Problem 2. We write this as

$$\tilde{T}(x,t_p) = 1 - u(x,t_p)$$

and

$$\partial_t \tilde{T}(x,t_p) = -\partial_t u(x,t_p).$$

Problem 2 is now formulated as

$$\begin{aligned} \partial_t^2 \tilde{T} + 2\gamma\, \partial_t \tilde{T} &= c^2\, \partial_x^2 \tilde{T} \\ \tilde{T}(0,t) = \partial_x \tilde{T}(1,t) &= 0 \\ \tilde{T}(x,t_p) &= T(x,t_p) = 1 - u(x,t_p) \\ \partial_t \tilde{T}(x,t_p) &= \partial_t T(x,t_p) = -\partial_t u(x,t_p), \end{aligned} \tag{6.9.4}$$

Our strategy to solve $\tilde{T}(x,t)$ relies on continuing to use $u(x,t)$ (for $t \geq t_p$). We define $Q(x,t) = \tilde{T}(x,t) + u(x,t)$. Then $\tilde{T}(x,t) = Q(x,t) - u(x,t)$ will satisfy the partial differential equation (6.9.4).

$Q(x,t)$ is then the solution of

$$\begin{aligned} \partial_t^2 Q + 2\gamma\, \partial_t Q &= c^2\, \partial_x^2 Q \\ Q(0,t) = \partial_x Q(1,t) &= 0 \\ Q(x,t_p) &= 1 \\ \partial_t Q(x,t_p) &= 0, \end{aligned} \tag{6.9.5}$$

For $t \geq t_p$ then, $Q(x,t) = u(x,t-t_p)$ and it follows that

$$\tilde{T}(x,t) = u(x,t-t_p) - u(x,t). \tag{6.9.6}$$

6.9.2 Single-pulse problem for DPL model

The general solution for the DPL model has the same form as for the C-V model:

$$\tilde{T}(x,t) = u(x,t-t_p) - u(x,t). \tag{6.9.7}$$

The results of Sections 6.2.2 and 6.2.7 are applied to solve for $u(x,t)$.

6.9.3 Single-pulse problem for Fourier model

The single-pulse problem is described by the following mathematical model

$$\begin{aligned} \partial_t T &= \alpha\, \partial_x^2 T \\ T(0,t) &= \begin{cases} 1, & 0 \le t < t_p \\ 0, & t \ge t_p \end{cases} \\ \partial_x T(1,t) &= 0 \\ T(x,0) &= 0 \end{aligned} \tag{6.9.8}$$

The solution strategy used for the C-V model, is applied here.

Problem 1: $T(0,t) = 1 \quad (0 \le t < t_p)$

Let $u(x,t) = 1 - T(x,t)$. Then

$$\begin{aligned} \partial_t u &= \alpha\, \partial_x^2 u \\ u(0,t) &= 0 \\ \partial_x u(1,t) &= 0 \\ u(x,0) &= 1 \end{aligned} \tag{6.9.9}$$

The results derived in Section 6.2.7 may then be applied to solve for $u(x,t)$ and consequently for $T(x,t)$.

Problem 2: $T(0,t) = 0 \quad (t \ge t_p)$

We denote the general solution to Problem 2 by $\tilde{T}(x,t)$. The value for $T(x,t_p)$ now becomes the initial conditions for Problem 2. The derivation of the solution is similar to Problem 2 for the C-V model.

Problem 2 is now formulated as

$$\begin{aligned} \partial_t \tilde{T} &= \alpha\, \partial_x^2 \tilde{T} \\ \tilde{T}(0,t) = \partial_x \tilde{T}(1,t) &= 0 \\ \tilde{T}(x,t_p) &= T(x,t_p) = 1 - u(x,t_p). \end{aligned} \tag{6.9.10}$$

Defining $Q(x,t) = \tilde{T}(x,t) + u(x,t)$, $Q(x,t)$ is then the solution of

$$\begin{aligned} \partial_t Q &= \alpha\, \partial_x^2 Q \\ Q(0,t) = \partial_x Q(1,t) &= 0 \\ Q(x,t_p) &= 1, \end{aligned} \tag{6.9.11}$$

and it follows that

$$\tilde{T}(x,t) = u(x,t-t_p) - u(x,t). \tag{6.9.12}$$

6.10 Single-pulse problem: numerical investigation

In this section, the solutions of the single-pulse problem for the Fourier, the C-V and the DPL models are compared. Our interest lies in how the different models predict the temporal and spatial behaviour of a heat pulse. Since the Fourier model assumes that heat transfer is instantaneous, *i.e.* there is no lagging effect, it is expected that the Fourier model will predict lower peak temperatures than those predicted by the C-V and DPL models. To test this theory, it is necessary to determine the comparative magnitudes of the predicted peak temperatures as well as the positions x where such peaks occur within the specimen at different times t.

All temperature profiles for $T(x,t)$ are calculated with dimensionless spatial increments $\Delta x = 0.0001$ and using $n = 3000$ terms. As before, the values for the models parameters are given by $\alpha = 0.0040732$, $\tau_q = 0.024875$, and $\tau_T = 0.0041782$ (DPL-I) and $\tau_T = 0.024875$ (DPL-II), unless otherwise indicated.

6.10.1 Temperature distributions at $t = t_p$

In order to observe how the temperature profile predictions of the C-V and DPL models differ from the temperature profiles predicted by the Fourier

model we need to decide on a suitable value for the dimensionless pulse length t_p. If t_p is too long, there will be no distinction between the results from the respective models. In Section 6.4, this time instant (referred to as the wane time t_w) is estimated as $t_w = 0.344$. In Section 6.6, we estimate the time when the results of the C-V model are approximately the same as those of the Fourier model to be $t \approx 0.35$. We did this by observing when the thermal wave front, characteristic of the C-V model, is no longer visible on the graph of the temperature distribution. See Figure 6.4 in Section 6.6. The pulse length t_p should be considerably shorter than 0.35. We found through numerical experimentation that $t_p = 0.075$ is a suitable value.

Before we start with the comparison, we first need to validate our numerical method. The solutions of Problem 1 for the models (Fourier, C-V, DPL-I and DPL-II) are presented and discussed in Sections 6.6 and 6.8. The solutions for the different models at $t = t_p = 0.075$ are shown in Figure 6.14. Recall that the solutions of Problem 1 are obtained by solving an equivalent problem with homogenous boundary conditions, and then setting $T(x,t) = 1 - u(x,t)$. See Figure 6.8 and 6.12 for the graphs of $u(x,t)$ at $t = 0.075$. These

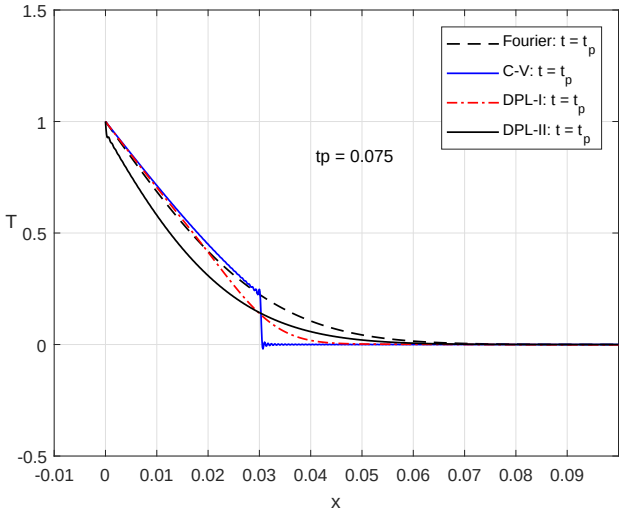

Figure 6.14: Spatial temperature distribution at $t_p = 0.075$; Fourier, C-V, DPL-I, DPL-II.

temperature profiles are used as initial values for Problem 2. Note that for all these profiles $T(0, t_p) = 1$. This means that there is again a discontinuity (resulting in the Gibbs phenomenon) at $x = 0$, as the boundary condition is given by $T(0,t) = 0$.

We start with the Fourier model. The temperature profiles for the Fourier

model are calculated using the solution for Problem 2 at time $t = t_p$ and the solution for Problem 2 at time $t = t_p + 0.0005$, that is 0.0005 time units after the pulse is switched off. See Figure 6.15.

As expected, oscillations are present near $x = 0$ for the case $t = t_p$ due to the discontinuity. These oscillations are due to the Gibbs phenomenon, since the oscillations diminish when more modes are used. Also, as expected for the parabolic partial differential equation, even after the short time interval up to $t_p + 0.0005$, the temperature profile has smoothed out. A similar

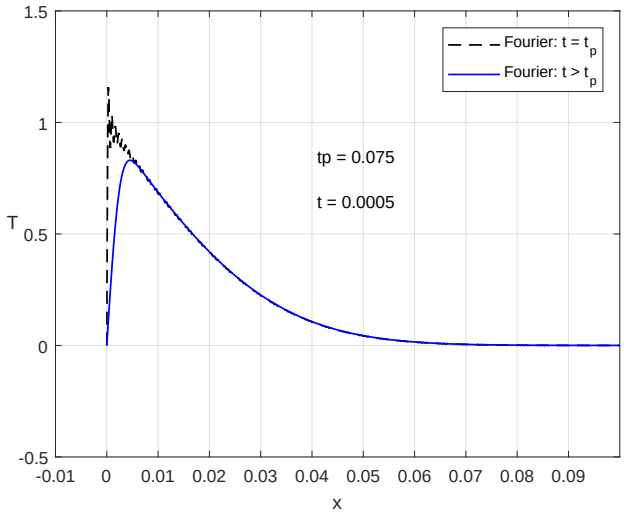

Figure 6.15: Spatial temperature distribution at $t = t_p$ and $t = t_p + 0.0005$; Fourier model.

calculation for the C-V model yields the temperature profiles at $t = t_p$ and $t = t_p + 0.0005$ as shown in Figure 6.16. There are hardly any difference between these profiles, and the profiles compare well with the solution for Problem 1 at $t = t_p$ as shown in Figure 6.14. The expected sharp wave front is clearly visible at approximately $x = 0.03$. A similar validation is done for both cases of the DPL model, and the results are displayed in Figure 6.17 and 6.18. For these models there are no visible difference between the temperature profiles at $t = t_p$ and $t = t_p + 0.0005$. As with the Fourier and C-V models, the Gibbs oscillations near $x = 0$ is a feature in these profiles.

This concludes the validation of our numerical method.

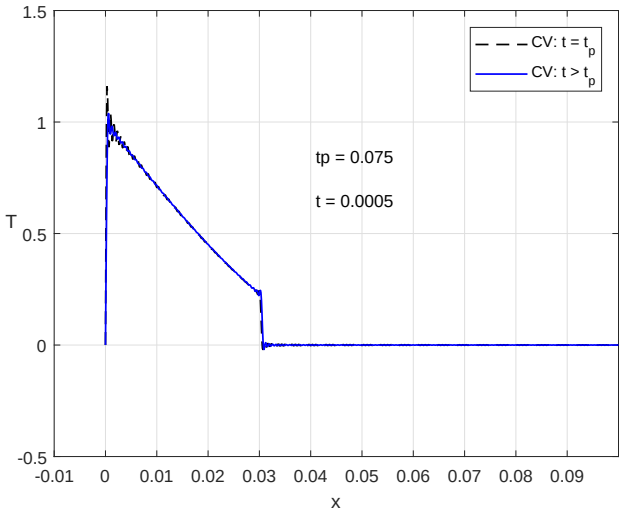

Figure 6.16: Spatial temperature distribution at $t = t_p$ and $t = t_p + 0.0005$; C-V model.

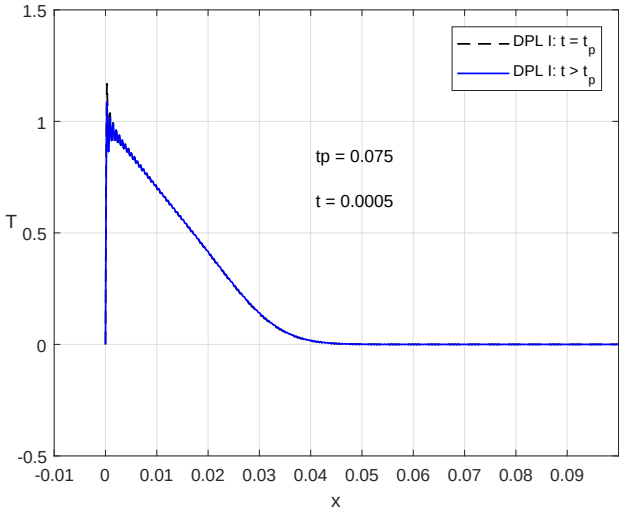

Figure 6.17: Spatial temperature distribution at $t = t_p$ and $t = t_p + 0.0005$; DPL-I model.

6.10.2 Comparing the C-V and Fourier models

We start with the C-V model. We choose a fixed pulse length $t_p = 0.075$ and examine the temperature profile at two time instances after the pulse has stopped: $t = t_p + 0.025$ and $t = t_p + 0.05$.

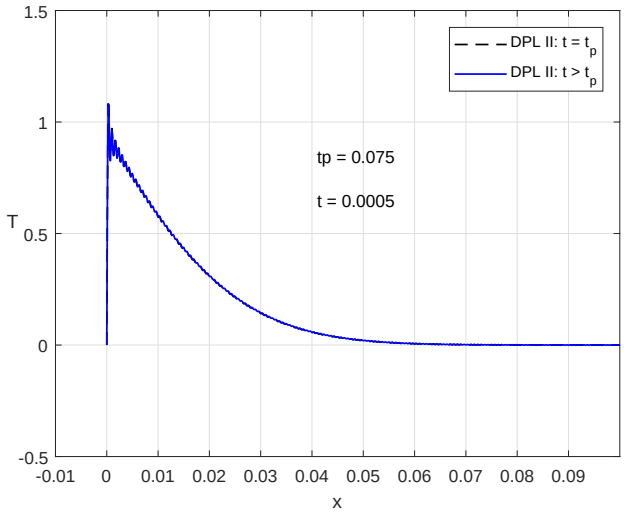

Figure 6.18: Spatial temperature distribution at $t = t_p$ and $t = t_p + 0.0005$; DPL-II model.

The C-V model predicts a sharp wave front close to the $x = 0$ boundary. The wave front is associated with the accumulation of heat energy in a localized area (or narrow strip) in the specimen due to the lagging behaviour. For $t = t_p + 0.025$, the wave front edge is at $x \approx 0.04$ (Figure 6.19), whilst for $t = t_p + 0.05$ it is at $x \approx 0.05$ (Figure 6.20). The peak temperature drops from about 0.8 to about 0.55 as t increases from 0.025 to 0.05. Note that the peak is significantly higher than the prediction of the Fourier model.

The C-V model under-predicts the temperature (compared to the Fourier model), in the region left of the wave front. To the right of the wave front, the specimen remains at its initial temperature. If we continue to increase t, the wave front moves further into the specimen, with its peak reduced, until it matches the temperature profile of the Fourier model, as was predicted earlier in Section 6.6. Another feature of the C-V model is the presence of oscillations at the two points of discontinuity *e.g.* when the pulse starts and stops. The oscillations are not visible at the right edge due to the scaling of the graph.

6.10.3 Comparing the DPL and Fourier models

In contrast to the C-V model, the DPL-I model predicts a smooth peak, progressing along the specimen. This peak is significantly higher and more

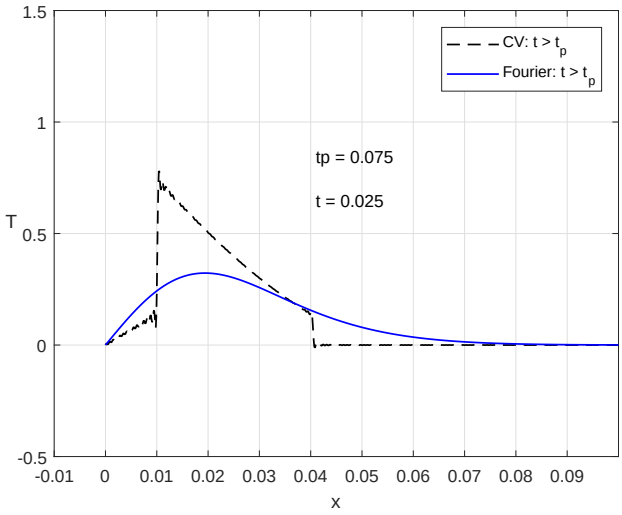

Figure 6.19: Spatial temperature distribution at $t = t_p + 0.025$; C-V vs Fourier model.

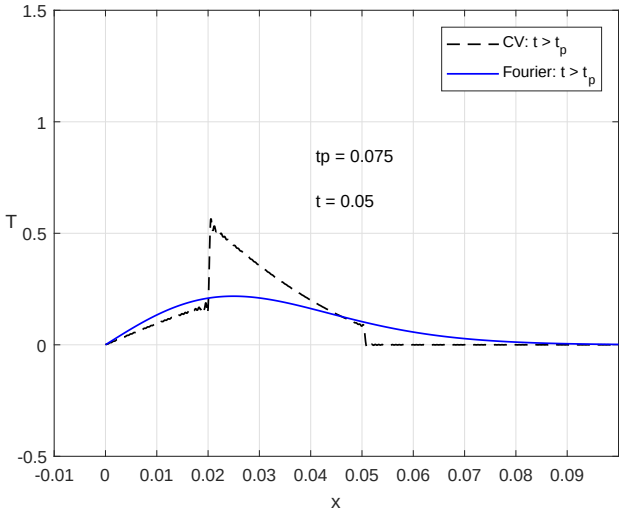

Figure 6.20: Spatial temperature distribution at $t = t_p + 0.05$; C-V vs Fourier model.

localised than the prediction of the Fourier model. For $t = t_p + 0.025$ (Figure 6.21), the temperature is over-predicted close to the $x = 0$ boundary and then under-predicted after a short distance, when compared to the Fourier model. For $t = t_p + 0.05$ (Figure 6.22), close to the $x = 0$ boundary (left of the peak), the DPL-I model corresponds very well with the Fourier model.

To the right of the peak, the DPL-I model under-predicts slightly when compared to the Fourier temperature profile. The peak temperatures for the two models appear at approximately the same positions.

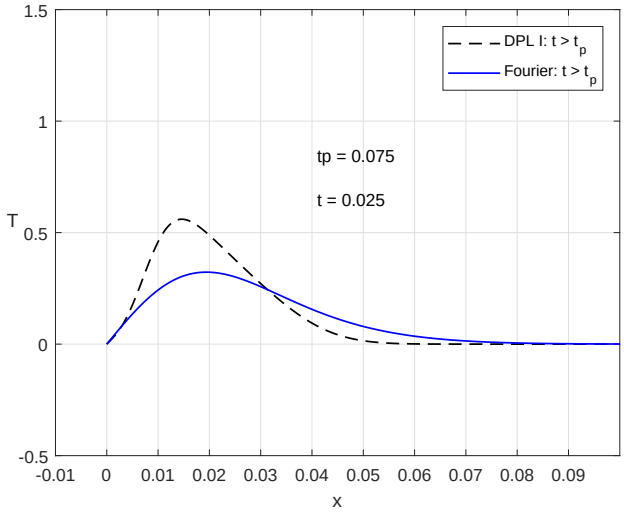

Figure 6.21: Spatial temperature distribution at $t = t_p + 0.025$; Fourier vs DPL-I model.

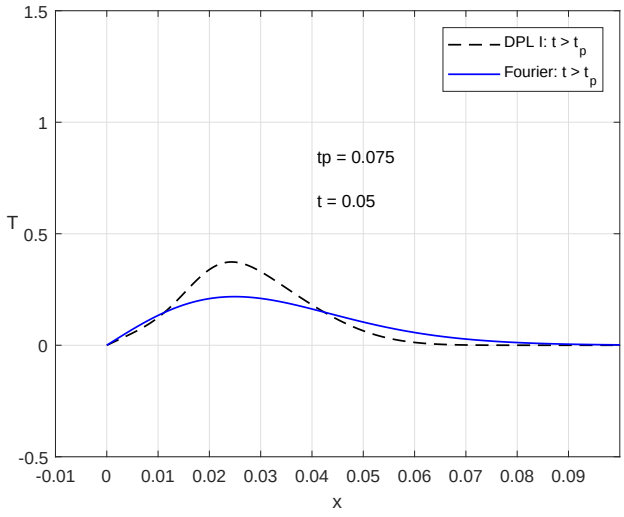

Figure 6.22: Spatial temperature distribution at $t = t_p + 0.05$; Fourier vs DPL-I model.

The DPL-II model is represented by Figures 6.23 and 6.24. In this case

the peak temperatures predicted by the DPL-II model is also higher than those predicted by the Fourier model, but the peak temperatures appear at positions much closer to the boundary at $x = 0$.

We notice another distinct feature: The Fourier, C-V and DPL-I models satisfy the boundary condition at $x = 0$ of Problem 2, but for the DPL-II model a significant jump still appears near $x = 0$. The discontinuity in the temperature at $x = 0$ has not been resolved at $t = t_p + 0.025$ or at $t = t_p + 0.05$, but the jump in temperature is reducing as the time increases.

When the value for τ_T is increased, the dissipative nature of the heat conducting process is enhanced, and the ability of the thermal wave to conduct heat energy into the specimen is reduced. Therefore, for the DPL-II model the discontinuity in the temperature at $x = 0$ when the heat pulse is stopped, requires considerable time before the discontinuity is resolved.

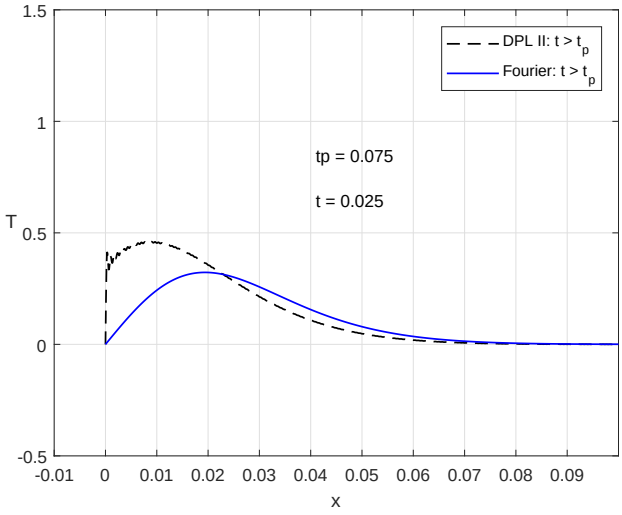

Figure 6.23: Spatial temperature distribution at $t = t_p + 0.025$; Fourier vs DPL-II model.

6.10.4 Temperature changes at a fixed position

One of the advantages of using the series solutions to generate approximate solutions, is that it is straightforward to gain insight into the temporal behaviour of the Fourier, C-V, DPL-I and DPL-II models.

We start off by investigating how the temperature changes with time t, at a fixed position $x = 0.02$ in the specimen. A prerequisite for comparing the

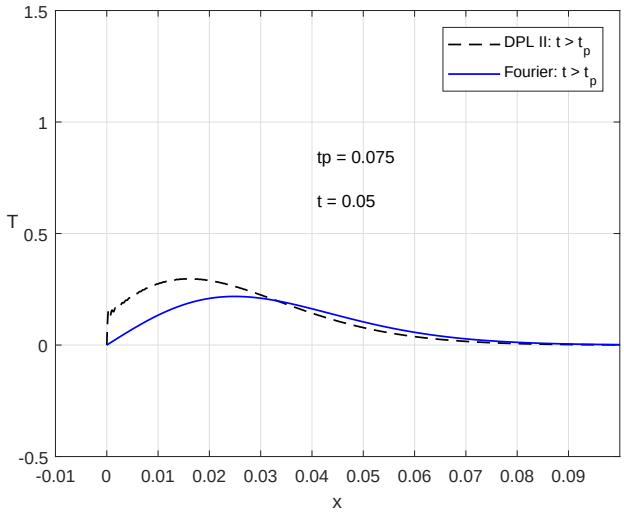

Figure 6.24: Spatial temperature distribution at $t = t_p + 0.05$; Fourier vs DPL-II model.

models is to ensure that the pulse length is long enough to allow all three models to predict similar peak temperatures. Numerical experimentation confirmed that $t_p = 0.075$ is sufficiently long. Figure 6.25 shows the predicted temperatures for the Fourier, C-V, DPL-I and DPL-II models, using the pulse length $t_p = 0.075$. Recall that for $0 < t < t_p = 0.075$, the heat pulse is on, and at $t = t_p = 0.075$ the pulse is stopped.

Figure 6.25 shows how the temperature changes with time t, at a fixed position $x = 0.02$ (number of modes $n = 3000$). For all the models the temperature T at $x = 0.02$ is initially at zero, as prescribed by the initial condition. A first observation is that the onset of the increase in temperature at $x = 0.02$ happens at different times for the different models.

For the Fourier model, the temperature starts to increase close to $t \approx 0$, and when the heat pulse is stopped at $t = t_p = 0.075$ the temperature starts to drop smoothly.

The C-V model predicts the longest delay for the onset of the temperature increase. At $t \approx 0.05$, the sharp thermal wave front reaches the point $x = 0.02$ and the expected sharp rise in temperature is observed. Note that after $t = t_p = 0.075$ when the heat pulse has been stopped, the increase in temperature continues for a while longer. The temperature reaches a peak value at $t \approx 0.125$ when the thermal wave has moved past $x = 0.02$ and then a sharp drop in temperature is observed. After that the temperature

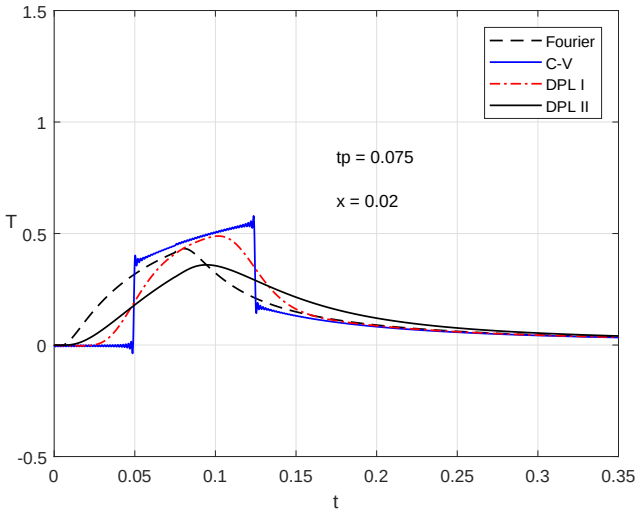

Figure 6.25: Temperature profiles at $x = 0.02$; Fourier, C-V, DPL-I and DPL-II models.

predicted by the C-V model approaches the value predicted by the Fourier model.

The DPL-I has a later onset of the temperature increase than the DPL-II model. Both the DPL models predict that the peak temperatures at $x = 0.02$ are reached some time after the heat pulse is stopped. The DPL-I model predicts a peak temperature comparable to that of the C-V model, but achieved at an earlier time. The peak temperature predicted by the DPL-II model is lower than that of the other models. The temperature predicted by the DPL models, also approach the value predicted by the Fourier model, as expected. At time $t = 0.35$ the temperatures predicted by the different models are all equal.

Sketching the graphs in Figure 6.25 required careful consideration of the calculations of the approximate solutions for the models. For the C-V and DPL models, using $T(x,t) = 1 - u(x,t)$ for the solutions for Problem 1 resulted in a small jump at $t = t_p$ between the solutions of Problem 1 and Problem 2. Replacing the solution for Problem 1 by $T(x,t) = u_0(x) - u(x,t)$ ensures continuity at $t = t_p$. In this case, all the expressions in the solutions are approximated using the same number of terms in the partial sum approximations.

The temporal behaviour of the models exhibit one of the key differences between the Fourier (parabolic) model, and the C-V and DPL (hyperbolic)

models. When the pulse is stopped, the Fourier model predicts an almost immediate decrease in temperature, while the hyperbolic models predict further increases in temperature before a sharp (C-V model) or slow (DPL model) decrease in temperature. For the Fourier model, the peak temperature, at the fixed position $x = 0.02$, is achieved close to the time $t = t_p$, and for the C-V and DPL models, the peak temperatures are achieved some time after the heat pulse has been stopped. This phenomenon is expected, as the boundary condition

$$\partial_t \tilde{T}(x, t_p) = -\partial_t u(x, t_p) \neq 0$$

for Problem 2 of the C-V and DPL models, means that the thermal wave contains momentum at $t = t_p$, that causes an increase in temperature even after the heat pulse has stopped.

Closer to the boundary, at the point $x = 0.005$ (as shown in Figure 6.26) the maximum temperatures predicted by the models are higher than at $x = 0.02$. We observe that the DPL-II model also predicts a decrease starting almost directly after $t = t_p$, although the drop is less sharp than for the other models. Next we investigate the effect of using a fixed position x very

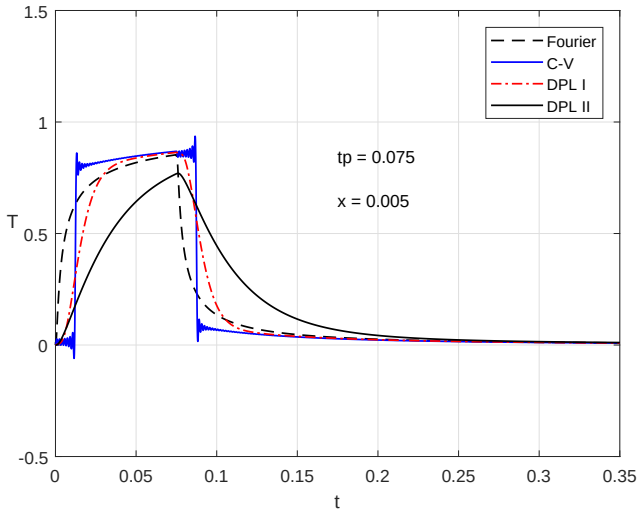

Figure 6.26: Temperature profiles at $x = 0.005$; Fourier, C-V, DPL-I and DPL-II models.

close to the boundary at $x = 0$. At the point $x = 0.001$ the predicted temperatures, obtained by using $n = 3\,000$ terms, are shown in Figure 6.27. Clearly these predictions are not acceptable approximate solutions as three of the models (Fourier, C-V and DPL-I) predict maximum temperature values

greater than 1. It is therefore necessary to increase the number of modes n when predicting the temperature values near the $x = 0$ boundary. We use the

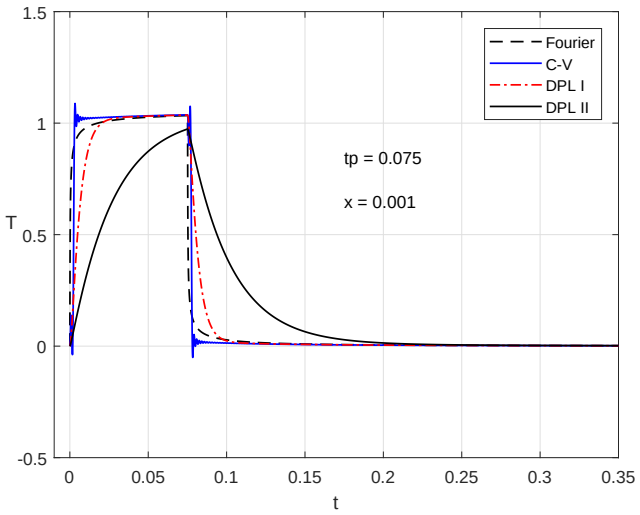

Figure 6.27: Temperature profiles at $x = 0.001$; Fourier, C-V, DPL-I and DPL-II models, with $n = 3\,000$.

approximation errors for $u_\delta(x)$ in Table 6.2 as a guideline for determining the number of modes to use. For $u_\delta(x)$ with $\delta = 0.001$ the relative energy norm error $\varepsilon_{rel}^{u_\delta,V} = 0.02022 \approx 2\%$ when using $n = 5\,000$ modes.

As $u_0(x) = u_\delta(x) = 1$ for $0.001 < x \leq 1$, this means that at least $5\,000$ modes are required for a good approximation of $u_0(x) = 1$. We determine through numerical experimentation that the number of modes required to achieve accurate temperature predictions is $n = 10\,000$. Note that the relative energy norm error $\varepsilon_{rel}^{u_\delta,V}$ when using $n = 10\,000$ modes, is $0.0101 \approx 1\%$. The predicted temperatures are shown in Figure 6.28. In summary, we observe that close to the boundary at $x = 0$ all four models predict an immediate drop in temperature after the pulse is stopped. We also observe that the closer a point is to the boundary at $x = 0$, the more similar are the temperature predictions of the Fourier, C-V and DPL-I models. The DPL-II model predicts a slower increase in temperature, as well as a slower decrease after the pulse is stopped.

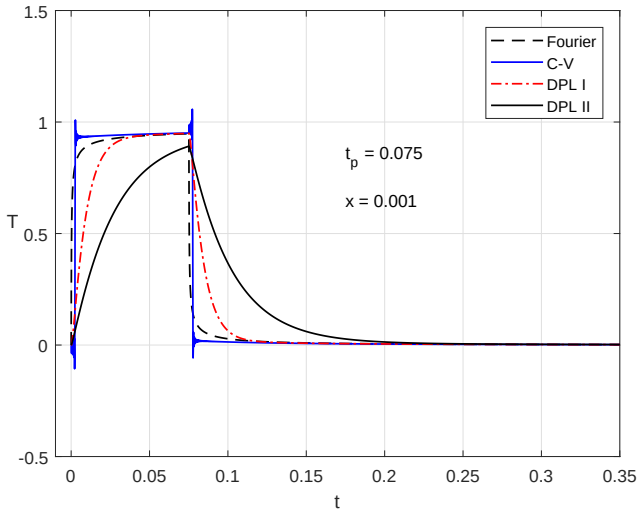

Figure 6.28: Temperature profiles at $x = 0.001$; Fourier, C-V, DPL-I and DPL-II models, with $n = 10\,000$.

6.10.5 Effect of τ_T on temperature profiles

For the DPL model y is the solution of

$$y'' + (2\gamma + 2\gamma\alpha\tau_T\lambda)\, y' + c^2\lambda y = 0, \tag{6.10.1}$$

and for the C-V model y is a solution of

$$y'' + 2\gamma y' + c^2\lambda y = 0. \tag{6.10.2}$$

If $\tau_T \approx 0$, the DPL-I model approaches the C-V model. This is verified in Section 6.8.1 by choosing $\tau_T = 0.0001$ in the DPL-I model, and then comparing the solutions of the C-V and DPL-I models at $t = 0.075$. See Figure 6.9. Note that in this case the first 16 modes of both the C-V and DPL-I models are overdamped.

For the solutions of the heat pulse problem the same observation holds. We start with the spatial profiles. In Figure 6.29 the solutions of the single-pulse problem at time $t = t_p + 0.025$ is shown for both the C-V and DPL-I model. The two solutions compare well, except that the solution of the DPL-I model is much smoother. Even the small lag time $\tau_T = 0.0001$ generates a significant reduction in the Gibbs oscillations at the two points of discontinuity. This is due to the increased damping of the underdamped modes of the DPL-I model, as explained in Section 6.6. The time temperature profiles for the C-V and

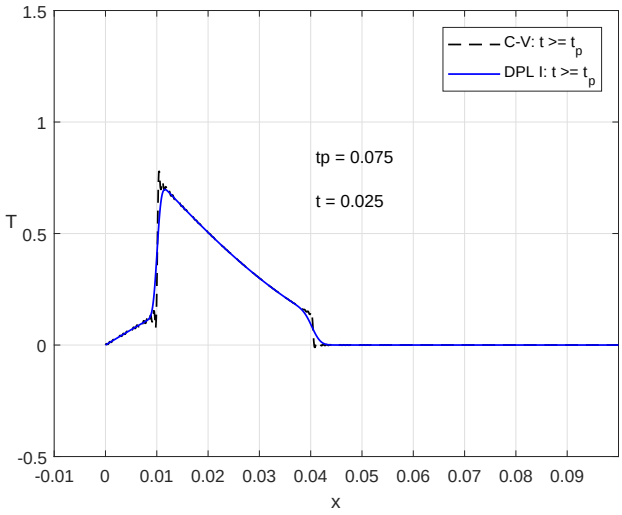

Figure 6.29: Spatial temperature distribution at $t = t_p + 0.025$; C-V vs DPL-I model, with $\tau_T = 0.0001$.

DPL-I models, at $x = 0.02$, for $\tau_T = 0.0001$, are shown in Figure 6.30. In this case, the profile of the DPL-I model also resembles that of the C-V model, with the main difference being that the DPL-I profile is smooth.

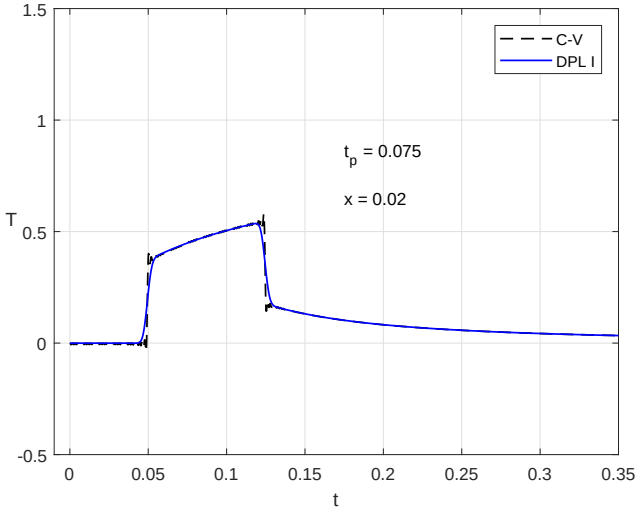

Figure 6.30: Temperature profiles at $x = 0.02$; C-V vs DPL-I model, with $\tau_T = 0.0001$

For comparison, the spatial temperature profiles for the C-V, DPL-I and

DPL-II models, at $t = t_p + 0.025$ are shown in Figure 6.31. For DPL-I, $\tau_T = 0.0041782$ and for DPL-II $\tau_T = 0.024875$ ($\delta \equiv \tau_T/\tau_q = 1$). Recall that, as calculated in Section 6.8.1, for $\tau_T < 0.0041782$ only the first 16 modes for the DPL-I model are overdamped. The value $\tau_T = 0.0041782$ is the smallest value for which the $17-$th mode of the DPL-I model is also overdamped. It is therefore an appropriate value for τ_T to use for investigating the difference between the C-V and DPL-I models.

As the same value for τ_q is used in both models, it also means that c^2 (and γ) has the same values in Eq. (6.10.1) and (6.10.2). We expect that the C-V and DPL-I models will predict similar rates for the progression of heat energy into the specimen. This can be motivated by the fact that the wave front speed c calculated for the C-V model (Section 6.4), is equal to the wave speed for the DPL-I model, since both models use the same dimensionless values for α and τ_q.

For the DPL-II model, the value of τ_T ensures that all the modes are overdamped. In this case a slower spatial progression of the heat wave into the specimen is expected. From the spatial profile, Figure 6.31, it can be seen how the maximum predicted temperature lags behind that of the C-V and DPL-I models. In fact, what we see from calculating time profiles at different fixed x positions (Figure 6.32, 6.33 and 6.34), is that the heat wave decelerates into the specimen, compared to the C-V and DPL-I models. Furthermore we see that the predicted peak temperatures for the DPL-I model are slightly lower than those of the C-V model, whereas the peak temperatures for DPL-II model are significantly lower. Choosing $\delta = 2$ ($\tau_T = 2\tau_q$) leads to a significant change in the predicted spatial profile. The temperature gradually decreases with x, with the jump at $x = 0$ still evident (Figure 6.35), and with the temperature at $x = 0$, slightly higher. The time profile, Figure 6.36 for $x = 0.02$, shows the peak temperature at a lower level.

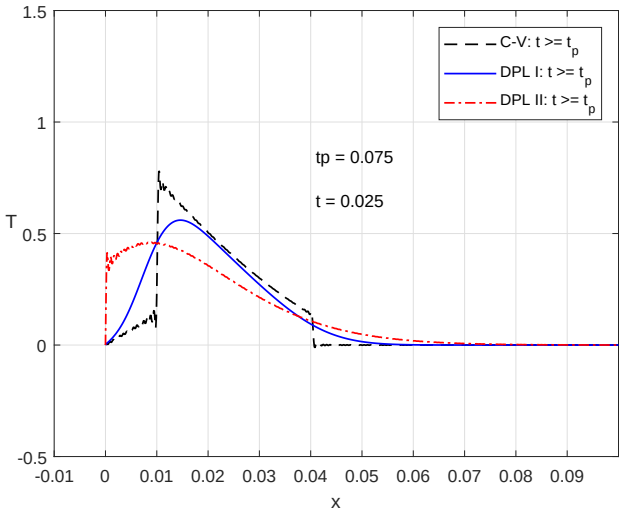

Figure 6.31: Spatial temperature distribution at $t = t_p + 0.025$; C-V, DPL-I and DPL-II models.

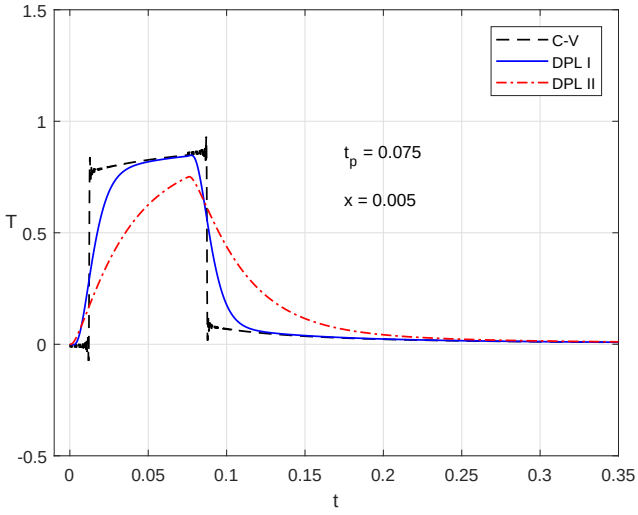

Figure 6.32: Temperature profiles at $x = 0.005$; C-V, DPL-I vs DPL-II models.

6.11 Conclusion

In this chapter, it is shown that the modal analysis of the hyperbolic heat conduction models, as presented in Chapter 5, provides an effective approach

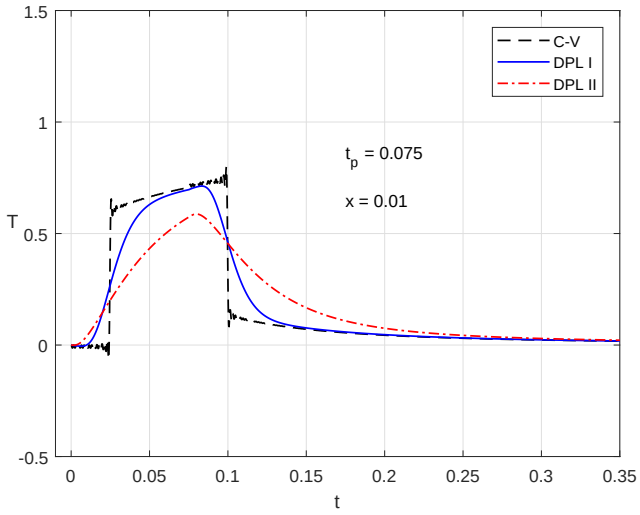

Figure 6.33: Temperature profiles at $x = 0.01$; C-V, DPL-I and DPL-II models.

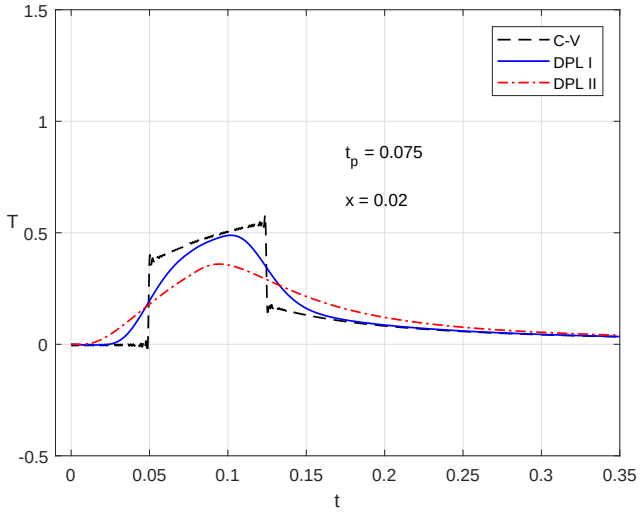

Figure 6.34: Temperature profiles at $x = 0.02$; C-V, DPL-I vs DPL-II model.

for finding approximate solutions. These approximate solutions are expressed as partial sums of series solutions, and are used for investigating and comparing the properties of the hyperbolic heat conduction models with that of the Fourier model.

A key result is that this approach allows one to determine a range of realistic

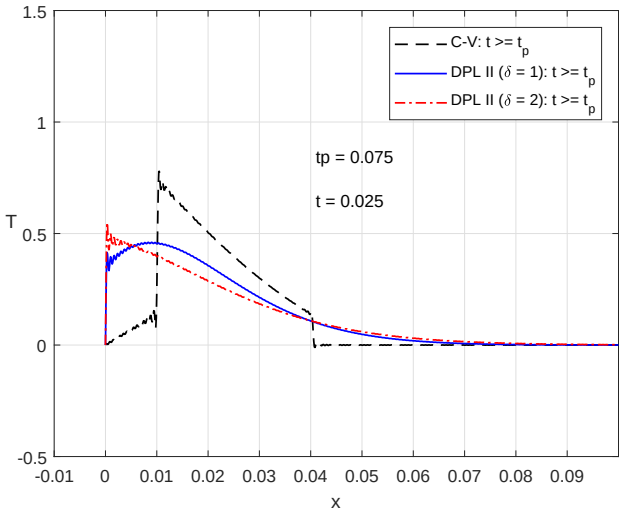

Figure 6.35: Spatial temperature distribution at $t = t_p + 0.025$; C-V vs DPL-II model, with $\delta = 1$ and $\delta = 2$.

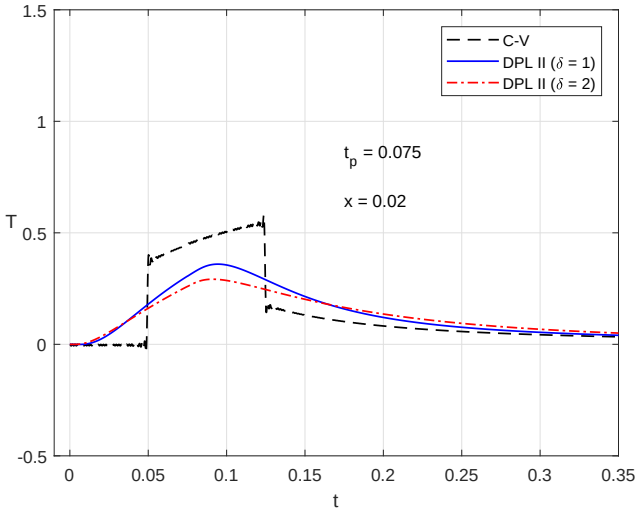

Figure 6.36: Temperature profiles at $x = 0.02$; C-V vs DPL-II model with $\delta = 1$ and $\delta = 2$.

values for the dimensionless lag times τ_q and τ_T based on the assumption that the Fourier model yields physically realistic results after sufficient time, and that the temperatures predicted by the hyperbolic models should be close to those of the Fourier model at that time.

Approximating the solutions of the respective models by partial sums requires careful consideration of the number of terms to use. To be confident that the comparisons between the models are valid and that genuine properties of the solutions are identified, the accuracy of the partial sum approximations had to be established. As the initial value for the model problems is a discontinuous function, the Gibbs phenomenon has a considerable effect on the predicted temperatures near the points of discontinuity. The discontinuous initial temperature distribution is successfully approximated by a continuous piecewise linear function that belongs to the energy space. The number of terms required in the partial sums is obtained through the calculation of the energy norm error for this function, and we show that the approximation error does not grow as time increases. We use these calculations in numerical experiments and confirm that it is indeed efficient in determining the required number of terms/modes to use for a particular problem.

The comparison between the different models focusses on how each model behaves close to $x = 0$, how the peak temperatures compare, and how the heat pulse propagates into the specimen.

The results from comparing the models include the following observations:

- We confirm that after a sufficiently long time, the predictions from the C-V and DPL models correspond to those of the Fourier model.
- The prominent thermal wave front expected for the C-V model is observed.
- Both over- and underdamped modes are required for accurate predictions for the C-V and DPL-I models.
- If $\tau_T \ll 1$, then the temperatures predicted by the DPL-I model approach those predicted by the C-V model, but with a smooth profile.
- The DPL-II stands out in that it does not resolve the discontinuity at $x = 0$.

In the next chapter we extend the solution strategy for the single-pulse problem to find a solution for the multi-pulse problem. Numerical experiments, based on two physical applications, are performed to illustrate the effectiveness of using truncated modal series solutions for multi-pulse problems.

Chapter 7

Multi-pulse problems

7.1 Introduction

In Chapter 6 we compare the Fourier model with the C-V and DPL models for the cases where continuous and single-pulse heating are applied to the boundary surface of the specimen. The aim of this chapter is to investigate how the modal series solutions that are derived in Chapter 6 can be adapted to the case of multi-pulse heating. Furthermore, we want to show that these solutions can be used to investigate heat transfer in two physical applications, namely thermoreflectance and bio-heating, where the multi-pulse heating parameter values differ significantly.

In Section 7.2 we briefly introduce these applications and identify the relevant heat pulse parameters used in these multi-pulse heating applications. The parameters include the duration of a single pulse (called the pulse width t_p), the separation time between the start of subsequent pulses (called the pulse period τ_p) and the duty ratio $r_d = t_p/\tau_p$. We provide typical parameters from thermoreflectance and bio-heating experiments. These applications provide a wide range of values for the duty ratio for the physical scenarios in our numerical experiments.

Section 7.3 introduces dimensionless versions of the multi-pulse problem for the one-dimensional Fourier, C-V and DPL models. It follows that the parameters used in the numerical experiments are limited to the lag times τ_q and τ_T and thermal diffusivity α of the specimen, and the pulse width t_p and pulse period τ_p of the heat source. The lag times are estimated using the method described in Section 7.3.4.

In Section 7.4 we consider multi-pulse problems for the Fourier, C-V and

DPL models. We start with parameter values as in Section 6.9 to be able to compare the properties of the temperature profiles for multi-pulse heating with those of single-pulse heating. The effect of the pulse period τ_p and the number of pulses m is also investigated. We then investigate typical scenarios, first from thermoreflectance (Section 7.5), and then from bio-heat applications (Section 7.6). For these applications, we use time-scaling factors (e.g. diffusion time and half-time) suitable to the physical scenario at hand to convert to the dimensionless problems. This simplifies the interpretation of results, and illustrate the flexibility of the series solution approximation.

Finally, Section 7.7 contains some concluding remarks.

7.2 Multi-pulse heating parameters

As mentioned already, the models introduced in Chapter 1 are routinely used to model heat transfer problems. Typical heat sources include various types of lasers or radio-frequency sources. The heat may be delivered to a specimen, either continuously, or in a pulsed fashion. The pulsed techniques are divided into single-pulse or multi-pulse techniques.

We choose to highlight two applications in our discussion of heating parameters: a measurement technique for the thermal diffusivity of thin film specimens (thermoreflectance), and bio-heating. The aim is to use parameters that represent extremes of *e.g.* pulse widths, pulse periods and thermal diffusivity values, in order to investigate how the different models predict heat transfer. Pulse widths can range from a few hundred femtoseconds (in the case of thermoreflectance) to a few hundred milliseconds (in the case of bio-heating), and thermal diffusivity values of specimens subject to bio-heating are typically much lower than those studied in thermoreflectance measurements. It must be stressed that we are not attempting to duplicate results reported in the fields of thermoreflectance and bio-heating, but rather to compare the different models, using our modal solution strategy.

The thermoreflectance technique is used to determine the thermal diffusivity α for metal and semiconductor thin films ([BTY11] [TBO01] [Bab10] [TBO99] [TYB09] [NTYB11]). Thermoreflectance infers the change in surface temperature of a specimen from the measured change in reflectivity of the specimen surface. The thin film thicknesses typically range from less than 100 nm to a few microns.

Typical experimental arrangements used are: heating the front surface whilst measuring the change in reflectance from the front surface; or heating the rear

surface whilst measuring the change in reflectance from the front surface. The latter configuration is similar to the laser flash method ([PJBA61] [Bab10] [AHZCB13]) in the sense that one surface is heated, whilst the opposite surface is probed to record the temperature rise over time. The general assumption is that heat transfer is governed by diffusion. The Fourier model is therefore used to derive a theoretical profile for the temperature rise at the rear face of the specimen. This temperature-rise is represented by the half-time $t_{1/2}$, which is the time required for the rear surface to reach half its maximum temperature rise. Another quantity used to characterise the temperature rise, is the heat diffusion time t_d, *i.e* the time required for the heat to diffuse across the specimen. It is related to the half-time by $t_d = t_{1/2}/0.1388$. The thermal diffusivity is calculated from

$$\alpha = d^2/t_d, \tag{7.2.1}$$

where d is the specimen thickness.

The lasers used in thermoreflectance setups are distinguished mainly by the duration of each single-pulse, and the separation time between consecutive pulses. We will refer to the pulse duration as the *pulse width* t_p and the separation time as the *pulse period* τ_p. Laser pulse widths range from about 100 fs to a few nanoseconds and pulse periods range from nanoseconds to several microseconds. Another useful parameter is the *duty ratio* defined as $r_d = t_p/\tau_p$. In practice, the laser pulses are not applied indefinitely but are applied to the specimen for a finite time so that one could refer to a *pulse-train* consisting of m number of pulses. One of the first successful femtosecond thermoreflectance experiments were performed on gold specimens. The reported value for the thermal diffusivity of gold is $\alpha = 1.2495 \times 10^{-4}$ m^{2}s^{-1} [BFI62].

In bio-heating, heating of the specimen is achieved by either continuous or multi-pulse heating. In multi-pulse heating the duty ratio r_d is used to control the amount of heat delivered to a target area or volume within a specimen. Bio-heat applications rely on controlling the heat delivery to ensure that the tissue surrounding the treated area is not damaged by heat accumulation ([MYSY21] [SK20] [YA20]). Ma *et al* [MYSY21] describes a numerical bio-heat experiment, where the pulse width t_p used, is either 0.3 s or 0.5 s, and the pulse period τ_p is 1 s, yielding a duty ratio $r_d = t_p/\tau_p = 0.3$ or 0.5. A typical value for the thermal diffusivity of blood is 5.881×10^{-8}m^2 s^{-1}.

Similar to Chapter 6 where we investigate the cases of constant and single-pulse heating, we want to determine how the individual model predictions will compare in the multi-pulse case.

7.3 Multi-pulse models

In this section, we formulate one-dimensional models for the case where multiple heat pulses are applied to the boundary of a specimen. We show how the modal solutions for single-pulse models, as derived in Section 6.9, can be adapted to solve these multi-pulse models. As was the case with the single-pulse model, we will not develop a full, realistic mathematical model of an actual physical process, and we retain the assumption that all the heat is absorbed at the boundary at $x = 0$.

7.3.1 Multi-pulse problem for the C-V and DPL models

The multi-pulse problem is similar to the single-pulse problem, with the difference that the heat pulse is modelled using a step function with multiple pulse cycles for the temperature $T(0,t)$ at the boundary.

To simplify the formulation of the multi-pulse problem and also the implementation of our numerical calculations, we define a pulse cycle as a "pulse ON" followed by a "pulse OFF" event. The first "pulse ON" starts at $t = 0$ and stops at $t = t_1$. The first "pulse OFF" stops at $t = t_2$. To be consistent with laser terminology, the pulse width is $t_p = t_1$ and the pulse period is $\tau_p = t_2$ (*i.e.* the total duration of "pulse ON" and "pulse OFF"). For a pulse-train consisting of m pulse cycles, the boundary condition at $x = 0$ is given by

$$T(0,t) = \begin{cases} 1, & t_{n-1} \leq t < t_n \\ 0, & t_n \leq t < t_{n+1} \\ 0, & t \geq t_{2m} \end{cases} \tag{7.3.1}$$

with $t_0 = 0$ and $n = 1, 3, 5, \ldots (2m-1)$.

Solving the multi-pulse problem for the first pulse cycle is done in the same way as for the C-V, DPL and Fourier model (refer to Sections 6.9.1 to 6.9.3. Note however that Problem 2 is formulated on a finite time interval. We use

the DPL model to illustrate the solution strategy:

$$\begin{aligned} \partial_t^2 T + 2\gamma\,\partial_t T - \tau_T c^2\,\partial_t \partial_x^2 T &= c^2\,\partial_x^2 T \qquad (7.3.2)\\ T(0,t) &= \begin{cases} 1, & t_{n-1} \le t < t_n \\ 0, & t_n \le t < t_{n+1} \\ 0, & t \ge t_{2m} \end{cases} \\ \partial_x T(1,t) &= 0 \\ T(x,0) &= 0 \\ \partial_t T(x,0) &= 0 \end{aligned}$$

where $2\gamma = 1/\tau_q$, $c^2 = \alpha/\tau_q$ and t_p is the pulse width. To solve this model, we start by considering the time interval $0 \le t < t_p$ and use the notation $T_1(x,t)$ for the temperature $T(x,t)$ restricted to this interval.

Problem 1 ("pulse ON"): $T_1(0,t) = 1 \quad (0 \le t < t_1 = t_p)$

To use the separation of variables method, we need to homogenize the boundary value by setting $u_1(x,t) = 1 - T_1(x,t)$ and then solve the equivalent problem (Problem 1) for $u_1(x,t)$. Problem 1 is formulated as

$$\begin{aligned} \partial_t^2 u_1 + 2\gamma \partial_t u_1 - \tau_T c^2 \partial_t \partial_x^2 u_1 &= c^2 \partial_x^2 u_1,\ 0 < x < 1,\ 0 < t < t_p \quad (7.3.3)\\ u_1(0,t) &= 0 \\ \partial_x u_1(1,t) &= 0 \\ u_1(x,0) &= 1 \\ \partial_t u_1(x,0) &= 0. \end{aligned}$$

As in Section 6.9.2, the solution for Problem 1 is given by $T_1(x,t) = 1 - u_1(x,t)$, for $0 \le t < t_1$, where $u_1(x,t)$ is the solution of the homogenized problem. The series representation of $u_1(x,t)$ is derived in Sections 6.2.2 to 6.2.5 using modal analysis.

Remark: In the remainder of this section, we show that the solutions of all further subproblems can be expressed in terms of the function $u_1(x,t)$. This is a key feature of the methodology used for simulating temperature profiles for the multi-pulse problems.

Problem 2 ("pulse OFF"): $T_2(0,t) = 0 \quad (t_1 \le t < t_2 = \tau_p)$

We denote the solution to Problem 2 by $T_2(x,t)$. The values for $T_1(x,t_1)$ and $\partial_t T_1(x,t_1)$ now become the initial conditions for Problem 2.

As in Sections 6.9.1 and 6.9.2, Problem 2 is formulated as

$$\begin{aligned} \partial_t^2 T_2 + 2\gamma\,\partial_t T_2 - \tau_T c^2\,\partial_t\partial_x^2 T_2 &= c^2\,\partial_x^2 T_2 \\ T_2(0,t) = \partial_x T_2(1,t) &= 0 \\ T_2(x,t_1) &= T_1(x,t_1) = 1 - u_1(x,t_1) \\ \partial_t T_2(x,t_1) &= \partial_t T_1(x,t_1) = -\partial_t u_1(x,t_1) \end{aligned} \tag{7.3.4}$$

To solve for $T_2(x,t)$ we use $u_1(x,t)$ for $t \geq t_1$ and define $Q_1(x,t) = T_2(x,t) + u_1(x,t)$. Then $T_2(x,t) = Q_1(x,t) - u_1(x,t)$ satisfies Eq. (7.3.4) and $Q_1(x,t)$ is the solution of

$$\begin{aligned} \partial_t^2 Q_1 + 2\gamma\,\partial_t Q_1 - \tau_T c^2\,\partial_t\partial_x^2 Q_1 &= c^2\,\partial_x^2 Q_1 \\ Q_1(0,t) = \partial_x Q_1(1,t) &= 0 \\ Q_1(x,t_1) &= 1 \\ \partial_t Q_1(x,t_1) &= 0 \end{aligned} \tag{7.3.5}$$

Equation (7.3.5) is the same as Eq. (7.3.3), except that the initial conditions are specified at $t = t_1$. From the linearity of the partial differential equation, it consequently follows that for $t \geq t_1$, $Q_1(x,t) = u_1(x,t-t_1)$ and therefore

$$T_2(x,t) = u_1(x,t-t_1) - u_1(x,t), \tag{7.3.6}$$

or, alternatively,

$$T_2(x,t) = T_1(x,t) + u_1(x,t-t_1) - 1. \tag{7.3.7}$$

The function $T_2(x,t)$ is the solution for Problem 2 for $t_1 \leq t < t_2$, but as the function $T_2(x,t)$ is defined for all t it can be used in the expressions for the solutions associated with the subsequent pulses.

For the second pulse cycle, as for the first cycle, two subproblems, Problem 3 and Problem 4, are considered for the "pulse ON" and "pulse OFF" events.

Problem 3 ("pulse ON"): $T_3(0,t) = 1 \quad (t_2 \leq t < t_3 = \tau_p + t_p)$

The values for $T_2(x,t_2)$ and $\partial_t T_2(x,t_2)$ are the starting values for Problem 3:

$$\begin{aligned} \partial_t^2 T_3 + 2\gamma\,\partial_t T_3 - \tau_T c^2\,\partial_t\partial_x^2 T_3 &= c^2\,\partial_x^2 T_3 \\ T_3(0,t) &= 1 \\ \partial_x T_3(1,t) &= 0 \\ T_3(x,t_2) &= T_2(x,t_2) = u_1(x,t_2-t_1) - u_1(x,t_2) \\ \partial_t T_3(x,t_2) &= \partial_t u_1(x,t_2-t_1) - \partial_t u_1(x,t_2) \end{aligned} \tag{7.3.8}$$

To homogenize this problem, we set

$$T_3(x,t) = 1 - u_2(x,t).$$

Problem 3 is equivalent to

$$\begin{aligned} \partial_t^2 u_2 + 2\gamma\,\partial_t u_2 - \tau_T c^2\,\partial_t\partial_x^2 u_2 &= c^2\,\partial_x^2 u_2 \\ u_2(0,t) &= 0 \\ \partial_x u_2(1,t) &= 0 \\ u_2(x,t_2) &= 1 - [u_1(x,t_2-t_1) - u_1(x,t_2)] \\ \partial_t u_2(x,t_2) &= -[\partial_t u_1(x,t_2-t_1) - \partial_t u_1(x,t_2)] \end{aligned} \tag{7.3.9}$$

To solve for $u_2(x,t)$ we continue using $T_2(x,t)$ for $t \geq t_2$ and define $Q_2(x,t) = u_2(x,t) + T_2(x,t)$.

Then $Q_2(x,t)$ is a solution of

$$\begin{aligned} \partial_t^2 Q_2 + 2\gamma\,\partial_t Q_2 - \tau_T c^2\,\partial_t\partial_x^2 Q_2 &= c^2\,\partial_x^2 Q_2 \\ Q_2(0,t) = \partial_x Q_2(1,t) &= 0 \\ Q_2(x,t_2) &= 1 \\ \partial_t Q_2(x,t_2) &= 0 \end{aligned} \tag{7.3.10}$$

and can be expressed in terms of $u_1(x,t)$.

For $t_2 \leq t < t_3$:

$$\begin{aligned} u_2(x,t) &= Q_2(x,t) - T_2(x,t) \\ &= u_1(x,t-t_2) - [u_1(x,t-t_1) - u_1(x,t)] \end{aligned}$$

The solution for Problem 3 is given by

$$T_3(x,t) = 1 - \{u_1(x,t-t_2) - [u_1(x,t-t_1) - u_1(x,t)]\}, \tag{7.3.11}$$

or, alternatively,

$$T_3(x,t) = 1 - u_1(x,t-t_2) + T_2(x,t). \tag{7.3.12}$$

Problem 4 ("pulse OFF"): $T_4(0,t) = 0 \quad (t_3 \leq t < t_4 = 2\tau_p)$

We denote the solution of Problem 4 by $T_4(x,t)$. The values for $T_3(x,t_3)$ and $\partial_t T_3(x,t_3)$ become the initial conditions for Problem 4:

$$\begin{aligned} \partial_t^2 T_4 + 2\gamma\,\partial_t T_4 - \tau_T c^2\,\partial_t\partial_x^2 T_4 &= c^2\,\partial_x^2 T_4 \\ T_4(0,t) = \partial_x T_4(1,t) &= 0 \\ T_4(x,t_3) &= T_3(x,t_3) = 1 - u_2(x,t_3) \\ &= 1 - \{u_1(x,t_3-t_2) - [u_1(x,t_3-t_1) - u_1(x,t_3)]\} \\ \partial_t T_4(x,t_3) &= \partial_t T_3(x,t_3) = -\partial_t u_2(x,t_3) \\ &= -\{\partial_t u_1(x,t_3-t_2) - [\partial_t u_1(x,t_3-t_1) - \partial_t u_1(x,t_3)]\} \end{aligned} \tag{7.3.13}$$

As before, to solve for $T_4(x,t)$ we continue using $u_2(x,t)$ for $t \geq t_3$ and define $Q_3(x,t) = T_4(x,t) + u_2(x,t)$.

Then $T_4(x,t) = Q_3(x,t) - u_2(x,t)$ will satisfy Eq. (7.3.13) and $Q_3(x,t)$ is the solution of

$$\begin{aligned} \partial_t^2 Q_3 + 2\gamma\,\partial_t Q_3 - \tau_{_T} c^2\,\partial_t \partial_x^2 Q_3 &= c^2\,\partial_x^2 Q_3 \\ Q_3(0,t) = \partial_x Q_3(1,t) &= 0 \\ Q_3(x,t_3) &= 1 \\ \partial_t Q_3(x,t_3) &= 0 \end{aligned} \tag{7.3.14}$$

For $t \geq t_3$, $Q_3(x,t) = u_1(x,t-t_3)$ and it follows that

$$T_4(x,t) = u_1(x,t-t_3) - \{u_1(x,t-t_2) - [u_1(x,t-t_1) - u_1(x,t)]\}\,, \tag{7.3.15}$$

or

$$T_4(x,t) = T_3(x,t) + u_1(x,t-t_3) - 1. \tag{7.3.16}$$

The solutions for Problems 1 to 4 can be summarised as:

$$\begin{aligned} T_1(x,t) &= 1 - u_1(x,t) && (t_0 \leq t < t_1) \\ T_2(x,t) &= T_1(x,t) + u_1(x,t-t_1) - 1 && (t_1 \leq t < t_2) \\ T_3(x,t) &= 1 - u_1(x,t-t_2) + T_2(x,t) && (t_2 \leq t < t_3) \\ T_4(x,t) &= T_3(x,t) + u_1(x,t-t_3) - 1 && (t_3 \leq t < t_4) \end{aligned}$$

For a pulse train with m pulse cycles the solution is given by a sequence of functions

$$\begin{aligned} T_n(x,t) &= 1 - u_1(x,t-t_{n-1}) + T_{n-1}(x,t) && (t_{n-1} \leq t < t_n) \\ T_{n+1}(x,t) &= T_n(x,t) + u_1(x,t-t_n) - 1 && (t_n \leq t < t_{n+1}) \end{aligned} \tag{7.3.17}$$

for $n = 1, 3, 5, \ldots, 2m-1$.

Note that $T_0(x,0) = 0$ and that $T_{2m}(x,t)$ is defined for $t \geq t_{2m-1}$.

For the multi-pulse problem for the C-V model, set $\tau_{_T} = 0$ in Eq. (7.3.2) and all subsequent problems.

7.3.2 Multi-pulse problem for the Fourier model

We solve the multi-pulse problem for the Fourier model in the same way as the C-V and DPL models, even though the partial differential equation is a

diffusion equation. For the multi-pulse problem, the boundary condition at $x = 0$ for the single-pulse problem (Eq. (6.9.8)), has to be adapted, similar to Eq. (7.3.1), so that the multi-pulse Fourier model is given by

$$\begin{aligned} \partial_t T &= \alpha\, \partial_x^2 T \\ T(0,t) &= \begin{cases} 1, & t_{n-1} \le t < t_n \\ 0, & t_n \le t < t_{n+1} \\ 0, & t \ge t_{2m} \end{cases} \\ \partial_x T(1,t) &= 0 \\ T(x,0) &= 0 \end{aligned} \tag{7.3.18}$$

with $t_0 = 0$ and $n = 1, 3, 5, \ldots (2m-1)$.

Problem 1 ("pulse ON"): $T_1(0,t) = 1 \quad (0 \le t < t_1)$

As before, the problem is homogenized by setting $u_1(x,t) = 1 - T_1(x,t)$. This problem is solved using separation of variables, and $T_1(x,t) = 1 - u_1(x,t)$ is the solution for Eq. (7.3.18) when $0 \le t < t_1$. The series representation for $u_1(x,t)$ is derived in Section 6.2.5.

Problem 2 ("pulse OFF"): $T_1(0,t) = 0 \quad (t_1 \le t < t_2)$

We denote the solution to Problem 2 by $T_2(x,t)$. The value for $T_1(x,t_1)$ is the initial condition for Problem 2.

Problem 2 is formulated as

$$\begin{aligned} \partial_t T_2 &= \alpha\, \partial_x^2 T_2 \\ T_2(0,t) = \partial_x T_2(1,t) &= 0 \\ T_2(x,t_1) &= T_1(x,t_1) = 1 - u_1(x,t_1) \end{aligned} \tag{7.3.19}$$

As before, to solve for $T_2(x,t)$ we use $u_1(x,t)$ for $t \ge t_1$. We define $Q_1(x,t) = T_2(x,t) + u_1(x,t)$. Then $T_2(x,t) = Q_1(x,t) - u_1(x,t)$ satisfies Eq. (7.3.19).

$Q_1(x,t)$ is the solution of

$$\begin{aligned} \partial_t Q_1 &= \alpha\, \partial_x^2 Q_1 \\ Q_1(0,t) = \partial_x Q_1(1,t) &= 0 \\ Q_1(x,t_1) &= 1 \end{aligned} \tag{7.3.20}$$

For $t \ge t_1$, $Q_1(x,t) = u_1(x, t-t_1)$ and it follows that

$$T_2(x,t) = u_1(x,t-t_1) - u_1(x,t). \tag{7.3.21}$$

The solution for the subsequent pulse cycles are derived in the same way as in Section 7.3.1 and are given by Eq. (7.3.17).

7.3.3 Series solution

For the numerical investigation of the multi-pulse problem, the series representation of the solutions $u_1(x,t)$ for the Fourier, C-V and DPL models are required. This section contains a short summary of these series representations as derived in Section 6.2.

All three models have the same associated eigenvalue problem, and the eigenfunctions (normalised with respect to the norm of the square integrable functions) are given by

$$w_k(x) = \sin \nu_k x \quad \text{with } \nu_k = \frac{(2k-1)\pi}{2} \text{ for } k = 1, 2, \ldots. \tag{7.3.22}$$

The series representation for the solution $u_1(x,t)$ follows as

$$u_1(x,t) = \sum_{k=1}^{\infty} y_k(t) w_k(x) \tag{7.3.23}$$

where $y_k(t)$ must be determined for each of the three models. The initial condition $u_1(x,0) = 1$ is used for all three models, and it is easy to check that

$$y_k(0) = \int_0^1 u_1(0,t) w_k(x)\, dx = \frac{2}{\nu_k}. \tag{7.3.24}$$

The additional initial condition $\partial_t u_1(x,0) = 0$, yielding $y_k'(0) = 0$ is required for the C-V and DPL models.

Fourier model:

We solve first order linear differential equations to find

$$y_k(t) = \frac{\sqrt{2}}{\nu_k} e^{-r_k t} \quad \text{with } r_k = \alpha \nu_k^2. \tag{7.3.25}$$

DPL model:

The DPL model is a second order hyperbolic differential equation, and we use the terminology from vibration analysis to describe properties of the eigenfunctions (or modes). We introduce the notation $\gamma_k = \gamma + \tau_{_T} c^2 \nu_k^2$ and consider two cases for the modes: the overdamped case ($\gamma_k^2 > c^2\nu_k^2$) and the underdamped case ($\gamma_k^2 < c^2\nu_k^2$).

In the overdamped case, let $r_1^k = -\gamma_k + \sqrt{\gamma_k^2 - c^2\nu_k^2}$, $r_2^k = -\gamma_k - \sqrt{\gamma_k^2 - c^2\nu_k^2}$ and $r_k = r_2^k / r_1^k$. Then

$$y_k(t) = a_k \left(e^{r_1^k t} - \frac{1}{r_k} e^{r_2^k t} \right) \quad \text{with } a_k = -\frac{\sqrt{2} r_k}{\nu_k (1 - \nu_k)}. \tag{7.3.26}$$

In the underdamped case, let $\omega_k^d = \sqrt{c^2\nu_k^2 - \gamma_k^2}$. Then

$$y_k(t) = c_k e^{-\gamma_k t}\left(\cos\omega_k^d t + \frac{\gamma_k}{\omega_k^d}\sin\omega_k^d t\right) \quad \text{with } c_k = \frac{\sqrt{2}}{\nu_k}. \tag{7.3.27}$$

When computing the series solution in Eq. (7.3.23) for the DPL model it must be checked for each k, whether Eq. (7.3.26) or Eq. (7.3.27) applies.

For the DPL model the constitutive equation is given by

$$q(x, t+\tau_q) = -\partial_x T(x, t+\tau_T),$$

where q is the heat flux and $\partial_x T$ the temperature gradient. A linear approximation of this constitutive equation is used to derive the model. For the numerical simulations in Sections 7.4 to 7.6, we distinguish between two cases. For $0 < \tau_T < \tau_q$, the temperature gradient precedes the heat flux vector [Tzo97]. We refer to this case as DPL-I. In this case, the first modes are overdamped, followed by some underdamped modes, and then all the remaining modes are overdamped. For $0 < \tau_q < \tau_T$ the temperature gradient follows after the heat flux vector. We refer to this case as DPL-II, and note that all the modes are overdamped. The case where $\tau_T = \tau_q$, is a special case, and in [Tzo97, Section 2.5] Tzou identifies this as a case where heat transfer occurs by diffusion. We include this special case with DPL-II, as all the modes are overdamped. It is convenient to define $\delta \equiv \tau_T/\tau_q$ – then $0 < \delta < 1$ indicates the DPL-I model and $\delta \geq 1$ indicates the DPL-II model. For the special case where $\delta = 1$, we expect the DPL-II model to display diffusive behaviour, i.e. similar to the Fourier model.

C-V model:

For the C-V model, we choose $\tau_T = 0$ in Eq. (7.3.26) and Eq. (7.3.27). This means that $\gamma_k = \gamma$ for all k.

For the C-V model, the first modes are overdamped, but all higher modes are underdamped at the same rate $e^{-\gamma t}$.

7.3.4 Parameter values for numerical investigation

The first issue is to decide on the number of terms n to use for the finite sum approximations for $u_1(x,t)$. In the simulations we use the discontinuous initial condition $u_1(x,0) = 1$. Recall that this is the same initial conditon used in the continuous and single-pulse heating cases in Chapter 6. We therefore follow the same procedure as described in Section 6.5. We use error

estimates as a guideline for the relative approximation error and determine the number of modes n by deciding on an acceptable relative approximation error. For $n = 3000$ modes, the relative approximation error (in the norm of the square integrable functions) is less than 4×10^{-5}, and we will use this value in most of the simulations. Note that the required number of modes does not depend on the values of the parameters α, τ_q and τ_T, as these parameters do not appear in the eigenfunctions.

Secondly, the value for the dimensionless thermal diffusivity α^* is required, which depends on t_0, the time scaling factor for the dimensionless time variable. For the simulations in Section 7.4, we use the value for t_0 as chosen for the continuous and single-pulse simulations in Chapter 6. This allows for easy comparison with the multi-pulse problems. We recall from Section 2.8.1 that at t_0, the fundamental modal solution for the Fourier model has decreased by 1%. We have

$$t_0 = -\frac{4\ln(0.99)d^2}{\pi^2\alpha} \approx 0.0040732\,\frac{d^2}{\alpha} \tag{7.3.28}$$

and consequently, the dimensionless thermal diffusivity follows as

$$\alpha^* = \frac{t_0\alpha}{d^2} = 0.0040732. \tag{7.3.29}$$

It is easy to use a different reference time t_0. In Section 7.5, for simulations linked to a thermoreflectance example, we use the diffusion time t_d as reference time. In this case,

$$t_0 = t_d = \frac{d^2}{\alpha} \text{ with } \alpha^* = 1. \tag{7.3.30}$$

In Section 7.6, we consider bio-heat applications and use the half-time $t_{1/2}$ as reference time which yields

$$t_0 = t_{1/2} = \frac{d^2}{\alpha} \text{ with } \alpha^* = 0.1388. \tag{7.3.31}$$

In all cases, due to the choice of t_0, the value for α^* is independent of the specimen thickness d and the thermal diffusivity α.

Thirdly, values for the dimensionless lag times τ_q^* and τ_T^* are required. In Sections 6.3 and 6.7 we derive upper bounds,

$$\tau_q^* \leq \frac{\varepsilon}{\alpha^*\pi^2} \quad \text{and} \quad \tau_T^* \leq \frac{4\varepsilon}{\alpha^*\pi^2} \tag{7.3.32}$$

for the lag times, with $\varepsilon \ll 1$ a user specified accuracy. Using $\varepsilon = 0.001$, we obtain the value $\tau_q^* = 0.024875$. The value for τ_T^* is chosen in such a way that sensible comparisons between the DPL and C-V models are possible. We obtain $\tau_T^* = 0.0041782$ for the DPL-I model, and $\tau_T^* = \tau_q^* = 0.024875$ for the DPL-II model. These values for the lag times are used in Section 7.4.

For the numerical investigations related to the thermoreflectance example in Section 7.5 and the bio-heat application in Section 7.6, we seek values of the lag times that result in distinct differences between the different model predictions. When deciding on the values for τ_q^* and τ_T^*, we ensure that values remain within an acceptable range. The upper bounds given in Eq. (7.3.32) are used, however, ε has to be specified in a consistent and realistic way. This is done by choosing a value for ε, finding r_1^1 and r_1^F respectively, and calculating the percentage fractional difference $100 \times |(r_1^F - |r_1^1|)/r_1^F|$. We decide on a maximum allowable percentage of approximately 10% and consistently use this value to ensure that for each choice of ε, the values for τ_q^* and τ_T^* remain within an acceptable range.

7.4 Comparison with single-pulse problem

In the remaining sections all variables and parameters are dimensionless and, for convenience, we return to using the original notation. Where physical parameters are referred to, it will be clear from the context, and the units are given.

Our investigation of the multi-pulse problem starts by finding the solutions for the Fourier, C-V and DPL models with the values for the dimensionless parameters as in Section 6.9, so that the single-pulse problems and the multi-pulse problems can be compared. These parameter values are: $\alpha = 0.0040732$, $\tau_q = 0.024875$, $\tau_T^I = 0.0041782$ (DPL-I model) and $\tau_T^{II} = \tau_q = 0.024875$ (DPL-II model). In this case $\delta^{II} = 1$. We use finite sum approximations of the series solutions, with $n = 3000$ modes, to find temperature distributions. These temperature profiles are temporally calculated at a fixed position in the specimen over time. In particular, we investigate the effects of changing the pulse period τ_p and the number m of pulse cycles in the pulse-train on the solutions.

Before starting with the investigation, we want to determine how accurately the temperature pulse mimics the incident heat pulse, at positions close to $x = 0$. In Section 6.10.4 we mention that at positions close to the $x = 0$ boundary, it is necessary to increase the number of modes n to ensure

accurate predictions. We find through experimentation that at $x = 0.001$, at least $n = 30000$ modes are required to ensure an accurate solution. Figure 7.1, with the pulse width $t_p = 0.075$ and the pulse period $\tau_p = 0.15$, shows that for all the models, except the DPL-II model, the temperature profile closely resembles the incident step heat pulse. The DPL-II temperature profile gradually ramps up, reaches a slightly lower maximum temperature value, and gradually decreases again. This deviation from the step pulse is expected considering the strong damping built into the DPL-II model.

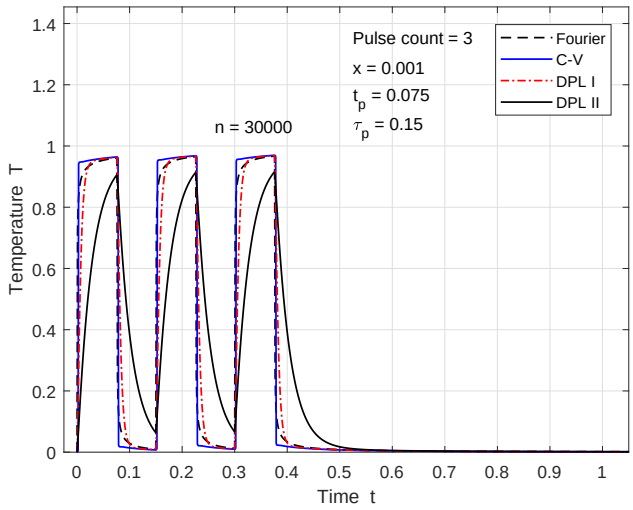

Figure 7.1: Temperature profiles at $x = 0.001$, close to the boundary

Figure 7.2 shows the temperature profiles for a three-pulse problem, calculated at a fixed position $x = 0.02$. The C-V temperature profile is characterised by sharp thermal wave fronts, that distinguish it from the profiles of the other models. Small amplitude Gibbs oscillations are present near these sharp wave fronts. (Using more modes reduces the amplitude of the Gibbs oscillations; this is also true near the discontinuities.)

The instant when the temperature at $x = 0.02$ starts to rise, also differs for the respective models. The Fourier and DPL-II models predict an immediate rise in temperature, followed by the DPL-I model. The C-V model however predicts a fairly long delay, compared to the other models, followed by a sudden jump in the temperature at the arrival of the thermal wave front. As expected, the temperature profiles for the first pulse cycle agree with the profiles for the single-pulse models in Figure 6.25.

Similar for each model, is the increase in the peak temperature value with each consecutive pulse. This is to be expected since the temperature does

not decrease to its original zero level before the next pulse is incident on the specimen. The most noticeable difference between the models is the difference in predicted peak temperatures. The highest temperatures are predicted by the C-V model, followed by the DPL-I, then Fourier, and lastly the DPL-II model. The difference does however reduce with each consecutive pulse. The time t at which the peak temperatures are reached also differ according to the model used. From first to last we have the Fourier, DPL-II, DPL-I and C-V model.

As anticipated, a sufficiently long time after the final pulse, the temperatures predicted by the four models are equal.

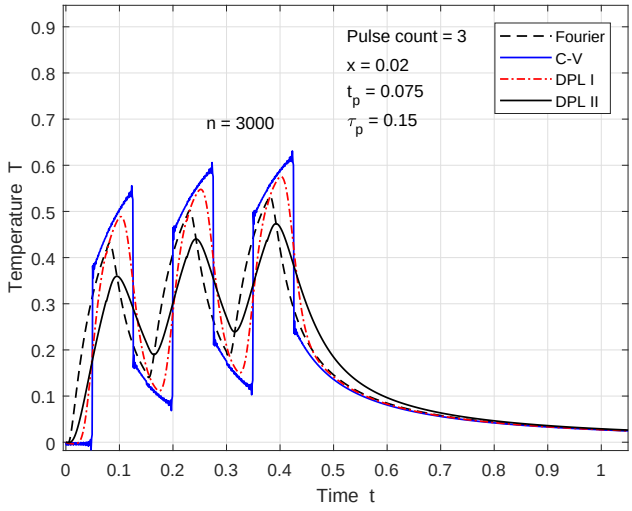

Figure 7.2: Temperature profiles at $x = 0.02$ for 3-pulse problem

Another interesting observation is obtained by choosing the fixed position x deeper into the specimen. Calculating the temperature profiles at say $x = 0.075$ (Figure 7.3) shows that the three pulses are starting to merge. However, the merging effect is less for the DPL-I model, and for the C-V model three distinct pulses are still clearly visible.

These properties of the temperature profiles agree with the physics of heat transfer. In the derivation of the heat transfer models in Section 6.9.1, we assume that all the optical energy is absorbed at $x = 0$. The absorbed energy increases the internal energy of the heat carriers in the surface region of the specimen. Initially, the gradient is small and therefore the diffusion of energy from the surface to the interior is slow. This results in a swift temperature rise in the surface region. Through interaction between the heat carriers,

the temperature gradient gradually increases with time, thereby promoting diffusion of energy from the surface to the interior. The diffusion process is slower than the absorption and the distinction between individual pulses becomes less with increasing x. The heat energy is distributed throughout the specimen resulting in a temperature level that is lower than the initial level in the surface region ([SYS07] [Yil12]).

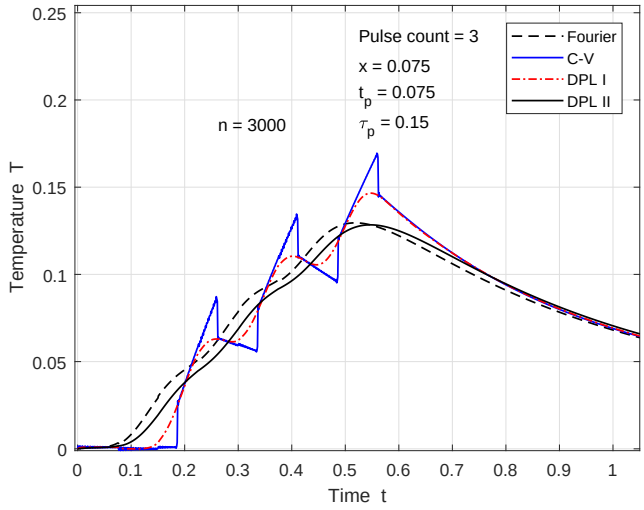

Figure 7.3: Temperature profiles at $x = 0.075$ showing merging of pulses

Next we investigate the effect of the pulse period on the temperature profiles. In Section 6.8 (Figures 6.10 and 6.13) it is shown that for the single-pulse problem, the four models predict the same temperatures from about $t = 0.35$. To determine the effect of the pulse period τ_p on the model predictions, we therefore increase the pulse period τ_p to 0.35, while keeping the pulse width unchanged at $t_p = 0.075$. The reason for this choice is to determine the effect when enough time elapses between consecutive pulses, for the temperature to return to zero before the next pulse starts. We then compare the temperature profiles at $x = 0.02$ with those in Figure 7.2 where $\tau_p = 0.15$.

Two properties are worth mentioning. Firstly, for the longer pulse period, the peak pulse heights increase at a slower rate. This is to be expected since more time is available for the temperature to decrease to a lower level before the arrival of the next pulse. We see in Figure 7.4 that all four models predict approximately the same temperature when the next pulse arrives, i.e. temperature values are within about 3 % of each other. In Figure 7.2 there are still significant differences between the model predictions when the next pulse arrives. Secondly, the solutions of the Fourier and DPL-I models start

to agree well before the arrival of the next pulse. This agreement between the solutions of these two models did not occur for the case $\tau_p = 0.15$ in Figure 7.2. The pulse period τ_p also has an effect on the merging of individual

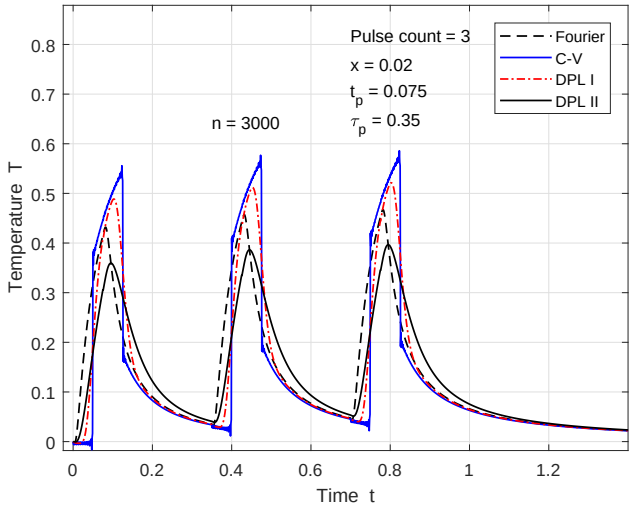

Figure 7.4: Temperature profiles at $x = 0.02$ with increased pulse period $\tau_p = 0.35$

pulses. Repeating the calculation with the same parameters as for Figure 7.3, but increasing the pulse period to $\tau_p = 0.35$ ($r_d = 0.075/0.35 = 0.214$), we see that the merging is reduced, and that three distinct temperature pulses are visible for all four temperature profiles (Figure 7.5). The peak pulse heights are also lower, compared to Figure 7.3. At a fixed point x deeper into the specimen, merging of the pulses will again be more prominent.

Next, we want to investigate the effect of increasing the number of pulses m. In Figure 7.4, we have $t_p = 0.075$ and $\tau_p = 0.35$. For three pulses, the heating duration is $2\tau_p + t_p = 0.775$. If the pulse period is reduced to $\tau_p = 0.175$ whilst keeping t_p fixed, the duty ratio is doubled ($r_d = 0.075/0.175 = 0.429$). To keep the heating duration unchanged, we increase the number of pulses from $m = 3$ to $m = 5$.

Using the DPL-I profile as reference we see that the maximum temperature has increased from $T \approx 0.52$ in the 3-pulse case (Figure 7.4) to $T \approx 0.59$ in the 5-pulse case (Figure 7.6). The other models show similar behaviour. This is due to the higher duty ratio for the 5-pulse case, implying that more heat energy is injected into the specimen during the heating stage. The increase in peak temperature per pulse is higher in the 5-pulse case.

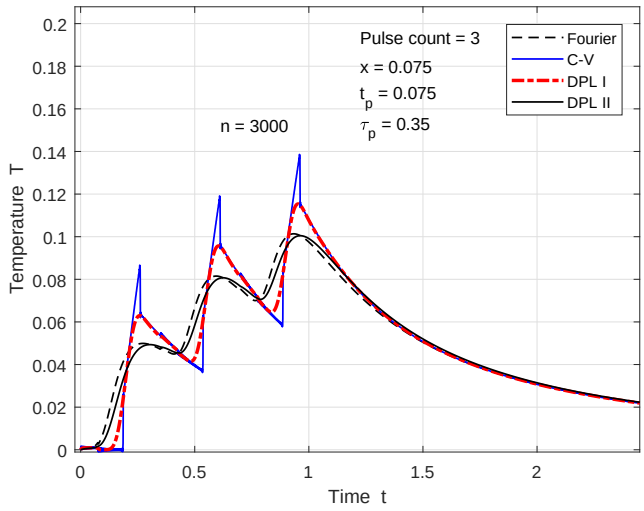

Figure 7.5: Merging of peaks at $x = 0.075$ with increased pulse period $\tau_p = 0.35$

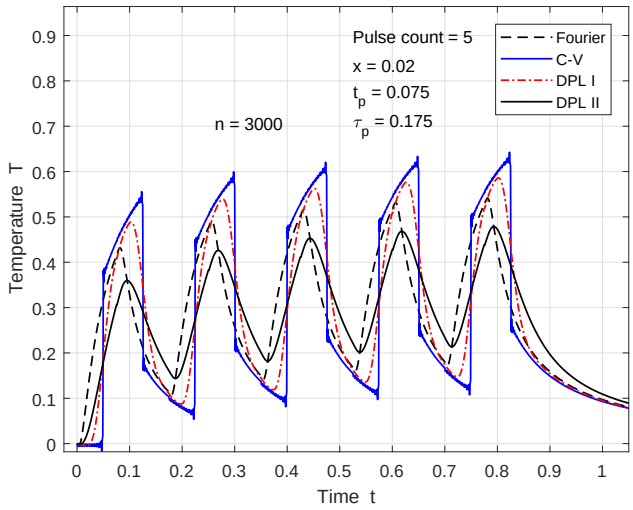

Figure 7.6: Temperature profiles at $x = 0.02$ for 5-pulse problem with fixed heating duration

If we do not restrict the heating duration and increase the number of pulses to $m = 20$, with $t_p = 0.075$ and $\tau_p = 0.175$, the peak temperatures gradually ramp up as shown in Figure 7.7. For instance, the peak temperatures for the DPL-I solution reaches a plateau value of $T \approx 0.63$, which is not much higher than the maximum after 5 pulses shown in Figure 7.6.

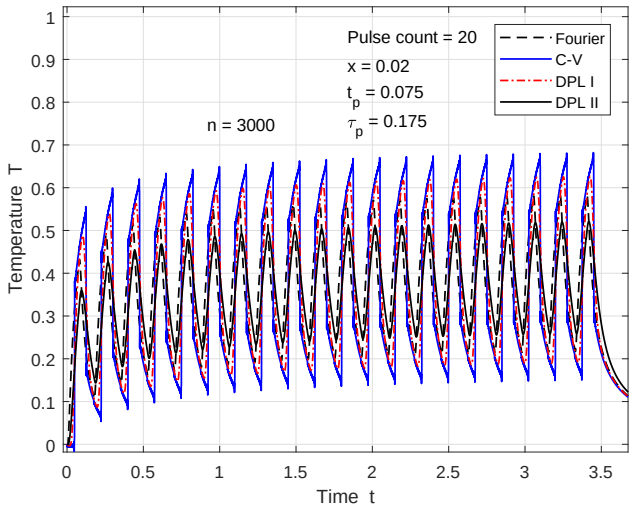

Figure 7.7: Temperature profiles at $x = 0.02$ for 20-pulse problem; reaching a plateau

Increasing the pulse period τ_p while keeping the pulse width t_p unchanged, decreases the duty ratio r_d. Decreasing r_d reduces the heat energy injected into the specimen, and will lead to lower peak temperatures and lower plateau values. We illustrate this effect with examples based on bio-heating in Section 7.6.

All the previous temperature profiles are calculated at a fixed point x in the interior of the specimen. In some applications the spatial temperature distribution is required, and in particular, the effect of the number of pulses on the temperature profile is of importance. The modal series solutions can be used to find spatial temperature distributions across the specimen at a fixed time t. This will be discussed in Section 7.6.

7.5 Thermoreflectance case study: low duty ratio r_d

The case we investigate here relates to femtosecond thermoreflectance experiments carried out on metal thin films. See, for instance, [Tzo97] and [Bro90] for early contributions. In a typical setup the front face is heated by the laser, while the rear surface is probed to determine the change in reflection, from which the change in temperature is determined. We choose a gold

thin film specimen with thickness $d = 50$ nm, and with thermal diffusivity $\alpha = 1.2495 \times 10^{-4}$ m^{2}s^{-1}. A typical laser pulse width is $t_p = 0.1$ ps.

For the dimensionless models, the front face is at $x = 0$ and the rear face at $x = 1$. For this example, we use the diffusion time as the time scaling factor, with $t_0 = t_d = d^2/\alpha = 20$ ps. The diffusion time is a concept that is well-known within the international materials metrology community, concerned with the measurement of thermophysical properties of materials ([BTY11][Bab10]), and it is easy to accommodate this different time scaling factor in the modal series solutions.

The following values are obtained for the dimensionless parameters with the new time scaling. Using Eq. (7.3.29) we calculate the dimensionless thermal diffusivity as $\alpha = 1$. The dimensionless pulse width is given by $t_p = 0.1/20 = 0.005$. The pulse period $\tau_p = 5$ is chosen to ensure that, for each model, subsequent pulse heights at a fixed interior point are almost equal. This means that the duty ratio is therefore $r_d = t_p/\tau_p = 0.001$.

The aim in this section is to study numerical examples where, at least initially, there is a distinct difference between the different model predictions. The lag times are determined by experimentation in order to achieve this. The experimentation is done using Eq. (7.3.32), with $\varepsilon = 0.125$ and checking that the percentage fractional difference $100 \times |(r_1^F - r_1^1)/r_1^F|$, introduced in Section 7.3.4, remains less than 10%.

The values $\tau_q = 0.012665$, $\tau_T^I = 0.002868$ (DPL-I model) and $\tau_T^{II} = 0.037995$ (DPL-II model) are obtained. We have the lag time ratios $\delta^I = \tau_T^I/\tau_q = 0.22645$ and $\delta^{II} = \tau_T^{II}/\tau_q = 3.0$. These lag time values are used in Figures 7.8 to 7.10. We focus on two aspects: the characteristics of the temperature pulses, specifically the pulse width and pulse height behaviour, and the effect of values used for the lag times, τ_q and τ_T, and consequently δ.

7.5.1 Characteristics of temperature pulses and wave fronts

Figure 7.8 shows the solutions for the four models, for three pulse cycles. Due to the low duty ratio (*i.e.* $r_d \ll 1$) no merging of pulses is observed. Three distinct pulses are predicted to reach the rear face at $x = 1$. Since the pulse period τ_p is long enough, the temperatures decrease to almost the same near zero value for all four the models before the next pulse starts. Subsequent pulses are therefore almost identical. The most noticeable feature of the temperature profile is the relatively high peak heights, and the narrow

peak widths (although not clearly visible in the figure) of the C-V model compared to the other three models.

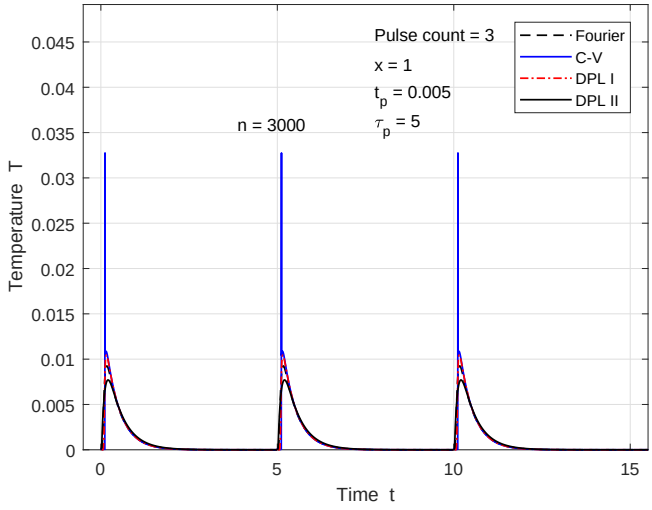

Figure 7.8: Temperature T at $x = 1$ showing 3 almost identical pulses. $\tau_q = 0.012665$; $\tau_T^I = 0.002868$ ($\delta^I = 0.2265$); $\tau_T^{II} = 0.037995$ ($\delta^{II} = 3$)

In Figure 7.9 we display the solutions for the first pulse only (observed at $x = 1$), in order to investigate the distinction between the different models in more detail. The DPL-I model predicts a pulse height higher than the Fourier model and the DPL-II model a pulse height lower than the Fourier model. The C-V model predicts a pulse more than three times the height of the DPL-I model. We also see that the DPL-II model predicts that the pulse arrives at $x = 1$ earlier, than for the Fourier model, and that the C-V model predicts the longest delay. To the right of the wave front, the C-V model coincides almost perfectly with the DPL-I model. After reaching their respective maximum temperatures, the model predictions coincide from $t \approx 0.4$. We can assume that from this time onwards, up to the start of the next pulse cycle, the transfer of heat in the specimen occurs by diffusion.

The maximum temperature values are relatively low at $x = 1$, *i.e.* $\sim 10^{-2}$. Compared to the boundary condition $T(0, t) = 1$, this implies an almost hundred-fold reduction in the temperature across the specimen. Analysing the numerical values in Figure 7.9, we see that the temperature pulse width predicted by the C-V model equals the original heat pulse width $t_p = 0.005$. At the same time, the other models predict a temporal pulse broadening up to about $t = 2.5$. This conservation of the pulse width and the sharp wave fronts, is in accordance with the theory of the C-V model [OT94] [Tzo97]. In

contrast to the C-V model, the pulse shapes predicted by the other models skew to the right.

Although not typically of interest in thermoreflectance, the large reduction in temperature across the specimen, prompts us to investigate the predicted temperature profiles in the interior of the specimen. Figure 7.10 shows the respective temperature profiles at $x = 0.2$. The maximum temperature values are approximately an order of magnitude higher than the values at $x = 1$. Calculating the temperature profiles at various x positions (results not shown here), shows that pulse width broadens with x (except for the C-V model), with a simultaneous decrease in pulse height. By comparing Figure 7.9 and Figure 7.10, we also notice that the pulse skewing increases with x.

Since the endpoint at $x = 1$ is insulated we expect that the thermal energy delivered at $x = 0$ by the pulsed source, will be conserved within the specimen, *i.e.* the area under the temporal profile will remain at a constant value. Following from our discussion in Section 6.9.1, the heat energy $\mathcal{E}$ delivered to (and therefore transferred through) the specimen by a single laser pulse is given by $\mathcal{E} = \int_0^{t_p} P_{peak}\, dt$, where P_{peak} is the laser peak power. Since we model the heat pulse as a temperature step function, we can say that $\int_0^{\tau_p} T(0,t)dt$ (with $T(0,t)$ defined in Eq. (7.3.1)) represents the amount of heat transferred into the specimen. With $t_p = 0.005$ in the present numerical example, we have $\int_0^{\tau_p} T(0,t)dt = \int_0^{t_p} T(0,t)\, dt = 0.005$. For the temperature profiles in Figures 7.9 and 7.10, the areas under the profile from $t = 0$ to $t = \tau_p = 5$ are calculated using numerical integration. Two observations are made: firstly, for a given x position, the areas for the respective models are equal at ≈ 0.005, and secondly, the area remains constant at a value of ≈ 0.005, irrespective of the x position.

The modal analysis summary in Section 7.3.3 provides an explanation for the pulse broadening and skewing of the pulse profile in the case of the C-V and DPL-I models. For the C-V model, from Equations (7.3.22), (7.3.23) and (7.3.27) (with $\gamma_k = \gamma$) the contribution to the series solution for $u_1(x,t)$ by the k-th mode is given by

$$\frac{2}{\nu_k} e^{-\gamma t} \left(\cos \omega_k^d t + \frac{\gamma}{\omega_k^d} \sin \omega_k^d t \right) \sin \nu_k x. \tag{7.5.1}$$

We consider only the underdamped modes since propagation speeds are not associated with overdamped modes. A standard trigonometric identity shows that

$$\cos \omega_k^d t \sin \nu_k x = \frac{1}{2} \left(\sin(\nu_k x + \omega_k^d t) + \sin(\nu_k x - \omega_k^d t) \right). \tag{7.5.2}$$

From standard wave theory, the function $\sin(\nu_k x - \omega_k^d t)$ represents a wave that is propagating to the right at a speed ω_k^d/ν_k and $\sin(\nu_k x + \omega_k^d t)$ a wave propagating to the left at the same speed. The product $\sin\omega_k^d t \sin\nu_k x$ can be expressed in a similar way. Therefore, for each of the underdamped modes of the C-V model, the propagation speed associated with the k-th mode is given by

$$\frac{\omega_k^d}{\nu_k} = c\sqrt{1-\frac{\gamma^2}{c^2\nu_k^2}} = c\sqrt{1-\frac{1}{4\alpha\tau_q\nu_k^2}} < c, \tag{7.5.3}$$

and

$$\frac{\omega_k^d}{\nu_k} \to c = \sqrt{\alpha/\tau_q} \text{ when } k \to \infty. \tag{7.5.4}$$

As the limit is approached from below, the wave front speed for the C-V model is given by $c = \sqrt{\alpha/\tau_q}$ as stated by [TZ98] and others. For the current parameter values only the first mode of the C-V model is overdamped, and the propagation speeds associated with the underdamped modes quickly approach c. Hardly any pulse broadening occurs as the individual contributions to the series solution from the underdamped modes are propagated at almost the same speed. All the underdamped modes are damped by the same factor $e^{-\gamma t}$ and the shape of the temperature pulse is also retained, but with a reduction in the height of the pulse.

For the DPL-I model the propagation speeds for the underdamped modes are given by

$$\frac{\omega_k^d}{\nu_k} = c\sqrt{1-\frac{\gamma_k^2}{c^2\nu_k^2}}. \tag{7.5.5}$$

In contrast to the C-V model, these propagation speeds for the underdamped modes differ widely and significant pulse broadening and changes to the shape of the pulse occur. Also keep in mind that for the DPL-I model the majority of the modes are overdamped, and for these modes no associated propagation speeds are available.

In the case of the Fourier model, where we have an infinite propagation speed for the thermal disturbance, a change in temperature at $x = 0$ is experienced simultaneously throughout the specimen. Initially the heat energy is concentrated close to the surface region, whereafter the energy is gradually distributed throughout the specimen, resulting in a broad temperature pulse that decreases with x. For the DPL-II model all the modes are overdamped, and there are no finite propagation speeds associated with the individual modal contributions to the series solution. This suggests that the pulse

broadening that occur for the DPL-II model can be explained in the same way as for the Fourier model.

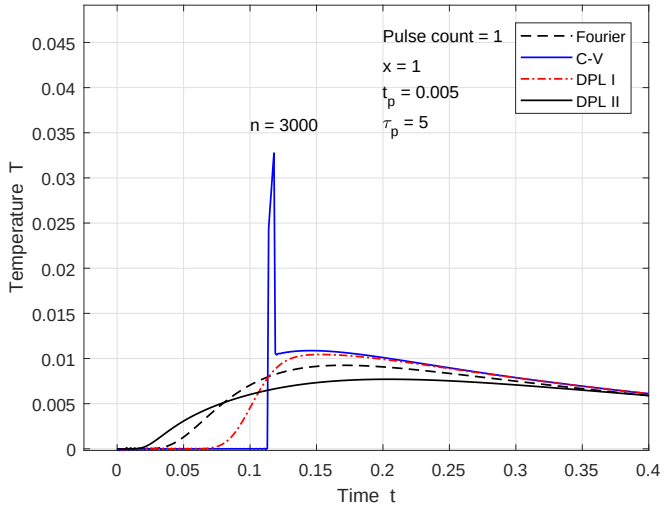

Figure 7.9: Temperature T at $x = 1$ displaying only the first pulse. $\tau_q = 0.012665$; $\tau_T^I = 0.002868$ ($\delta^I = 0.2265$); $\tau_T^{II} = 0.037995$ ($\delta^{II} = 3$)

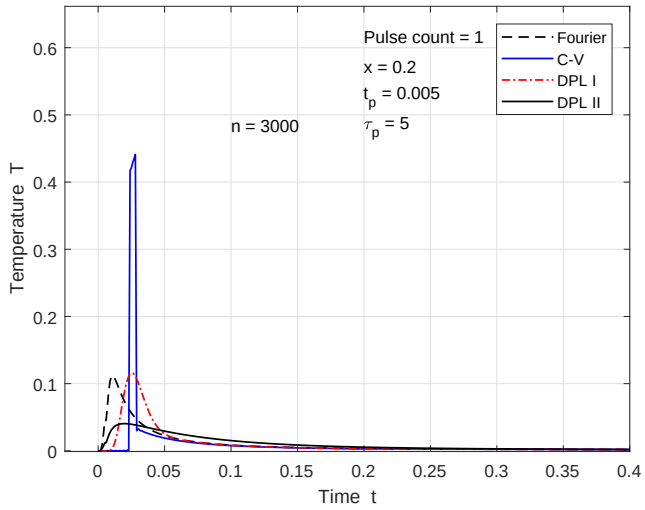

Figure 7.10: Temperature T at $x = 0.2$ displaying only the first pulse. $\tau_q = 0.012665$; $\tau_T^I = 0.002868$ ($\delta^I = 0.2265$); $\tau_T^{II} = 0.037995$ ($\delta^{II} = 3$)

It is well known that the C-V model predicts that when a heat pulse is incident at one boundary of a specimen, the wave front is reflected off the

opposite boundary ([CT82] [LC04] [OT94]). Since the DPL-I model, with $\tau_T \ll 1$, approaches the C-V model, we choose to examine both models to see if we can find evidence of wave front reflection – the Fourier model is included as a reference. Firstly, both the C-V and the DPL-I model predict reflected pulses. In Figure 7.11 the peak values of the reflected pulses at $x = 0.8$ are lower than that of the incoming pulses. At a fixed position closer to $x = 1$, the reflected pulses have higher peak values. In Figure 7.12, at $x = 1$, only one temperature pulse appears which is the superposition of the incoming and reflected pulses.

Secondly, the DPL-I model shows the same behaviour as the C-V model, with respect to its predicted pulse width. The pulse width remains constant and the peak height decreases with x. The reflected pulse widths of both models are the same as the incoming pulses. The peak heights for the DPL-I model are approximately equal to the heights of the sharp thermal wave fronts of the C-V model at $x = 0.8$ when they arrive at this position. The areas under the temperature profiles are calculated for $x = 0.2$, $x = 0.8$ and $x = 1$ (note that $\tau_T^I \ll 1$ for the DPL-I model in this case) and are found to remain at the same value of ≈ 0.005 as the areas determined for Figures 7.9 and 7.10. The area is again conserved, even though there is hardly any broadening of the pulse widths and the pulse shapes are retained. Noticeable reflected pulses are present and these contribute to the calculated area.

It is interesting to see that the wave front arrival times correspond to the times predicted by the theory. As discussed earlier, the dimensionless speed of the wave front is given by $c = \sqrt{\alpha/\tau_q}$. Using this equation, the predicted arrival time of the wave front at $x = 0.8$ is $t = 0.0903$, which corresponds well with the wave front arrival time in Figure 7.11 ($t = 0.092$). A similar calculation, assuming that the wave front has traveled a dimensionless distance of 1.2, shows that the reflected wave front is expected to arrive back at $x = 0.8$ at $t = 0.135$. Again this corresponds well with the value observed in Figure 7.11.

7.5.2 Effect of lag time ratios δ

In the following numerical experiments, we investigate how the value of δ influences the differences and similarities between the DPL, C-V and Fourier model predictions. Referring to Section 6.8, the range of possible values for δ is: $0 < \delta^I < 1$ and $\delta^{II} \geq 1$.

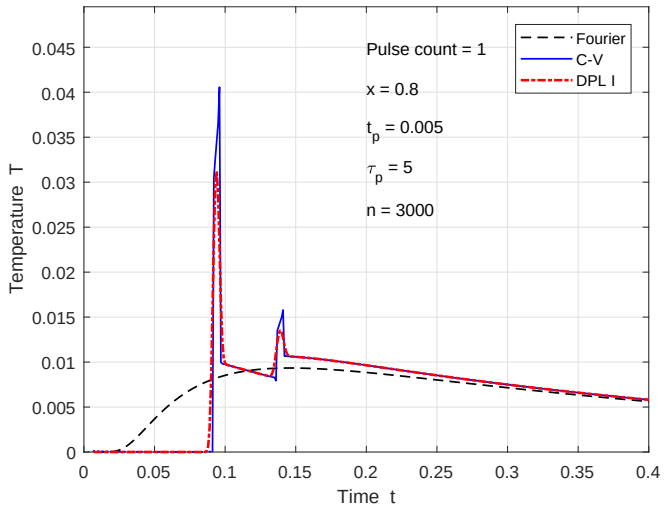

Figure 7.11: Temperature T at $x = 0.8$ displaying only the first pulse; including the C-V model.
$\tau_q = 0.012665$; $\tau_T^I = 0.000025$ ($\delta^I = 0.001974$)

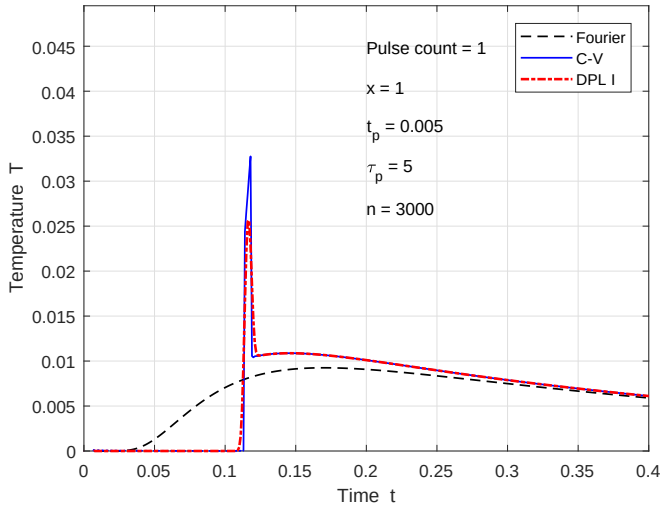

Figure 7.12: Temperature T at $x = 1$ displaying only the first pulse; including the C-V model.
$\tau_q = 0.012665$; $\tau_T^I = 0.000025$ ($\delta^I = 0.001974$)

Case $\delta^I \to 0$:

In the first experiment we investigate what happens when $\delta^I \to 0$. We do this

by either reducing τ_T^I and keeping τ_q fixed at the reference value, or increasing τ_q and keeping τ_T^I fixed at the reference value. The former case is already discussed in Section 7.5.1 (Figures 7.11 and 7.12). For $\tau_T^I = 0.000025$ (or $\delta^I = 0.001974$) the DPL-I temperature profiles at $x = 0.8$ and $x = 1$, have narrow smooth pulses with the pulse width equal to that of the C-V profile. This resemblance is expected as $\tau_T^I << 1$.

Increasing τ_q by a factor 4 to 0.05066 whilst keeping $\tau_T^I = 0.002868$, we have $\delta^I = 0.0566$. We compare the DPL-I profile with the Fourier profile (looking at the insert in Figure 7.13), and at the same compare this result with Figure 7.10, where $\delta^I = 0.2265$. In Figure 7.10 the Fourier and DPL-I temperature peaks are almost the same and the DPL-I profile starts to increase shortly after the Fourier profile. In the case of Figure 7.13 the DPL-I temperature peak is more than double the Fourier peak, and the delay before the temperature increase starts, is longer. With Figures 12 and 13 showing that the DPL-I model (with $\delta^i = 0.001974$) approaches the C-V model, the indication is that the DPL-I model in this case, with $\delta^I = 0.0566$, is approaching the C-V model. This suggests that the DPL-I model shows C-V behaviour not only when $\tau_T^I \ll 1$ but also when $\delta^I \ll 1$ ($\delta^I \to 0$).

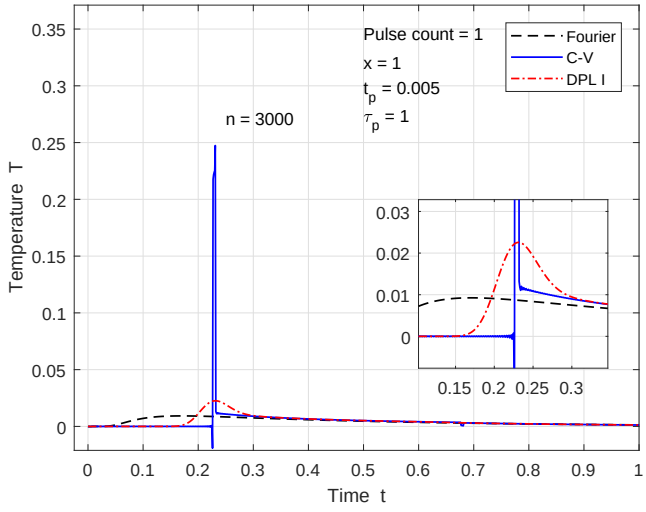

Figure 7.13: Temperature T at $x = 1$, displaying only the first pulse. $\tau_q = 0.05066$; $\tau_T^I = 0.002868$ ($\delta^I = 0.0566$)

Case $\delta^I \to 1$:

The second experiment investigates the case when $\delta^I \to 1$. We first use $\tau_T^I = 0.002868$ and decrease τ_q by a factor of 4 to 0.00316625 (Figure 7.14 – profile 'DPL I'), and then fix τ_q at the reference value of 0.012665 and increase τ_T^I by a factor of 4 to 0.011472 (Figure 7.14 – profile 'DPL I a'). We find that $\delta^I = 0.906$. In the 'DPL I' case, the DPL-I temperature profile coincides almost perfectly with the Fourier profile. This is ascribed to the fact that the lag times are relatively small (almost negligible), ensuring an almost perfect match between the DPL-I and Fourier models. Due to the substantially longer lag times, compared to the 'DPL I' case, the 'DPL I a' temperature profile is shifted slightly to the right of the Fourier profile, even though δ^I is the same for both 'DPL I' and 'DPl I a' cases.

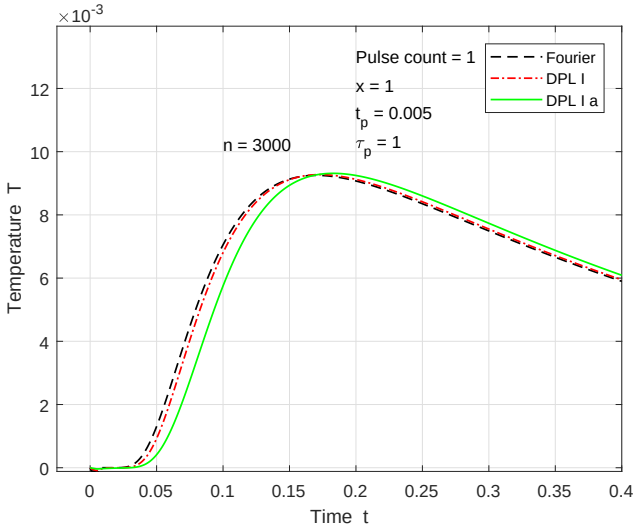

Figure 7.14: Temperature T at $x = 1$, displaying only the first pulse. $\tau_q = 0.00316625$; $\tau_T^I = 0.002868$ ($\delta^I = 0.906$)

Case $\delta^{II} = 1$:

The third experiment's aim is to study how the DPL-II model predictions compare with the Fourier model. We start by decreasing τ_T^{II} to 0.012665, with τ_q fixed at the reference value, (*i.e.* $\delta^{II} = 1$). The result is that the DPL-II temperature profile closely follows the Fourier profile, although lagging slightly behind the Fourier profile (Figure 7.15 – profile 'DPL II'). This result is in agreement with Tzou's prediction that the Fourier and DPL models correspond when $\delta^{II} = 1$ (see Section 2.5.2). Next, we increase τ_q to 0.037995, with τ_T^{II} fixed at the reference value, (*i.e.* $\delta^{II} = 1$). The result is

that the lag between the DPL-II temperature profile and the Fourier profile increases, with the peak temperature also reducing (Figure 7.15 – profile 'DPL II a').

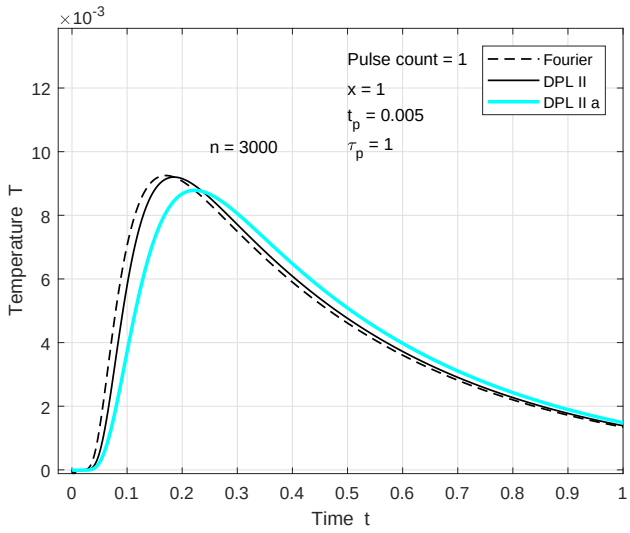

Figure 7.15: Temperature T at $x = 1$ displaying only the first pulse. $\delta^{II} = 1$

Case $\delta^{II} > 1$:

We already have an example of the effect when $\delta^{II} > 1$ (Figure 7.9 illustrates the case where $\delta^{II} = 3$). We explore here what happens if we increase δ^{II} even further. We start by increasing τ_T^{II} by a factor of 2 to 0.07599, with τ_q fixed at the reference value, (*i.e.* $\delta^{II} = 6$). The DPL-II temperature peak is considerably lower than the Fourier model's peak and the temperature rise starts earlier (Figure 7.16 – plot 'DPL II'). Decreasing τ_q by a factor of 2 to 0.0063325, with τ_T^{II} fixed at the reference value, (*i.e.* $\delta^{II} = 6$), we find that the peak temperature value increases, although still lower than the Fourier peak temperature (Figure 7.16 – plot 'DPL II a').

In summary, we conclude that if δ^I is close to 0, the DPL-I model shows a sharp thermal wave front similar to the C-V model. If δ^I is close to 1, then the DPL-I model predictions are close to the Fourier model, although the relative magnitudes of the lag times should also be considered. Similarly, if δ^{II} is close to 1, then the DPL-II model predictions are close to the Fourier model. In general, we see that if $\delta < 1$, the temperature rise starts later and the lower the δ value is, the higher the peak temperature values. In contrast, if $\delta > 1$, the temperature rise starts at an earlier stage and the higher the δ

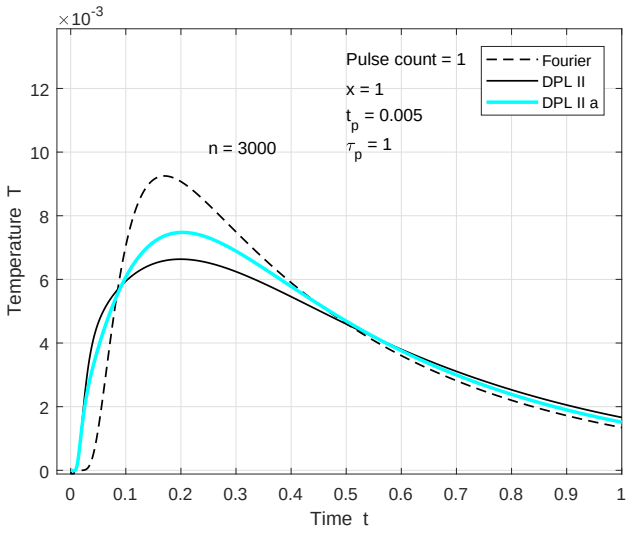

Figure 7.16: Temperature T at $x = 1$ displaying only the first pulse. $\delta^{II} = 6$

value, the lower the predicted temperature peak values become. In all cases the DPL, C-V and Fourier models predict the same temperature values, after a sufficiently long time.

7.6 Bio-heating case study: high duty ratio r_d

In this section we use experimental and specimen parameters applicable to bio-heating [MYSY21]. The example is a blood specimen, with thickness $d = 2$ mm and thermal diffusivity $\alpha = 5.881 \times 10^{-8}$ m^{2}s^{-1}. With no preference for either the diffusion time t_d or the half-time $t_{1/2}$ found in literature, we choose the half-time $t_{1/2}$ to be the scaling parameter, since we prefer a scaling factor closest to the typical pulse widths used in our numerical experiments ([BTY11] [PJBA61]). Then $t_0 = 0.1388d^2/\alpha \approx 10$ s. A typical heating pulse width is $t_p = 0.5$ s and the duty ratio $r_d = 0.5$, implying that $\tau_p = 1$ s.

The dimensionless pulse width and pulse period are $t_p = 0.05$ and $\tau_p = 0.1$ respectively, and the dimensionless thermal diffusivity is $\alpha = 0.1388$. Our first aim is to find lag times that, during an initial time interval, yield distinct differences between the temperature profiles predicted by the respective models. Again, this is done following the guidelines in Sections 6.3 and 6.7 on how to determine appropriate lag times. We find $\tau_q = 0.024333$,

$\tau_T^I = 0.017395$ and $\tau_T^{II} = 0.072999$. The lag time ratios are $\delta^I = 0.72$ and $\delta^{II} = 3.0$.

In bio-heat applications one is generally interested in the temperature at the incident surface as well as in the interior of the specimen. We also notice that the duty ratio in this case has roughly the same magnitude as that used in Section 7.4. An investigation of the temporal profiles will therefore lead to the same results as in Section 7.4, *i.e.* the C-V model is characterised by a sharp wave front; the instants at which the temperature starts to rise, as predicted by the different models, follow the same sequence (Fourier first, then DPL-II, DPL-I and lastly C-V); the peak temperature increases with each consecutive pulse; and the peak temperatures predicted by each model, differs.

As an example, In Figure 7.17, we show the temporal temperature profiles at $x = 0.5$ for a 7-pulse case. Except for the C-V model, almost complete merging of the individual pulses have occurred. On the insert the 7 wave fronts for the C-V model are visible. The DPL-II model predicts the lowest temperature, the DPL-I and Fourier, an equal and slightly higher temperature, with the C-V model the highest temperature. Apart from the slight peak difference, the models predict the same profile over the time span of the merged pulse. When compared to the temperature profiles in Figure 7.3, in this case the merging of pulses resulting from pulse broadening is more advanced.

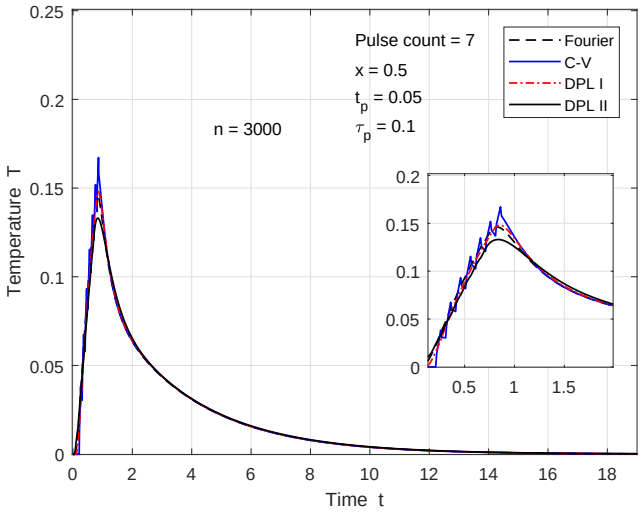

Figure 7.17: Temperature T at $x = 0.5$ for a 7-pulse problem

We also know from Section 7.4 that the temperature reaches a plateau level after a sufficient number of pulses, and that the pulses merge at some point in the interior of the specimen. These observations follow from the temporal profiles at fixed x points in Section 7.4. We now turn to spatial temperature distributions at fixed times t.

We ascribe the temperature increase per pulse to the fact that, due to the high duty ratio ($r_d = 0.075/0.15 = 0.5$), the temperature at a given x position does not return to its original zero level before the next pulse is incident at $x = 0$. This suggests that on the spatial temperature profiles more than one pulse will be visible at a fixed time t. In Figure 7.18 we use a three-pulse example, with $t_p = 0.05$ and $\tau_p = 0.1$, to evaluate the spatial temperature distribution at $t_{ev} = 0.199$ (t_{ev} indicates the evaluation time), just before the third pulse starts (*i.e.* during a "pulse OFF" event). We immediately notice that all the models, except the C-V model, predict single, merged pulses. The C-V model predicts two separate pulses, indicated by the sharp wave fronts. For the DPL-I and DPL-II temperature distributions the sharp rises close to $x = 0$ is noticeable. This is due to the delays τ_T^I and τ_T^{II} in forming temperature gradients. As $\tau_T^I < \tau_T^{II}$ the DPL-I model has a shorter delay and more quickly adjusts to the zero temperature at $x = 0$ after the start of the "pulse OFF" event. Ignoring the C-V profile's wave front, the models agree from about $x = 0.4$ onwards.

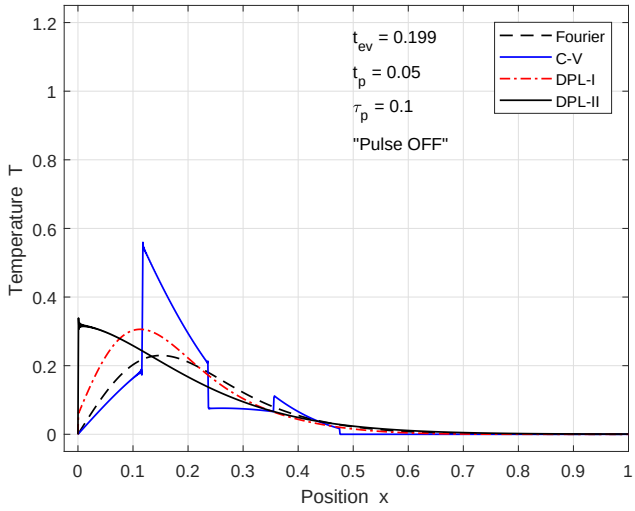

Figure 7.18: Spatial temperature distribution at $t_{ev} = 0.199$

At $t_{ev} = 0.205$ ("pulse ON" event) we see how the third pulse deposits heat energy into the specimen close to $x = 0$ (Figure 7.19). The temperature

disturbance due to the first two pulses are present as a single merged peak for both the Fourier and DPL-I model, whilst the DPL-II temperature profile smoothly decreases from $x = 0$ to the interior of the specimen. The C-V model maintains distinct wave fronts, and Gibbs oscillations occur near $x = 0$.

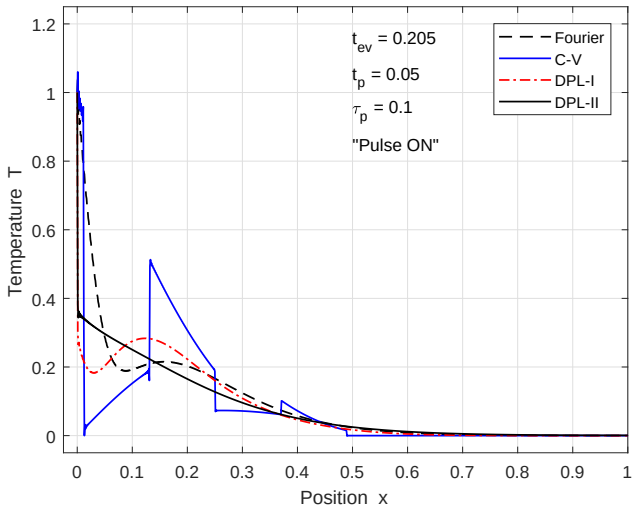

Figure 7.19: Spatial temperature distribution at $t_{ev} = 0.205$

We next investigate the effect of a large number of pulses on the spatial distribution of the temperature in the specimen. We study a 50-pulse example, using the same pulse parameters and lag times as for Figure 7.18. Figure 7.20 gives the result just before the 50th pulse starts, and Figure 7.21 just after. Increasing the number of pulses leads to a more uniform temperature distribution throughout the specimen, except for the region up to $x \approx 0.3$ where the different models predict different distributions.

We are also interested in the effect of reducing the duty ratio r_d. We reduce r_d by either reducing the pulse width t_p whilst maintaining the pulse period at $\tau_p = 0.1$, or maintaining t_p whilst increasing τ_p. We first reduce the duty ratio from $r_d = 0.5$ by a factor of 2 to 0.25, by choosing $t_p = 0.025$ and $\tau_p = 0.1$. We see that the temperature level in the second half of the specimen reduces by the same factor of 2 from $T \approx 0.4$ (Figure 7.22) to $T \approx 0.2$ (Figure 7.23). In Figure 7.24 we maintain $t_p = 0.05$ and increase τ_p by a factor of 2 to 0.2, with r_d remaining at 0.25. The temperature level in the second half of the specimen increases to $T \approx 0.24$. On the C-V profile only one wave front is visible as opposed to the two wave fronts in Figure 7.23. From these results we deduce that there does not

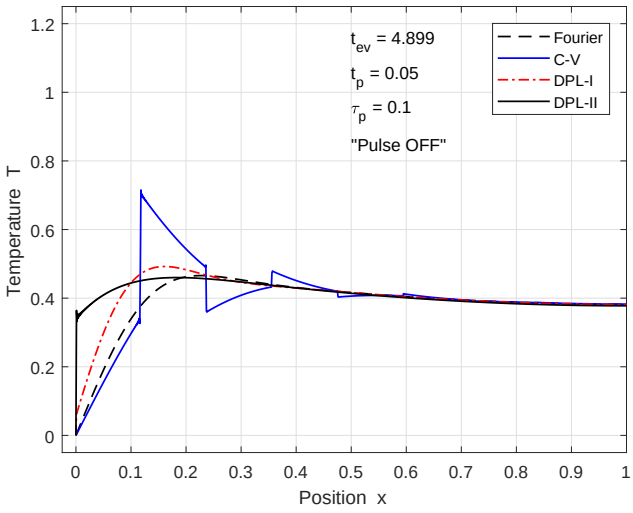

Figure 7.20: Spatial temperature distribution at $t = 4.899$; before pulse 50 starts; $r_d = 0.5$.

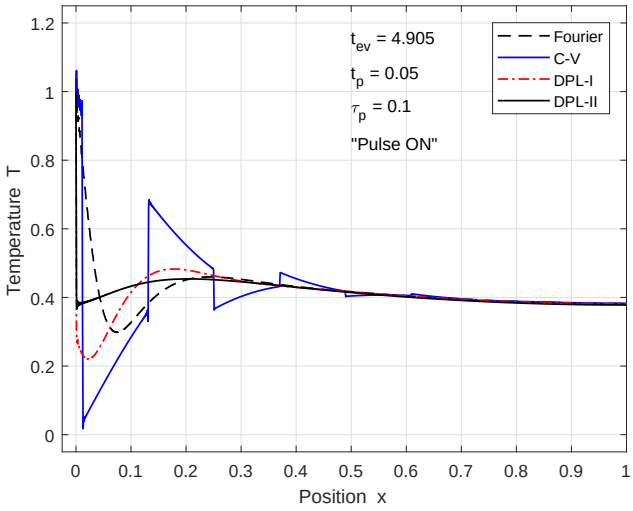

Figure 7.21: Spatial temperature distribution at $t = 4.905$; after pulse 50 starts; $r_d = 0.5$.

necessarily exist a direct relation between the factor by which the duty ratio r_d is reduced and the corresponding reduction in the temperature level. The two examples we give here, has the same duty ratio, but the pulse width t_p differs, resulting in different temperature levels.

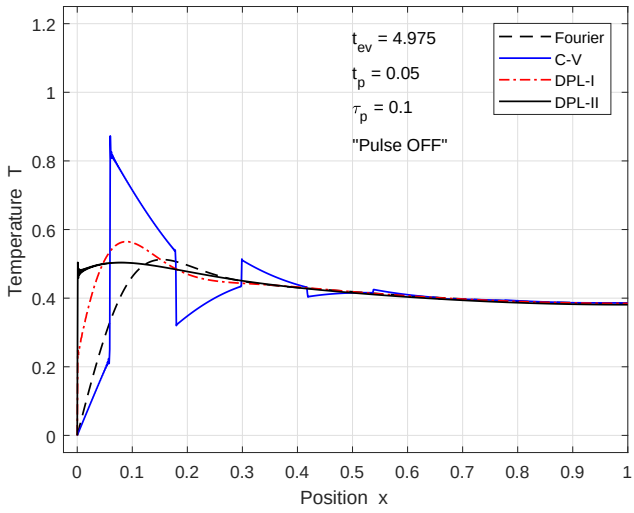

Figure 7.22: Spatial temperature distribution at $t = 4.975$, after pulse 50 stops; $r_d = 0.5$.

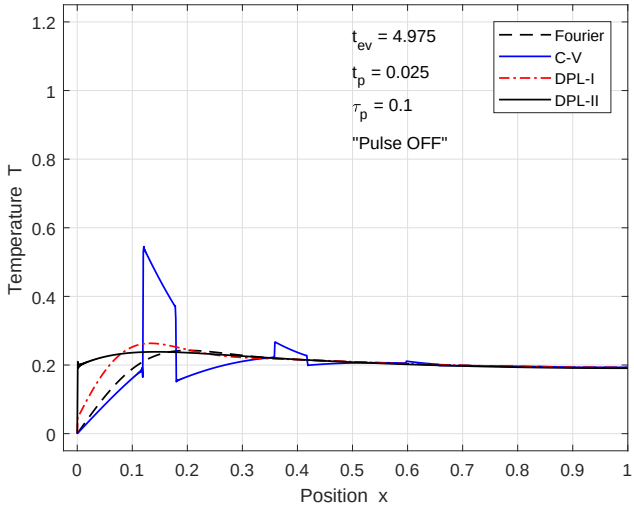

Figure 7.23: Spatial temperature distribution at $t = 4.975$; $r_d = 0.25$.

7.7 Conclusion

Heat transfer behaviour in a specimen subject to multiple heat pulses is investigated, for the Fourier, Cattaneo-Vernotte and dual phase lag models respectively. One dimensional models are used, and as is commonly done,

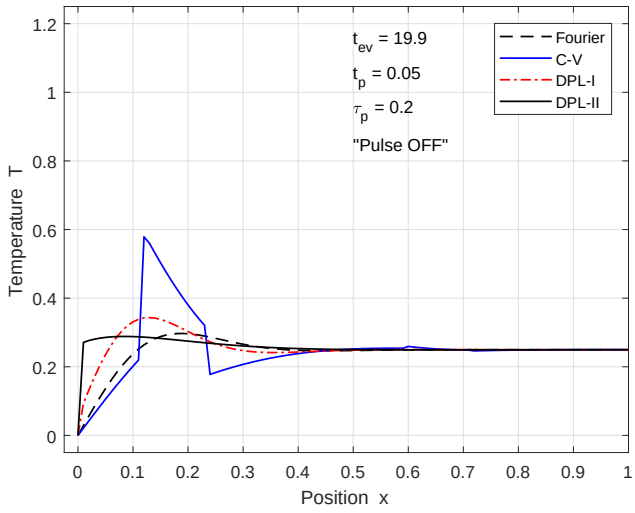

Figure 7.24: Spatial temperature distribution at $t = 9.95$; τ_p increased; $r_d = 0.25$.

the effect of the heat pulses is modelled as a temperature step function at the one endpoint. To solve the multi-pulse problem, a series of single-pulse problems is considered where the final temperature distribution for a given pulse cycle, provides the initial temperature for the subsequent pulse cycle. We successfully adapt the separation of variables procedure in Section 6.9 for calculating the modal series solution for a single-pulse problem to solve the multi-pulse problem. In addition, the solution for the multi-pulse problem is expressed in terms of the solution of a homogenised problem associated with the single-pulse problem. Using the truncated modal series as an approximate solution proved to be an effective method for a numerical investigation into the properties of the solutions of multi-pulse problems. Both temporal temperature profiles (temperature versus time at a fixed position) and spatial profiles (temperature versus position at a fixed time) are readily available.

The aim of the numerical experiments is two-fold: to compare the temperature predictions by the Fourier, C-V and DPL models, and to identify situations where the C-V and DPL temperature profiles differ significantly from those of the Fourier model. The numerical simulations cover a wide range of physical parameters. Two experimental techniques where pulsed heating is used, thermoreflectance and bio-heating, provide realistic physical parameters for the heat pulses. These values are used for designing numerical experiments that cover a wide range of physical scenarios. Values for the phase lags in the C-V and DPL models are harder to find, and we use

the upper bounds given in Section 7.3.4 as guidelines. These upper bounds ensure that the temperature predictions for the C-V and DPL models approach those of the Fourier model after some time, as in many heat transfer situations the Fourier model provides acceptable results after a sufficiently long time.

As a first step, the parameter values are chosen as for the single-pulse problem in Section 6.10, and the temperature profiles are compared with the multi-pulse case. There are obvious similarities between the single-pulse and multi-pulse cases, but we observe two interesting phenomena for the multi-pulse case, namely the merging of temperature pulses when observed at fixed points deeper into the specimen, and when increasing the duty ratio, and/or the number of pulses, a plateau value is established in the specimen for the peak temperatures.

For simulations associated with thermoreflectance experiments we use the diffusion time t_d as the time scaling factor, as this is a well-known concept in the field. In this case the duty ratio of the laser pulses is low and the temporal temperature profiles at the insulated endpoint of the specimen is of main interest. Key findings for these simulations are that distinct pulses persist in the temperature profiles throughout the specimen, even though a broadening of the pulses occur towards the insulated eindpoint. Reflected temperature waves are observed in some of the temperature profiles of the C-V model, as well as in some of those of the DPL model.

For bio-heat applications the duty ratio is high and the spatial temperature profiles are of interest. In this case we use the half-time $t_{1/2}$ as the time scaling factor. Key findings for these simulations are the noticeable merging of pulses, leading to a uniform spatial temperature distribution, as well as the clear effect of the time lag in the temperature gradient at the onset and termination of each pulse. Although numerical calculations were performed for example problems including up to 50 pulses, the computational time never exeeded one minute.

The truncated modal series solution proved to be an efficient procedure for investigating the properties of the multi-pulse heat transfer problems, and modal properties provide insight into the behaviour of the solutions.

Chapter 8

Conclusion and future research

8.1 Overview

The aim of our research was to study heat transfer in specimens subject to short-pulse heating. Literature studies showed that other models are proposed as alternatives to the Fourier model, which is considered to be inadequate in predicting the temperature in certain cases ([TZ98]). Our main interest is in the C-V ([OT94]) and DPL ([Tzo95a]) models, frequently suggested as alternatives to the Fourier model. We observed two interesting aspects during our literature study: the occurence of unwanted or spurious oscillations when approximating the C-V model using numerical techniques; and the lack of reliable values for the lag times τ, τ_q and τ_T that appear in the C-V and DPL models. We therefore focused our efforts on the comparison of the Fourier, C-V and DPL models, and determining the origin of the unwanted oscillations, with the intention of proposing a solution.

In Chapter 2 the derivation of the model equations is presented, including a summary of the characteristics of the Fourier, C-V and DPL models. The discussion of the DPL model is preceded by a section on the microscopic effects of heat transfer in metals and the derivation of the two-step heat transfer model, from which the DPL model follows. We discussed the heat absorption process in a specimen as it determined how we formulated the boundary conditions in our model problems. We derived the dimensionless versions of the heat conduction models, together with the boundary and initial conditions on which this study was based.

The issue of unwanted oscillations, related to the CT-benchmark problem (a special case of the C-V model), was investigated in Chapter 3. This problem

was originally formulated by Carey and Tsai in 1982 [CT82]. It was shown that the unwanted oscillations is the result of an ill-posed problem and not due to the choice of the numerical technique used to solve the problem. The CT-benchmark problem was re-formulated to a problem that has a smooth initial condition. The problem was divided into three auxiliary problems. D'Alembert's method was used to obtain exact solutions for the first two auxiliary problems, and the finite element method was used to obtain an approximate solution to the third auxiliary problem. A numerical algorithm was developed, resulting in a solution method that can successfully track the sharp wave front but without a discontinuity, *i.e.* free of oscillations.

In Chapter 4 we started off by introducing model problems for mechanical vibrations. The similarities with the hyperbolic-type heat conduction problems (*i.e.* the C-V and DPL models) were pointed out, and the terminology, *e.g.* overdamped and underdamped modes, were adopted for use with the heat conduction problems. General abstract formulations were developed for the Fourier, C-V and DPL models. Following this, variational forms were derived and expressed in terms of defined bilinear forms. Ultimately, weak variational forms of these models were derived to apply existence theory to the C-V and DPL models.

In Chapter 5 we applied the modal analysis method to the general second order hyperbolic equation expressed in variational form. Substitution of a trial solution into this abstract equation led to an eigenvalue problem. With the requirement that the eigenvectors form an orthogonal sequence, a formal series solution was derived. In order to apply the model formulations derived in Chapter 4 to subsequent chapters, the formulations were adapted to include the physical parameters that appear in the heat conduction models. The convergence of the series solution was expressed in terms of the energy norm $\|.\|_V$ and inertia norm $\|.\|_W$. It was found that the partial sum $u_N(t)$ converges to the solution $u(t)$ in the energy norm and $u'_N(t)$ to the derivative $u'(t)$ in the inertia norm, for all $t > 0$. Therefore, the accuracy of these approximations relies on the accuracy of the partial sum approximations at time $t = 0$.

Chapter 6 is devoted to a comparison between the Fourier, C-V and DPL heat conduction models. Two important aspects had to be dealt with before starting with the comparison: deciding on the initial value for the numerical experiments, and determining realistic values for the lag times used in the numerical experiments.

Series solutions were derived for the model problems based on the C-V, DPL and Fourier models in Section 6.2. We proposed a smooth temperature distri-

bution function to approximate the initial value. It is however not practical to calculate the Fourier coefficients for this initial value and we therefore opted to use the simpler, discontinuous initial condition. In order to ensure that the accuracy achieved when using this discontinuous initial value is acceptable, error estimates in the energy and inertia norms were calculated and used as a guideline to decide on the number of terms required in the series approximation.

To determine realistic lag times for our numerical experiments, we relied on the premise that, given a sufficiently long time has elapsed, the model predictions from the C-V and Fourier models will correspond. For $\tau_q \ll 1$, this means that for the first mode, the respective time dependent functions for the C-V model will be equal to that of the Fourier model after a sufficiently long time. To determine $\tau_{_T}$ we further assumed that $\tau_{_T} \ll 1$, ensuring that the DPL model approaches the Fourier model (refer to Section 6.7). We derived upper bounds for the lag times τ_q and $\tau_{_T}$, given by

$$\tau_q \leq \frac{\varepsilon}{\alpha\pi^2} \text{ and } \tau_{_T} \leq \frac{4\varepsilon}{\alpha\pi^2},$$

with ε a user specified accuracy and α the dimensionless thermal diffusivity. The transformation of α to the dimensionless value is done using a reference time t_0, which can be adjusted to represent the time scales characteristic of the physical scenario being investigated. Adjusting t_0, scales α and consequently τ_q and $\tau_{_T}$ to achieve a range of values for the lag times that are realistic for a given numerical experiment.

In Section 6.4 we introduced the concept of a *wane time* t_w as the time instant at which the wave front, characteristic of the C-V model, disappears. We predicted that the solutions for the Fourier and C-V models will be the same at the time that the wave front disappears. An expression was derived for the wane time, $t_w = -2\tau_q \ln(\sigma)$, where σ is equal to the ratio of the reduced wave front height at $t = t_w$, to the original height at $t = 0$.

The comparison between the Fourier, C-V and DPL models for the continuous heating model problem started off by testing our assumption that the respective model predictions will agree after a sufficiently long time has elapsed, *i.e.* at $t \approx t_w$. Additional numerical experiments were performed to study the respective contributions of the overdamped versus underdamped modes to the predicted temperature profiles, and especially how it affects the wave front present in the C-V model. The DPL-I model's dependency on the over- and underdamped modes to achieve accurate temperature predictions, was investigated. Also of interest was the behaviour of the DPL models close to $x = 0$, in view of the discontinuity that exists at $x = 0$.

The approach to solving the single-pulse model problem was to divide the problem into two sub-problems corresponding to the different boundary conditions at $x = 0$ (refer to Section 6.9.1). We referred to the sub-problems as "Problem 1" and "Problem 2" respectively. The solution derived for the continuous heating model problem was used to solve Problem 1, *i.e.* when the pulse is applied. To solve Problem 2 (when the pulse is stopped), the end temperature distribution for Problem 1 is assigned as the initial temperature distribution for Problem 2, continuing with the solution for Problem 1 to obtain the solution for Problem 2. The model comparison mainly focused on how each model behaves close to $x = 0$, how the peak temperatures compare, and how the heat pulse propagates into the specimen. Interesting observations were made regarding the resemblance between the DPL-I model and the C-V model when $\tau_{_T} \ll 1$, and the behaviour of the respective models when the pulse is stopped.

In Chapter 7 we considered the multi-pulse model problem. It is similar to the single-pulse problem, except that the multiple of m identical heat pulses is modelled as a periodic step function consisting of m steps. The model problem was divided into $2 \times m$ sub-problems, where the end temperature distribution for a given sub-problem becomes the initial distribution for a subsequent sub-problem. The solution to the multi-pulse problem with m pulse cycles is given by a sequence of functions

$$T_n(x,t) = 1 - u_1(x, t - t_{n-1}) + T_{n-1}(x,t) \quad (t_{n-1} \leq t < t_n)$$

$$T_{n+1}(x,t) = T_n(x,t) + u_1(x, t - t_n) - 1 \quad (t_n \leq t < t_{n+1})$$

for $n = 1, 3, 5, \ldots, 2m - 1$. This solution is made possible since continuity allows linking of the solutions of the sub-problems. The focus of the model comparison was to examine the effect of the duty ratio r_d and the number of pulses m on the predicted temperature profiles. Numerical experiments were performed using parameter values typical of thermoreflectance and bio-heating applications.

8.2 Key results

It was shown that the unwanted oscillations related to the CT-benchmark problem, as formulated by Carey and Tsai in 1982, is the result of an ill-posed problem and not due to the choice of the numerical technique used to solve the problem. The CT-benchmark problem was re-formulated to have a smooth initial condition, and divided into auxiliary problems that were solved using D'Alembert's and the finite element method. The solution method is able to track the wavefront without a discontinuity, ensuring oscillation-free results.

The theory and terminology of vibration analysis were incorporated into the heat conduction models. Weak variational formulations of these models (in terms of bilinear forms) were presented and the well-posedness of the DPL and C-V model problems was established, based on a general existence result by Van Rensburg and Van der Merwe in 2002.

The modal analysis method was applied to the general second order hyperbolic equation and the formal series solution of the heat conduction problems were derived. Convergence of the series solution was proved in terms of the energy and inertia norms. An important conclusion was that the accuracy of the partial sum approximations of the series solutions, relies on the accuracy of the partial sum approximations at time $t = 0$.

The comparison between the Fourier, C-V and DPL heat conduction models started with the task of deciding on a suitable initial condition. The discontinuous initial condition was preferred above a smooth temperature distribution function since it simplifies the calculation of the Fourier coefficients. Expressions were derived for the energy and inertia norm errors and were used as a guideline to determine the number of terms required for the calculation of the partial sums of the series solutions. This ensured accurate approximations for the solutions of the model problems, even though the discontinuous initial condition was used.

In order to perform numerical experiments with realistic lag time values, upper bounds for the lag times τ_q and τ_T were derived using modal analysis. The derivation relied on the assumption that the solutions for the C-V and Fourier models will be the same after a sufficiently long time. The lag times can be scaled using the expressions for the upper bounds, to represent the physical scenario of interest.

We introduced the concept of a *wane time* t_w as the time instant at which the wave front disappears, and predicted that the Fourier and C-V models will correspond at $t = t_w$. The comparison based on the continuous heating model

problem, proved that t_w is a reliable way to quantify the time required for the Fourier model and the C-V and DPL models to correspond. Regarding the respective contributions from the overdamped and underdamped modes, it was found that it is essential to initially include the underdamped modes of the C-V model since these modes capture the wave front. The DPL-I model requires both over- and underdamped modes to achieve accurate temperature predictions. Numerical experimentation showed that the DPL-II model does not resolve the discontinuity at $x = 0$ caused by the discontinuous initial value.

The solution strategy for the single-pulse problem was to divide the problem into two sub-problems, and assign the end temperature distribution for the first sub-problem, as the initial temperature distribution for the second sub-problem. The solutions for the sub-problems, linking the solutions in the end. We highlight two interesting observations. If $\tau_{_T} \ll 1$, the DPL-I model resembles the C-V model, predicting a prominent wavefront, but with a smooth profile. When the pulse is stopped, the Fourier model predicts a sudden drop in temperature, whilst the other models further increase in temperature before experiencing a sharp drop in the C-V model case, and a gradual drop in the DPL case.

The solution strategy for the multi-pulse problem was similar to the single-pulse problem in that the identical heat pulses were modelled as a sequence of sub-problems, with the solution expressed as a corresponding sequence of functions. With a low duty ratio r_d (*e.g.* in the thermoreflectance application) we observed distinct temperature pulses in the temperature profiles throughout the specimen, although a broadening of the pulses occur towards the insulated eindpoint at $x = 1$ for the Fourier and DPL models. In the case of the C-V model the pulse width remained constant. For a high duty ratio r_d (*e.g.* bio-heat application) the temperature pulses merge in the interior of the specimen, and increasing the number of pulses at the same time, result in a temperature plateau being established in the interior of the specimen.

In conclusion, modal analysis proved to be successfull in determining reliable dimensionless values for the lag times τ_q and $\tau_{_T}$, and was effective for the numerical investigations into the properties of the solutions of our model problems.

8.3 Future research

8.3.1 Background

In Chapters 6 and 7 we compared the Fourier, C-V and DPL heat conduction models using simplified model problems as test cases. The simplifications involved restricting ourselves to one-dimensional versions of these models, and the assumption that all the heat is absorbed instantaneously at the boundary $x = 0$. Both simplifications are justified: one-dimensional models are accepted in the thermophysical metrology community when determining the thermal diffusivity α, and the heat absorption model is one that was regarded as sufficient by Tzou ([Tzo97]), and Baumeister and Hamill ([BH69]) to study the lagging and wave behaviour of the DPL and C-V models respectively. Our model problems, together with the use of modal analysis, proved to be effective in gaining insight into the characteristics of the heat conduction models. In addition we also determined reliable values for the lag times τ_q and τ_T using modal analysis.

In Chapter 2 we discussed instances where researchers criticised each others experimental methodologies and approach in analysing the measurement results ([OA12]). In some cases researchers performed similar experiments, with some claiming they observed hyperbolic effects, whilst others claimed that the Fourier model is valid. Maillet ([Mai19]) also stated that proper experimental design is essential when comparing models and attempting to derive heat transfer parameters from the results.

Our suggestions for future research are aimed at addressing two aspects in heat transfer research:

1. Formulating realistic model problems that resemble properly designed measurement setups, thereby facilitating comparison with reliable experimental techniques.

2. Identifying suitable mathematical techniques to solve these model problems. In addition this requires that reliable values for model parameters (*e.g* lag times) are determined, and that model problems are well-posed and convergence of solutions proved.

In our opinion the experimental methodology applied by the thermophysical metrology community can be regarded as *state-of-the-art* with respect to the measurement of thermophysical parameters and have the potential to serve as a reliable validation of theoretical model predictions. We motivate

this as follows: the thermal diffusivity α is an important heat transfer parameter used in engineering applications, and having accurately measured values is therefore important. The expectation of scientists and engineers using thermophysical properties (*e.g.* α) in thermal modelling and design, is that these are reliably known and traceable to the International System of Units (SI), published by the *Bureau International des Poids et Mesures* (BIPM). The responsibility of coordinating international efforts to ensure reliable measurements of thermophysical properties of materials is assigned to the various working groups within the Consultative Committee for Thermometry (CCT), operating within the BIPM ([Bab10]).

We briefly introduced the two *standardized* methods used to measure α in Section 7.2: the laser flash method for measuring α in bulk specimens, and the thermoreflectance methods (also known as the ultrafast laser flash methods) used to measure α in thin film type specimens ([BTY11]). Both techniques rely on heat transfer modeling to calculate the value of α from the measurement results. The laser flash method relies solely on the one-dimensional Fourier (diffusion) model to analyse the measurement data ([AHZCB13]). In the case of the thermoreflectance methods, the metrology community has been relying on the Fourier model for the data analysis for quite some time, but experimental evidence exists that shows that the Fourier model is not adequate in describing the heat transfer behaviour for the *femtosecond* thermoreflectance method ([BFI62] [Bro90] [NTYB11]).

Thermoreflectance has the potential to exhibit both Fourier and non-Fourier heat transfer behaviour and we therefore suggest that model problems should be based on the technique of thermoreflectance, as developed and approved by the thermophysical metrology community.

8.3.2 Research suggestions

We suggest a two-fold approach to formulate realistic model problems. Firstly, an accurate source model should be formulated, *e.g.* the laser pulse's temporal characteristics, as well as the spatial absorption by the specimen have to be described by this model. Secondly, alternatives to the linearized DPL heat conduction model should be considered. Motivation for alternative heat conduction models can be found with the attempts to explain the results obtained during femtosecond thermoreflectance measurements. Nakamura *et al* ([NTYB11]) reports that their experimental results during approximately the first 2 picoseconds are not explained by the Fourier model. They studied the model predictions from two other models, namely the two-temperature

model and the *non-thermal* model and the conclusion was that the non-thermal model best explained the results during the first 2 picoseconds. The non-thermal model takes into account ballistic transport effects, *i.e.* implying longer electron-thermalization times, up to approximately 700ps ([HMWM97] [Sin10] [SVAIF94]) – see Section 2.4.1. Therefore the electron-thermalization time can be longer than the laser pulse width. Using a source model that assumes instantaneous heat absorption is therefore not going to track the ballistic phase of the electrons, the laser's temporal behaviour, and the transition to a diffusive heat transfer condition.

Suggestions for alternative heat conduction models include, but are not limited to:

- Linearized DPL with source term
- Two-temperature model (TTM) – also known as parabolic-two-step model (PTS); with source term
- Hyperbolic-two-step model (HTS) – with source term
- Second-order DPL model – with source term

The choice of mathematical technique used to solve any of these models will be determined by the model equation itself as well as the requirement to prove convergence. At the same time it would be required that the models are well-posed. The requirement to determine reliable values for model parameters, remains.

We present an example model of a realistic source term $S(x,t)$ whereafter example model formulations, based on the above mentioned heat conduction models, will follow.

Source term $S(x,t)$

A model that describes both the temporal nature of a laser pulse, as well as the absorption profile in the specimen would be required. A typical laser pulse source $S(x,t)$ is modelled as follows ([QT93a] [TM94] [Tzo97])

$$S(x,t) = 0.94\left(\frac{1-R}{t_p\delta}\right)\exp\left[\left(-\frac{x}{\delta}\right) - 2.77\left(\frac{t}{t_p}\right)^2\right], \tag{8.3.1}$$

where R is the optical reflectivity, t_p is the laser pulse width and δ is the optical penetration depth of the laser.

To derive a specific model problem, $S(x,t)$ is included in the energy conservation equation

$$\rho c_p \partial_t T = -\partial_x q + S. \tag{8.3.2}$$

As shown in Chapter 2, the energy conservation equation is combined with the relevant constitutive equation. As an example we choose the linearized DPL constitutive equation,

$$q + \tau_q \, \partial_t q = -k \, \partial_x T + k \, \tau_T \partial_t (\partial_x T), \tag{8.3.3}$$

and arrive at the linearized DPL model equation, including a source

$$\partial_t^2 T + 2\gamma \partial_t T = c^2 \partial_x^2 T + c^2 \tau_T \partial_t \partial_x^2 T + \frac{c^2}{k} S + \frac{c^2}{k} \tau_q \, \partial_t S. \tag{8.3.4}$$

Linearized DPL model with source term

The dimensionless single-pulse model problem with a source term is given by

$$\begin{aligned} \partial_t^2 T + 2\gamma \, \partial_t T &= c^2 \, \partial_x^2 T + \tau_T c^2 \, \partial_t \partial_x^2 T + 2\gamma S + \partial_t S \qquad (8.3.5) \\ \partial_x T(0,t) &= 0 \\ \partial_x T(d,t) &= 0 \\ T(x,0) &= T_0 \\ \partial_t T(x,0) &= 0. \end{aligned}$$

The initial condition $T(x,0) = T_0$ assumes that heating starts from a stationary state. Since the typical heating period is very short it is assumed that the heat loss from the boundaries are negligible, therefore the boundaries are insulated. The initial conditions stem from the assumption that the specimen is at a constant temperature before the heating starts.

Two-temperature model with source term

The source term is included in the electron-energy equation

$$C_e \partial_t T_e = k \partial_x^2 T_e - G(T_e - T_\ell) + S. \tag{8.3.6}$$

From the three coupled equations, representing the two-temperature model, follows

$$\left(\frac{C_e C_\ell}{kG} \right) \partial_t^2 T + \left(\frac{C_e + C_\ell}{k} \right) \partial_t T = \partial_x^2 T + \left(\frac{C_\ell}{G} \right) \partial_t (\partial_x^2 T) + \frac{1}{k} S. \tag{8.3.7}$$

This equation (where $T = T_e = T_\ell$) governs either the lattice or the electron temperature.

Hyperbolic two-step (HTS) model with source term

So far, none of the models make provision for the electrons undergoing non-diffusive ballistic transport. This is a requirement to model femtosecond thermoreflectance measurements according to Nakamura *et al* ([NTYB11]). The hyperbolic two-step model fulfils this requirement by modifying the constitutive equation to have a form similar to that of the C-V model's constitutive equation

$$q = -k\,\partial_x T_e - \tau_{_F}\,\partial_t q, \tag{8.3.8}$$

where $\tau_{_F}$ is the thermalisation time of the electron gas [Dug16][Tzo95b], and $\tau_{_F}\,\partial_t q$ represents the thermalisation stage in the electron gas. Combining the coupled equations associated with the HTS model, including the source term as in Eq. (8.3.6) leads to

$$\begin{aligned} \tau_{_F}\left(\frac{C_e C_\ell}{kG}\right)\partial_t^3 T \;&+\; \left(\frac{\tau_F(C_e+C_\ell)}{k}+\frac{C_e C_\ell}{kG}\right)\partial_t^2 T + \left(\frac{C_e+C_\ell}{k}\right)\partial_t T \\ &= \partial_x^2 T + \left(\frac{C_\ell}{G}\right)\partial_t(\partial_x^2 T) + \frac{1}{k}\left(S+\tau_{_F}\partial_t S\right). \end{aligned} \tag{8.3.9}$$

Second-order DPL model with source term

Tzou proposed a second-order DPL model, that according to him, correlates with the HTS model. This variation of the DPL model is based on the first-order effect in $\tau_{_T}$ and the second-order effect in τ_q, so that the DPL constitutive equation becomes

$$q + \tau_q\,\partial_t q + \frac{\tau_q^2}{2}\,\partial_t^2 q = -k\left[\partial_x T + \tau_{_T}\partial_t\left(\partial_x T\right)\right]. \tag{8.3.10}$$

Combining this constitutive equation with the energy equation, Eq. (8.3.2), yields the second-order DPL model equation

$$\begin{aligned} \frac{\tau_q^2}{2\alpha}\partial_t^3 T \;&+\; \frac{\tau_q}{\alpha}\partial_t^2 T + \frac{1}{\alpha}\partial_t T \\ &= \partial_x^2 T + \tau_{_T}\partial_t(\partial_x^2 T) + \frac{1}{k}\left(S + \tau_q\partial_t S + \frac{\tau_q^2}{2}\partial_t^2 S\right). \end{aligned} \tag{8.3.11}$$

The model is therefore characterised by the addition of a third-order term describing the transient temperature response. The intention with second-order DPL model is to account for non-diffusive ballistic heat transfer in an electron gas.

Bibliography

[AA15] H. Askarizadeh, H. Ahmadikia, Analytical study on the transient heating of a two-dimensional skin tissue using parabolic and hyperobolic bioheat transfer equations, *Appl. Math. Modelling* **39** (2015), 3704-3720.

[AHZCB13] M. Akoshima, B. Hay, J. Zhang, L. Chapman, T. Baba, International Comparison on Thermal-Diffusivity Measurements for Iron and Isotropic Graphite Using the Laser Flash Method in CCT-WG9, *Int. Jnl. Thermophys* **34** (2013), 763-777.

[AKP74] S. I. Anisimov, B. L. Kapeliovich, T. L. Perel'man, Electron emission from metal surfaces exposed to ultr-short laser pulses, *Sov. Phys. - JETP* **39**, (1974), 375-377.

[Bab10] T. Baba, Measurements and data of thermophysical properties traceable to a metrological standard, *Metrologia* **47** (2010), S143-S155.

[BCO81] E. B. Becker, G. F. Carey, J. T. Oden, *Finite elements. Volume I. An introduction*, The Texas Finite Element Series, I. Prentice-Hall Inc., Englewood Cliffs, NJ, (1981).

[BDFW00] M. Bonn, D. N. Denzler, S. Funk, M. Wolf, S. S. Wellershoff, J. Hohlfeld, Ultrafast electron dynamics at metal surfaces: Competition between electron-phonon coupling and hot-electron transport, *Phys Rev B* **61**(2), (2000), 1101-1105.

[BDV14] M. Basson, M. de Villiers, N. F. J. van Rensburg, Solvability of a Model for the Vibration of a Beam with a Damping Tip Body, *Jnl. Applied Mathematics Volume 2014*, Article ID 298092. http://dx.doi.org/10.1155/2014/298092

[BFAPB12] E. Balčiūnas, G. Y. Fan, G. Andriukaitis, A. Pugžlys, A. Baltuška, High-power top-hat pulses from Yb master oscillator power

amplifier for efficient optical parametric amplifier pumping, *Optics Letters* **37**(13) (2012), 2547-2549.

[BFI62] S. D. Brorson, J. G. Fujimoto, E. P. Ippen, Femtosecond electronic heat transfer dynamics in thin gold film, *Phys. Rev. Lett.* **59**, (1987), 1962-1965.

[BH69] K. J. Baumeister, T. D. Hamill, Hyperbolic heat conduction equation - a solution for the semi-infinite body problem, *ASME Jnl. of Heat Transfer* **91**, (1969), 543-548.

[Bla74] J. S. Blakemore, *SOLID STATE PHYSICS" (SECOND EDITION)*, (1974), W B Saunders Company Philadelphia, London, Toronto.

[Bro90] S. D. Brorson, *Femtosecond Thermomodulation Measurements of Transport and Relaxation in Metals and Superconductors*, RLE Technical Report No. 557 June 1990.

[BSV17] M. Basson, B. Stapelberg, N. F. J. Van Rensburg, Error estimates for semi-discrete and fully discrete Galerkin finite element approximations of the general linear second order hyperbolic equation, *Numerical Function Analysis and Optimization* **38**(4), (2017), 466-485.

[BTY11] T. Baba, N. Taketoshi, T. Yagi, Development of ultrafast laser flash methods for measuring thermophysical properties of thin films and boundary thermal resistances, *Jpn. Jnl. Appl. Physics* **50**, (2011), 11RA01.

[BV13] M. Basson, N. F. J. Van Rensburg, Galerkin finite element approximation of general linear second order hyperbolic equations, *Numerical Function Analysis and Optimization* **34**(9), (2013), 976-1000.

[BYTW10] T. Baba, N. Yamada, N. Taketoshi, H. Watanabe, M. Agoshima, T. Yagi, H. Abe, Y. Yamashita, Research and development of metrological standards for thermophysical properties of solids in the National Metrology Institute of Japan, *High Temperatures - High Pressures* **39**, (2010), 279-306.

[Cat48] M. C. Cattaneo, Sulla conduzione de calore (On the conduction of heat), *Atti del Semin. Mat. e Fis. Univ. Modena* **3**(3), (1948), 83-101.

[Cat58] M. C. Cattaneo, Sur une Frome de L'équation de la Chaleur Éliminant le Paradoxe D'une propagation Instantanée, *C. R. Acad. Sci. Paris Ser. I Math.* **247**, (1958), 431.

[CDL77] C. Cohen-Tannoudji, B. Diu, F. Laloë, *Quantum Mechanics, Volume One*, Wiley-Interscience Publication, John Wiley & Sons (1977).

[CT82] G. F. Carey, M. Tsai, "Hyperbolic heat transfer with reflection" Num. Heat Transfer **5**, (1982), 309-327.

[CVV18] D. Civin, N. F. J. Van Rensburg, A. J. Van Der Merwe, "Using energy methods to compare linear vibration models", Applied Mathematics and Computation, **321** (2018) 602-613. https://doi.org/10.1016/j.amc.2017.11.008

[CXW08] L. Cheng, M. Xu, L. Wang, "From Boltzmann transport equation to single-phase-lagging heat conduction", Int. Jnl. Heat Mass Transfer **51**, (2008), 6018-6023.

[DA08] A. Soleimani Dorcheh, M. H. Abbasi, "Silica aerogel; synthesis, properties and characterization", Journal of Materials Processing Technology **199** (2008), 10-26.

[DD19] B. Dekka, J. Dutta, Finite element methods for non-Fourier thermal wave model of bio heat transfer with an interface, Inter. J. Appl. Math. Comput., doi.org/10.1007/s12190-019-01304-8, 2019.

[Dug16] S. B. Dugdale, "Life on the edge: a beginner's guide to the Fermi surface", Phys. Scr. **91** (2016), 053009.

[EGJA06] R. A. Escobar, S. S. Ghai, M. S. Jhon, C. H. Amon *et al*, "Multi-length and time scale thermal transport using the lattice Boltzmann method with application to electronics cooling", Int. Jnl. Heat Mass Transfer **49**, (2006), 97-107.

[Eva98] L. C. Evans, "Partial differential equations", American Mathematical Society, 1998.

[GK66] R. A. Guyer, J. A. Krumhansl, "Solution of the Linearized Boltzmann Equation", Physical Review **148**(3) (1966), 766-778.

[HAA20] A. Hobiny, F. Alzahrani, I. Abbas, "Analytical estimation of temperature in living tissues using the TPL bioheat model with experimental verification", Mathematics **2020**, 8, 1188.

[Hil62] S. Hildebrandt, "Rand- und Eigenwertaufgaben bei stark elliptischen Systemen linearer Differentialgleichungen", Math. Analen, 148, 411-429.

[HMWM97] J. Hohlfeld, J. G. Müller, S. S. Wellershof, E. Matthias, "Time-resolved thermoreflectivity of thin gold films and its dependence on film thickness", Applied Physics B **64**, (1997), 387-390.

[HN09] P. E. Hopkins, P. M. Norris, "Contribution of Ballistic Electron Transport to Energy Transfer During Electron-Phonon Nonequilibrium in Thin Metal Films", Hnl. Heat Transf. **131**, April 2009, 043208-1–043208-8.

[HW06] C. Huang, H. Wu, An inverse hyperbolic heat conduction equation problem in estimating surface heat flux by the conjugate gradient method, J. Phys. D: Appl. Phys. 39 (2006), 4087-4096.

[Inm] D. J. Inman, "Engineering vibration", Prentice-Hall Inc, 1994, Englewood Cliffs, New Jersey.

[JLZ02] F. Jiang, D. Liu, J. Zhou, Non-Fourier Heat Conduction Phenomena in Porous Material Heated by Microsecond Laser Pulse, Microscale Thermophysical Engineering 6 (2002), 331-346.

[JO22] B. K. Jha, I. O. Oyelade, The role of dual-phase-lag (DPL) heat conduction model on transient free convection flow in an vertical channel, Partial Differential Equations in Applied Mathematics **5** (2022), 100266.

[JP89] D.D. Joseph, L. Preziosi, Heat Waves , Rev. Mod. Phys. 61(1) (1989), 41-73.

[JP90] D.D. Joseph, L. Preziosi, Addendum to the paper 'Heat Waves', Rev. Mod. Phys. 62(2) (1990), 375-391.

[Kam90] W. Kaminski, "Hyperbolic Heat Conduction Equation for Materials With a Nonhomogeneous Inner Structure", Jnl. Heat Transfer **112**(3), (1990), 555-560.

[KG07] K. Kim, Z. Guo, Multi-time-scale heat transfer modeling of turbid tissues exposed to short-pulsed irradiations, Computer Methods and Programs in Biomedicine **86** (2007), 112-123.

[Kit05] C. Kittel, "Introduction to Solid State Physics" (Eigth Edition), (2005), John Wiley & Sons, Inc.

[KKR16] D. Kumar, P. Kumar, K. N. Rai, "A study on DPL model of heat transfer in bi-layer tissues during MFH treatment", Computers in Biology and Medicine **75**, (2016), 160 - 172.

[KLT57] M. I. Kaganov, I. M. Lifshitz, M. V. Tanatarov, "Relaxation between electrons and crystalline lattices", Soviet Physics JETP, Vol. 4, 173-178.

[Kre89] E. Kreyszig, "Introductory Functional Analysis with Applications" (1989), John Wiley & Sons.

[KSR16] D. Kumar, S. Singh, K. N. Rai, "Analysis of classical Fourier, SPL and DPL heat transfer model in biological tissues in presence of metabolic and external heat source", Heat and Mass Transfer **52**(6), (2016), 1098-1107.

[Lam13] T. T. Lam, Int Jnl Heat and Mass Transfer 56 (2013), 653-666.

[LC04] K. Liu, H. Chen, Numerical analysis for the hyperbolic heat conduction problem under a pulsed surface disturbance, Appl. Math. Comp. 159 (2004), 887-901.

[LCP05] J. Li, P. Cheng, G.P. Peterson, J.Z. Xu, Rapid Transient Heat Conduction in Multilayer Materials with Pulsed Heating Boundary, Num. Heat Transf. A 47 (2005), 633-652.

[LT20] A. Lakatos, A. Trnìk, "Thermal Diffusion in Fibrous Aerogel Blankets", Energies **2020**, 13, 823.

[Mai19] D. Maillet, "A review of the models using the Cattaneo and Vernotte hyperbolic heat equation and their experimental validation", Int. Jnl. Thermal Sciences **139** (2019), 424-432.

[Max67] J. C. Maxwell, "On the Dynamical Theory of Gases", Phil. Trans. Royal Society of London, **157**, (1867), 49-88.

[MF53] P. M. Morse and H. Feshbach, "Methods of Theoretical Physics", McGraw-Hill, New York, (1953).

[MKVM95] K. Mitra, S. Kumar, A. Vedevarz and M. Moallemi, "Experimental Evidence of Hyperbolic Heat Conduction in Processed Meat", J. Heat Transfer **117**(3), (1995), 568-573.

[MR16] T. N. Mishra, K. N. Rai, "Fractional single-phase-lagging heat conduction model for describing anomalous diffusion", Propulsion and Power Research **5**(1), (2016), 45-54.

[MS21] E. Majchrzak, M. Stryczyński, Dual-phase lag model of heat transfer between blood vessel and biological tissue, Mathematical Biosciences and Engineering **18**(2) (2021), 1573-1589.

[MT14] E. Majchrzak, L. Turchan, "A numerical analysis of heating tissue using the two-temperature model", WIT Transactions on Engineering Sciences **83**, (2014), 477 - 488.

[Mul87] I. Müller, "ISIMM Kinetic theory and extended thermodynamics", Symposium on Kinetic Theory and Extended Thermodynamics, edited by I Müller and T Ruggeri (Pitagora Editrice, Bologna) (1987), 245.

[MYSY21] J. Ma, X. Yang, Y. Sun, J. Yang, "Theoretical analysis on thermal treatment of skin with repetitive pulses", Nature: Scientific Reports (2021)11:9958.

[NBB15] F. Nasri, M. F. Ben Aissa, H. Belmabrouk, Micoscale thermal conduction based on Cattaneo-Vernotte model in silicon on insulator and Double Gate MOSFETs, Appl. Therm. Engineering **76** (2015), 206-211.

[NTYB11] F. Nakamura, N. Taketoshi, T. Yagi, T. Baba, "Observation of thermal transfer across a Pt thin film at a low temperature using a femtosecond light pulse thermoreflectance method", Meas. Sci. Technol. **22** (2011), 024013 (9pp).

[OA12] J. Ordóñez-Miranda, J. J. Alvarado-Gil, "Determination of thermal properties for hyperbolic heat transport using a frequency-modulated excitation source", Int. Jnl. Eng. Sci. **50** (2012), 101-112.

[OT94] M. N. Özisik, D. Y. Tzou, "On the Wave Theory in Heat Conduction", Trans. ASME Jnl. Heat Transfer **116**, (1994), 526-535.

[Pat72] R. K. Pathria, "Statistical Mechanics", International Series in Natural Philosophy Volume 45, Pergamon Press Ltd, Headington Hill Hall, Oxford OX3 0BW, England.

[PJBA61] W. J. Parker, R. J. Jenkins, C. P. Butler, G. L. Abbott, "Flash method of determining thermal diffusivity, heat capacity, and thermal conductivity", Jnl. Appl. Phys. **32** (1961), 1679-1684.

[PR05] Y. Pinchover, J. Rubinstein, "An introduction to partial differential equations", Cambridge University Press, 2005.

[PRDSS00] G. S. Prakash, S. S. Reddy, S. K. Das, T. Sundararajan, K. N. Seetharamu, "Numerical Modelling of Microscale Effects in Conduction for Different Thermal Boundary Conditions", Num. Heat Transfer **A 38**, (2000), 513-532.

[QT92] T. Q. Qiu, C. L. Tien, "Short-pulse laser heating on metals", Int. Jnl. Heat Mass Transfer **35**(3), (1992), 719-726.

[QT93a] T. Q. Qiu, C. L. Tien, "Heat transfer mechanisms during short-pulse laser heating of metals", ASME Jnl. Heat Transfer **115**, (1993), 835-841.

[QT93b] T. Q. Qiu, C. L. Tien, "Size effect on nonequilibrium laser heating of metals", ASME Jnl. Heat Transfer **115**, (1993), 842-847.

[Ros90] H. M. Rosenberg, "The Solid State" (Third Edition), Oxford Universty Press, Walton Street, Oxford OX2 6DP, (1990).

[RPD03] W. Roetzel, N. Putra, S. K. Das, "Experiment and analysis for non-Fourier conduction in materials with non-homogeneous inner structure", Int. Jnl. Thermal Sciences **42**, (2003), 541-552.

[Sch71] M. Schechter, Principles of functional analysis, Academic Press, New York and Londen, 1971.

[SF73] G. Strang, G. J. Fix, An Analysis of the Finite Element Method, Prentice-Hall, Englewood Cliffs, New Jersey, 1973.

[Sho77] R. E. Showalter, "Hilbert space methods for partial differential equations".Pitman, London, 1977.

[Sin94] R. K. Singh, "Target ablation characteristics during pulsed laser deposition of thin films" Jnl. Non-Crystalline Solids **178**, (1994), 199-209.

[Sin10] N. Singh, "Two-Temperature Model of non-equilibrium electron relaxation: A Review", Int. Jnl. Modern Physics B **24(09)**, (2010), 1141-1158.

[SK20] S. K. Sharma, D. Kumar, "A Study on Non-Linear DPL Model for Describing Heat Transfer in Skin Tissue during Hyperthermia Treatment", Entropy **2020**, 22, 481.

[Sos18] G. C. Sosso, "Understanding the Thermal Properties of Amorphous Solids Using Machine-Learning-Based Interatomic Potentials Molecular Simulation", Volume 44, 2018 - Issue 11: Machine Learning.

[SS14] G. R. Ströher, G. L. Ströher, "Numerical thermal analysis of skin tissue using parabolic and hyperbolic approaches", Int. Comm. Heat and Mass Transf. **57**, (2014), 193-199.

[SV11] R. H. Sieberhagen, N. F. J. van Rensburg, "Tracking a sharp crested wave front in hyperbolic heat transfer", Appl. Math. Modelling **36**(8), (2011), 3399-3410.

[SVAIF94] C. K. Sun, F. Vallée, L. H. Acioli, E. P. Ippen, J. G. Fujimoto, "Femtosecond-tunable measurement of electron thermalization in gold", Phys. Rev. B **50**(20), (1994), 337-348.

[SYS07] S. Z. Shuja, B. S. Yilbas, S. Z. Shazli, Laser repetitive pulse heating influence of pulse duty on temperature rise, Heat Mass Transfer **43** (2007), 949-955.

[TA99] D. W. Tang, N. Araki, "Wavy, wavelike, diffusive thermal responses of finite rigid slabs to high-speed heating of laser-pulses", Int. J. Heat Mass Transfer **42** (1999), 855-860.

[TBO99] N. Taketoshi, T. Baba, A. Ono, "Observation of heat diffusion across submicrometer metal thin films using a picosecond thermoreflectance technique", Jpn. J. Appl. Phys. **38** (1999), L1268-L1271.

[TBO01] N. Taketoshi, T. Baba, A. Ono, "Development of a thermal diffusivity measurement system for metal thin films using a picosecond thermoreflectance technique", Meas. Sci. Technol. **12** (2001), 2064-2073.

[TC94] C. L. Tien, G. Chen, "Challenges in microscale conductive and radiative heat transfer", Jnl. Heat Transfer **116**, (1994), 799-807.

[TC01] D. Y. Tzou, K. S. Chiu, "Temperature-dependent thermal lagging in ultrafast laser heating", Int. Jnl. Heat Mass Transfer **44**, (2001), 1725-1734.

[TM94] G. Tas, H. J. Maris, "Electron diffusion in metals studied by picosecond ultrasonics", Phys. Rev. B **49**(21) (1994), 15046-15054.

doi:10.3390/en11113163

[TWZWO18] S. Tan, J. Wu, Y. Zhang, M. Wang, Y. Ou, A model of ultrashort pulsed laser ablation of metal with considering plasma shielding and non-Fourier effect, Energies **11** (2018), 3163.

[TYB09] N. Taketoshi, T. Yagi, T. Baba, "Effect of Synthesis Condition on Thermal Diffusivity of Molybdenum Thin Films Observed by a Picosecond Light Pulse Thermoreflectance Method", Jpn. J. Appl. Phys. **48** (2009), Number 5S2.

[TZ98] K. K. Tamma, X. Zhou, "Macroscale and microscale thermal transport and thermo-mechanical interactions: some noteworthy perspectives", Jnl. Thermal Stresses **21**, (1998), 405-449.

[Tzo93b] D. Y. Tzou, "An engineering assessment to the relaxation time in thermal wave propagation", Int. J. Heat Mass Transfer **36(7)**, (1993), 1845-1851.

[Tzo95a] D. Y. Tzou, "A Unified Field Approach for Heat Conduction from Macro- to Micro-Scales", Trans. ASME Jnl. Heat Transfer **117**(9), (1995), 8-16.

[Tzo95b] D. Y. Tzou, "The generalized lagging response in small-scale and high-rate heating", Int. Jnl. Heat Mass Transfer **38**(17), (1995), 3231-3240.

[Tzo95c] D. Y. Tzou, "Experimental support for the lagging behaviour in heat propagation", Journal of Thermophysics and Heat Transfer **9**(4), (1995), 686-693.

[Tzo97] D. Y. Tzou, "Macro- to Microscale Heat Transfer: The Lagging Behaviour", Series in chemical and mechanical engineering, Taylor and Francis, Washington (1997).

[ULY21] T. Ullsperger, D. Liu, B. Ýurekli, G. Matth́aus, L. Schade, B. Seyfarth, H. Kohl, R. Ramm, M. Rettenmayr, S. Nolte, "Ultra-short pulsed laser powder bed fusion of Al-Si alloys: Impact of pulse duration and energy in comparison to continuous wave excitation", Additive Manufacturing 46 (2021), 102085.

[Ver58a] P. Vernotte, Les Paradoxes de la Théorie Continue de L'équation de la Chaleur, C. R. Acad. Sci. Paris Ser. I Math., 246 (1958), 3154-3155.

[Ver58b] P. Vernotte, "La Véritable Équation de la Chaleur", C. R. Acad. Sci. Paris Ser. I Math., **247**, (1958), 2103.

[VS19] N. F. J. van Rensburg, B. Stapelberg, "Existence and uniqueness of solutions of a general linear second-order hyperbolic problem", IMA Journal of Applied Mathematics **84**(1), (2019), 1-22.

[VV02] N. F. J. Van Rensburg, A. J. Van Der Merwe, "Analysis of the solvability of linear vibration models", Applicable Analysis **81**(5), (2002), 1143-1159.

[VVS21] A. J. Van Der Merwe, N. F. J. Van Rensburg, R. H. Sieberhagen, "Comparing the dual phase lag, Cattaneo-Vernotte and Fourier heat conduction models using modal analysis", Appl. Math. Comp. **396** (2021), 125934.

[Wei95] H.F. Weinberger, A First Course in Partial Differential Equations: with Complex Variables and Transform Methods, Dover Publications Inc, New York (1995).

[WHGM99] S. S. Wellershoff, J. Hohlfeld, J. Güdde, E. Matthias, "The role of electron-phonon coupling in femtosecond laser damage of metals", Applied Physics A 69, (1999), S99-S107.

[Win16] M. C. Wingert, "Thermal transport in amorphous materials: a review", Semicond. Sci. Technol. **31**(11), (2016), 113003.

[WXZ01] L. Q. Wang, M. T. Xu, X. Zhou, "Well-posedness and solution structure of dual-phase-lagging heat conduction", Int. Jnl. Heat Mass Transfer **44**, (2001), 1659-1669.

[YA20] H. M. Youssef, N. A. Alghamdi, "The exact analytical solution of the dual-phase-lag two-temperature bioheat transfer of a skin tissue subjected to constant heat flux", Nature: Scientific Reports (2020)10:15946.

[YKN04] B. S. Yilbas, O. Khan, I. Z. Naqavi, Laser pulse heating and thermal stress developments: elastoplastic analysis, Proceedings of the Institution of Mechanical Engineers Part B: Journal of Engineering Manufacture, April 2004, 375-388.

[Yil93] B. S. Yilbas, "Analytical solution for the heat conduction mechanism appropriate to the laser heating process", Int. Comm. Heat Mass Transfer **20**, (1993), 545-555.

[Yil97] B. S. Yilbas, "Analytical solution for time unsteady laser pulse heating of semi-infinite solid", Int. J. Mech. Sci. **39**(6), (1997), 671-682.

[Yil12] B. S. Yilbas, Laser Heating Applications: Analytical Modelling, Elsevier, 225 Wyman Street, Waltham, MA 02451, USA, First Edition (2012).

[YS97a] B. S. Yilbas, S. Z. Shuja, "Heat transfer analysis of laser heated surfaces – conduction limited case" Appl. Surf. Science **108**, (1997), 167-175.

[ZCG14] M. Zhang, B. Cao, Y. Guo, "Numerical studies on damping of thermal waves", Int. Jnl. of Thermal Sciences **84** (2014), 9-20.

[ZCL17] Y. Zhang, B. Chen, D. Li, "Non-Fourier effect of laser-mediated thermal behaviors in bio-tissues: A numerical study by the dual-phase-lag model", **108**, (2017), 1428-1438.

[Zei95] E. Zeidler, "Applied Functional Analysis: Applications to Mathematical Physics", Springer-Verlag, New York, 1995.

[Zie77] O. C. Zienkiewicz, The finite element method, New York : McGraw-Hill, c1977, 3rd expanded and revised edition.

[ZSY20] Q. Zhang, Y. Sun, J. Yang, "Bio-heat response of skin tissue based on three-phase-lag model", Scientific Reports: Nature Research, (2020) 10:16421.

Appendix A

Frequently used notation

Table A.1 includes frequently used or important mathematical notation, indicating where a definition or reference to it occurs in the thesis.

Table A.2 includes nomenclature associated with heat transfer and laser pulse parameters.

Table A.1: Mathematics notation

Symbol	Description	Section
Ω	n-dimensional bounded domain	4.2
$\partial\Omega$	Boundary of Ω	4.2
$(f,g)_\Omega$	Inner product: $(f,g)_\Omega = \int_\Omega fg$	4.3
J	Bounded or unbounded interval containing zero	4.4
$\mathcal{L}^2(\Omega)$	Square integrable functions	4.3
$u'(t) \in Y$	Weak partial derivative w.r.t. norm of Y	4.4
$H^m(\Omega)$	Sobolev space: the subspace of functions in $\mathcal{L}^2(\Omega)$ with weak partial derivatives up to order m	4.4

Table A.2: Physics notation

Symbol	Description
α	Thermal diffusivity
q	Heat flux
T	Temperature
τ	Relaxation time
τ_q	Lag time associated with q
τ_T	Lag time associated with ∇T
t	Time
d	Length
t_d	Heat diffusion time
$t_{1/2}$	Half-time
t_p	Pulse width
τ_p	Pulse period
r_d	Duty ratio: $r_d = t_p/\tau_p$